Enhanced Diagnosis of Breast Cancer through Detection of Exosomes using *ex-situ*, *in-situ,* and Solid State Dewetted Nanoplasmonic Platforms

Duraichelvan Raju

A Thesis

In the Department of

Mechanical, Industrial and Aerospace Engineering

Presented in Partial Fulfillment of the Requirements

For the Degree of

Doctor of Philosophy (Mechanical Engineering)

at Concordia University

Montréal, Québec, Canada

May 2024

CONCORDIA UNIVERSITY
School of Graduate Studies

This is to certify that the thesis prepared

By: **Duraichelvan Raju**

Entitled: **Enhanced Diagnosis of Breast Cancer through Detection of Exosomes using *ex-situ*, *in-situ,* and Solid State Dewetted Nanoplasmonic Platforms**

and submitted in partial fulfillment of the requirements for the degree of

Doctor of Philosophy (Mechanical Engineering)

complies with the regulations of the University and meets the accepted standards with respect to originality and quality.

Signed by the final examining committee:

Dr. Wei-Ping Zhu	Chair
Dr. Krishnan Venkatakrishnan	External Examiner
Dr. Pouya Valizadeh	Arms-Length Examiner
Dr. Sivakumar Narayanswamy	Examiner
Dr. Behrooz Yousefzadeh	Examiner
Dr. Anirban Ghosh	Thesis Co-Supervisor
Dr. Muthukumaran Packirisamy	Supervisor

Approved by

Dr. Martin D. Pugh, Chair
Department of Mechanical, Industrial and Aerospace Engineering

July, 5 , 2024

Dr. Mourad Debbabi, Dean
Gina Cody School of Engineering and Computer Science

Abstract

Enhanced Diagnosis of Breast Cancer through Detection of Exosomes using *ex-situ*, *in-situ,* and Solid State Dewetted Nanoplasmonic Platforms

Duraichelvan Raju, Ph.D.

Concordia University, 2024

Breast cancer is one of the leading causes of death and the second most common among women in Canada. This thesis aims to develop sensing nanoplasmonic platforms for the early diagnosis of breast cancer through the detection of exosomes. The adsorption of bio or organic molecules on metallic nanoparticles leads to a plasmon band shift towards longer wavelengths; a phenomenon central to Localized Surface Plasmon Resonance (LSPR). This study aims to develop nano-structured arrays of plasmonic platforms for the high-performance detection of sub-micron biological entities such as viruses, exosomes, and other extracellular vesicles (EVs) ranging from 30 - 1000 nm.

This thesis particularly focuses on developing and optimizing unique plasmonic platforms for detecting EVs/exosomes derived from breast cancer cell lines. These EVs/exosomes are nano-sized (30 - 100 nm), cargo-bearing vesicles secreted by almost all cell types, consisting of a lipid bilayer encasing a semi-fluid core of cytoplasmic materials, including proteins, nucleic acids, and exhibit significant heterogeneity, reflecting their cellular origin. Despite their potential as biomarkers for diseases like cancer, their heterogeneity and overlapping physicochemical properties with other vesicles pose challenges for effective detection, separation, and purification.

In the beginning, two different types of platforms, one fabricated by an *ex-situ* method and the other by an *in-situ* method, were investigated to find out which was more convenient in terms of sensitivity for detecting EVs/exosomes. Different fabrication conditions have been explored and the sensitivity of the platforms has been measured. A sensing protocol involving several steps has been developed and optimized for detecting EVs/exosomes. It has been found that the platform prepared by an *ex-situ* method, that is, by convective assembly of gold colloidal particles, is more sensitive than the silver (Ag)-PDMS and gold (Au)-PDMS nanocomposite platforms fabricated by an *in-situ* method. In the case of gold (Au)-PDMS, gold is segregated under the surface of the polymer, without direct contact with the environment, and thus not suitable for detection.

Additionally, to improve the refractive index sensitivity, novel platforms have been investigated. This thesis is further dedicated to developing and characterizing new plasmonic platforms, based on nano-islands/particles, fabricated from thin gold films e-beam deposited on an adhesion layer. The nano-islands/particles fabricated by the dewetting of the uniform gold films deposited on Chromium (Cr) (Cr-Au) and Indium Tin Oxide (ITO) adhesion layers (ITO-Au), respectively. Subsequently, based on the characterization results, the Cr-Au platform has been identified for the detection of EVs/exosomes. In addition, a direct detection method as well was developed without any surface chemistry modification of the plasmonic platform. The detection results obtained by using this novel platform and method were compared with the results of the *ex-situ,* and *in-situ* platforms studied earlier in this thesis work. It was found that, with the novel platform and method, the sensitivity of detection improved around 1.5 times, and the time taken for the detection was reduced by around one-fourth of the time of the earlier method.

This work also provided invaluable information, regarding the adhesion layers, and their characteristics, especially stability, in association with very thin gold films. The phenomena of interdiffusion and oxidation during the deposition and heat treatment and their effect on detection have been studied as well.

Overall, this work contributes to the development of cost-effective, high-performance nanoplasmonic platforms, for early diagnosis of breast cancer establishing a foundation for their broader application in detecting and analyzing diverse biological and environmental samples.

Acknowledgments

This thesis is the culmination of a joyful, challenging, and memorable phase of my academic journey. Words cannot express how thankful I am to everyone who has been a part of this journey with me. To express my gratitude, I will do my best to articulate it but there are simply no words that can convey the depth of my thankfulness and respect for all of you. People who know me well, won't be surprised that this acknowledgment is going to be lengthy.

Firstly, I would like to begin my acknowledgment by acknowledging Concordia University which is located on unseeded Indigenous lands. The Kanien'kehá:ka Nation is recognized as the custodians of the lands and waters on which we gather today. Tiohtià:ke/Montréal is historically known as a gathering place for many First Nations. Today, it is home to a diverse population of Indigenous and other peoples. We respect the continued connections with the past, present, and future in our ongoing relationships with Indigenous and other peoples within the Montreal community. This doctoral research work was accomplished at Concordia University.

I would like to extend my heartfelt gratitude and sincere thanks to my supervisor, Prof. Muthukumaran Packirisamy, for providing me with the opportunity to do this doctoral research under his guidance and it is a great honor for me to carry out the research under his supervision. I am sincerely grateful for his consistent support, guidance, and planned vision in research, which have been vital assets and a great driving force throughout this process.

I would like to emphasize that during my academic journey, Prof. Muthu provided me with the opportunity to help establish a Class 2 Biolab as part of the Optical Bio Microsystems Laboratory and an aeroelasticity lab as part of the Mechanical Industrial and Aerospace Engineering. He also allowed me to collaborate with other members of the grant team, which enhanced my leadership skills and improved my grant writing abilities. It is important to mention that his assistance has been invaluable and overwhelming during my academic endeavour. Therefore, I am profoundly indebted to him.

I am extremely thankful to my co-supervisor Dr. Anirban Ghosh for his invaluable guidance, and insightful teaching on the biological aspects of this research work since the beginning of my academic journey and continuing. So, I want to express my sincere appreciation to him.

I want to express my sincere gratitude to Dr. Simona Badilescu for her unwavering love, inspiration, guidance, and support during this journey. Without her, I would feel incomplete. She has been instrumental in teaching me the fundamentals of this research work from the beginning and continues to do so. These principles are crucial to my ability to conduct my research, and I owe her a great deal.

I am profoundly grateful to Prof. Sivakumar Narayanswamy and Prof. Rama Bhat, for their invaluable guidance and support during my Ph.D. studies. I particularly appreciate their unwavering support whenever I have requested a time limit extension for this academic journey.

I would like to express my sincere gratitude to the members of my Ph.D. examination committee. This includes the chair, Dr. Wei-Ping Zhu; the external examiner, Dr. Krishnan Venkatakrishnan; the arms-length examiner, Dr. Pouya Valizadeh from the ECE department; and the examiners, Dr. Sivakumar Narayanswamy and Dr. Behrooz Yousefzadeh from the MIAE department. I appreciate their acceptance of this role, their time in reading my thesis, and their valuable suggestions and comments. Thank you so much for being part of this final journey.

I am thankful to Prof. Subhash Rakheja for his concern about the progress of my research work and for motivating me.

I would like to thank Dr. Srinivas Bathini, Keshava Praveena Neriya Hegade, Kyana Mohammadi, Dhilippan Mamsapuram Panneerselvam, and Sanaz Naghdi for their collaboration, support and discussions as part of this research work.

I also wanted to thank Dr. Shanmugasundaram Pakkiriswami for his collaboration, motivation, discussion, and support as part of this research work.

I want to express my gratitude to the following people for their assistance with the following measurements: Mr. Mazen Samara and Dr. Dmytro Kevorkov (Concordia University) for their assistance with SEM imaging, Ms. Moraille Patricia (Université de Montréal) for helping with AFM measurements, Dr. Lise Guichaoua and Mr. Nicolas Brodusch (McGill University) for their help with FESEM imaging, and Dr. Daniel Chartrand (Université de Montréal) for his assistance with XRD measurement.

I would like to thank Dr. Jayan Ozhikandathil for his ongoing support and inspiration thus far, as well as for teaching me all the fundamentals of micro-nano manufacturing and experimental work at the start of this journey and for continuing with the PhD study.

I would like to thank Dr. Arvind Chandrasekaran, and Dr. Pierre Pottier, for their navigation and support at the beginning of this journey and for teaching me the fundamental concepts of microsystems and optics, and Dr. Imran Deen for helping me out while preparing the thesis.

I am delighted to be a member of the Optical Bio Microsystems (OBML), and I am grateful to my amazing lab partners, with whom I have shared many moments and conversations. Without their help and support, I could not have made this Ph.D. journey. Therefore, I would like to thank all the past and present members of the OBML lab, Dr. Mohsen Habibi, Dr. Mostapha Marzban, Dr. Jalal Abdul Hadi, Dr. Ahmad Sohrabi Kashani, Dr. Kirankumar Kuruvinashetti, Dr. Hemanth Kumar Tanneru, Dr. Ehsan Yazdan Panah Moghadam, Dr. Naghmeh Bandari, Dr. Subhathirai Subramaniyan Parimalam, Mahdi Derayatifar, Mehdi Kharazmi, Mohammad Reza Fasihani Fard, Vahid Karamzadeh, Shervin Foroughi, Hassan Gharaei, K. R. Jolvis Pou, Iris Handa, Donna Legault, Michael Fanous, Soroush Rahimi, Saber Haghgoo, and Floriane Miquet-Westpha.

I am grateful for the financial assistance I received for my studies from the School of Graduate Studies (SGS), Gina Cody School of Engineering (GCS), and the Mechanical, Industrial, and Aerospace Engineering (MIAE) Department. I was also awarded a Doctoral Fellowship, an International Tuition Fees Remission Award from the SGS, and a Doctoral Seminar poster presentation award from the MIAE department.

I would like to thank Prof. Martin Pugh, the Chair of the MIAE department for all his concerns, motivation, support, and guidance throughout this journey.

I am greatly thankful to Prof. Mourad Debbabi, the Dean of GCS for all his timely assistance and support whenever I reached out to him and also for his constant encouragement throughout the Ph.D. study. I am also thankful to Associate Dean Dr. Emad Shihab for his assistance and support. I would like to extend my thanks to the Associate Deans and all the staff of the GCS Dean’s office.

I want to express my gratitude to SGS Dean Dr. Effrosyni (Faye) Diamantoudi for all of her help, encouragement, and care. I would like to express my gratitude to the associate deans and staff of the SGS Dean's office, particularly Mr. Raja Bhattacharya and Mr. Nadeem Butt, for their unwavering support.

I would like to express my thankfulness to Dr. Anne Whitelaw, Provost and Vice-President Academic, for her unwavering care and support.

I am thankful to all the staff of the Mechanical, Industrial, and Aerospace Engineering Department for their kind assistance, especially Ms. Leslie Hossein, Dr. Peter Tzenov, and Ms. Maureen Thuringer, who supported me throughout my doctoral journey. I also want to express my gratitude to Ms. Charlene Wald, Ms. Arlene Zimmerman, Mr. Peter Sakaris, Mr. Tianhe Wen, Ms. Sophie Merineau, Ms. Natalie Charles, and others for their support.

I am grateful for the support and assistance of my friends Dr. Hari Babu Boppudi, Dr. Sharham Shokouhfar, Dr. Amir Hooshiar, Dr. Hamid Ebrahimi Orimi, Dr. Shambhu Kumar Gupta, Darshan Dorugade, Navaneethan Sundaresan, Vinodh Krishna Caralapatti, Satvik Jagadeesh and others as my list might be an endless one, during this PhD journey.

I would like to express my sincere gratitude to Prof. Avinash Deshpande, Prof. Biswajit Paul, Prof. N. Udaya Shankar, Prof. Andal Narayanan, and Prof. V. Lakshminarayanan for supporting my application to the PhD program. I am also thankful to all my well-wishers, especially Mr. Ateequlla Mohamed, Mr. Ramesh Raman., Rishin P.V, Mr. Sridhar. B, Mr. P. Sasi Kumar, Dr. A. Raghunathan, Dr. Dhanajay Anand, Ibrahim, Mr. P.Srinivasa, Mr. K. Krishnama Raju, and the active and retired members of the Mechanical Engineering Services and Electronics Engineering Group Department of the Raman Research Institute in Bengaluru, India. Their encouragement and inspiration have played a significant role in my decision to pursue a Ph.D. Additionally, Prof. V. Radhakrishnan (son of Nobel laureate Sir. C.V. Raman), Dr. A. Krishnan, and Prof. Hema Ramachandran would be pleased to learn that I am in the final stage of my Ph.D. Sadly, they are no longer with us.

I am very much thankful to my childhood friend K. Mohammed Billal who encouraged and supported me during my difficult times.

I would like to express my sincere thanks to Dr. Packirisamy's family for having extended their support and help whenever needed.

Last but not least, I owe a huge debt of gratitude to my beloved wife, and daughter without their love, support, inspiration, companionship, and sacrifices none of my life's achievements would have been possible. I also want to extend my thanks to my sisters-in-law, brother-in-law, mother-in-law, and their family for their unwavering support throughout this journey. I am grateful to my brother Mahendiran and sister Nagalakshmi for taking care of my parents while I was away. Lastly, I want to thank my father and mother for their efforts throughout my life. Their prayers and blessings have always been with me.

This Thesis Work Is Dedicated

To

My Wife *(Yamuna)*, Daughter *(Mokshita)*,

My Father *(Raju)* and Mother *(Rajeswari)*

Contribution of Authors

The authors have reviewed and approved the contents of each final manuscript presented in the literature review and this study, and have contributed to the work as follows:

*Chapter 2: **Raju, D**.; Bathini, S.; Badilescu, S.; Ghosh, A.; Packirisamy, M. Microfluidic Platforms for the Isolation and Detection of Exosomes: A Brief Review. Micromachines, **2022**,13, 730. https://doi.org/10.3390/mi13050730.*

Here is the contribution of authors to this literature review:

Duraichelvan Raju: contributed to conceptualization, writing - original, review/editing, and visualization.

Bathini Srinivas: writing-review/editing, and visualization.

Simona Badilescu: contributed to conceptualization, writing- review/ editing.

Anirban Ghosh: contributed to conceptualization, writing- review/ editing, and supervision.

Muthukumaran Packirisamy: contributed to conceptualization, writing- review/ editing supervision.

*Chapter 3: S. Badilescu, **D. Raju**, S. Bathini, M. Packirisamy, "Gold Nano-Island Platforms for Localized Surface Plasmon Resonance Sensing: A Short Review", Molecules, 2020, 25(20), 4661.*

Here is the contribution of authors to this literature review:

Simona Badilescu: contributed to conceptualization, writing - original draft.

Duraichelvan Raju: contributed to conceptualization, writing- review/editing, and visualization.

Bathini Srinivas: contributed to conceptualization, figures, writing- review/editing.

Muthukumaran Packirisamy: contributed to conceptualization, writing- review/editing, and supervision.

Chapter 4: ***D. Raju,*** *S. Bathini, S. Badilescu, R.J. Ouellette, A. Ghosh, M. Packirisamy, "Exosomes Detection by a Label-free Localized Surface Plasmonic Resonance Method", ECS Trans. 2016, Vol. 75, Issue 17, 11-17.*

Here is the contribution of the authors to this study:

Duraichelvan Raju: contributed to conceptualization, experimental work, data curation, writing - original draft, writing- review/editing.

Bathini Srinivas: contributed to conceptualization, help in experimental work, figures, and writing-review/editing.

Simona Badilescu: contributed to conceptualization, writing- review/editing.

Rodney J. Ouellette: provided the materials.

Anirban Ghosh: contributed to conceptualization, writing- review/editing, and supervision.

Muthukumaran Packirisamy: contributed to conceptualization, writing- review/editing, and supervision.

Chapter 5: ***D. Raju****, S. Bathini, S. Badilescu, R.J. Ouellette, A. Ghosh, M. Packirisamy, "Study of Detection and Capture of Exosomes by Using the Morphologies of Ex-Situ and In-Situ Nanostructures", J. Electrochem. Soc., 2019, 166(9) B3001-B3006.*

Here is the contribution of the authors to this study:

Duraichelvan Raju: contributed to conceptualization, experimental work, data curation, writing - original draft, writing- review/editing.

Bathini Srinivas: contributed in conceptualization, help in experimental work review, writing-review/editing.

Simona Badilescu: contributed to conceptualization, writing- review/editing. Rodney J. Ouellette: provided the materials.

Anirban Ghosh: contributed to conceptualization, review, and editing.

Muthukumaran Packirisamy: contributed in conceptualization, review/editing, and supervision.

*Chapter 6: S. Bathini, **D. Raju**, S. Badilescu, M. Packirisamy, "Effect of Cross-Linking and Thermal Budget on Plasmonic Sensing and Sub-Surface Segregation of In-Situ Synthesized Gold in Polymer-Nano Composite", J. Nanopart Res, 2021, 23, Article 21.*

Here is the contribution of the authors to this study:

Duraichelvan Raju: contributed to conceptualization, data curation, writing - original draft, writing- review/editing.

Bathini Srinivas: contributed to conceptualization, data curation, writing - original draft, writing-review/editing.

Simona Badilescu: contributed to conceptualization, writing- review/editing.

Muthukumaran Packirisamy: contributed to conceptualization, writing- review/editing, and supervision.

*Chapter 7: **D. Raju**, S. Bathini, S. Badilescu, R.J. Ouellette, A. Ghosh, M. Packirisamy, "LSPR Detection of Extracellular vesicles using a silver-PDMS nano-composite platform suitable for sensor networks", Enterprise Information System (EIS), 2018, 14(4), 532-541.*

Here is the contribution of the authors to this study:

Duraichelvan Raju: contributed to conceptualization, data curation, writing - original draft, writing- review/editing.

Bathini Srinivas: contributed to conceptualization, figure, writing- review/editing.

Simona Badilescu: contributed to conceptualization, writing- review/editing. Rodney J. Ouellette: provided the materials.

Anirban Ghosh: contributed to conceptualization, writing- review/editing, and supervision.

Muthukumaran Packirisamy: contributed to conceptualization, writing- review/editing, and supervision.

Chapter 8: Development of Gold Nano-island Platforms Prepared Through Dewetting of e-beam Deposited Films for the Detection of Extracellular Vesicles (EVs).

Here is the contribution of this study:

Duraichelvan Raju: contributed to conceptualization, experimental work, data curation, writing - original draft, review/editing.

Kyana Mohammadi: contributed to the conceptualization and helped in the experimental work.

Simona Badilescu: contributed to conceptualization, writing- original draft, review/editing.

Imran Deen: contributed to the visualization

Anirban Ghosh: contributed to conceptualization, writing- review/editing, and supervision.

Muthukumaran Packirisamy: contributed to conceptualization, writing- review/editing, and supervision.

Table of Contents

List of Figures

List of Tables

List of Nomenclature

List of Symbols

A	Hamaker constant
a.u	Absorbance units
$A\gamma_{12}$	Interfacial free energy
A	Surface area
C	Concentration
d	Adsorbate layer thickness
F_s	Surface free energy
ΔF_s	Surface free energy change
f(θ)	Geometric factor, based on the particle contact angle θ
l_d	Decay length of the electromagnetic field
m	Refractive sensitivity of the nanostructure
θ	Particle contact angle
γ	Surface tension of the metal
γ_1	Surface tension of the particle
γ_{12}	Interfacial tension
t	Time
t_{synth}	Synthesis time
T	Temperature
Δn	Change in Refractive Index
Ø	Diameter
λ	Wavelength
λ_{max}	Peak wavelength

$\Delta\lambda_{max}$	Peak wavelength shift
$\Delta\lambda_{90\%}$	Bandwidth at 90% of peak wavelength
η	Monomer ratio

Abbreviations

AFM	Atomic force microscopy
ATCC	American Tissue and Culture Collection
Ag	Silver
Au	Gold
AuNPs	Gold nanoparticles
BCA	Bicinchoninic acid assay
CCM	Cell-conditioned medium
CT	Computed Tomography
CTC	Circulating tumor cells
ctDNA	Circulating tumor DNA
Cr	Chromium
DNA	Deoxyribonucleic acid
DIW	De-ionized Water
DMF	Dimethylformamide
DLS	Dynamic light scattering
EDC	N-(3-Dimethylaminopropyl)-N′-ethyl carbodiimide hydrochloride
ELISA	Enzyme-linked immunosorbent assay
EM	Electron microscopy
EVs	Extracellular Vesicles
FBS	Fetal Bovine Serum

FC	Flow cytometry
FE	Finite element
FESEM	Field Emission Scanning Electron Microscopy
FTO	Fluorine-doped tin oxide
GBM	Glioblastoma
GCS	Gold colloidal solution
HSP	Heat Shock Proteins
IGF	Insulin-like growth factor
ILV	Intraluminal Vesicles
IPA	Isopropyl Alcohol
ISTH	International Society for Thrombosis and Haemostasis
ISEV	International Society for Extracellular Vesicles
ITO	Indium tin oxide
LC-MS/MS	Liquid chromatography-tandem mass spectrometry
LOC	Lab-on-a-Chip
LSPR	localized surface plasmon resonance
MF	Microfluidic
MPTMS	3-mercaptopropyl-trimethoxysilane
MVE	Multivesicular endosomes
MCF-7	Michigan Cancer Foundation-7
mRNA	Messenger Ribonucleic acid
microRNA	Micro Ribonucleic acid
NTA	Nanoparticle tracking analysis
NGS	Next-generation sequencing

NHS	N-Hydroxy succinimide
PBS	Phosphate-buffered saline
PDMS	Poly (dimethyl siloxane)
PEG	Polyethylene glycol
POC	Point-of-care
POCT	Point-of-care testing
rBST	Recombinant Bovine Somatotropin
RNA	Ribonucleic acid
rRNA	Ribosomal ribonucleic acid
RI	Refractive Index
RIU	Refractive index unit
RIA	Radioimmunoassay
SAM	Self-assembled monolayer
SEC	Size exclusion chromatography
SEM	Scanning Electron Microscopy
SERS	Surface-Enhanced Raman Scattering
SPP	Surface plasmon polaritons
SPR	Surface plasmon resonance
TRPS	Tunable resistive pulse sensing
UC	Ultracentrifuge
WB	Western blotting
XPS	X-ray photoelectron spectrometry
XRD	X-ray diffraction
3D	Three dimensional

Chapter 1. Introduction

1.1. Background

The basic building blocks of any living entity are the cells. The human body contains trillions of cells as shown in Figure 1-1 and each of them sheds smaller vesicles, in response to internal and external stimuli. These smaller vesicles are collectively termed extracellular vesicles (EVs) and they are released by both eukaryotic and prokaryotic cells[1] [1,2]

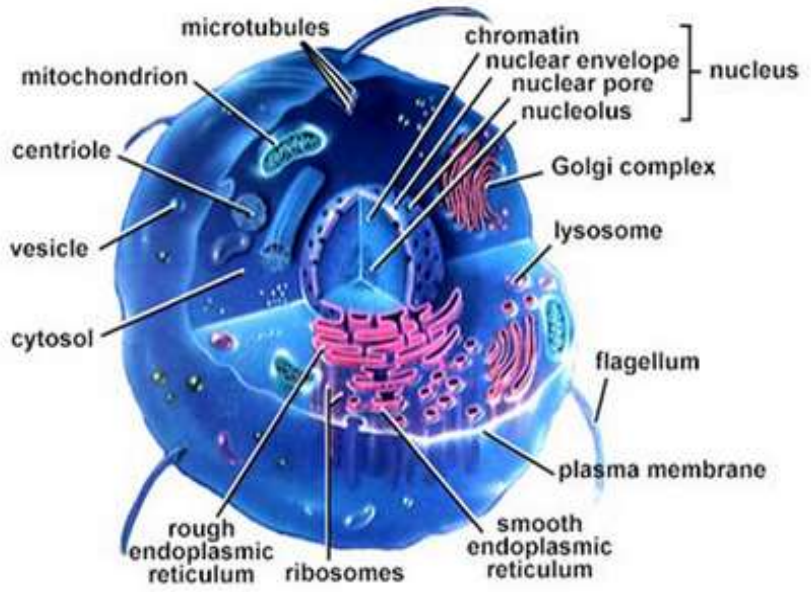

Figure 1-1: Structure of cell [3].

EVs are of different sizes, mostly spherical particles, and are enclosed by a phospholipid bilayer. The typical diameter of these vesicles ranges from 30 to 1000 nm [4–8], which is about 100-fold smaller than the smallest cell. The cells release these vesicles in their outer environment and which is why body fluids like blood, urine, saliva, breast milk, amniotic fluid, seminal fluid contain them. The vesicles are also released into culture media (called conditioned media) when cells are grown in the laboratory. Thus both, body fluids and conditioned culture media (CM) contain numerous cell-derived vesicles with varying concentrations [9–12].

[1] Cells with a true nucleus, or a nucleus enclosed in a membrane, are called **eukaryotic cells**. This is in contrast to **prokaryotic cells** that do not have a membrane-bound nucleus.

Increasingly, EVs are linked to multiple fundamental physiological and cellular functions and are found to play a major role in intercellular communications, coagulation, disease initiation/progression, and waste management**.** In recent years, a growing interest and attention in the clinical applications of EVs have been noticed because of their presence in the body fluids. The blood-brain barrier is a highly selective permeability barrier that maintains the separation of the circulating blood from the brain extracellular fluid. Thus, EVs are potentially useful for disease prognosis, and biomarker identification including cancers of the central nervous system. Owing to their small size and heterogeneity there is a challenge in their detection and classification [13,14].

EVs were first discovered in 1946 by Chargaff and West [15]. Two decades later in 1967, Wolf et al. studied them by SEM and named them "platelet dust". The platelets (thrombocytes) are cells in the blood that possess coagulant properties. The size of this "platelet dust" is between 20 and 50 nm and the density was found to be 1.020 to 1.025 g/ml [16].

Henceforth, research on the diversified role of EVs in biology has gained momentum during the last few years due to their usefulness as valuable source material for liquid biopsy [17]. Interestingly, the Nobel Prize awarded for Physiology/ Medicine in 2013 jointly to James E. Rothman, Randy W. Schekman, and Thomas C. Südhof for their discoveries of machinery regulating vesicle traffic, a major transport system in our cells has further attracted many researchers to work on these EVs in depth.

1.2. Breast cancer MCF 7 EVs/exosomes

Breast cancer is a cancer that develops from breast tissues and it is one of the leading causes of death in Canada [18]. MCF-7[2] is a breast cancer cell line isolated in 1970 from a 69-year-old white woman. The breast cancer cell line (MCF7) was purchased from the American Tissue and Culture Collection (ATCC) and adapted for continuous long-term conditioned cell culture media harvest in the two-compartment bioreactor at the Atlantic Cancer Research Institute. The EVs/exosomes were derived from the cell culture media after a series of centrifuge and ultra-centrifuge steps. In the next section potential techniques that could be adopted for the detection and isolation of techniques.

[2] **MCF-7** is the acronym of Michigan Cancer Foundation-7, referring to the institute in Detroit where the cell line was established in 1973

1.3. Localized surface plasmon resonance (LSPR) technique for detection and isolation of EVs/exosomes

In the past, for the detection of bovine growth hormone (bGH), also known as bovine somatotropin (bST a polypeptide molecule having a chain of 191 amino acids [19]) the label-free LSPR technique has been used, and proven to be effective. It is also noticeable from the sensitivity plot as shown in Figure 1-2 that the LSPR technique is best suited, as the detection limit is in the range of 1-5 ng/ml among the various LOC methods [20]. As the EVs/ exosomes are complex vesicular cargo of proteins therefore for their detection and isolation the LSPR technique could be used.

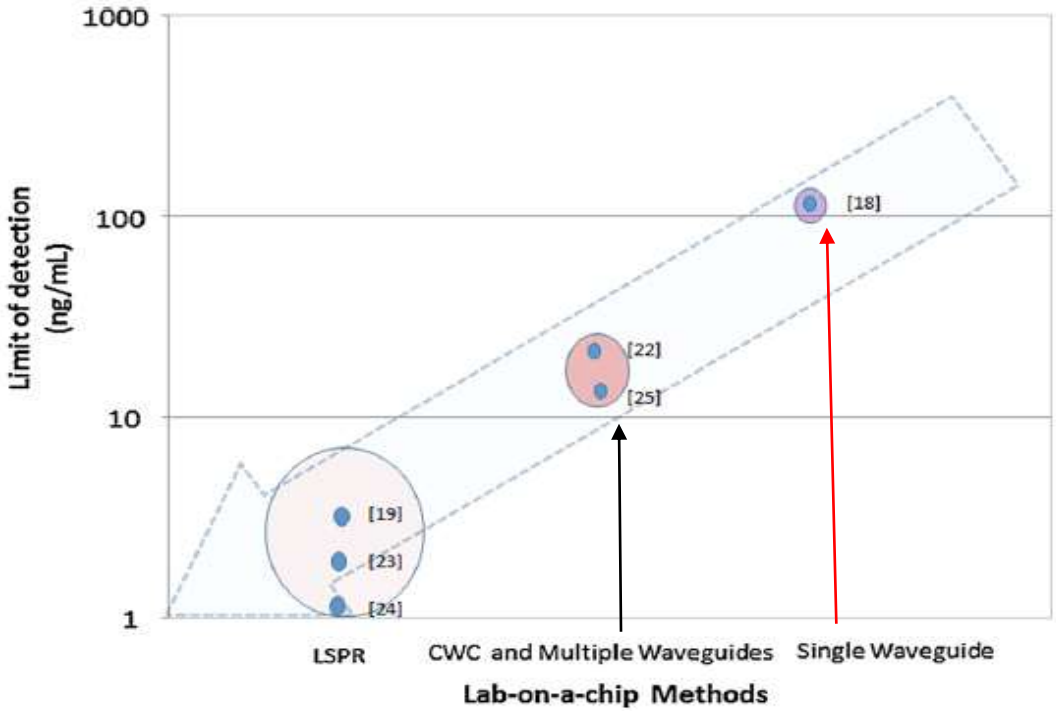

Figure 1-2: Sensitivity of various LOC detection methods of bovine growth hormone [20].

1.4. Motivation

This research is focused on the development and improvement of unique plasmonic platforms for biomolecular detection of sub-micron sized particulate entities to demonstrate the validity of these new nanoplatforms to analyze nanoparticles like viruses, EVs/exosomes, cancer derived exosomes, etc.

EVs hold immense potential as they can be used as promising biomarkers for early cancer detection, prognosis, and therapy. For these reasons, developing a detection method that could be used in clinical practice is important. For several years, our group has been developing detection methods by utilizing LSPR methods. Different plasmonic platforms have been investigated, tested, and evaluated in terms of accuracy and refractive index sensitivity. Despite some important improvements, the platforms are still not sensitive enough, and the established sensing protocols are longer and more expensive because of the special reagents used for different steps. This formed the basic motivation for developing a new category of plasmonic platforms, namely those fabricated by a physical deposition method, having a more uniform morphology, compared to films prepared by chemical methods.

1.5. Thesis Objective and Scope

The overall objective of this thesis is to develop nanoplasmonic platforms for the detection and isolation of EVs/exosomes derived from the MCF7 breast cancer cell line. The specific objectives of this research are:

1) Evaluating the performance of the *ex-situ* synthesized gold (Au) platform for the detection of EVs/exosomes using the LSPR technique.
2) Evaluating the performance of *in-situ* synthesized silver (Ag) - Polydimethylsiloxane (PDMS) nanocomposite platform for the detection of EVs/exosomes using the LSPR technique.
3) Evaluating the performance of *in-situ* synthesized gold (Au) - Polydimethylsiloxane (PDMS) nanocomposite platform for the detection of EVs/exosomes using the LSPR technique.
4) Fabrication, characterization, and testing of novel plasmonic platforms to detect EVs using the LSPR technique.
    a) Fabrication of various plasmonic platforms, and their comparison. This objective involves the e-beam deposition of gold and chromium adhesion layer on the borosilicate substrate in the case of the first platform and the deposition of the ITO adhesion layer on the substrate by sputtering for the second platform.

b) The next objective consists of annealing the two platforms to different temperatures and durations to form the nano-island film by dewetting the gold films.
c) The next objective consists of the characterization of the nano-island films through a plethora of methods and the evaluation of their refractive index sensitivity.
d) The next objective consists of the selection of the most appropriate platform and quantitative measurements of EVs/exosomes.
e) Comparison of the detection sensitivity of EVs/exosomes with the previously developed method.

1.6. Thesis Contribution

The main contributions and novelties of this research work are:

1) Evaluating the performance of the *ex-situ* synthesized gold (Au), *in-situ* synthesized silver (Ag), and gold (Au) - Polydimethylsiloxane (PDMS) nanocomposite platforms for the detections of EVs/exosomes using LSPR technique that was used for the detection of growth hormones in the past by our research group.
2) Fabrication, characterization, and testing of novel plasmonic platforms to detect EVs using the LSPR technique.
3) Improvement in sensitivity of detection of EVs/exosomes as compared to the *ex-situ* and *in-situ* platforms.
4) Reduction in time and cost in the detection of EVs/exosomes

1.7. Thesis Layout

This thesis is prepared in manuscript-based style according to the "Student's Guide to Thesis Preparation, Examination Procedures and Regulations of School of Graduate Studies, Concordia University, September 1, 2023 for Manuscript-based Thesis". It includes nine chapters and three appendixes.

Chapter 2: Microfluidic Platforms for the Isolation and Detection of Exosomes: A Brief Review: This chapter is reproduced from the review paper, published in *Micromachines*, journal (MDPI).

The first part of the paper discusses the main characteristics of different cell-derived vesicles, EV functions, and their clinical applications. In the second part, various microfluidic platforms suitable for the isolation and detection of exosomes are described, and their performance in terms of yield, sensitivity, and time of analysis is discussed. It is concluded that microfluidic isolation and detection methods represent clear progress compared to conventional strategies. Nevertheless, first-generation devices are not yet ready to be translated into clinical analysis. The main reason for this is the lack of standardization and validation of the microfluidic methods and the relatively low processing capacity.

Chapter 3: Gold Nano-Islands Platforms for LSPR Sensing: This chapter is reproduced from the review paper published in the journal *Molecules.*

Nano-islands are entities (droplets or other shapes) that are formed by spontaneous dewetting (agglomeration, in the early literature) of thin and very thin metallic (especially gold) films on a substrate, done by post-deposition heating or by using other sources of energy. In addition to thermally generated nano-islands, more recently, nanoparticle films have also been dewetted, to form nano-islands. The localized surface plasmon resonance (LSPR) band of gold nano-islands was found to be sensitive to changes in the surrounding environment, making it a suitable platform for sensing and biosensing applications. In this chapter, we revisit the development of the concept of nano-island(s), the thermodynamics of dewetting of thin metal films, and the effect of the substrate on the morphology and optical properties of nano-islands. A special emphasis is made on nanoparticle films and their applications to biosensing.

Chapter 4: Nanostructured Gold-Based Plasmonic Platform Fabricated and Tested for Detection of EVs: This chapter is reproduced from the article published in *ECS Trans.*

This chapter is aimed at the bio-sensing of exosomes by gold nano-island structures formed by annealing of gold multilayers, deposited by the convective self-assembly method. The sensing platforms developed by this method are tested for the detection of EVs exosomes based on their interaction with biotin-PEG-Vn96. Vn96 is a peptide (27 amino acids) designed and validated to capture exosomes. The method has to be still optimized to enhance the sensitivity toward exosomes at low concentrations.

Chapter 5: Study of Detection and Capture of Exosomes by Using the Morphologies of *Ex-Situ* and *In-Situ* Nanostructures: This chapter is reproduced from the article published in *J. Electrochem. Soc.*

Looking for the most sensitive platform for the detection of EVs, other methods, called *in-situ*, structures were fabricated and investigated as well. In this category, gold and silver nanocomposites Ag-PDMS and Au-PDMS have been prepared by *in-situ* methods and tested for the LSPR detection of EVs/exosomes.

In this chapter, Ag-PDMS has been prepared and studied as a plasmonic platform and the results were compared to the nano-island-based platform. It is found that the refractive index sensitivity of the *ex-situ* synthesized Au nano platform is considerably higher than that of the *in-situ* synthesized Ag-PDMS nanocomposite and consequently, this platform is much more performant for sensing exosomes.

Chapter 6: Effect of Cross-Linking and Thermal Budget on Plasmonic Sensing and Sub-Surface Segregation of *In-situ* Synthesized Gold in PDMS: This chapter is reproduced from the article published in the *Journal of Nanoparticle Research*.

This chapter focuses on the gold-PDMS nanocomposites that were prepared by the *in-situ* synthesis of gold by using the gold precursor solution. After the synthesis, AuNPs diffuse into the PDMS matrix through heat treatment. The interplay between the reduction of gold ions and the continuous diffusion of the cross-linking agent toward the surface is also discussed in detail. The effect of sub-surface segregation of AuNPs and their subsequent spatial distribution on the sensing capability of the nanocomposite are presented.

Chapter 7: LSPR Detection of Extracellular Vesicles Using a Silver-PDMS Nano-composite Platform Suitable for Sensor Networks: This chapter is reproduced from the article published in the *Journal Enterprise Information System*.

This work is an attempt to bring a plasmonic biosensing method to a superior level, in line with Industry 4.0's requirements. A new method to detect exosomes in cell cultures has been developed, first in a discontinuous manner and later on in a microfluidic environment that is directly amenable to be integrated into a network of sensors. The preliminary results showed that

a label-free technique, based on the sensitivity of the Ag-LSPR band to the surrounding environment, is promising for the detection of exosomes.

Chapter 8: Development of Gold Nano-island Platforms Prepared Through Dewetting of e-beam Deposited Films for the Detection of Extracellular Vesicles (EVs): This part of the work is yet to be submitted to a journal.

This chapter focuses on the fabrication and characterization of plasmonic platforms of very thin gold films fabricated by e-beam deposition. To improve the adhesion of gold, a thin chromium layer or an ITO layer is deposited as well. The morphology of the platforms annealed at temperatures between 250 °C and 650 °C for different durations was investigated by SEM and AFM and the size distribution of Au nano-islands (in the case of Cr adhesion layer) and nanoparticles (in the case of ITO) have been studied. Importantly, the refractive index sensitivity of the two platforms has been determined. Further, the EVs/exosomes detection experiments have been performed and the direct detection method was evaluated and compared with the previously developed immuno affinity method.

Chapter 9: Conclusion and Future Work

This chapter focuses on concluding the performance of the developed nanoplasmonic platforms as part of the thesis work and provides potential ways to expand and enhance this research work.

To comply with Concordia's thesis regulations, the numbering of figures, tables, and equations may have been modified from the original submitted or published articles. Consequently, the references for all articles have been consolidated and are presented at the end of the thesis.

1.8. Publications

Published Journals:

1. **Raju, D**.; Bathini, S.; Badilescu, S.; Ghosh, A.; Packirisamy, M. Microfluidic Platforms for the Isolation and Detection of Exosomes: A Brief Review. *Micromachines*, **2022**,*13*, 730. https://doi.org/10.3390/mi13050730.

2. S. Bathini, **D. Raju**, S. Badilescu, M. Packirisamy, "Effect of Cross-Linking and Thermal Budget on Plasmonic Sensing and Sub-Surface Segregation of *In-Situ* Synthesized Gold in Polymer-Nano Composite", J. Nanopart Res, 2021, 23, Article 21.

3. S. Bathini, **D. Raju**, S. Badilescu, S. Pakkiriswami, A. Ghosh, R. J. Ouellette, M. Packirisamy, "Microfluidic Isolation of Extracellular Vesicles and Validation through AFM and DNA Amplification", Euro J. of Extracell. Ves., 2020, Vol.1, 3-10.

4. S. Badilescu, **D. Raju**, S. Bathini, M. Packirisamy, "Gold Nano-Island Platforms for Localized Surface Plasmon Resonance Sensing: A Short Review", Molecules, 2020, 25(20), 4661.

5. **D. Raju**, S. Bathini, S. Badilescu, R.J. Ouellette, A. Ghosh, M. Packirisamy, "LSPR Detection of Extracellular vesicles using a silver-PDMS nano-composite platform suitable for sensor networks", Enterprise Information System (EIS), 2020, 14(4), 532-541.

6. **D. Raju**, S. Bathini, S. Badilescu, R.J. Ouellette, A. Ghosh, M. Packirisamy, "Study of Detection and Capture of Exosomes by Using the Morphologies of Ex Situ and In Situ Nanostructures", J. Electrochem. Soc., 2019, 166(9) B3001-B3006.

7. S. Bathini, **D. Raju**, S. Badilescu, A. Kumar, R. J. Ouellette, A. Ghosh, M. Packirisamy, "Nano-Bio Interactions of Extracellular Vesicles with Gold Nanoislands for Early Cancer Diagnosis," Research, vol. 2018, Article ID 3917986, 10 pages, 2018.

8. S. Bathini, **D. Raju**, S. Badilescu, M. Packirisamy, "Microfluidic Plasmonic Bio-Sensing of Exosomes by Using a Gold Nano-Island Platform", Intl. J. of Biomed. Biol. Engg (WASET). 2018, Vol. 12, No. 5, 226 – 229.

9. **D. Raju**, S. Bathini, S. Badilescu, R.J. Ouellette, A. Ghosh, M. Packirisamy, "Comparison of *Ex-Situ* and *In-situ* Nano Plasmonic Platforms for Capture and Detection of Exosomes", ECS Trans. 2018, Vol. 85, Issue 13, 1407-1414.

10. **D. Raju,** S. Bathini, S. Badilescu, R.J. Ouellette, A. Ghosh, M. Packirisamy, "Exosomes Detection by a Label-free Localized Surface Plasmonic Resonance Method", ECS Trans. 2016, Vol. 75, Issue 17, 11-17.

Conference Publications:

1. **Raju, D**., Mohammadi, K., Badilescu, S., Ghosh, A., & Packirisamy, M. (2023, June). Nano-Islands from ultra-thin gold films for plasmonic sensing application., Proceedings of the 7th International Conference on Theoretical and Applied Nanoscience and Nanotechnology (TANN'23) Canada – June 01-03, 2023.
2. K. Mohammadi, **D. Raju**, D. M. Panneerselvam, S. Badilescu and M. Packirisamy, "Simulation and Evaluation of Refractive Index-Based Sensor Platform for Bio-detection," *2023 Photonics North (PN)*, Montreal, QC, Canada, 2023, pp. 1-2, doi: 10.1109/PN58661.2023.10223007.
3. S. Bathini, **D. Raju**, S. Badilescu, S. Pakkiriswami, A. Ghosh, R. J. Ouellette, M. Packirisamy, "Genetic Validation of Physical Modeling of Nano-Bio Interactions between Extracellular Vesicles and Different Morphologies of Gold Nano Particles", *MRS-ISEV Conference on Extracellular Vesicles in Cancer*, August 2019, Nashville, USA.
4. **D. Raju**, S. Bathini, S. Badilescu, S. Pakkiriswami, A. Ghosh, R. J. Ouellette, M. Packirisamy, "Plasmonic biosensing of exosomes using a microfluidic device (lab-on-a-chip) and its validation using droplet digital PCR", MRS-ISEV Conference on Extracellular Vesicles in Cancer, August 2019, Nashville, USA.
5. S. Bathini, **D. Raju**, S. Badilescu, R.J. Ouellette, A. Ghosh, M. Packirisamy, "Comparison of Extracellular vesicles detection by microfluidic plasmonics of gold nano-island and nanocomposite platforms", International Society for Extracellular Vesicles (ISEV), April 2019, Kyoto, Japan.
6. S. Bathini; **R Duraichelvan**; S Badilescu; A Ghosh; M Packirisamy, “Gold nano-island platform for the microfluidic plasmonic detection of exosomes”, International Conference of Theoretical and Applied Nanoscience and Nanotechnology (TANN'18), June 2018, Niagara Falls, Canada.
7. S. Bathini; **R Duraichelvan**; S Badilescu; M Packirisamy, “Microfluidic Plasmonic Bio-Sensing of Exosomes by Using a Gold Nano-Island Platform”, 20th International Conference on Mechanical Engineering (ICME), May 2018, Montreal, Canada.

8. **R. Duraichelvan**, B. Srinivas, S. Badilescu, A. Ghosh, M Packirisamy, "Comparison of *Ex-Situ* and *In-Situ* Nano Plasmonic Platforms for Capture and Detection of Exosomes",233rd ECS Meeting, May 2018, Seattle, USA

9. **D. Raju**, S. Bathini, S. Badilescu, A. Ghosh, RJ. Ouellette, M. Packirisamy, "Gold Nanoparticle Ring and Hole Structures-Based Platforms for Capture and Label-free Detection of Exosomes", International Society for Extracellular Vesicles (ISEV2018) Annual Meeting, May 2018, Barcelona, Spain.

10. A. Ghosh, S. Bathini, **D. Raju**, S. Badilescu, A. Kumar, R. J. Ouellette, M. Packirisamy, "Capture and label-free detection of extracellular vesicles on gold-nano-island based microfluidic Lab-on-a-CHIP device using synthetic-peptide Vn96", ISEV2018 Annual Meeting, May 2018, Barcelona, Spain.

11. S. Bathini; **R Duraichelvan**; S Badilescu; M Packirisamy, "Plasmonic detection of Extracellular vesicles in a microfluidic environment using synthetic-peptide (Vn96) based affinity capture", International Society for Extracellular Vesicles (ISEV2017), May 2017, Toronto, Canada.

12. **R Duraichelvan**; S. Bathini; S Badilescu; M Packirisamy, "Label-free Detection of Extracellular Vesicles Using Plasmonic Platforms", TEXPO 2016 Conference, October 2016, Montreal, Canada.

13. **R Duraichelvan**; Bathini; S Badilescu; M Packirisamy, "Exosomes Detection by a Label-free Localized Surface Plasmonic Resonance Method", ECS Conference, October 2016, Hawaii, USA.

14. **R Duraichelvan;** S. Bathini; S Badilescu; M Packirisamy, "Label-free Detection of Extracellular Vesicles Using Nanocomposite Platform", Keystone Symposia Conference, June 2016, Colorado, USA.

Chapter 2. Microfluidic Platforms for the Isolation and Detection of Exosomes

This chapter is reproduced from the article published in *Micromachines* 13, 730, 2022.

2.1. Outline

Extracellular Vesicles (EVs) are a group of communication organelles[3] enclosed by a phospholipid bilayer, secreted by all types of cells. The size of these vesicles ranges from 30 to 1000 nm, and they contain a myriad of compounds such as RNA, DNA, proteins, and lipids from their origin cells, offering a good source of biomarkers. Exosomes (30 to 100 nm) are a subset of EVs, and their importance in future medicine is beyond any doubt. However, the lack of efficient isolation and detection techniques hinders their practical applications as biomarkers. Versatile and cutting-edge platforms are required to detect and isolate exosomes selectively for further clinical analysis. This chapter focuses on the literature review on the biogenesis of extracellular vesicles (EVs)/Exosomes and lab-on-chip devices for capturing, detecting, and isolating the EVs/Exosomes. The first part of the chapter discusses the main characteristics of different cell-derived vesicles, their functions, and their clinical applications. In the second part, various microfluidic platforms suitable for the isolation and detection of exosomes are described, and their performance in terms of yield, sensitivity, and time of analysis is discussed.

2.2. Introduction

EVs are spherical particles enclosed by a phospholipid bilayer released from eukaryotic and prokaryotic cells. EVs are present in blood and body fluids such as urine, saliva, breast milk, and cultured media [6,7,21–23]. The typical diameter of exosomes, a subset of EVs, is between 30 -100 nm, much smaller than red blood cells. It consists of DNA[4], RNA[5], mRNA[6], microRNA[7],

[3] **Organelles** are membrane-lined structures that compartmentalize subcellular biochemical functions.
[4] **Deoxyribonucleic acid (abbreviated DNA)** is the molecule that carries genetic information for the development and functioning of an organism.
[5] **Ribosomal ribonucleic acid (rRNA)** is a type of non-coding RNA that is the primary component of ribosomes, essential to all cells.
[6] **Messenger RNA (abbreviated mRNA**) is a type of single-stranded RNA involved in protein synthesis.
[7] **MicroRNA (miRNA)** are small, single-stranded, non-coding RNA molecules containing molecules involved in the regulation of gene expression.

proteins, nucleic acids, heat shock proteins (HSP70 and HSP90), the tetraspanins such as CD9, CD63, and CD81, RAB proteins that regulate docking and membrane fusion of EVs with recipient cells adhesion molecules (integrins and lactadherin). They facilitate intercellular communication and regulate crucial cell processes such as coagulation, inflammation, and cellular homeostasis [16,24–30]. There is a growing interest in the clinical applications of exosomes as biomarkers for disease diagnosis, therapy, prognosis, and diagnosis. Despite the increasing scientific and clinical interest, no standard procedures are available to isolate, detect, and characterize exosomes because their size is below the reach of conventional detection methods.

Exosomes are released from the cell when multivesicular bodies fuse with the plasma membrane, or directly from the plasma membrane. Exosomes may be released in two ways, as shown in Figure 2-1 firstly the "classic pathway" that involves the formation of Intraluminal Vesicles (ILVs) within the Multivesicular Endosomes (MVEs). They, in turn, fuse the membrane of MVE with, either lysosome for cargo degradation or the plasma membrane, resulting in the release of ILVs called exosomes. The second way is the direct budding of the plasma membrane called the "direct pathway". The extent to which such exosomes are released from other cells or in vivo (e.g., in biological fluids) is unknown. The other types of cell-derived vesicles are microvesicles and apoptotic vesicles, as shown in Figure 2-2.

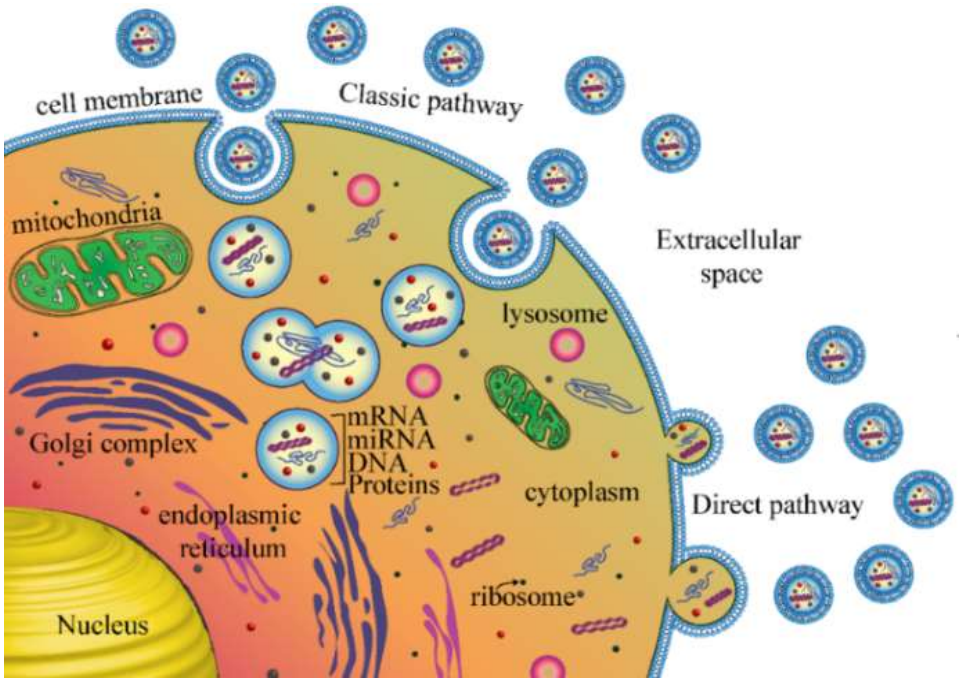

Figure 2-1: Extracellular Vesicles Biogenesis.

Many excellent review papers on microfluidic detection have been published in the last decade [31–34]. However, they have not evaluated, critically the performance of various devices in terms of the complexity of the devices and the results. This chapter aims to discuss in depth the principle of the technique and its benefits for future clinical assays.

The immune properties [8]of different exosomes suggest that they may be helpful as vaccines for infectious diseases [35]. Thus, exosomes may be potential sources of anticancer vaccines and may eliminate infections [36]. Therefore, exosomes are considered for clinical applications in treating ailments such as toxoplasmosis, diphtheria, tuberculosis, and typical severe acute respiratory syndrome and autoimmune diseases. As exosomes play a vital role in drug delivery systems, researchers are trying to find applications in treating autoimmune/inflammatory diseases [37].

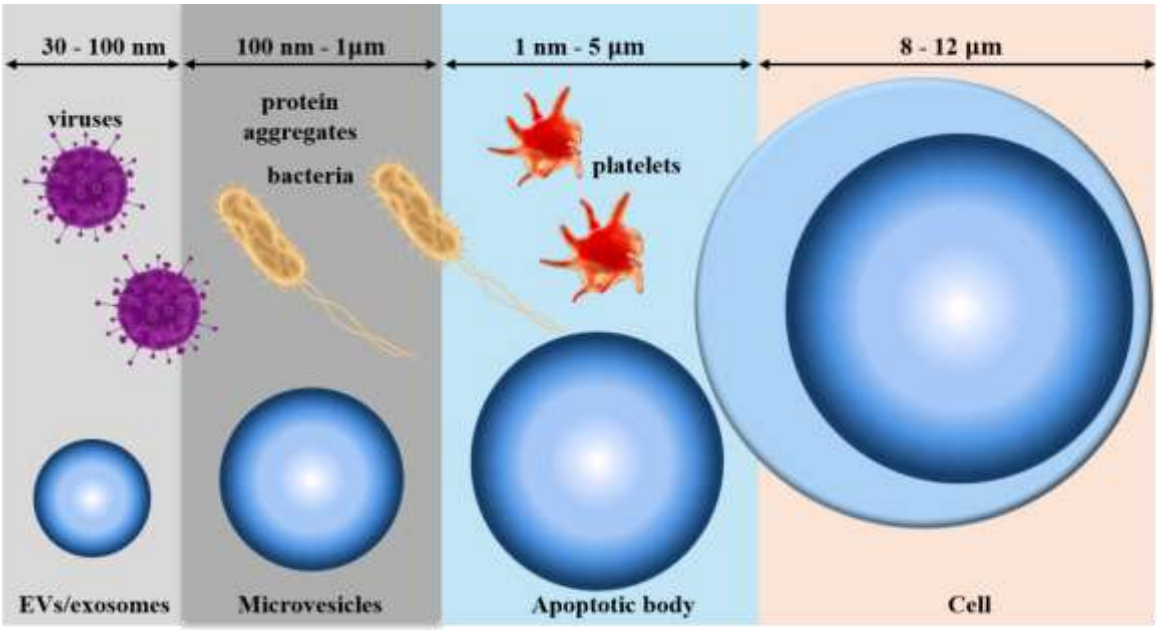

Figure 2-2: Comparison of the size of various types of extracellular vesicles with that of a cell (Modified from György B. et al. [6], Cell. Mol. Life Sci.).

2.3. Exosomes as reliable biomarkers for early diagnosis of cancer

As mentioned previously, extracellular vesicles are enclosed by a phospholipid bilayer and are present in all biological fluids [4,5,8,38–41]. They play a crucial role in intercellular communication by transporting and delivering cargo between their cells, promoting disease

[8] **Immune properties** - A complex network of substances they make that helps the body fight infections and other diseases.

progression. Exosomes, circulating tumor cells (CTC), and circulating tumor DNA (ctDNA) have attracted much attention in the past decades as biomarkers for the early diagnosis of cancer. The major challenge in the isolation of CTCs and ctDNA is that the isolation and analysis of CTCs are challenging as they are infrequent and heterogeneous [42]. At the same time, the ctDNA is not stable in the blood or the other body fluids and may be highly fragmented [43,44]. Because of these intrinsic limitations of CTCs and ctDNA, their definite isolation and precise detection remain challenging even though there are many advancements in technology. Compared to CTCs and ctDNA, exosomes have a lot of advantages in terms of stability, quantity, and accessibility. Moreover, the exosome concentration increases tremendously (by many folds) between cancerous and non-cancerous cells as the tumor progresses when compared to the other biomarkers such as tumour antigen, CTC, and ctDNA. For example, in the case of a glioblastoma (GBM) patient's plasma study, the concentration of exosomes is approximately 50 times higher than that of a healthy patient [45].

Further, from Figure 2-3, it is noticeable that the expression level of exosomes is relatively higher than that of CTCs and tumor antigens in stage I, which is the early stage of cancer [17]. Exosomes are highly stable and capable of protecting nucleic acids and proteins closely related to cancer development. Many studies have shown that cancer cell-derived exosomes contain specific nucleic acids and proteins that reflect the origin of cancer cells and the type of cancer [46,47]. Therefore, exosomes can be potentially utilized for therapy, prognosis, and promising biomarkers for early cancer diagnosis.

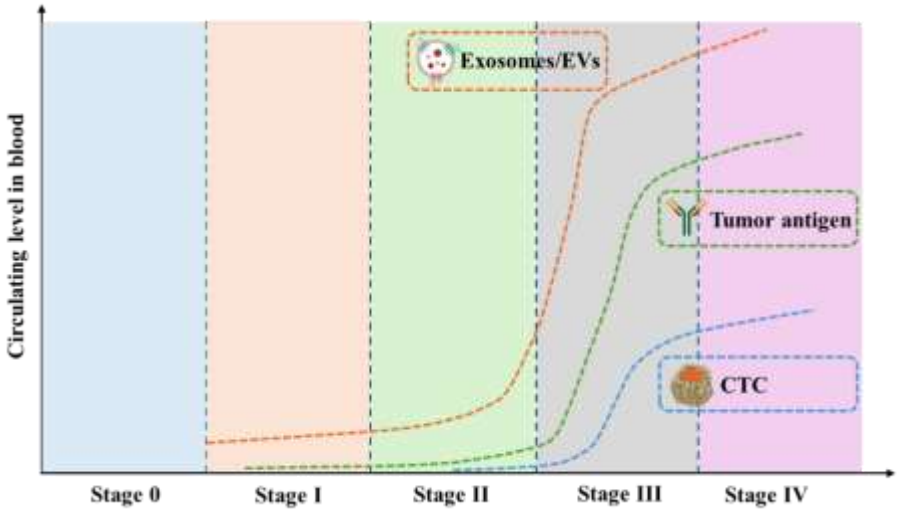

Figure 2-3: The circulating levels of Tumor antigens, CTCs, and exosomes in blood during cancer progression (Modified from He M, Zeng Y [17], J Lab Autom. 2016).

2.4. Isolation and Detection Techniques

The problem impeding the advancement of exosomes research is the standardization of sample collection protocols such as sample collection, sample processing, and sample analysis for translating exosomes to suitable clinical biomarkers. Exosomes are present in a wide range of body fluids. Low-speed centrifugation is enough for removing cells and large vesicles, but for pelleting exosomes, high-speed ultra-centrifugation is required [48]. Repeated ultracentrifugation steps can damage the exosomes and thus reduce their yield, potentially impacting their content's proteomics and RNA analysis [49]. Therefore, both the International Society for Thrombosis and Haemostasis (ISTH) and the International Society for Extracellular Vesicles (ISEV) have described the guidelines and recommendations regarding the standardization of sample collection and handling protocols [50] as shown in Figure 2-4.

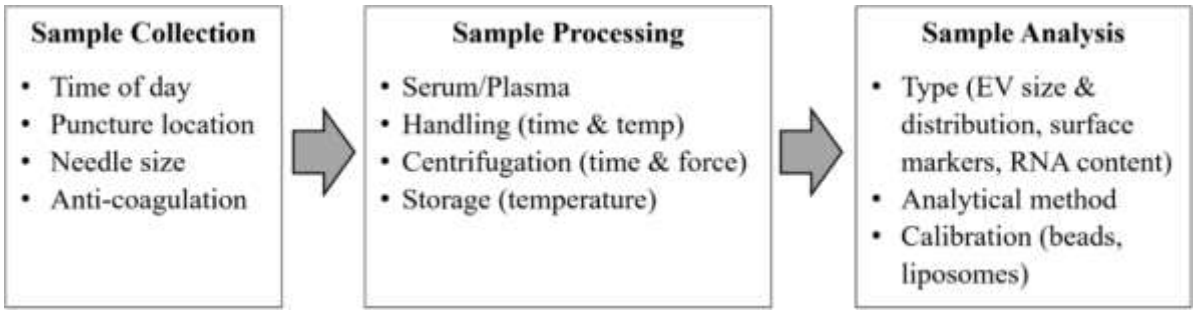

Figure 2-4: Critical standardization issues for exosomes analysis from blood samples (Modified with permission from van der Meel et al. [50], Copyright 2014 John Wiley and Sons).

Despite the increasing scientific and clinical interest, no standard procedures are available to isolate, detect, and characterize exosomes because their size is below the reach of conventional detection methods. Given the growing evidence that exosomes may be a clinically relevant biomarker source, there is a great demand for their efficient and straightforward detection from bio-fluids. Most affinity-based methods rely on antibodies directed against exosome surface markers. Therefore, choosing the best protocol and customizing it based on the study seems necessary.

2.4.1. Exosomes Isolation Methods Based on Their Physical Properties

The traditional methods are presented in Figure 2-5 for exosomes physical characterization and molecular analysis. The technique used to study the morphology of the exosomes is scanning electron microscopy (SEM) and atomic force microscopy (AFM). The size and concentration of

exosomes can be determined by nanoparticle tracking analysis (NTA), dynamic light scattering (DLS), tunable resistive pulse sensing (TRPS), or flow cytometry (FC). Nucleic acid quantification and analysis of exosome proteins can be done by methods such as bicinchoninic acid (BCA) assay, western blotting (WB), and enzyme-linked immunosorbent assay (ELISA), liquid chromatography-tandem mass spectrometry (LC-MS/MS), nucleic acid extraction, polymerase chain reaction (PCR).

Typically, the isolation methods can be classified into four types: density-based, size-based, surface component-based, and precipitation methods, as shown in Figure 2-6 (a) Density-based methods such as differential ultracentrifugation and density gradient centrifugation were developed during early-stage research of exosomes. In differential ultracentrifugation, large cell debris and cells were initially removed at a low speed of around 20000 x g. After this, the proteins were removed by precipitating exosomes at higher speeds (higher than 100000 x g). At the same time, in density gradient centrifugation, a series of solutions with different densities are preloaded into a centrifugal tube before the addition of the sample. Exosomes can then be isolated via ultracentrifugation due to differences in the densities once the balance is achieved between centrifugal force and buoyancy. Expensive equipment and more significant time duration limit ultracentrifugation in the clinical setup for isolating exosomes. In addition, these techniques include multiple steps and take around 5 to 6 hours [51,52].

The isolation techniques based on size include membrane filtration, size exclusion chromatography (SEC), and other isolation methods that may be carried out in microfluidic chips. Filtration is a high-throughput and straightforward method in which the exosomes are isolated based on the size differences of the particles in the sample. Size exclusion chromatography (SEC) enables the separation of polymers or proteins based on their size or hydrodynamic volume. In this method, a porous matrix is usually packaged into a column as a stationary phase, as shown in Figure 2-6 (b). When a sample passes, the components smaller than the pore diameter can enter the porous material and take a longer time to pass through the column, while the larger ones cannot enter the pores.

Therefore, at different elution times, several components can be separated. Thus, this method extensively isolates exosomes [53–55]. However, there is a high chance that exosomes or contaminant aggregates will get trapped in the pores, possibly damaging them.

The polymer precipitation method for the isolation of exosomes ensures a high yield by simplifying the process and reducing the handling time. Companies have commercialized these polymer-based precipitation methods as ExoQuick, Total exosomes isolation, and Exospin because of their simple protocols and fast isolation [56]. In this method, polymers are dissolved in the sample to reduce the solubility, because of which, low-speed centrifugation can precipitate Exosomes for isolation. Polyethylene glycol (PEG) is used as a precipitation agent to isolate exosomes [52,57]. Though this method is simple, fast, and high yield, exosomes lack purity as the protein aggregates and other contaminants may be co-precipitated. Besides, it may change exosome structure and surface characteristics [58]. These drawbacks can severely affect the further analysis of exosomes.

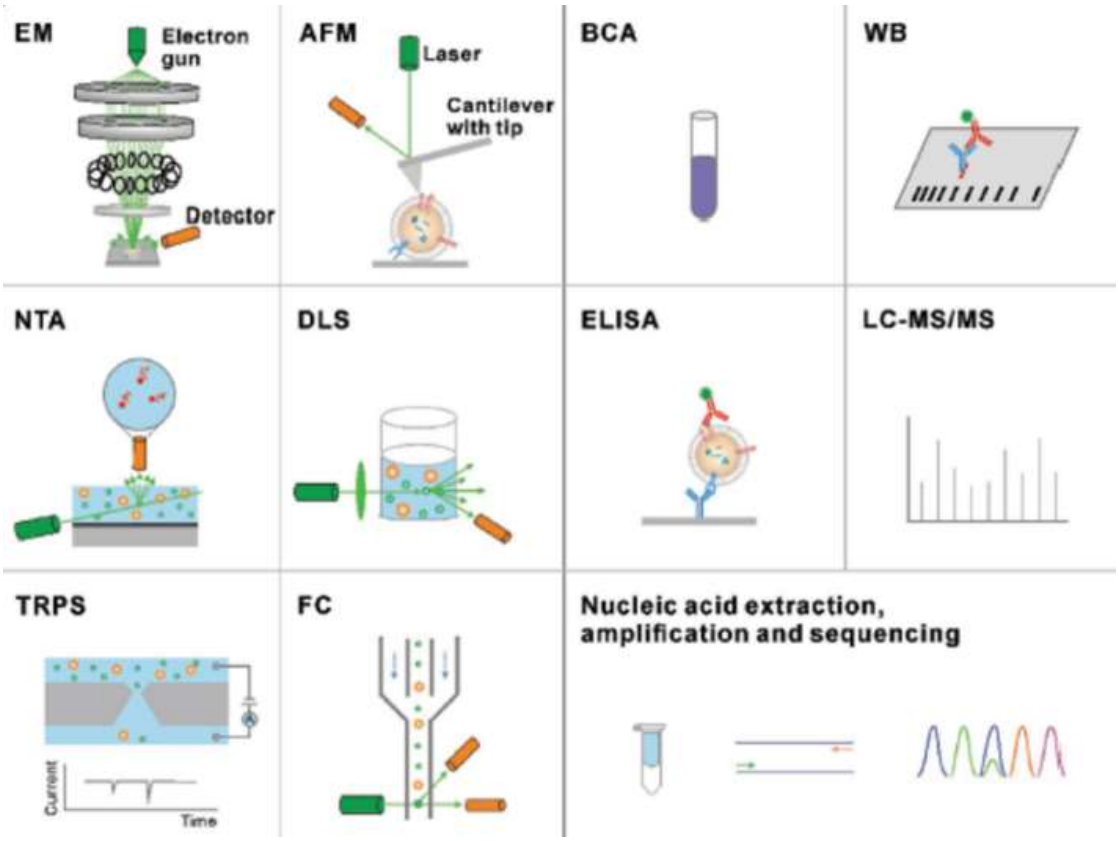

Figure 2-5: Traditional methods for the characterization of exosomes. Characterization techniques to measure physical properties (morphology, size, and zeta potential) (Reproduced with permission from Wang W et al. [52], Copyright 2018 John Wiley and Sons).

The presence of many proteins and the lipid bilayer on the surface of exosomes make the immunoaffinity-based methods highly suitable for their isolation. The frequently used technique for specific capture and isolating exosomes is affinity-based isolation. These methods are based

on binding antibodies or aptamers[9] by a lipid probe, as shown in Figure 2-7. An antibody with affinity to exosome proteins is usually modified on a solid surface such as magnetic beads or a microfluidic channel to separate exosomes from a culture media or nonspecific vesicles and other contaminants [59]. In addition to beads or microfluidic chips, nanoparticles or nanomaterials may provide more suitable substrates to capture exosomes because of increased binding sites on their surface. Similar to antibodies, polypeptides can also be used as affinity agents to isolate exosomes [60].

Besides antibodies and peptides, the DNA aptamer can also separate exosomes, expressing a specific protein. The aptamer is a screened nucleic acid fragment with a particular sequence. Therefore, they can bind with a high affinity towards specific proteins. The usage of aptamers for the isolation of exosomes has benefits such as low cost, high stability, and easy production [61].

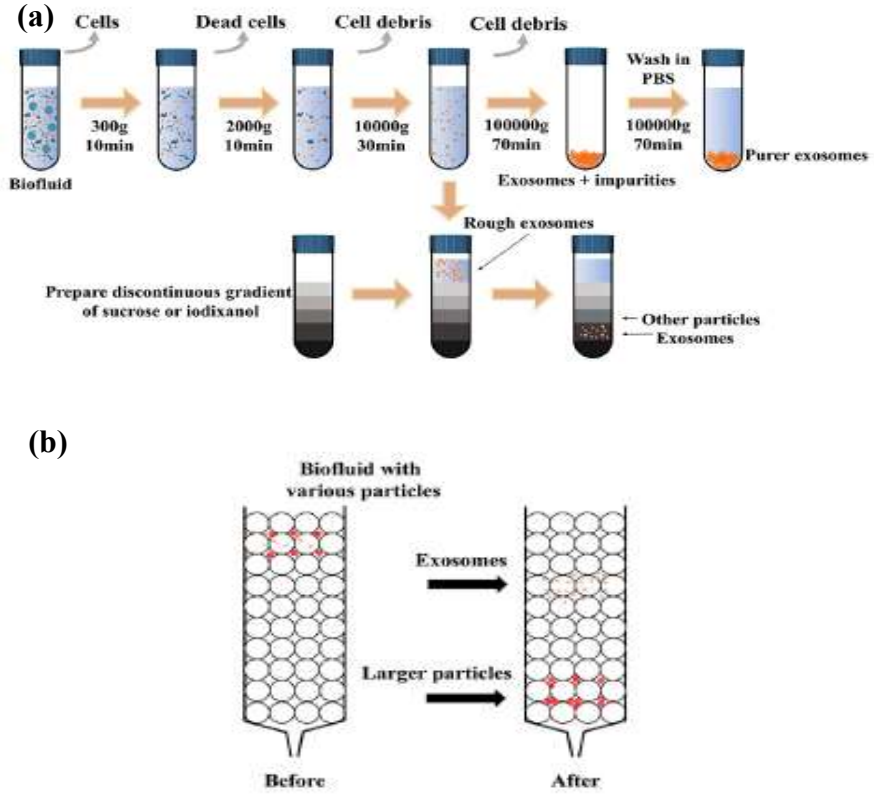

Figure 2-6: Schematics of the common exosomes isolation methods. (a) Ultracentrifugation and Density gradient centrifugation. (b) Size-exclusion chromatography (SEC). (Modified from Chen J et al. [55], Front Booing Biotechnol. 2022).

[9] **Aptamers** are oligomers of artificial ssDNA, RNA, XNA, or peptides that bind a specific target molecule or family of target molecules.

Though aptamers have advantages over antibodies, their rare availability with a specific affinity to exosomes is their major drawback. To avoid the disadvantages of affinity-based isolation methods, an alternative approach to isolate the exosomes is to bind them with the lipid bilayer by designing a lipophilic isolation probe. Thus, capturing efficiency can be improved by ensuring the designed lipid probes have a high affinity toward exosomes lipid membranes. Wan et al. [62] reported using magnetic extraction to isolate exosomes in a short processing time of 15 min. The resulting exosomes purity is higher than that obtained by ultracentrifugation, and the processing is faster. Further, the lipid probe isolation method can capture exosomes irrespective of their size and surface antigen, consequently escaping the loss conveyed by the surface marker.

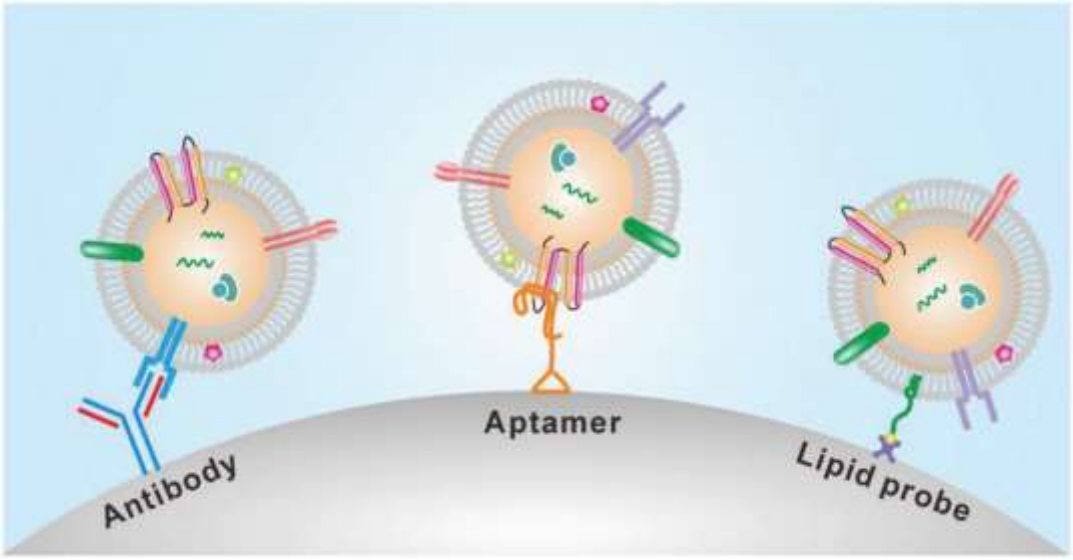

Figure 2-7: Immunoaffinity-based isolation of exosomes (Reproduced with permission from Wang W et al. [52], Copyright 2018 John Wiley & Sons Inc.).

2.4.2. Lab-on-a-Chip (LOC)/Microfluidics for Isolation and Detection of Exosomes

For an improved treatment and control of the progression of the disease, a rapid and early diagnosis is required. Common detection methods such as polymerase chain reaction (PCR) and enzyme-linked immunosorbent assay (ELISA) depend heavily on expensive and sophisticated equipment. Lab-on-a-chip (LOC) technology emerged during the last two decades and has drawn significant interest in biomedical applications. A microfluidic device or a lab-on-a-chip (LOC) may integrate conventional isolation methods by applying fluid dynamics principles. The advantages of LOC include high throughput, low sample and reagent consumption, short assay time, and multiplexed detection [63–65].

Further, the large surface-area-to-volume ratios accelerate heat and mass transport within the micro-channels and help rapid and controllable mixing, cooling, and manipulating variables such as temperature, concentration gradient, and pressure. These merits are also crucial for various applications. LOC technology has shown the potential to improve biomarker detection by offering sensitive and wide-ranging measurements in a compact format.

Therefore, researchers have recently started integrating different methods based on the physical properties of exosomes with the design of the microfluidic device. Thus, microfluidics-based isolation techniques have developed and evolved over the years [66–84]. The following sections will discuss some of the most interesting methods mostly based on the immunoaffinity approaches. Some combined with nanoplasmonics detection and integrated with microfluidics to capture and detect the exosomes.

Immunoaffinity capture methods use immunoaffinity interactions between antigens, exosomes membrane proteins, and monoclonal antibodies. Exosomes specific proteins displayed on exosome membranes are principally tetraspanins proteins, for example, CD9, CD81, CD82, CD87, and CD63, heat-shock proteins produced in response to stress, as well as other proteins involved in cell adhesion and signaling. Immunomagnetic bead based exosome isolation is one of the most common immunoaffinity based capture methods that results in high-purity exosomes. In this case, the magnetic beads are coated with antibodies specific to the surface proteins of exosomes.

2.4.2.1. Immunoaffinity Methods to Capture and Detect Exosomes

This approach has been frequently utilized to capture exosomes, and some suggested devices are briefly described below.

Chen et al. [45] designed an easy and rapid microfluidic immunoaffinity-based method to isolate microvesicles from small volumes of serum blood samples and conditioned medium from cells in culture. As shown in Figure 2-8, they developed two different microfluidic device designs with a straight flow channel for processing sample volumes of 400 μL and even smaller, with herringbone groves on their ceiling. Their design achieved a 42–94% yield of exosomes with high specificity and shot isolation time. To improve the capture yield of the chip, the authors considered modifying parameters such as the dimensions of the microchannel, including structures inside the microchannel, increasing the transverse flow and the coverage of active antibodies. The main

advantage of this design is that the device can sort the microvesicles directly from the serum in a single step.

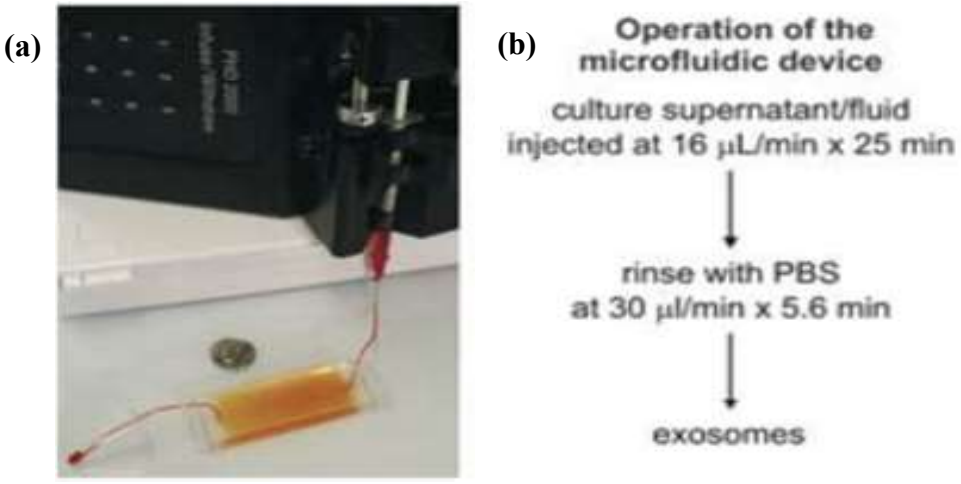

Figure 2-8: Experimental setup of microfluidic devices. (a) Photo of the device with a syringe pump. (b) Procedure for the isolation of microvesicles from the microfluidic device. (Reproduced from Chen et al. [45], Lab Chip. 2010).

A couple of years later, Wang et al. [85], designed and fabricated a microfluidic device based on porous silicon nanowires on a micropillar structure as shown in Figure 2-9. With the help of a prototype design, they could trap exosome-like lipid vesicles within 15 min while filtering out proteins and cell debris. Besides, the trapped lipid vesicles can be recovered intact, with a yield of 67-60%, by dissolving the porous nanowires in a PBS buffer. But still, the recovery time is about one day which is a critical concern.

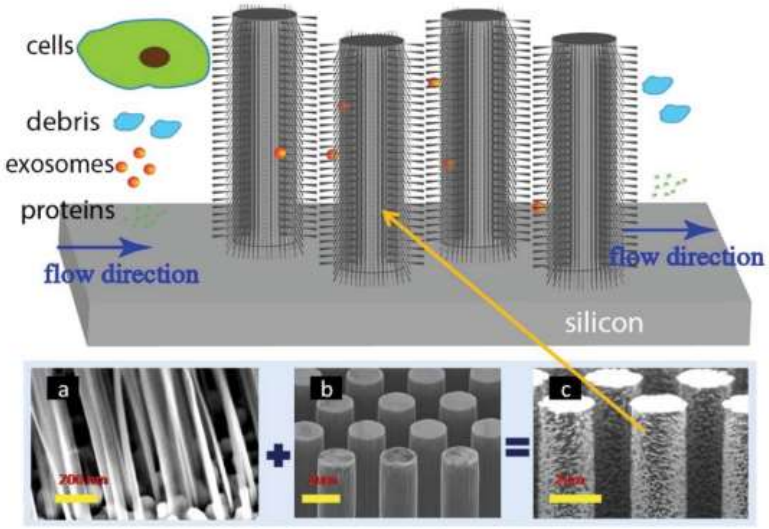

Figure 2-9: Schematic of the ciliated micropillar array. (a) representative porous silicon nanowire forest. (b) micropillars. (c) representative ciliated micropillars. (Reproduced from Wang Z et al. [85], Lab Chip, 2013).

Jorgensen et al. [86,87] using a non-contact printer printed 24 microarray spots, as shown in Figure 2-10. The micro spots were printed with a cocktail of antibodies against the tetraspanins CD9, CD63, and CD81, selected to ensure that all exosomes were detected. With their approach, the authors could detect the exosomes with a sensitivity of 5000 particles/µL.

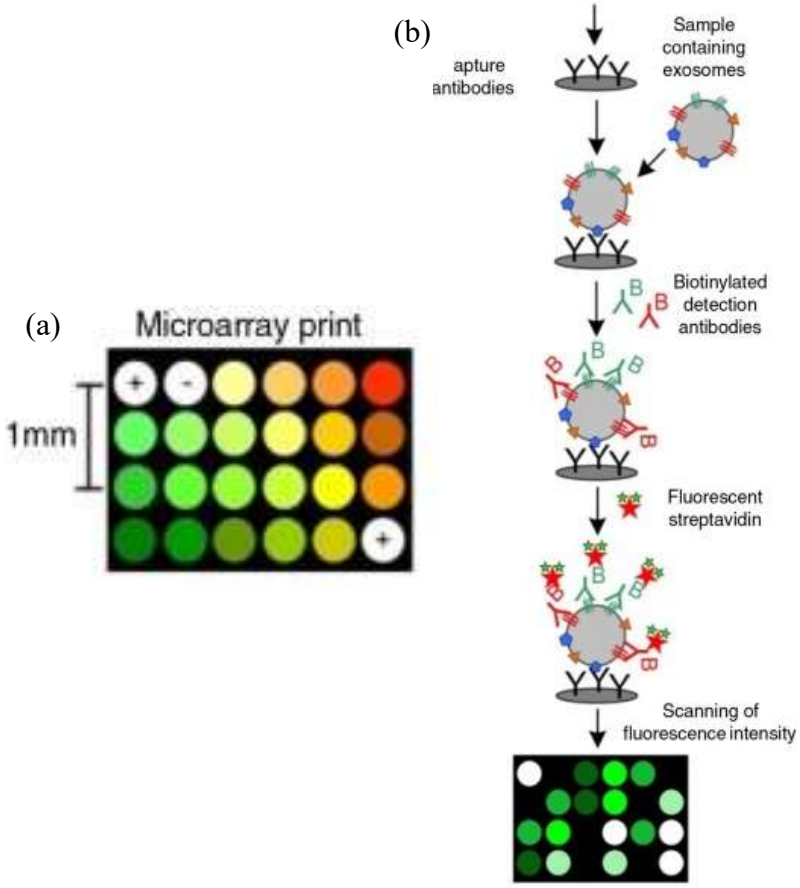

Figure 2-10: Extracellular vesicle detection using a customized protein microarray "EV Array." (a) A microarray printed with spots of 21 different antibodies. (b) Workflow for capturing exosomes with biotinylated antibodies followed by fluorescence-labelled streptavidin. (Modified from Jorgensen et al. [86], J Extracell Vesicles, 2013).

He et al. [88] developed microfluidic devices with serpentine channels and integrated specific immunoaffinity isolation of targeted proteins with immunomagnetic beads to isolate the exosomes directly from the human plasma, as shown in Figure 2-11 With their techniques, the isolation of a selective subpopulation of biomarkers from plasma samples (30 µL) was possible in 1.5 hours, with markedly improved detection sensitivity and a yield of 42-97.3 %. However, the method is specific only to CA125, EpCAM, and CD24 proteins. Due to the simplicity of their

design, scaling up for the high-throughput screening of cancer and non-cancerous diseases is possible.

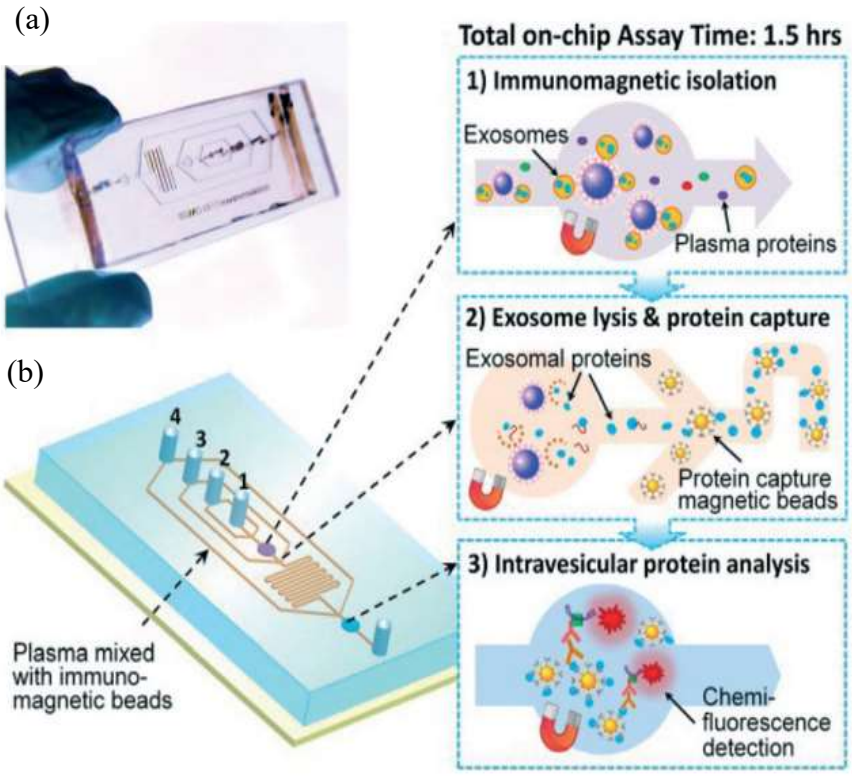

Figure 2-11: Integrated microfluidic exosome analysis directly from human plasma. (a) The photo of the prototype chip with the cascading microchannel for multi-stage exosome capture and analysis. (b) Schematic of the chip with the workflow. 1–4 indicates the inlet for exosome capture beads, washing/lysis buffer, protein capture beads, and ELISA reagents. (Reproduced from He M. et al. [88], Lab Chip, 2014).

Kanwar et al. [89] designed and fabricated a simple, low-cost microfluidic-based device to isolate cirEVs enriched in exosomes directly from blood serum to simultaneously capture and quantify the exosomes within a single device. The schematic and the fluorescence detection scheme of the device are shown in Figure 2-12. The microfluidic device was fabricated using polydimethylsiloxane (PDMS) and then functionalized with antibodies against CD63, an antigen commonly overexpressed in exosomes. Subsequently, it was stained with a fluorescent carbocyanine dye (DiO) that labels the exosomes. The exosomes were quantified using a standard plate reader. The authors achieved a yield of 15-18 µg of total proteins, and the scaling of their device is relatively easy.

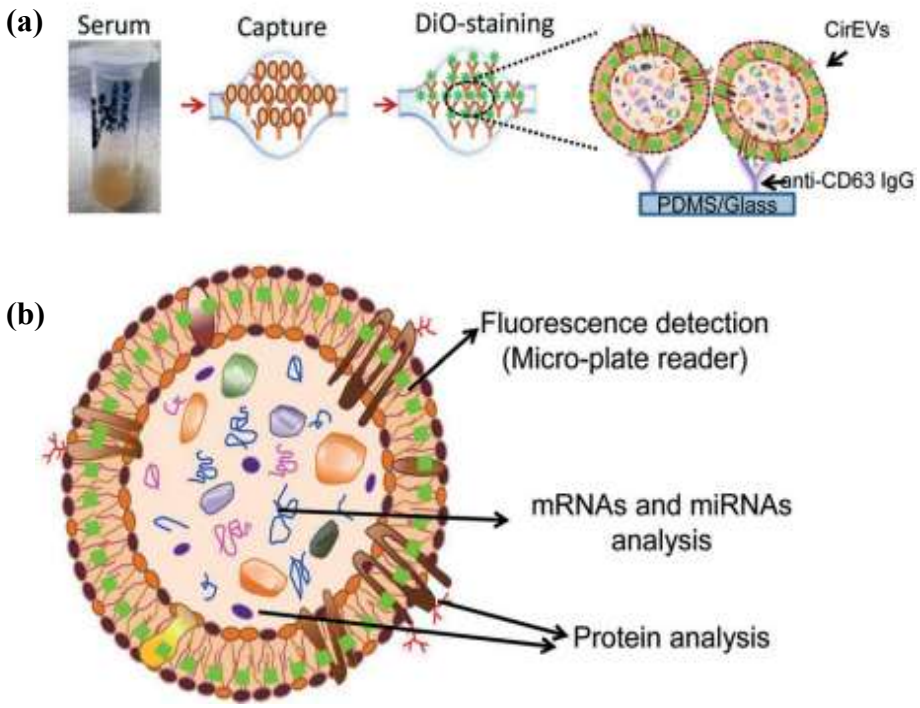

Figure 2-12:Experimental strategy for exosomes immobilization and characterization using ExoChip (a) Schematic of exosomes capture and analysis used in ExoChip. (b) Schematic for CirEVs fluorescence detection in micro-plate readers. (Reproduced from Kanwar S. S et al. [89], Lab Chip, 2014).

Using a different approach, Lee et al. [90] incorporated an acoustic nano filter system in their design that separates EVs continuously, as shown in Figure 2-13. They used the separation of ultrasound standing waves to apply differential acoustic forces on MVs according to their size and density. By optimizing the design of the ultrasound transducers and the underlying electronics, they could achieve >90% separation yield and permitted in situ control of size cutoff. To expand the functionality of their design, they suggested that several aspects of the system can be further developed, such as having different transducer designs to control the acoustic force and improve the sample throughput. Additionally, to realize a portable lab-on-chip for MV analyses integrating analytical components such as sensors and polymerase chain reaction into the same platform will assist clinical applications.

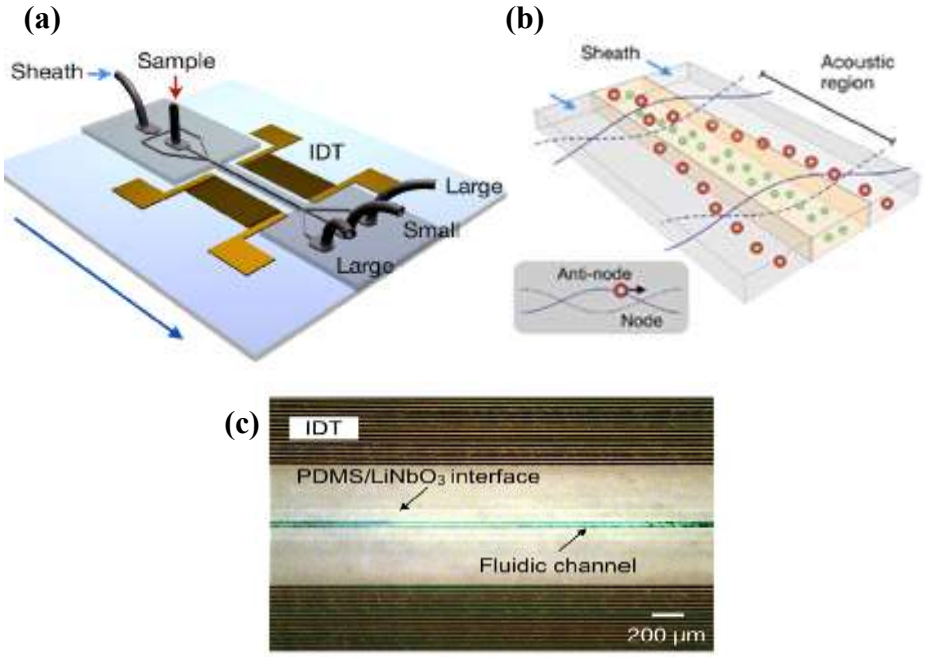

Figure 2-13: Acoustic nanofilter for label-separation of microvesicles (MVs). (a) Device schematic. (b) Filter operation indicates MVs transported to the acoustic pressure region (inset). (c) SEM image of the prototype device (Adapted with permission from Lee K et al. [90]. Copyright 2015 American Chemical Society).

Zhao et al. [91] developed a microfluidic ExoSearch chip that is easy to operate to detect the three exosomal tumor markers (CA-125, EpCAM, CD24), as shown in Figure 2-14. With their design, the authors were able to detect the exosomes with a limit of 750 particles/µL, which is 1000 times more sensitive than conventional methods such as Western blotting.

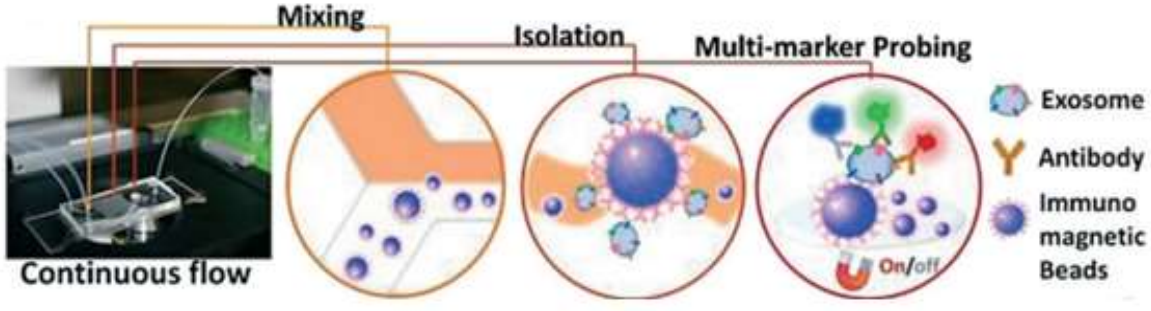

Figure 2-14: The setup and workflow of the ExoSearch chip for continuous mixing, isolation, and in situ, multiplexed detection of circulating exosomes. (Reproduced from Zhao Z et al. [91], Lab Chip, 2016).

A microfluidic device (nano-IMEX) with a single channel, as shown in Figure 2-15, was developed by Zhang et al. [92]. The nano-IMEX chip contains Y-shaped microposts functionalized with graphene oxide (GO), and the induced nanostructured polydopamine (PDA) film by the microfluidic layer-by-layer deposition, thus permitting simple covalent protein conjugation

through the PDA chemistry. Through their technique, the authors have demonstrated that the nanostructured GO/PDA interface can significantly improve the efficiency of exosome immuno-capture, suppressing the nonspecific exosome adsorption. Based on this nano-interface, they could achieve a detection limit of ~50 exosomes/μL, substantially better than the existing methods.

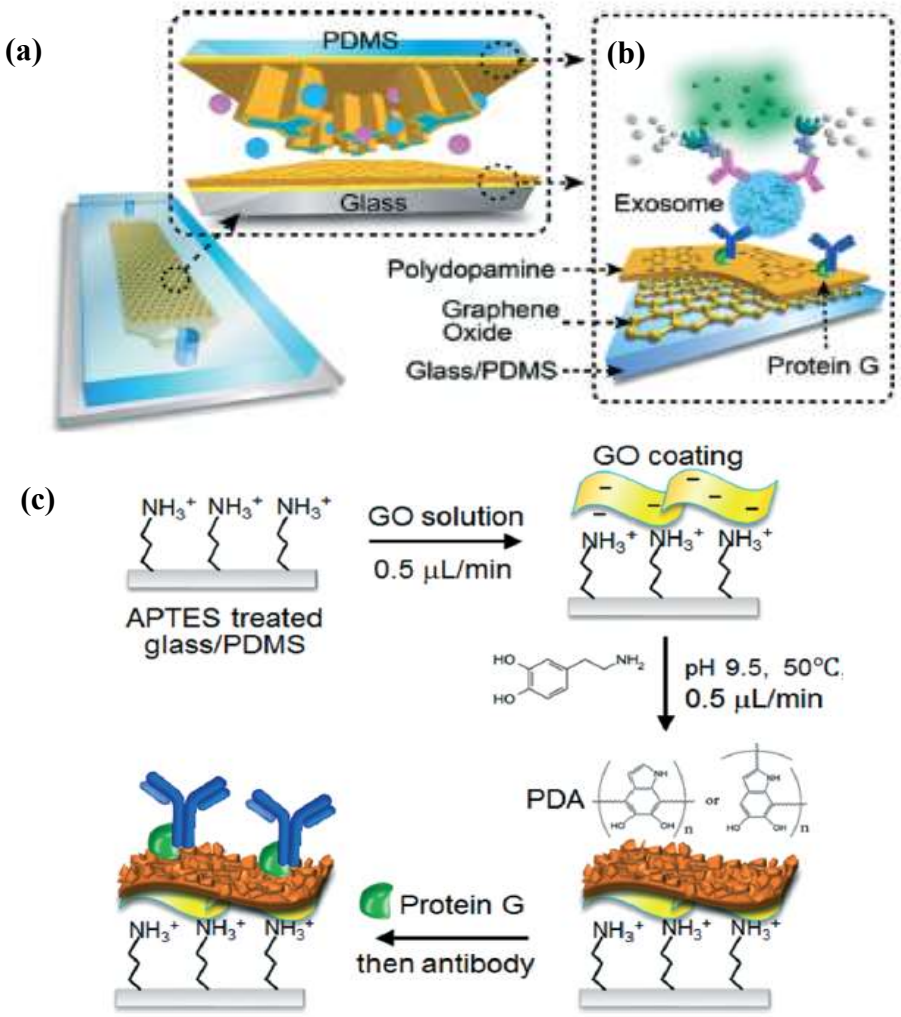

Figure 2-15: Nano-interfaced microfluidic exosome platform (nano-IMEX). (a) Schematic of a single-channel PDMS/glass device, with the exploded view highlighting the coated PDMS chip containing an array of Y-shaped micro posts. (b) Schematic showing the surface of the channel and micro posts coated with graphene oxide (GO) and polydopamine (PDA). (c) The protocol involved the surface functionalization of the microfluidic chips. (Reproduced from Zhang P et al. [92], Lab Chip, 2016).

A microfluidic device for the immunocapture of circulating exosomes from both cell culture medium and patient plasma from a low sample volume was developed by Fang et al. [93] as shown in Figure 2-16. For capturing the exosomes, CD63 antibodies conjugated with magnetic nanoparticles (Mag-CD63) were used. Their study found that the amount of the exosomal tumor

marker EpCAM was much higher in the plasma of breast cancer patients than in healthy controls. The authors concluded that the microfluidics device might become a valuable tool for breast cancer diagnosis due to advantages such as better purity, intact yield, simplicity of operation, less time, and low cost.

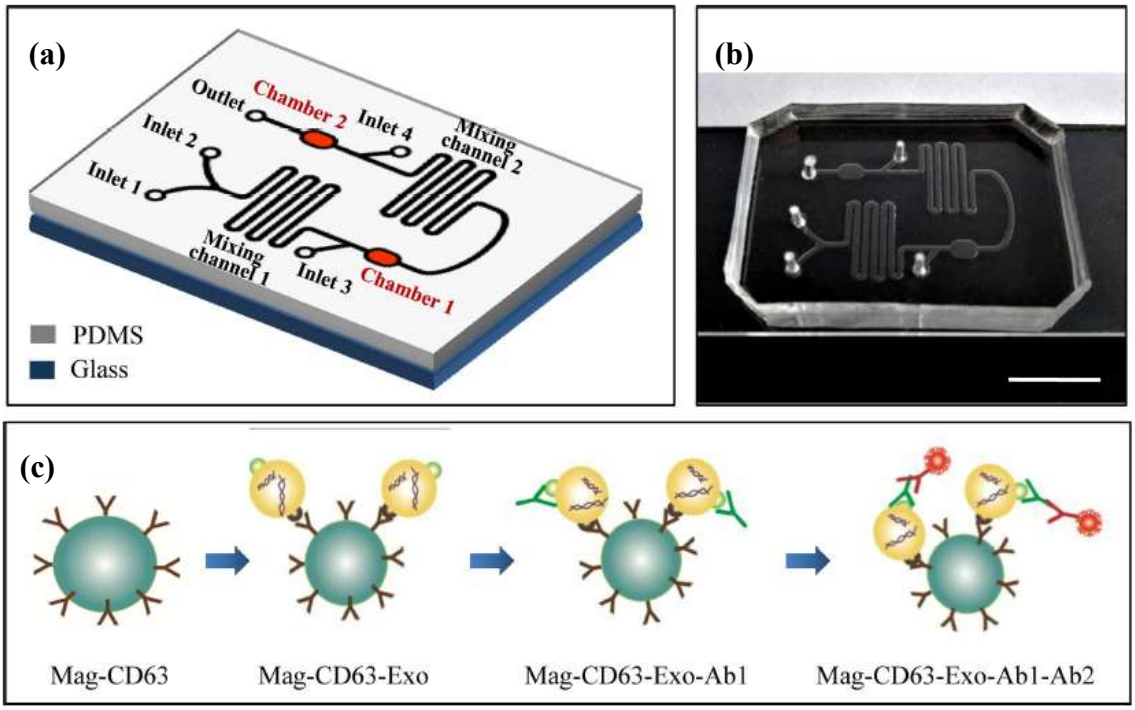

Figure 2-16: Chip design and principle for exosome capture and detection. (a) The microfluidic chip schematic representation. (b) Photo of the chip. The scale bar represents 1 cm. (c) Workflow for the immunomagnetic capture and detection of exosomes. (Reproduced from Fang S et al. [93], PLoS ONE, 2017).

More recently, our group [94] has developed a magnetic particle-based liquid biopsy chip to isolate EVs by using a synthetic peptide, Vn96, which specifically binds to heat shock proteins (HSP). In this design, a 3D mixer is integrated within the chip, as shown in Figure 2-17, improves capture efficiency and a sedimentation unit that allows the EV-captured magnetic particles to settle based on gravity. The significant advantages of the label-free technique implemented using the streptavidin coated magnetic particles include faster isolation of EVs from CCM (around 20 min) and easy removal of magnetic particles using a magnet after elution. The maximum isolation efficiency obtained was about 90% with 8.0 - 9.9 µm streptavidin-coated magnetic particles when 0.2 ml CCM was used.

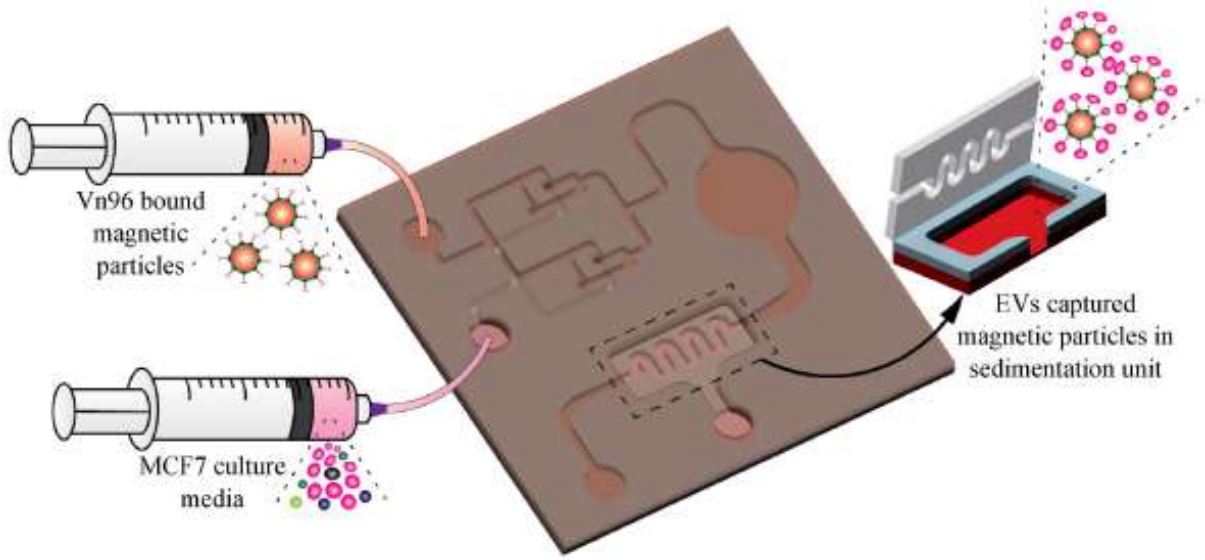

Figure 2-17: Isolation of EVs from the MCF7 CCM A) Schematic of the EV-isolation from the CCM in the microfluidic device. (Reproduced with permission from Bathini S et al. [94]. Copyright 2021 Elsevier Science).

2.4.2.2. Immunoaffinity Methods with Nanoplasmonic Detection of Exosomes

Im et al. [95] developed for the first time a nanoplasmonic exosome (nPLEX) assay based on the surface plasmon resonance principle. As shown in Figure 2-18, periodic nanohole arrays are the exosomes detection sites. They detected the exosomes derived from ovarian cancer cells, expressing CD24 and EpCAM. Therefore, the nanohole arrays were functionalized with antibodies against CD63. The detection sensitivity of the nPLEX assay was determined to be 1000 particles/μL, 10^4 times higher than the Western blotting and 10^2 times higher than the ELISA method.

A multiplexed microfluidic device based on tunable alternating current electrohydrodynamic (acEHD, nano shearing) was developed by Vaidyanathan et al. [96], as shown in Figure 2-19. Using their device, they detected exosomes derived from cells expressing the human epidermal growth factor receptor 2 (HER2), prostate-specific antigen (PSA), and CD9. Through their method, the detection sensitivity of 2760 exosomes/μL was achieved, which means a 3-fold enhancement, compared to the hydrodynamic flow-based assays (8300 exosomes/μL).

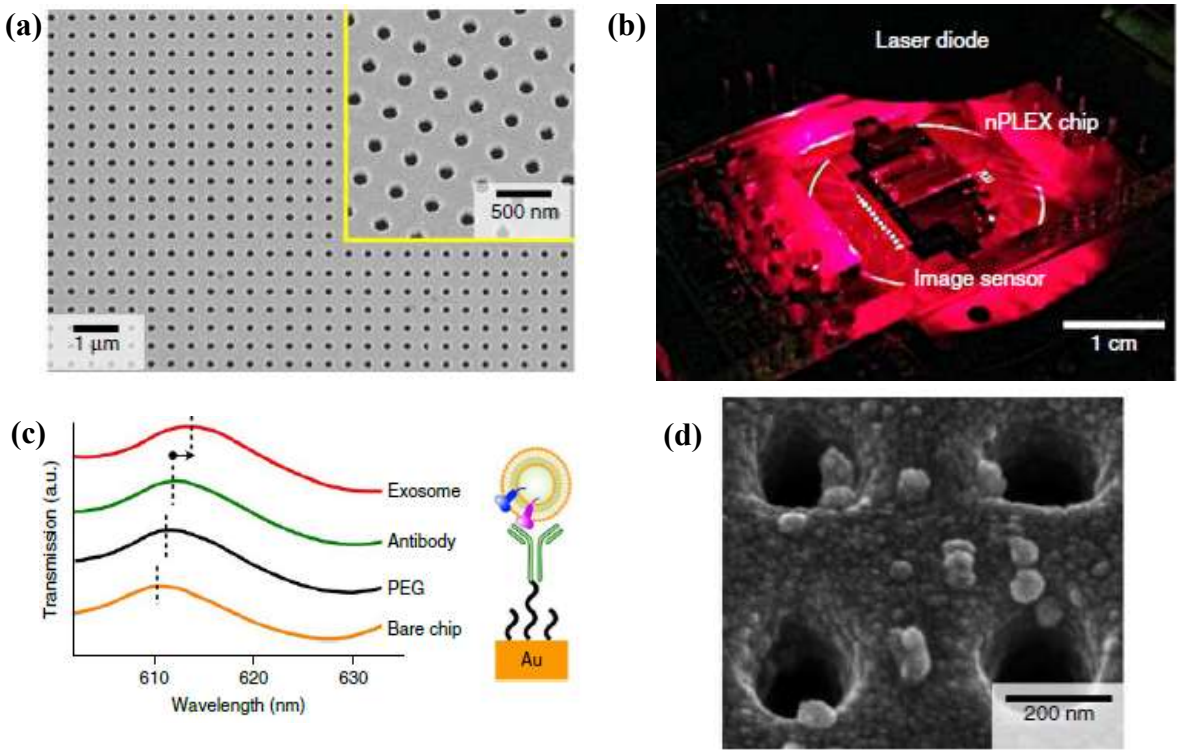

Figure 2-18: Label-free detection of exosomes with the nPLEX sensor. (a) A scanning electron Image of the periodic nanoholes in the nPLEX sensor. (b) A prototype of the nPLEX imaging system. (c) Schematic to represent the changes in transmission spectra to show the exosome detection with the nPLEX device. d) Scanning electron microscopy image showing the exosome capture near the nanoholes array. (Reproduced from Im H et al. [95], Nat Biotechnol., 2014).

Zhu et al. [97] presented a real-time, label-free method to detect and characterize tumor-derived exosomes in CCS without enrichment or purification, as shown in Figure 2-20. They used surface plasmon resonance imaging (SPRi) with antibody microarrays specific to exosome transmembrane proteins such as CD9, CD63, and CD81. Thus, with this approach, they could achieve a detection sensitivity of 4.87×10^4 particles/µL.

Our group, Bathini et al. [98,99] developed a simple microfluidic device to detect MCF-7 exosomes using an immune-affinity approach, Vn96 polypeptide, and LSPR detection. The schematic of the device and the sensing protocol are shown in Figure 2-21. The results indicate that the label-free technique, based on the sensitivity of the Au-LSPR band to the surrounding environment, is a promising approach. The Au nano-island platform can capture a high number of extracellular vesicles present in the MCF7, providing a detection range covering early stages to advanced stages of cancer. However, the authors did not mention the sensitivity of the detection of their method.

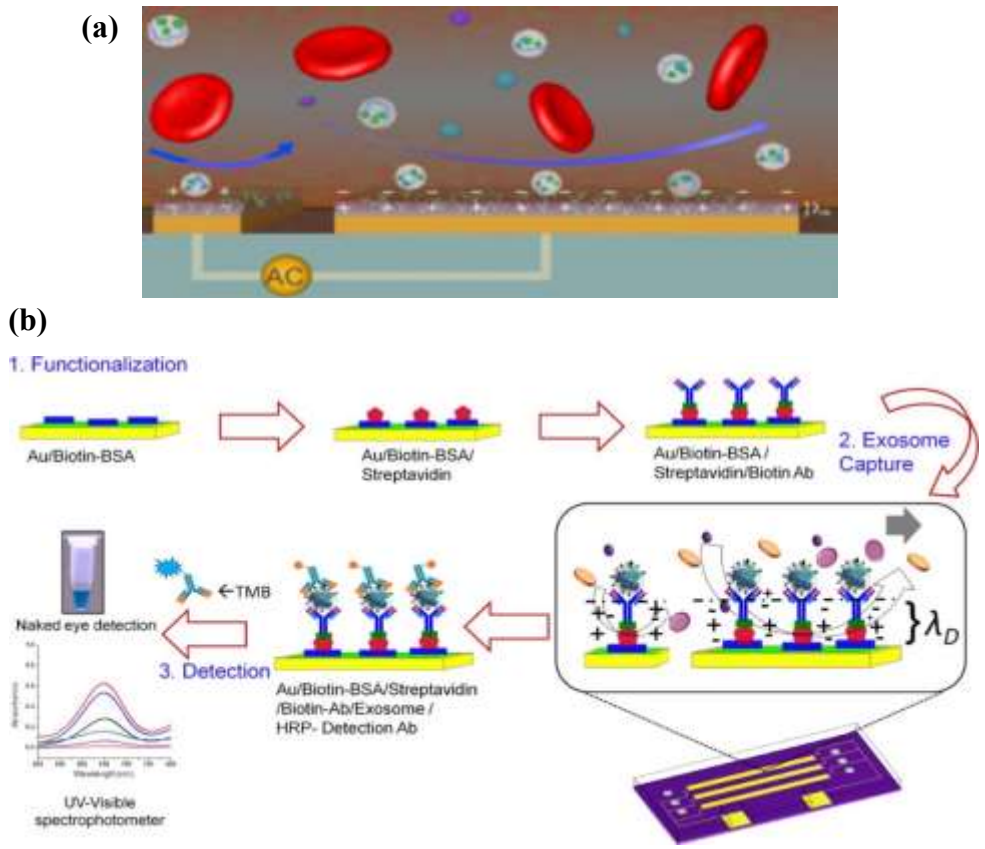

Figure 2-19: Tunable alternating current electro hydrodynamic nano shearing device for the detection of exosomes. (a) Schematic representation of ac-EHD induced device (appear as white spherical particles). (b) Schematic representation of the functionalization protocol. (Reproduced with permission from Vaidyanathan R et al. [96], Copyright 2014 American Chemical Society).

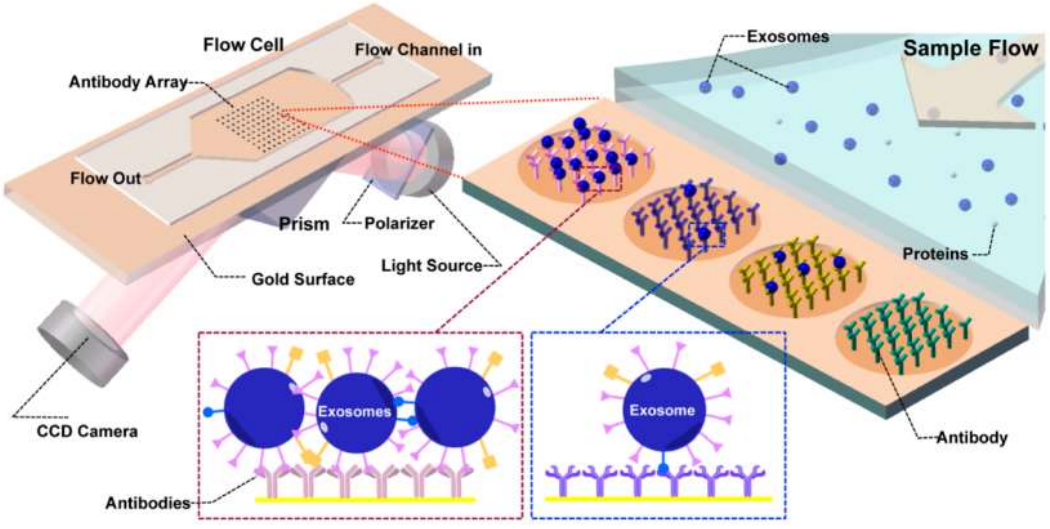

Figure 2-20: Label-free SPRi method for the detection and characterization of tumor-derived exosomes. Schematic view of SPRi combined with antibody microarray and measurement setup. (Reproduced from Zhu L et al. [97], Anal Chem., 2014).

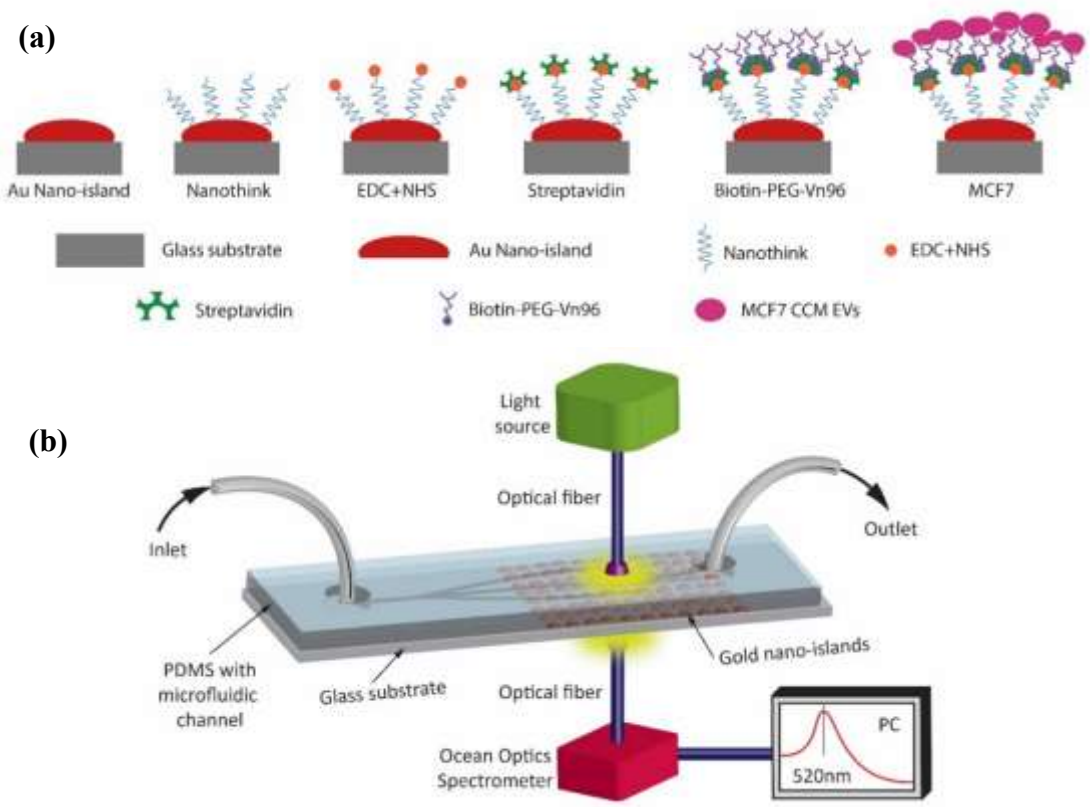

Figure 2-21: Label-free LSPR microfluidic device to detect MCF-7 exosomes. (a) Schematic of the microfluidic device with nano-island structures. (b) The biosensing protocol used to detect MCF-7 exosomes (Reproduced from Bathini S et al. [86], The European J Extracellular Vesicles, 2020).

Raghu et al. [100] developed a nanosensing array, combining the nano and microfabrication techniques for single exosome detection. As shown in Figure 2-22, plasmonic nanopillars were fabricated to accommodate at most one exosome. Therefore, to target the tetraspanins CD63 membrane-bound proteins in exosomes secreted by MCF7 breast adenocarcinoma cells, the plasmonic nanopillars were functionalized with anti-CD63 antibodies. Using this approach, the authors could achieve three orders of magnitude sensitivity improvement over previously reported real-time, multiplexed platforms.

A plasmonic platform based on gold nano-ellipsoids with an integrated microfluidic device was developed by Xiaoqing Lv et al. [101]. The nano-ellipsoids were fabricated using an anodic aluminum template as a shadow mask. Then, the nano-ellipsoids' surface was functionalized with the anti-CD63, specific to exosome transmembrane proteins. Figure 2-23 shows the schematics of the sensing protocol. The authors claim that the uniform adsorption of exosomes on the functionalized nano-ellipsoids enhanced the detection sensitivity of their design.

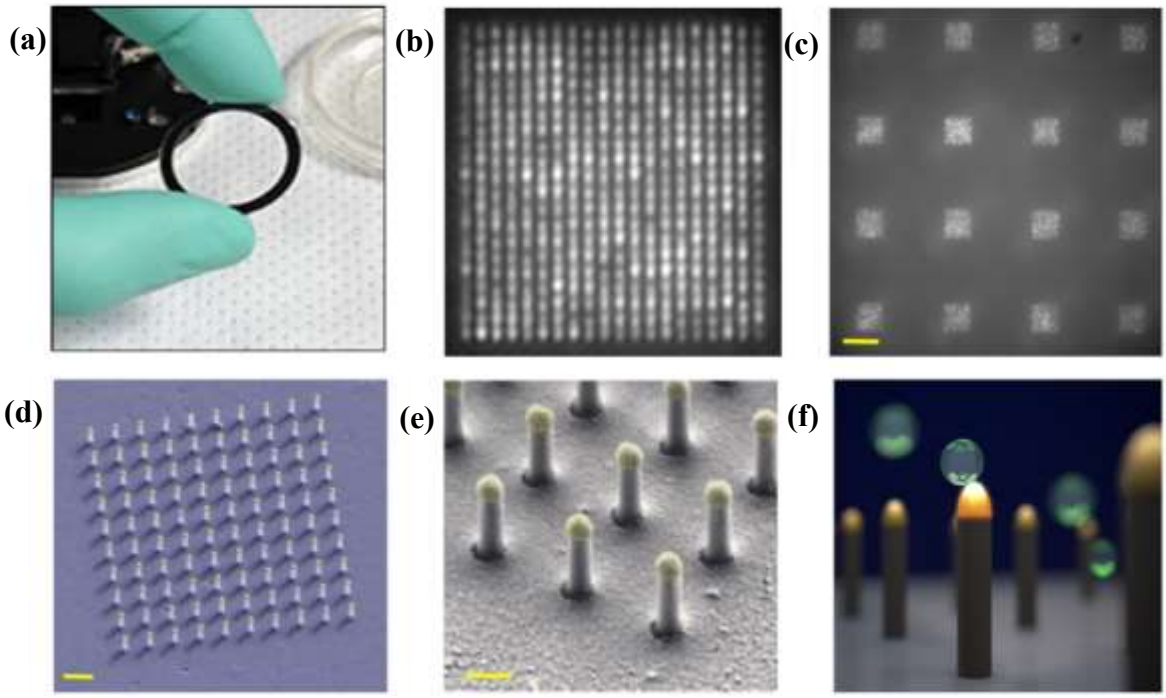

Figure 2-22: Nanoplasmonic pillars engineered for single exosome detection (a) Picture of the 25.4 mm diameter LSPRi sensor chip. (b) Scanning electron microscope image of the device for a 20 × 20 array, with a pitch size of 600 nm scale bar: 1 µm. (c) Image of sixteen arrays, each consisting of 400 plasmonic nanopillars in a 20 × 20 square lattice and 500 nm pitch, scale bar: 10 µm. (d) False coloured SEM image of a 10 × 10 nanopillar array, scale bar: 1 µm. (e) High-magnification false-coloured SEM image showing a detailed view of individual nanopillars, scale bar: 200 nm. (f) Picture illustrating the size matching of individual nanopillars diameter (d = 90 nm) to that of exosomes (~50 nm < d < 200 nm). (Reproduced from Raghu D et al. [100], PLoS ONE, 2018).

Based on the markers used for detection, the yield sensitivity, the yield capability, advantages, disadvantages, and the year the work was published, some of the most interesting immunoaffinity and nanoplasmonic approaches integrated with microfluidics-based techniques are summarized and tabulated in Table 2.1 and Table 2.2. The tables show that the microfluidic/LOC technology developments have enhanced exosome capture and detection in terms of their efficiency, compared to previous complicated and time-consuming methods.

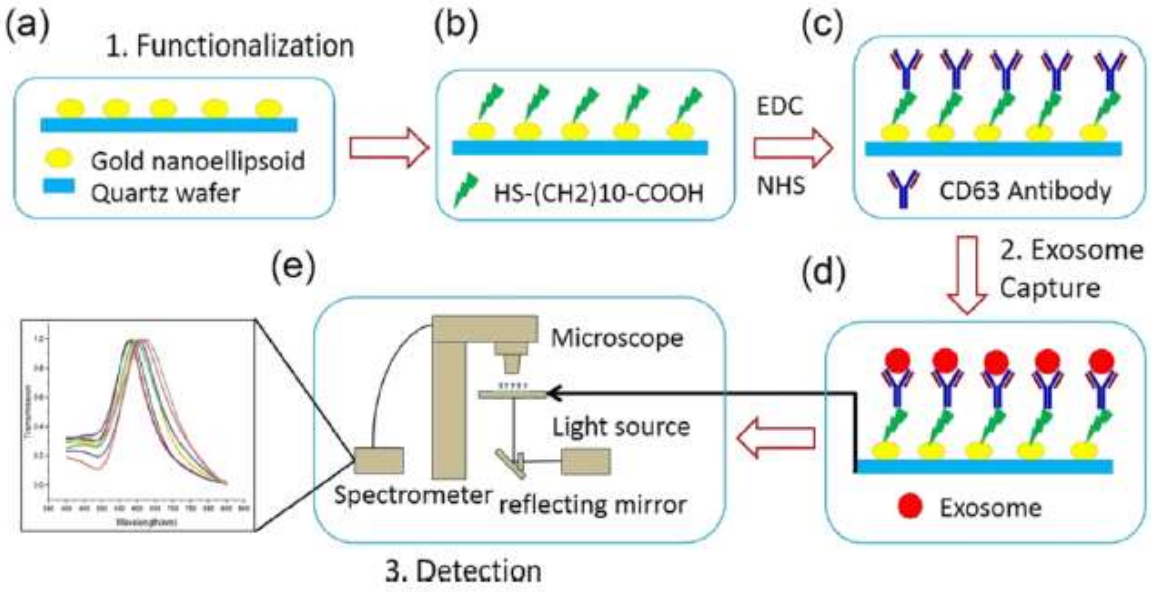

Figure 2-23: Schematic of the LSPR-based biosensor for the detection of the exosomes. (a) Fabricated gold nano-ellipsoid arrays on the quartz substrate. (b) Functionalization of the gold nano-ellipsoids with the Au−S bond. (c) Functionalization of anti-CD63 antibody (d) Exosomes injected into the microchannel and captured on the sensor substrate. (e) LSPR detecting platform (Reproduced with permission from Xiaoqing Lv et al. [101]. Copyright 2019 American Chemical Society).

Table 2.1: Immunoaffinity approach integrated with microfluidics technique to capture and detect exosomes

Techniques/Approaches	Markers used for Detection	Sample used and its volume	Detection Sensitivity (LOD)	Yield	Throughput of Isolation [µL/min]	Advantages	Disadvantages	Year of Publication
Anti-CD63 functionalized surface with herringbone groves [45]	CD63	Serum of 100 – 400 µL	NA	42 –94%	13.1	High specificity, Isolation time(~1h)	Specific only for CD63	2010
An array of porous silicon nanowire-on-micropillar [85]	Liposomes (83, 120 nm)	Liposomes of 30 µL	NA	45 – 60%	10	Trapping is relatively fast (~10min), High purity recovery of liposomes	Recovery time (~1 day), Not validated with clinical samples and no analysis of cargo protein	2013
Microarray spots (non-contact printing) - EV array [86]	CD9, CD63, CD81	Plasma of 1-10µL	2.5×10^4 exosomes per sensing spot	NA	NA	Multiplexed - 24 analytes per array, highly sensitive and high-throughput	Isolation time (~ 3 days), The study carried out only on healthy donors	2013
Microarray spots (contact printing) - EV array [87]	60 markers simultaneously	Plasma of 1-10µL	NA	NA	NA	Multiplexed - >60 analytes per array, Higher sensitivity due to the contact printing	Isolation time (~ 3 days), The study carried out only on healthy donors	2015
Online mixing in a serpentine channel with immunomagnetic beads [88]	EpCAM, α-IGF-1R, CA125, CD9, CD81, and CD63	Plasma of 30µL	0.28 - 0.38 pg/ml	42–97.3%	2	High specificity, Isolation time (~1.5h)	Specific for CA 125, EpCAM, and CD24	2014
An array of surface-functionalized circular	CD63 and extract total	400 µL serum	0.5 pM	15 –18 µg of	4	Easy scale-up, On-chip quantification	Low capture capacity, No Multiplexity	2014

microchambers ExoChip [89]	RNA			total proteins				
Acoustic nanofilter chip [90]	Exosome markers: CD63, Flotillin-1, HSP90, HSP70, Microvesicles marker: β1-integrin	10 µL Cell culture media & Packed RBC	NA	80-90%	~0.24	90% separation yield, *In-situ* control of size	Specific only for the Microvesicles	2015
Multiplexed continuous mixing in a serpentine channel with immunomagnetic beads (ExoSearch) [91]	CA 125, EpCAM, and CD24	Plasma of 10 µL-10mL	750 exosomes/ µL	90%	0.8	Isolation time ~ 40 min	Specific for CA 125, EpCAM, and CD24	2016
Nano-IMEX microfluidic chip with Y-shaped microposts coated with (GO/PDA) [92]	CD9, CD63, CD81, EpCAM	Plasma of 2 µL	~50exosomes/µL	NA	0.05	Enhanced efficiency, Scalability	NA	2016
Microfluidic device integrated with immunomagnetic capture [93]	EpCAM, HER2	~1000 µL Cell culture medium and Patient plasma	NA	NA	2	Higher purity and Intact yield	NA	2017
Microfluidic chip integrated with a 3D mixer and streptavidin coated magnetic particles [94]	HSP	0.2 ml of MCF 7 CCM EVs	NA	90%	NA	High yield, Faster isolation time, Isolation time ~ 20 min	Specific only for HSP	2021

Table 2.2: Immunoaffinity approach integrated with microfluidics technique and nanoplasmonic detections to capture and detect exosomes

Techniques/Approaches	Markers Detected	Sample used and its volume	Detection Sensitivity (LOD)	Yield	Throughput of Isolation [µL/min]	Advantages	Disadvantages	Year of publication
Periodic Au nanohole arrays (nPLEX) chip [95]	CD45, CD63, CA125, CA19–9, D2–40, EpCAM, EGFR, HER2, CLDN3, and MUC18	Ascites of 150 µL	~3000 exosomes	NA	8.3	Isolation time (~30min)	NA	2014
Microfluidic device with AC-EHD-induced [96]	HER2, CD9, PSA	Serum of 500 µL	~2760 exosomes/ µL	NA	4.2	Multiplexed sensing, 3-fold enrichment in detection sensitivity compared to a normal hydrodynamic flow	NA	2014
Printed antibody microarray on an Au coated surface (SPRi) [97]	CD9, CD41, CD63, CD82, EpCAM, and E-cadherin	Cell culture supernatant (CCS) exosomes	~ 4.87×10^7 exosomes/ cm^2	NA	NA	Real-time, label-free, and quantitative method	No multiplexity	2014
Au nano-island microfluidic device using LSPR [98,99]	HSP	100 µL of MCF7 Cell culture media (CCM) exosomes	NA	NA	NA	Label-free technique	Specific for HSP	2018

Au nanoplasmonic array for LSPR based digitalized detection (LSPRi) [100]	CD 63	MCF7 secreted exosomes (1×10^5 exosomes/ml)	3 folds	NA	NA	Multiplexed measurements, one exosome can be detected and individually imaged in real-time	NA	2018
Nano-ellipsoid arrays integrated with a microfluidic chip using LSPR [101]	CD63	Lyophilized exosomes	1 ng/mL	NA	NA	Low-cost, time-saving, and applicable to large areas	NA	2019

It is not easy to compare the methods discussed in section 2.3.2 and summarized in Table 2.1 and Table 2.2 because of their complexity and diversity. Several of them can detect exosomes in a reasonable timeframe, with high sensitivity and a good yield, but their design is generally not straightforward. Many published methods involve complex structures such as micro posts, micro, nanopillars, nano-ellipsoids, etc., requiring complex microfabrication methods. Some of the techniques are using printed arrays that can be fabricated easily. The results in terms of sensibility are very promising. Good results, especially, regarding exosomes isolation, have also been obtained using functionalized magnetic particles.

2.5. Outlook

Microfluidic isolation and detection methods represent clear progress compared to conventional strategies. Nevertheless, first-generation devices like those described in this chapter are not yet ready to be translated into clinical analysis. The main reason for this is the lack of standardization and validation of the microfluidic methods and the relatively low processing capacity. Additionally, because of the complexity of all the biological samples, the overlap of size between exosomes and other EVs, and the heterogeneity of exosomes, the purity of the isolated exosomes is lower. For this reason and other considerations, conventional methods like ultracentrifugation still account for 56% of all exosome isolation techniques employed in exosome research. However, despite the large sample capacity and high yield, the equipment is expensive, the run-time is long, and it cannot be used at the point of care. In addition, during the ultracentrifugation, the exosomes might get damaged. The main advantage of microfluidic separation is the possibility of integration on the chip of downstream analysis to detect all the components of exosomes directly. Microfluidic immunoaffinity methods have resulted in highly purified exosomes but work only with cell-free samples, and therefore the cost might be high, primarily because of the cost of antibodies. Microfluidic devices are highly portable and easily integrated with micromixers and other parts. The success of the isolation depends on the quality of pre-enriched exosomes.

We believe, as stated above, that the conventional methods will not be replaced by microfluidic devices or maybe only for specific applications like point-of-care where portability is necessary. It has to be stressed that lab-on-a-chip devices will evolve, and new functionalities will improve the quality and yield of microfluidic isolation. Magnetic immunocapture is an especially

valuable method. Thus, some of them have already been commercialized as exosome isolation kits. Most important for the future of microfluidic research is the standardization and validation of methods that will allow accurate comparison between different laboratories.

In conclusion, researchers interested in working in this field should be aware of the existing challenges and be ready to use their skills and creativity.

2.6. Conclusions

In this chapter, EVs/ exosomes and their importance as potential biomarkers for cancer diagnosis have been briefly discussed. EVs/exosomes are incredibly complex biological species, carrying information from the cancer cells that released them as very early signals. Their isolation and subsequent detection methods are complicated and not satisfactory for the time being. However, they are evolving and enriched by discoveries in nanoscience, microfluidics, plasmonics, etc. Significantly, the new microfluidic techniques such as 3D and 4D printing will simplify the microfabrication techniques used to produce devices. At the same time, the exosomes isolation and detection sensitivity could be enhanced by integrating several new designs of nanostructures with microstructures. The crucial importance of EVs/exosomes in cancer research is a powerful impetus for fast advances in their detection and isolation detection techniques.

Therefore, in the next chapter (Chapter 3) a comprehensive review of the available methods, techniques, and fabrication processes that could be potentially used to detect and isolate the EVs/exosomes as a biomolecule will be discussed.

Chapter 3. Gold Nano-Island Platforms for Localized Surface Plasmon Resonance Sensing

This chapter is reproduced from the article published in *Molecules*, 25, 20, 4661, 2020.

3.1. Outline

Nano-islands are entities (droplets or other shapes) that are formed by spontaneous dewetting, (agglomeration, in the early literature) of thin, and very thin metallic, especially, gold films on a substrate, by post-deposition heating or by using other sources of energy. In addition to thermally generated nano-islands, more recently, nanoparticle films have also been dewetted, to form nano-islands. The Localized Surface Plasmon Resonance (LSPR) band of gold nano-islands was found to be sensitive to changes in the surrounding environment, making them suitable platforms for sensing and biosensing applications. In this chapter, we revisit the development of the concept of nano-island(s), the thermodynamics and mechanism of dewetting of thin metallic films, and the effect of the substrate on the morphology and optical properties of nano-islands. A special emphasis is made on nanoparticle films and their applications to biosensing, with ample examples from the authors' work.

3.2. Introduction

This chapter covers the most significant achievements that occurred in recent years, but also, revisits early discoveries in the field of nano-islands, their fabrication, optical properties, and later, their application as plasmonic sensing platforms. Historically, nano-islands, as entities, emerged from thin metal film studies. They were generated by the annealing of thin films deposited by physical methods and their formation, driven mostly by the minimization of surface energy. As-deposited thin and very thin metal films are not stable thermodynamically, and by dewetting, will coalesce into small, droplets, called nano-islands [102–105]. Dewetting of metal thin films, showing the evolution of solid structures, is considered an important structure-directing mechanism. Thermally-generated nano-islands are random, their size distribution is quite wide and their adhesion to glass substrates is not strong enough for sensing purposes. The adhesion has been improved by using various under- or overlayers, or by partially embedding them in the glass substrate. Detailed investigations have demonstrated the high sensitivity of

nano-island's plasmon bands to changes in the surrounding environment, thus, making them suitable for sensing purposes. Historically, they were the first to be investigated as plasmonic sensors for LSPR (Localized Surface Plasmon Resonance) and Surface-Enhanced Raman Spectroscopy (SERS) applications. Further, many attempts have been made to improve the size and size distribution of nano-islands, especially, for LSPR sensing, for example, multiple dewetting, alternating with annealing, or the fabrication of micro-patterned arrays of Au and Ag nano-islands through template confined deposition.

Only in the last decade, after the complete development of synthesis methods of nanoparticles, nano-islands started to be prepared from nanoparticle films using wet methods. There are only a few publications on the fabrication and characterization of these nano-islands; however, they have been used successfully for analytical purposes. Extremely important, under the present circumstances, is the application of plasmonic photothermal biosensors, based on gold nano-islands, for the fast and accurate detection of SARS-CoV-2 [106].

This chapter is structured as follows: Section 3.3.1 is dedicated to nano-islands fabricated from thin films and plasmonic sensing based on thermally generated nano-islands. Section 3.4 introduces and briefly discusses the main plasmonic technologies, with an emphasis on Localized Surface Plasmon Resonance (LSPR), the core technology used in this work. Section 3.5 describes the nano-island platforms from nanoparticle films, together with their more recent LSPR sensing applications. This section also discusses the work of the authors' group in the field of plasmonic detection of biomolecules and biological entities, such as bovine growth hormone and exosomes, respectively, and the integration of the sensing methods in a microfluidic environment. We also briefly discuss the most relevant examples of the use of plasmonic biosensors for real bioanalytical and clinical applications. In this context, the applications of plasmonic biosensors on a chip for point-of-care (POC) are discussed in a separate section.

At the end of this chapter, our knowledge of nano-islands and their applications are summarized, and future work in the field of nanoplasmonics that may bring new ideas is emphasized.

3.3. Solid-State Dewetting of Thin Metal Films: Principle and Driving Force

3.3.1. Nano-island Platforms from Thin Metal Films

Most thin metal films deposited by physical methods such as thermal evaporation, sputtering, etc. are not stable structures because they are formed far from equilibrium [102–104]. When applying an external energy, for example, heating at temperatures below the melting point of the metal, the metal thin film will transform, spontaneously into nano-islands. Other methods to initiate this transformation, are ion bombardment, mechanical stress, and laser irradiation (CW or pulsed). The process is called solid-state dewetting or, agglomeration, and is driven by minimization of surface energy as well as of the free energy associated with interfaces.

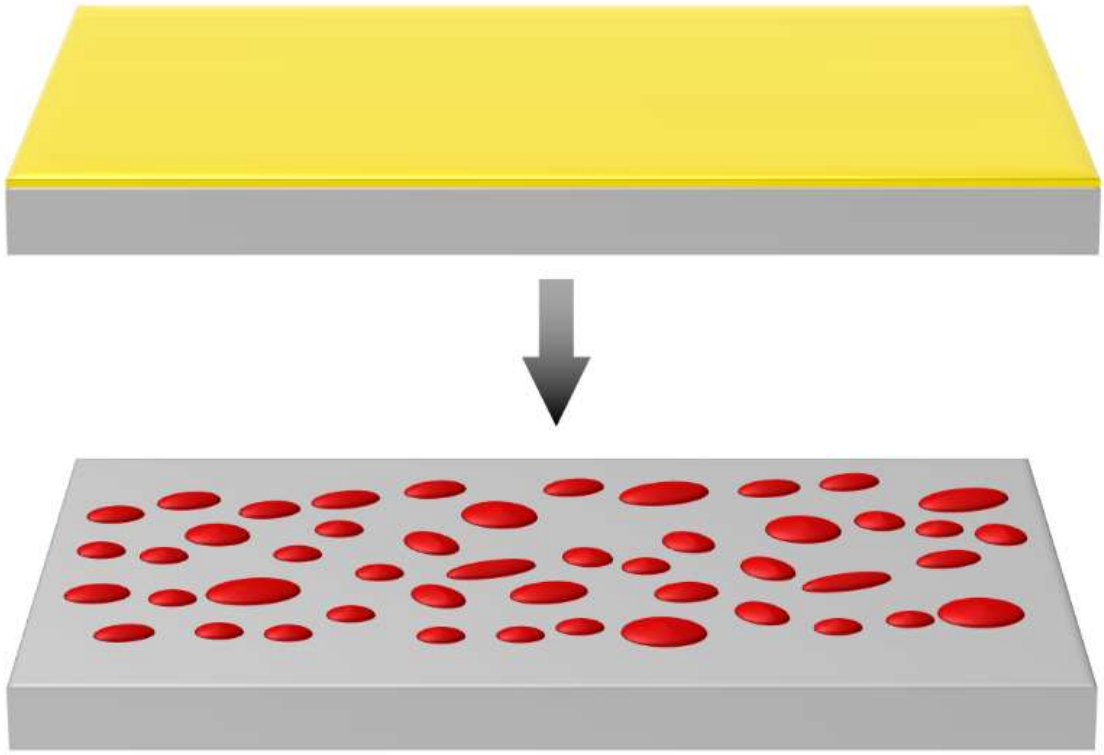

Figure 3-1: Dewetting of a thin gold film with the formation of nano-islands.

Abbott et al. [104] defined solid-state dewetting as the process by which thin solid films will coalesce into small particles as seen in Figure 3-1, at temperatures far below the melting point, driven by surface energy minimization. Dewetting of metal thin films, showing the evolution of solid structures, is considered an important structure-directing mechanism. Work on this topic started to be published in the 1970s, and since then, many studies on the

phenomenology of dewetting contributed to the understanding of its mechanism and pointed to ways toward various applications.

A fundamental study on the thermodynamics and kinetics of film agglomeration was published by Srolovitz and Goldiner in 1995 [107]. They defined agglomeration as the process by which an initially flat continuous film “dewets”, or uncovers a substrate. They analyzed in detail the forces that could contribute to the destabilization of a continuous film, such as surface tension principally but also stresses (especially tensile) within a film. The authors demonstrated that agglomeration (dewetting) is largely a hole nucleation and growth phenomenon. They thought that the main mechanism is the heterogeneous nucleation of holes at defects, such as grain boundaries, or even holes left through the deposition and processing of the film. As the hole grows, it pushes material out of its way, piling it up along the periphery of the hole.

The process may begin at edges or preexisting holes in as-deposited films, exposing the substrate. If holes or other defects, such as, for example, contaminants or capping layers in the case of nanoparticle films, do not already exist, they can be formed by ruptures in the film, and the holes will grow when the temperature increases and the growing holes will impinge upon each other.

Three different mechanisms have been proposed to explain dewetting: heterogeneous, initiated from a defect at the film surface; homogeneous, due to a small thermal density fluctuation; and spinoid dewetting, which is typical of liquid films [103,108]. Dewetting leads to the formation, not only of separate objects like droplets but also of stripes and pillars. Depending on the temperature, the substrate of the metal film (especially in the case of very thin films), and the time of annealing, dewetting may be incomplete, in which case no islands are formed. However, the structures formed in this way may be useful - for example, as electrodes in microstructures [109].

The principal parameters that affect the dewetting of thin metal films are the thickness of the film, the temperature of annealing, and the substrate [110]. It has been recently demonstrated that the temperatures at which nano-islands form vary for different substrate materials [111]. The grain size, in the case of polycrystalline films, may also affect the dewetting phenomenon. The diameter of the nano-islands formed by dewetting depends on the thickness of the film as shown in equation 3.1. The following relationship was proposed by Trice et al. [112]:

$$D = \left[\frac{24\pi 3\gamma}{Af(\theta)}\right]^{\frac{1}{3}} h^{\frac{5}{3}} = C$$

3.1

where f(θ) is the geometric factor, based on the particle contact angle θ; γ is the surface tension of the metal; and A is the Hamaker constant. This relation was observed in several experimental studies and is valid only at the temperature at which the nano-islands appear, as seen in SEM (Scanning Electron Microscopy) images.

The tendency to dewet depends largely on the surface diffusivity of the metal [104]. Gold has a very high surface diffusivity; therefore, thin gold films will dewet easily, resulting in the formation of nano-islands. However, for some applications, this high tendency to dewet may be a drawback that can be reduced by alloying with metals like Pt or Ti [113].

Both continuous gold films and gold films of thicknesses below the percolated threshold (typically 5–10 nm nominal (mass) thickness) have been dewetted [114]. It has to be mentioned that in the literature there is no consensus regarding the definition of "thin", "very thin", and "ultrathin" films. For the sake of further discussion, films having 1–3 nm thickness will be considered very thin with a well-defined plasmon band, while 4–10 nm will define thin (semi-continuous) films.

It can be seen in Figure 3-2 that very thin films (2 and 3 nm) show a well-defined plasmon band around 567 nm and 578 nm respectively, corresponding to discrete nanostructures, while the 5 and 10 nm films that are (semi-) continuous show a large plateau toward the NIR (Near Infrared) region of the spectrum.

The authors investigated the transformation from percolated film to islands by in situ transmission spectroscopy, using a temperature-controlled tube furnace and doing measurements all along the annealing process.

Nano-islands have been prepared not only from Au films, but from Ag, Pt, Pd, and Cu as well [115,116]. Large area nano-islands with nanogap spacing have been prepared by multiple dewetting. It has to be mentioned that dewetting the same metal film on different substrates will result in nano-islands with different sizes, showing the important role of interfacial energy [117].

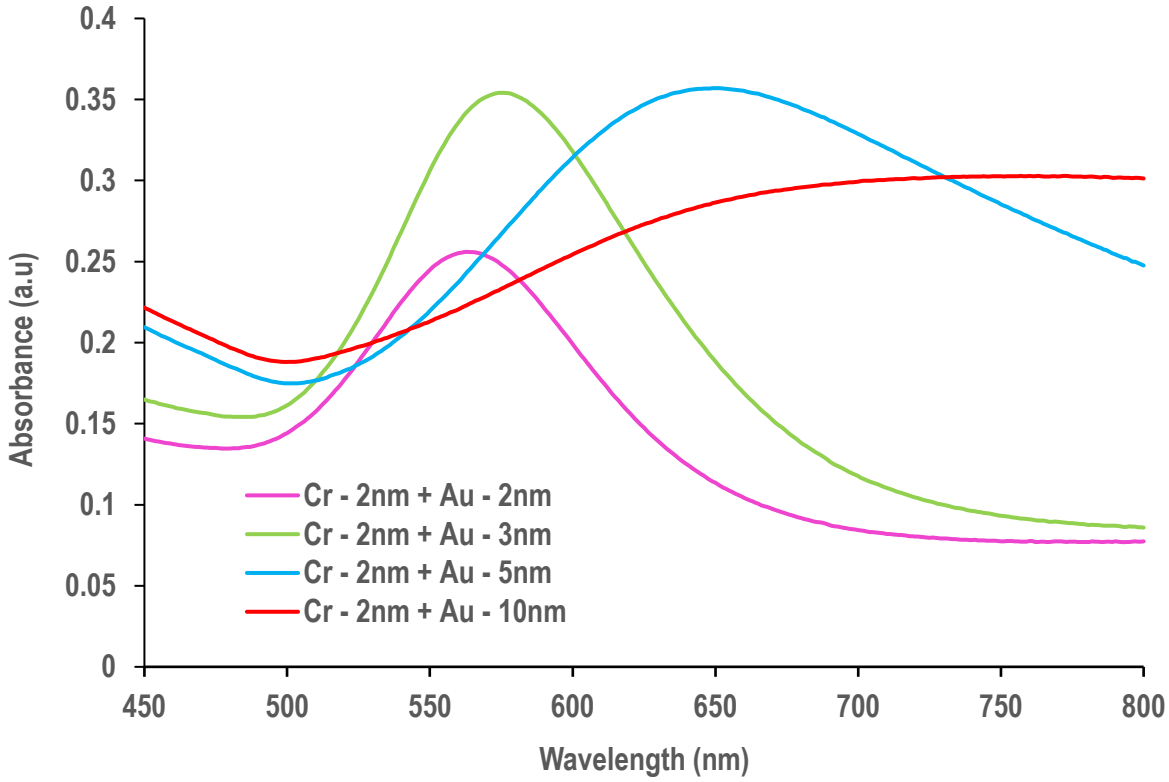

Figure 3-2:Visible spectra of e-beam evaporated gold films annealed at 500 °C for 2 hrs with different nominative film thicknesses of Gold (Au) with 2nm of Chromium (Cr) underlayer.

For example, nano-islands deposited on single-layer graphene by physical vapor deposition or *in-situ*, solution-phase chemical synthesis exhibit completely novel properties. For this reason, it has been called a composite film, which can be regarded as a metamaterial [118]. The optical and electronic properties of this material, controlled by the morphology of nano-island films, can be modulated in ways reminiscent of semiconductors. B. C. Marin et al. emphasized that the role of graphene in this material is not only of support but principally, graphene is the active component that determines the optical and electronic properties of the composite. The surface energy of the substrate supports that graphene influenced the morphology of the nano-island films, and thus, a wide range of morphologies could be produced, from isolated islands to percolated networks. These graphene nano-island composite films exhibit tunable morphologies and small gaps between adjacent nano-islands and could be transferred to flexible substrates [119].

The most important applications of metal nano-islands on graphene, especially in sensing, will be discussed in Section 3.5. The nano-island graphene composite films contain gaps between

the nano-islands, which, when functionalized with benzene thiolate, behave as hot spots for surface-enhanced Raman scattering (SERS). The authors have shown that the mechanical strain in the film increases the sizes of the gaps; this attenuates the electric field, and thus, the SERS signal. This “piezo-plasmonic” effect can be quantified, and the sensor is among the most sensitive mechanical sensors of any type.

A simple sputtering, annealing, re-sputtering, and re-annealing process was proposed to tune the structural and optical characteristics of Au nano-islands on a glass substrate [120].

It was found that the size and inter-particle distance of nano-islands depend on the annealing time and temperature. High temperature annealing tends to increase the size and inter-islands distance of Au nano-islands. Re-sputtering and reannealing under different conditions made possible again the tuning of the size and inter-particle distance. Investigations of the optical characteristics of Au nano-islands demonstrated that the surface plasmon resonance peak of islands was tunable from 510 nm to 620 nm. The authors found that the best results in terms of refractive index sensitivity were obtained when the re-annealing temperature was 500 °C for 5 h. These results suggest that the scheme “sputtering, annealing, re-sputtering, and re-annealing” is an effective method to tune the structure and increase the refractive index sensitivity of sputtered Au islands.

Different kinds of adhesion layers have been investigated to increase the adhesive strength between the gold film and the glass surfaces, without damping the LSPR in gold nano-islands [121,122]. Improvement of the adhesion is commonly achieved by evaporating 5-10 nm Cr, Ni, or Ti underlayers. The metal underlayer is light absorbing and thus interferes with the absorption signal. Pre-coating the glass substrate with a self-assembled layer of mercapto- or amino-functionalized silane has been shown to improve metal adhesion. To overcome the disrupting effect of the adhesion layer, dielectric materials are of interest, due to their low absorption of electromagnetic energy. MPTMS (3-mercaptopropyl-trimethoxysilane) is an alkoxysilane molecule with a thiol functional group. It can be grafted to a glass silicate substrate through a reaction, establishing strong chemical bonds with gold nanoparticles. [123].

A mild annealing (200 °C, 20 h) has allowed the optimization of the optical response [121,122]. Post-coating with an ultrathin, sol-gel-derived silica film was also proposed by

Rubinstein's group as an alternative, to stabilize gold nanostructures formed on silanized glass [124,125].

The authors investigated the optical properties of Au island films prepared by direct thermal evaporation onto indium tin oxide (ITO) substrates, without the need for pre- or post-coating stabilization of the surface. The effect of mild thermal annealing (150 °C, 12 h) or short, high-temperature annealing (500 °C, 1 min) on the morphology of the gold nanostructures was investigated [125]. Because of the poor stability of gold and silver islands in water and various solvents, adhesion layers of Cr and sometimes Ni and Ti are used, especially in sensing experiments [104,125]. The drawback of these materials is their potential diffusion into the Au film during the annealing process [126]. In addition, their possible alloying with gold may result in damping of optical properties [104,127].

Au/Ag alloyed nano-islands with the desired composition have been prepared by thermal dewetting of thin metal films that are thermally evaporated. The complete miscibility of alloyed nano-islands results in the possibility of tuning the plasmon resonance wavelength in the visible range, opening up a new direction for plasmonic enhancement in surface-enhanced Raman scattering or plasmon-enhanced fluorescence. The performance of bimetallic nanostructures may even surpass individual properties and display new properties, often explained by synergistic effects.

Alloyed nano-islands with well-defined sizes and shapes can be obtained by using successive thermal evaporation of thin Au and Ag films, as well as low-temperature thermal dewetting [128]. Successive thin film evaporation and thermal dewetting enable the large-area nanofabrication of Au/Ag alloyed nano-islands with well-defined sizes and shapes. The complete miscibility of Au and Ag leads to the tailoring of plasmon resonance over the wavelength region by simply changing the film thickness ratio.

Another method for stabilizing the nano-islands was proposed by the Rubinstein group [129] and involves high temperature annealing that results in a partial embedding of the nano-islands in the glass substrate, as shown in Figure 3-3.

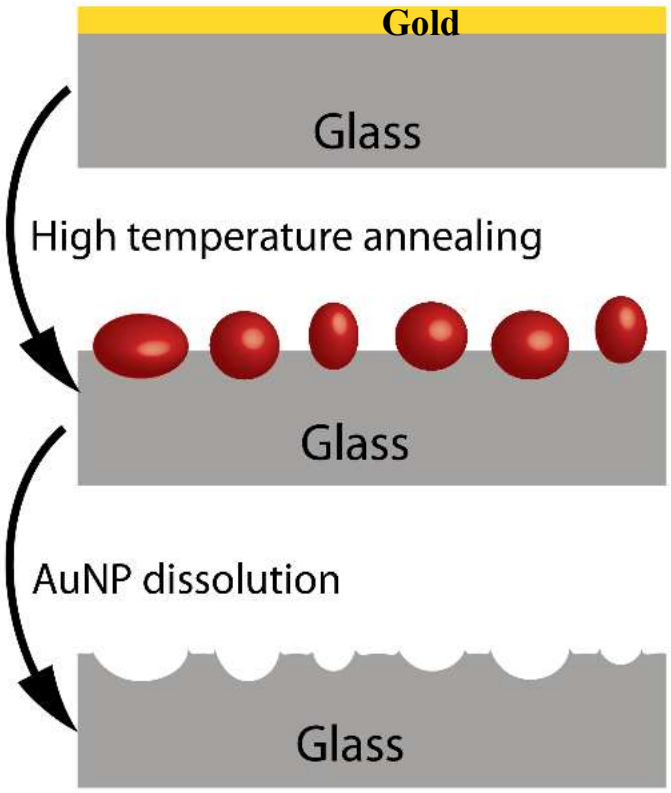

Figure 3-3: Schematic showing the traces of nano-islands in glass, after their removal by dissolution.

After dissolving the gold, the authors could see the traces of the nano-islands in the AFM (Atomic Force Microscopy) and SEM images. If the nano-islands are not stabilized, immersion in the solvents and drying during the sensing process could result in changes in their morphology, and implicitly, in their optical properties. Previous authors have explained the poor adhesion of gold and silver to glass and other oxide substrates by their weak chemical interaction with substrates such as glass. To obtain better adhering nano-islands, dielectric layers of mercapto silane have been used as well [121,130].

Other adhering layers, such as the highly transparent and conductive ITO (indium tin oxide) [125] and FTO (fluorine-doped tin oxide) [131] have also been suggested. Ghorbanpour and Falamaki [132] have replaced the Cr and Ti intermediate layers with silver, followed by an annealing treatment.

Post-coating with a very thin silica film was also used to stabilize the gold structure [124]. In another work [125], the authors prepared Au nano-island films by thermal evaporation onto ITO and studied the effect of mild annealing (150 °C, 12 h) or short, high-temperature annealing

(500 °C, 1 min) on the morphology of Au nanostructures. They investigated the mechanical, chemical, and optical stability of interfaces. To stabilize the islands, SiOx overlayers were also deposited on them. The results have shown that 4 and 6 nm films formed connected the gold structures by dewetting, while 2 nm films formed almost spherical Au nanostructures and small nano-islands. The highest sensitivity was found for the 2 nm film. The authors demonstrated the possibility of real-time sensing by monitoring the absorption of biotin–BSA (Bovine Serum Albumine) and the interaction with avidin.

An interesting technique has been developed by De Almeida et al. [133] and others [134] to grow thin metallic layers on the top of optical fiber surfaces and dewet them thermally to form nano-islands. These configurations, as seen in Figure 3-4, were used for LSPR and SERS applications and will be discussed more in detail in the following sections of this chapter.

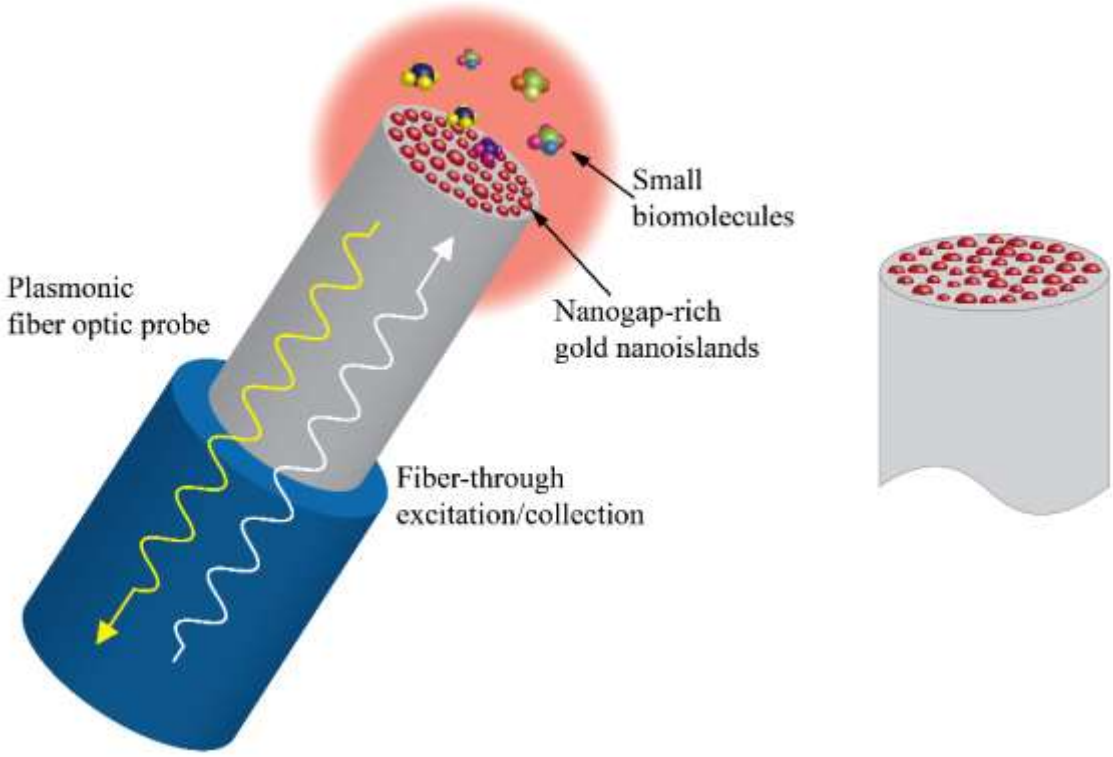

Figure 3-4: Fiber-optic plasmonic probe for surface-enhanced Raman scattering (SERS) with nanogap-rich Au nano-islands on the top surface of the fiber (modified from Kwak [134], free to read and use under the Creative Commons License).

3.4. Surface Plasmon Resonance (SPR) and Localized Surface Plasmon Resonance (LSPR) as Core Sensing Technologies

Optical biosensors, particularly those utilizing plasmonic technology as illustrated in Figure 3-5, have recently gained attention as a potential solution for disease diagnostics at the point-of-care (POC) level. There is a growing need for cost-effective, affordable, and robust POC platforms for diagnosing infectious and chronic diseases. These platforms should require minimal sample volumes and be capable of delivering real-time responses with high sensitivity. A biosensor platform incorporating small integrated devices could facilitate rapid, label-free assays.

Surface plasmons can be excited using a coupling prism and a thin gold layer, as shown in Figure 3-6 (a). They propagate parallel to the metal surface at the metal/dielectric interface. The confinement and enhancement of light result in a significant increase in the scattering signal of molecules adsorbed on the thin metal film, thereby enabling surface-enhanced assays such as surface-enhanced Raman spectroscopy (SERS). Additionally, the resonance between the incident light field in the visible/near-infrared wavelength range and the electron clouds of a nanoscopic metal structure can occur. Plasmonic materials comprise metallic (primarily gold and silver) nanostructures that support surface plasmon polaritons.

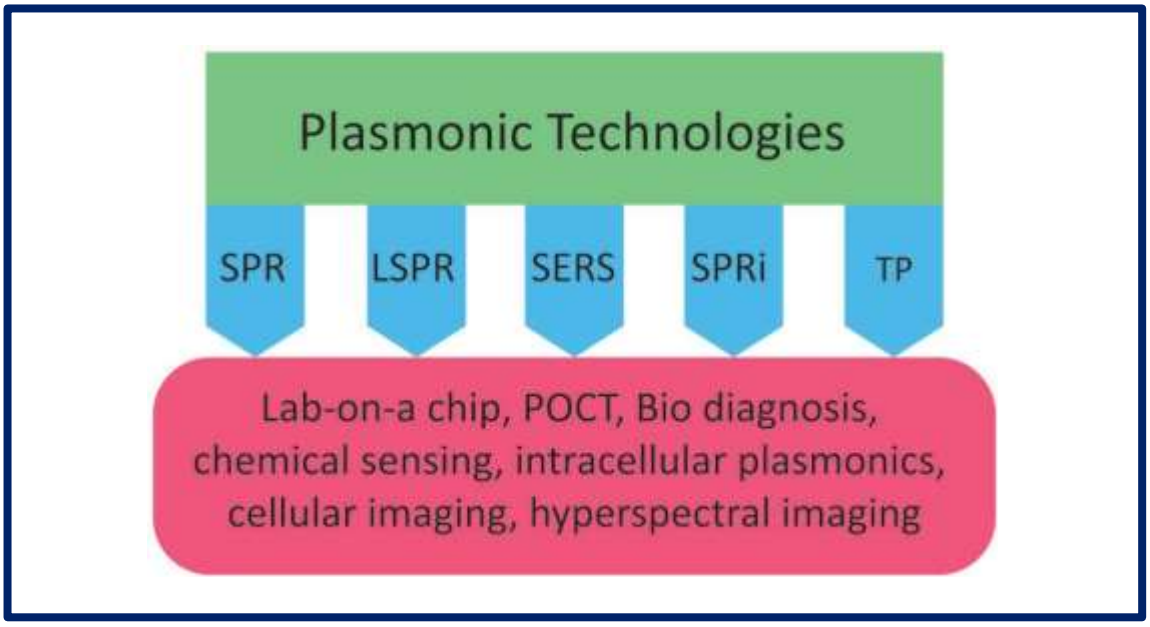

Figure 3-5: Plasmonic technologies [135].

Localized Surface Plasmon Resonance (LSPR) occurs when the diameter of a nanoparticle is significantly smaller than the wavelength of the incident light, as illustrated schematically in Figure 3-6 (b). This phenomenon involves the confinement of light and the coupling between the coherent oscillation of the conduction electrons in nanostructured noble metals and the incident light. This interaction leads to a shift in the position of the plasmon band and an enhancement in the intensity of the extinction. Both of these effects are utilized for sensing purposes by immobilizing the analyte on the surface of the metal layer or nanostructure.

LSPR induces a strong enhancement of the electromagnetic field around a nanoparticle. The position of the LSPR band wavelength maximum, λ_{max}, is sensitive to the dielectric properties of the surrounding environment, and since the dielectric constant is proportional to the refractive index, LSPR sensing is generally referred to as refractometric sensing. The dependence of the plasmon band shift on changes in the dielectric properties of the environment is described by the following relationship, shown in equation 3.2.

$$\Delta\lambda_{max} = m\Delta n[1 - exp\ (-2d/l_d)] \qquad \textbf{3.2}$$

where 'm' is the refractive sensitivity of the nanostructure, 'Δn' is the change in the refractive index upon the adsorption of the analyte[10], 'd' is the distance of the analyte from the surface (the adsorbate layer thickness), and 'l_d' is the decay length of the electromagnetic field (EM). The sensitivity factor, m, can be optimized by choosing an adequate shape and size of the nanoparticle. Because the refractive index increases as a result of the adsorption of an analyte, the shift of the plasmon band is expected to be toward longer wavelengths (i.e., a red shift). Even if the bulk sensitivity of the SPR sensors outperforms LSPR it has been demonstrated that the surface sensitivity of LSPR is considerably higher, especially in the case of low concentrations, because this kind of sensor is more sensitive to the changes near the surface. For SPR, the bulk sensitivity is much higher, because the decay of the EM field is larger, typically hundreds of nanometers, compared to only a few nanometers for an LSPR configuration.

[10]**Analyte**- a chemical or biomolecular substance that is being found and measured.

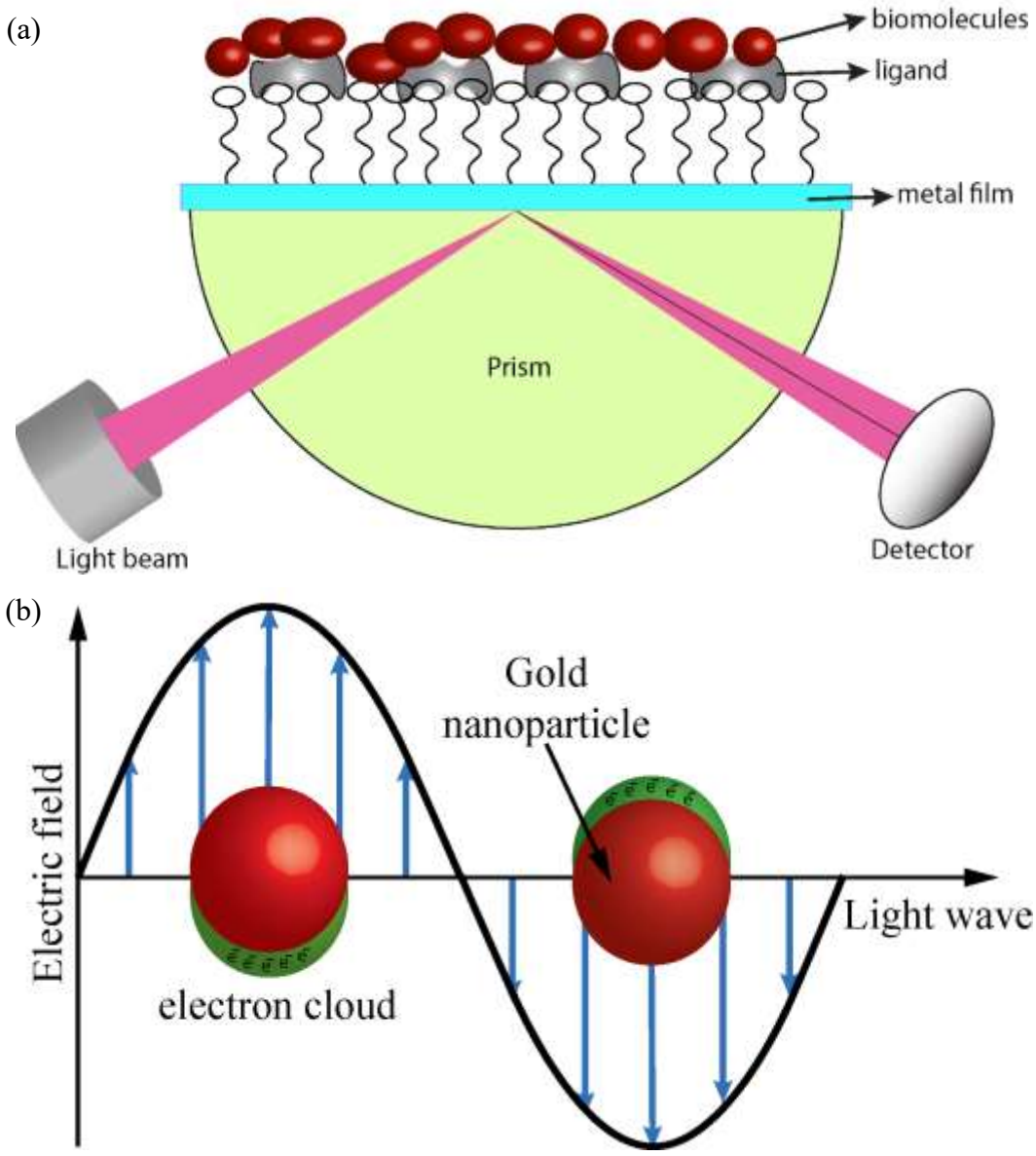

Figure 3-6: Diagram illustrating (a) the Kretschmann configuration for excitation of propagating surface plasmons. (b) the resonance between the conduction electron clouds of the metal nanostructure and the incident light [135].

It is well established that the decay length of the electromagnetic field for LSPR sensors depends on the size, shape, and composition of nanoparticle or nanostructure and, in any case, is not more than 5-15 nm, permitting the detection of very thin layers of adsorbate molecules. The interest in LSPR-based biosensors relies on their unique properties, allowing label-free and real-

time biomolecular analysis with possible detection of biomolecular interactions (antigen-antibody interaction, DNA hybridization, etc.) at low concentrations. It has to be stressed that any plasmonic detection process is possible only if the analyte molecules can be strongly tethered to the sensor surface, usually through a linker molecule.

3.5. Plasmonic sensing based on thermally generated nano-islands

The different sensing applications of nano-islands are illustrated schematically in Figure 3-7.

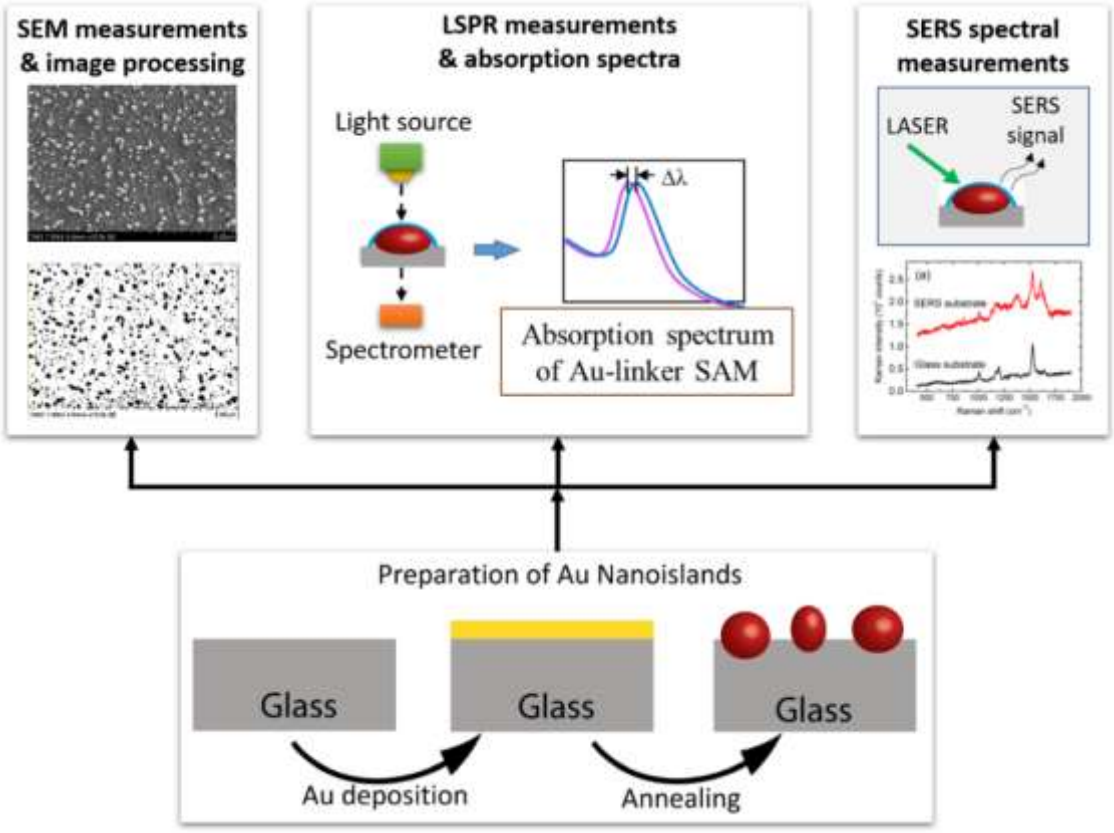

Figure 3-7: Localized surface plasmon resonance (LSPR) and SERS sensing applications of nano-islands.

As shown in Figure 3-2, very thin films of gold with discrete nanostructures display a well-defined plasmon band in the UV-visible spectrum. After annealing, the random nano-islands formed by dewetting will show a much better defined, narrow LSPR band, situated around 520–530 nm or even at higher wavelengths. It has been found that this Au plasmon band is highly sensitive to the medium surrounding the nano-islands. The plasmon band shifts toward longer wavelengths when the refractive index of the environment increases. The following equation 3.3

describes the dependence of the spectral intensity change of the nano-island sensor on the refractive index sensitivity [136]:

$$R = m\Delta\eta[1 - \exp(-\mathrm{d}/\mathrm{l})] \qquad 3.3$$

where 'R' is the sensor response (shift of the plasmon band or/and change in the absorbance); 'm' is the refractive index sensitivity (RIS) that is, spectral intensity change per refractive index unit (RIU) change; 'Δη' is the change in the refractive index of the surrounding medium due to the binding of the adsorbate, 'd' is the thickness of the adsorbate(dielectric) layer, and 'l' is the plasmon effective decay length. This rather empirical relationship shown in equation 3.3 can be useful for sensing applications, even though it does not distinguish between absorption and scattering [136,137].

The sensing performance of plasmonic structures can be characterized by the figure of merit (FoM) = $S_{bulk}/\Delta\lambda$, where $\Delta\lambda$ is the resonance width and S_{bulk} is the bulk sensitivity, defined as $S_{bulk} = \partial\lambda/\partial n$ - that is, the shift of the resonance wavelength upon a change of the refractive index of the surrounding medium n.

The application of thermally-generated nano-islands to sensing was pioneered by Rubinstein's group [122,136,138–140], and subsequently, many other groups have investigated the optical properties and the sensitivity of various platforms for sensing applications [137,141–143]

3.6. Nano-island platforms from nanoparticle films

Our group principally investigated the analytical performance of nano-islands, prepared by the dewetting of gold nanoparticle films [98,137,144–147]. The principal motivation for this work was the need for a simple and rapid method of detection of growth hormone levels in milk and milk products. A simple method for the preparation of multilayers of gold nanoparticles on glass substrates was developed by our group by modifying Prevo et al.'s method [148]. The nanostructure obtained from the angled deposition, as shown in Figure 3-8, has chain-shaped structures with a broad UV-visible absorbance spectrum.

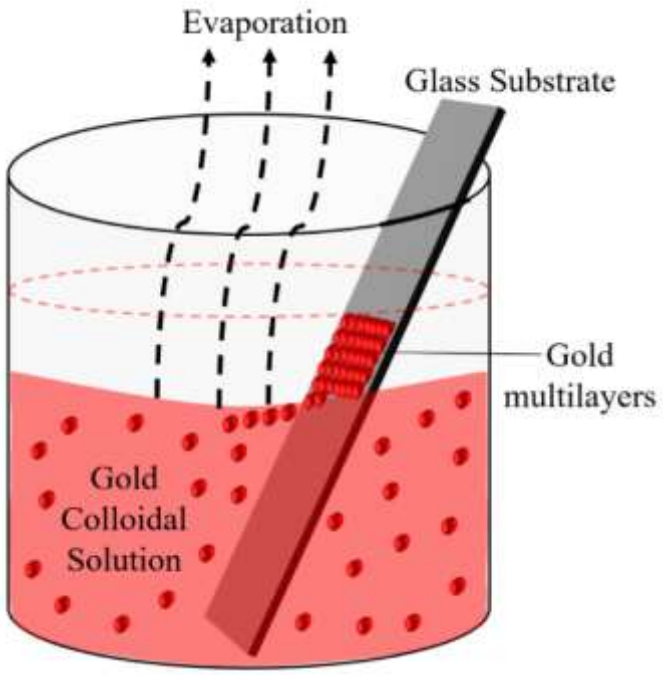

Figure 3-8: Schematic of the deposition of AuNP (Nanoparticle) multilayers by a thermal convection method (modified from Bathini [98]).

The morphology of the non-annealed structures was modified by dewetting to a nano-island like structure as shown in Figure 3-9, by annealing at various temperatures. The sensitivity of both non-annealed and annealed platforms was investigated by using solvents with known refractive indices. The sensing results showed a higher sensitivity for the annealed samples that is, for the nano-island structure. The annealed platform was used for the sensing of bovine somatotropin (bST), using an immunoassay format. The proposed sensing platform showed a detection limit as low as 5 ng/mL of bST. Further, the sensing platform was integrated into a microfluidic device, and sensing experiments were carried out. The results demonstrated the suitability of nano-island structures integrated into a lab-on-a-chip device to detect bovine somatotropin with good sensitivity.

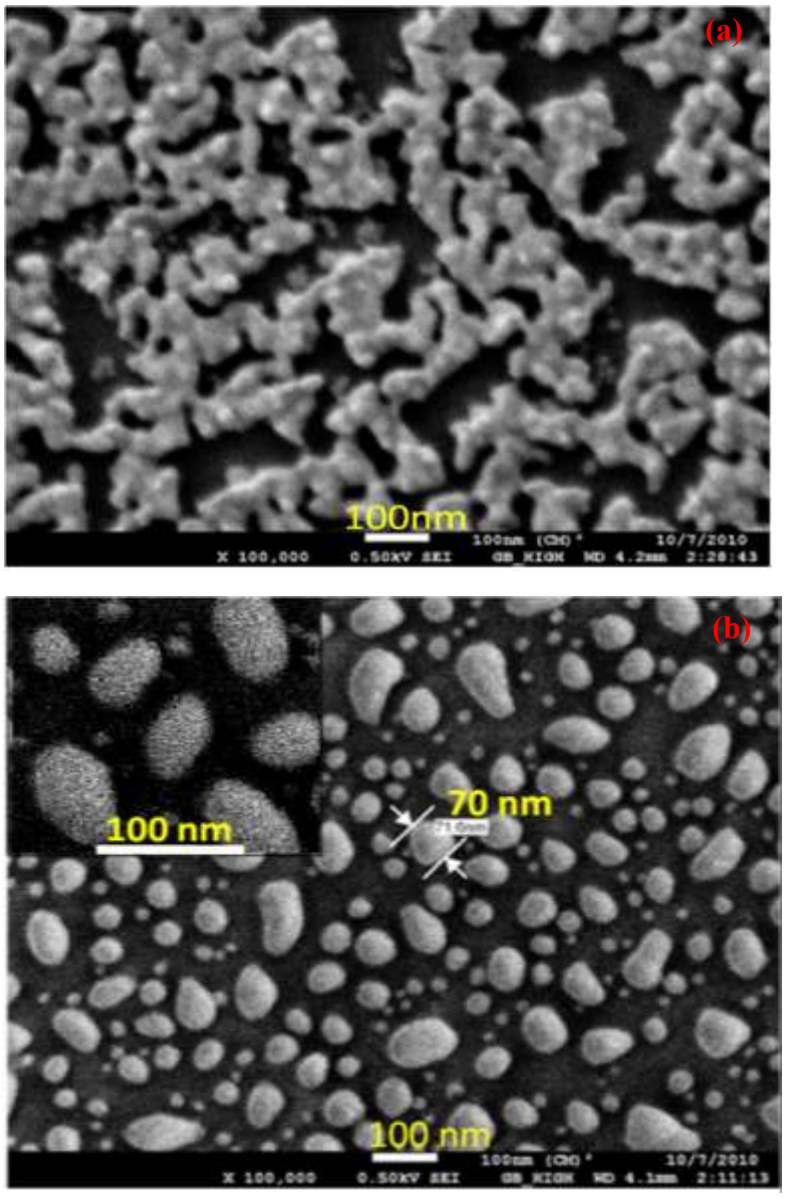

Figure 3-9: SEM images of three-dimensional (3-D) gold nanostructures. (a) as-deposited and (b) after annealing at 550 °C for 1 h (reproduced from [144], open access paper).

Figure 3-9 (a) clearly shows the presence of linear aggregates of gold in the sample deposited by thermal convection. After high-temperature annealing, random nano-islands are formed with quite a wide size distribution as shown in Figure 3-9 (b). The mechanism of dewetting of nanoparticle films is thought to be similar to that of thin metal films, but, in this case, dewetting is initiated by defects that originate from capping layers or contaminants. As in the case of metal films, the driving force is the minimization of the energy.

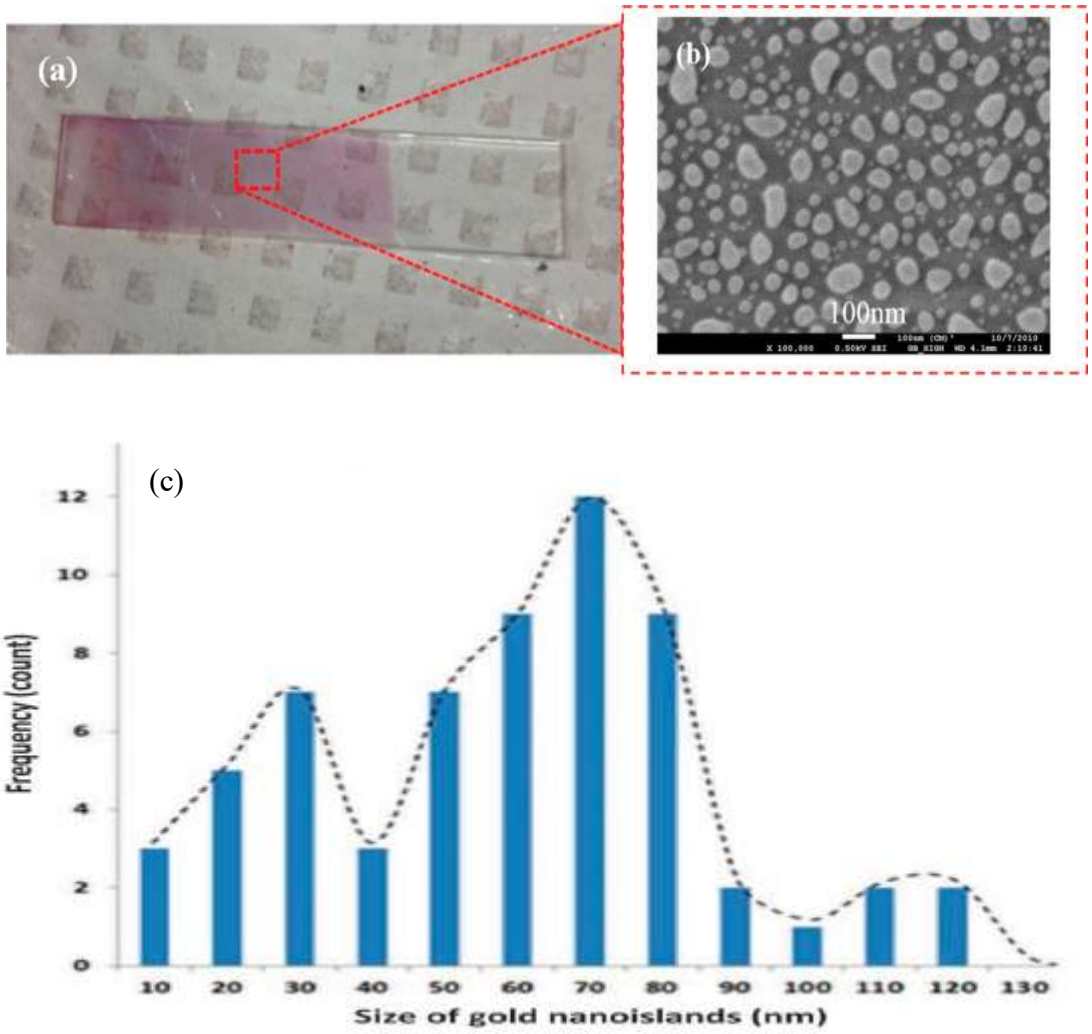

Figure 3-10: (a) Glass substrate with gold nano-islands. (b) scanning electron micrograph of gold nano-islands, and (c) size distribution of nano-islands (reproduced with permission from [145], copyright 2015, American Dairy Science Association).

The lighter and darker alternating strips seen in Figure 3-10 (a) originate from the mechanism of the deposition of gold nanoparticles in the case of thermal convection. Because of the various interactions between the nanoparticles and NP–glass substrate, capillarity, etc., the deposition is not continuous. The consequence of this strip-like morphology is the necessity of multiple measurements for at least 4 –5 different heights in the beam of the incoming light, and of averaging the positions and absorbances of the gold plasmon band at each step of the sensing protocol.

The schematic of the immune-sensing protocol for detection of growth hormone is shown in Figure 3-11. The protocol is similar to the plasmonic detection of other biomolecules and biological entities.

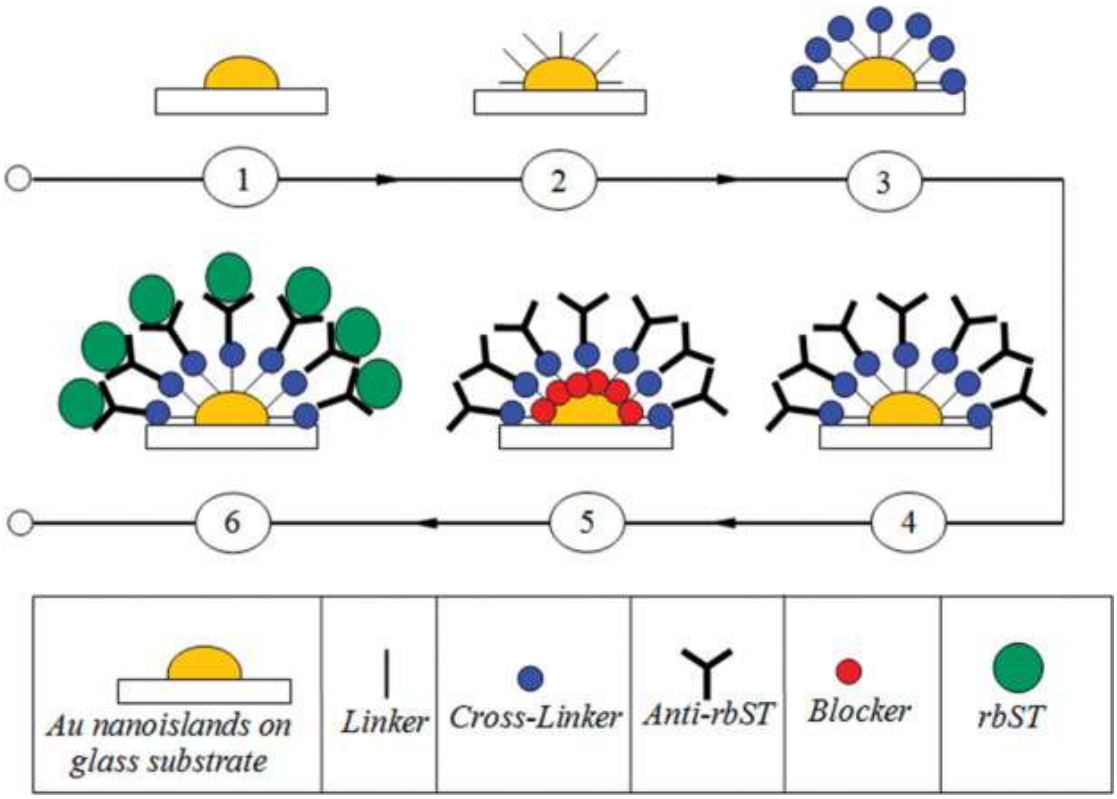

Figure 3-11: Immunoassay protocol for the detection of recombinant bST (rbST). (1) Sample with gold nano-islands, (2) gold nano-islands with the linker. (3) sample after adding cross-linker. (4) sample after adding anti-bST. (5) sample after adding a blocker, and (6) sample after adding rbST (reproduced with permission from [145], copyright 2015, American Dairy Science Association).

The nano-island structure has proved to be adequate for the detection of bovine growth hormone, by using an immunoassay method based on the localized surface plasmon resonance band of gold. The nano-island structures were integrated into a microfluidic device, as shown in Figure 3-12, and the spectral measurements were carried out by introducing the device directly in the light beam of an ultraviolet-visible spectrophotometer. A portable assay system using disposable lab-on-chip devices was built as well.

The gold nanoparticles are prepared and deposited on a glass substrate by the thermal convection method, and the gold nano-island structures are formed by annealing the deposited multilayers of gold nanoparticles [149]. Polydimethylsiloxane (PDMS), the polymer commonly used for microfabrication, is prepared in the ratio of 10:1 by weight with their base and curing

agent. PDMS was cast onto a silanized mold to make the microchannel layer. The PDMS layer containing microchannels is bonded with the glass substrate containing the gold nano-islands using oxygen plasma. This microfluidic platform was tested for the isolation and detection of extracellular vesicles (EVs) based on their interaction with Vn96 [60]. Vn96 is a peptide specifically designed to capture EVs by binding to the heat shock proteins present on their surface.

A biosensing protocol has been designed and optimized for the isolation of EVs, where various biochemical entities are infused into the fabricated device to functionalize the gold nano-islands to bind Vn96 and capture EVs [150]. Specifically, the first step in any experiment is to measure the absorption spectrum of the gold nano-islands in the collection chamber of the microfluidic channel. Then, a NanoThinks11 solution is infused into the device at a flow rate of 10 μL/min continuously for 10 min, and the spectrum is measured after an incubation of 30 min to observe the shift ($\Delta\lambda$) in the LSPR peak. A positive shift in the spectrum confirms the molecular binding with the gold nano-islands. Then, an EDC + NHS mixture is passed at the same flow rate, and the spectrum is measured after incubation. The same procedure is repeated with the streptavidin, biotin–PEG (Polyethylene Glycol) –Vn96. and then EVs. With the adopted protocol, a shift in the peak of the Au LSPR in each spectrum is observed at every stage, confirming the molecular binding of each compound.

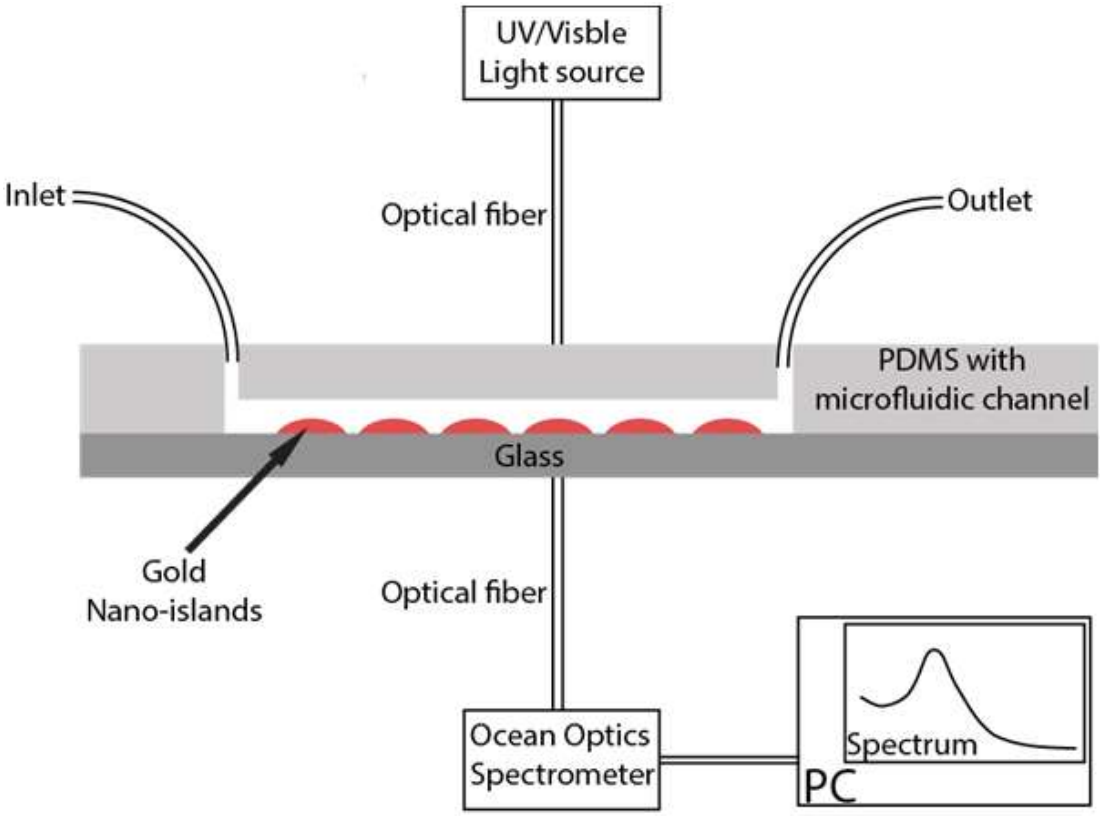

Figure 3-12: Schematic of the microfluidic device with nano-island structures (reproduced with permission from Int. J. Biomed. Biol. Eng. [150]).

Nano-islands were prepared by Feng et al. [151] from a gold colloidal solution mixed with an aqueous solution of polyvinyl alcohol and drop-casted on glass and ITO substrates, respectively. After drying, the samples were annealed at high temperatures for long durations. During the annealing process, the polymer decomposed, and all the organic components were removed, leaving on the substrate only the gold nano-islands, without any contaminant.

As seen in Figure 3-13, the size of the nano-islands was found to increase with the increasing annealing time, temperature, or volume of PVA (Polyvinyl alcohol) –AuNPs solution. At the same time, the LSPR peak of AuNPs was also gradually red-shifted with the increase in the size of nano-islands, and some hexagonal islands were observed for long annealing times. In addition, the type of substrate surface (ITO or bare glass) also influenced the characteristics of gold nanostructures. The proposed method seems to be a simple and efficient method for the deposition of AuNPs upon bare glass and ITO, as well as the fabrication of the corresponding nano-islands.

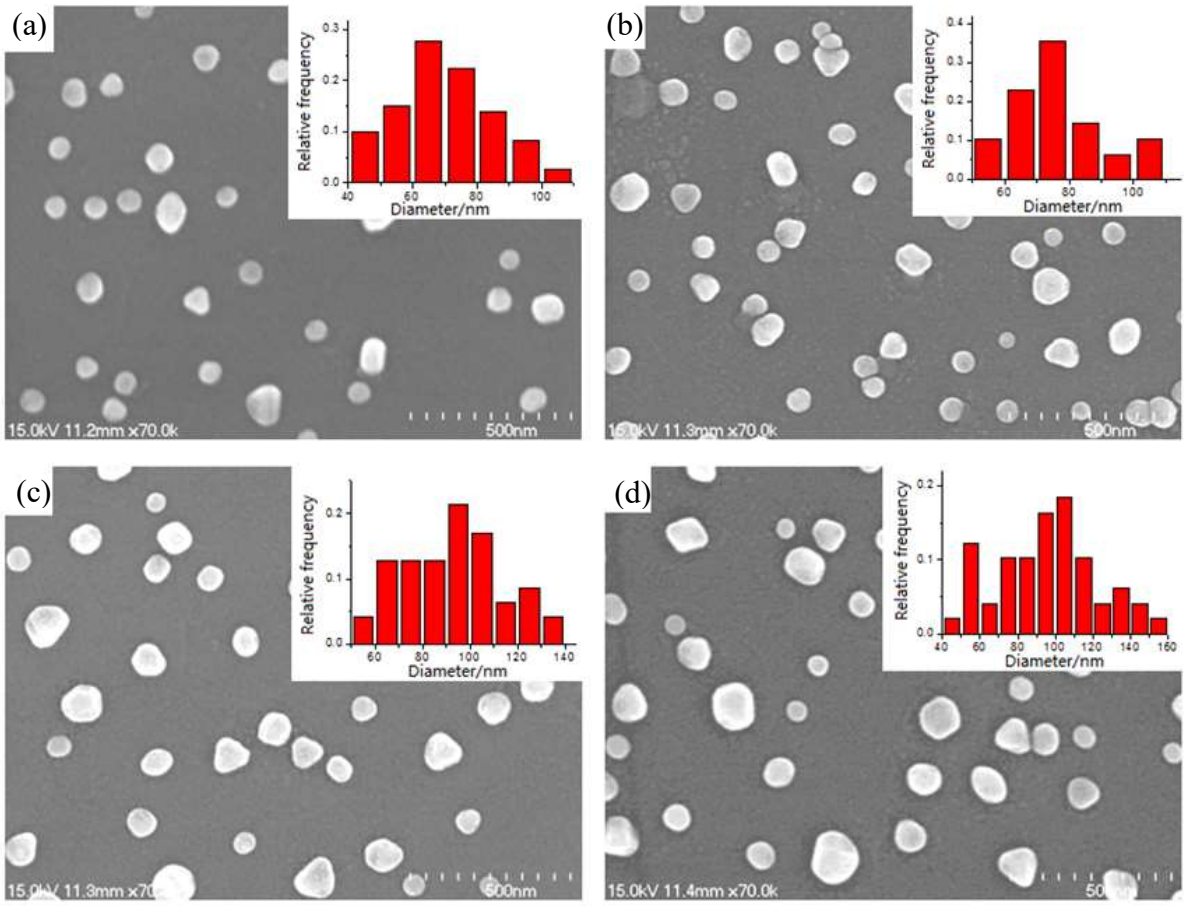

Figure 3-13: SEM images of AuNPs deposited on ITO glass after annealing at 600 °C for 0.5 (a), 2 (b), 4 (c) and 10 h (d). Inset: size distribution (reproduced with permission from Feng et al. [151]).

It was found that higher annealing temperatures (600 °C) and shorter annealing times (0.5 h) lead to higher LSPR refractive index sensitivities, which are strongly connected to the increased island sizes and smaller gap distances. Based on the findings of the plasmonic sensitivity and surface enhancement of thermally generated gold nano-islands, the authors suggested using thicker initial layers and decreasing the inter-particle separation between the particles with shorter annealing times.

3.7. Integrated Biosensors for Medical and Clinical Diagnostics

Next-generation healthcare equipment and devices are in great demand for point-of-care (POC), given their applications in rapid disease diagnosis, personalized medicine, portable or mobile health care, etc. Localized surface plasmon resonance (LSPR) biosensors, based on noble-metal nanostructures that may provide fast, real-time biochemical detections, have become one

of the leading candidates for POC. The advances in nanofabrication, molecular biotechnology, and optoelectronics integration technology have promoted LSPR biosensing to low-cost, easy-to-use, and on-site POC.

The main step in building a device appropriate for clinical diagnosis consists of combining a nanostructure-based LSPR biosensor with a microfluidic device in the most convenient way. As a result, because of the inherent advantages of microfluidics, the performance of the integrated biosensors is significantly improved. Indeed, a microfluidic device significantly reduces the required sample/reagent volume, and the speed of reactions can be accelerated because of the enhanced diffusive mixing. The chip may have several channels or chambers to process the multiplex detection of analytes of interest, and several separation operations can also be implemented. In addition, miniaturized channel footprints may result in accelerated antigen-antibody interactions and a fast response.

As shown already, three-dimensional gold nanostructures (nano-islands), fabricated through the convective assembly method, were treated thermally to obtain a nano-island morphology. The nano-island structures were integrated into a microfluidic device, and the spectral measurements were carried out by introducing the device directly into the light beam of an ultraviolet-visible spectrophotometer. A portable device enabling the detection of rbST hormone in milk had been built up. The device can be inserted into a POC device for biosensing, and it could also be used in the future for anti-doping control. A comparison of the sensitivities of the different devices developed in our laboratory shows that the nano-islands-integrated LOC shows the highest sensitivity, that is, the lowest limit of detection.

However, the POC applications of nano-island platforms can be considered in their infancy, probably because they are subject to less control on the size and distribution of plasmonic enhancement hot spots, chip-to-chip variation, and therefore, low reproducibility for quantitative measurements and continuous monitoring. Many other platforms, such as arrays of nanoparticles with various shapes, nanohole arrays, etc., are today successfully used for POC purposes. The interested reader may see several comprehensive review papers on this topic, including our papers [152–155]. Medical applications are rapidly coming to the forefront by combining communications and sensor output to deliver new functions. Devices can gather and share information with the cloud so that data can be collected and analyzed accurately. In the future,

the global system of medical devices will be comprised of a multitude of devices and applications, using sensors, actuators, microcontrollers, and mobile communication devices, and healthcare will be delivered more effectively and at lower cost. It will include not only the collection of patient data for preventive care but also diagnostics and treatment results. Automation and real-time aspects will reduce errors and improve quality and efficiency. Today, wireless sensor-based systems gather medical data that have never before been accessible and deliver care directly to patients. Healthcare will be based on a network of devices that connect directly with one another to capture and share data through a server in the cloud, and then to caregivers. Data captured via sensors will be analyzed, and medical professionals will wirelessly access the information and make treatment recommendations. Remote monitoring means that more patients will have access to adequate healthcare. Progress in sensor technology will, in this way, change the role of hospitals, outpatient sites, and homes. Over the last few years, continuous efforts have been made by researchers to develop integrated point-of-care (POC) biosensor networks, capable of automatically delivering results. Biosensor networks are generally a multidisciplinary technological work, based on biological micro-electro-mechanical systems (MEMS). The medical needs of the future can be met by using a combination of wireless MEMS and biosensor networks.

3.8. Conclusions and Outlook

The concept of nano-island(s), as it first emerged from early thin film studies, has been described and explained here using the dewetting phenomenon and its mechanism. The literature regarding the fabrication of nano-islands and their optical properties was revisited, with an emphasis on thermally generated islands. Being historically the first, these islands served as models for developing a dewetting mechanism of thin and very thin films under various conditions. Once their enhanced refractive index sensitivity was discovered, it was logical to envisage nano-islands as “building blocks” of the future plasmonic platforms. The first SPR and LSPR sensing platforms were created based on thermally generated nano-islands. Only after the development of the methodology of nanoparticle synthesis did nanoparticle films become the starting point for designing a novel category of nano-islands. Despite their lack of uniformity in terms of size (diameter and height), these platforms proved, nevertheless, to be highly sensitive,

and thus suitable for sensing and biosensing applications. Advanced methods, based on nano-islands integrated into a microfluidic environment, have been described as well.

Among the emerging plasmonic platforms are the composite materials, based on metal nano-islands on graphene that have extremely attractive electrical, optical, and mechanical properties and a wide range of applications. Novel materials, prepared by transferring the nano-islands to flexible substrates, such as PDMS, are becoming important, especially for point-of-care medical diagnostics. As a general tendency, the morphology and properties of nano-islands on a variety of substrates are now studied for nanophotonic applications.

Some of the novel applications of nano-islands that enter the current research landscape are oriented toward the enhancement of light absorption in solar cells' photoactive layers by using a nanoparticle spraying method and the generation of nano-islands by heat treatment [156]. Nano-islands are used more and more to improve the catalytic properties of metals like Pt. The irradiation of the high intensity of light on the Pt film causes the surface energy-driven diffusion of Pt atoms and forms an array of nano-islands on CNT (Carbon Nanotubes) through a photothermal dewetting process [157].

An example of the new, reliable approaches for the fabrication of large-area, periodic metallic structures, including nano-island arrays, are the nano-patterning methods by different template lithography-based techniques [158].

Special gold nanostructures on gold metal films that show a highly sensitive refractive index response, due to the high local field enhancement in their inter-particle junction, have been recently reported [159]. It is interesting to mention the use of phase-change materials in tailoring efficient and tunable plasmonic devices [160].

So, in the next chapter (Chapter 4) we will look at the fabrication of *ex-situ* synthesis-based gold nanostructured plasmonic platforms, and evaluate it for the detection of Extracellular vesicles (EVs) as in the past this platform was used for the detection of bovine somatotropin (bST) growth hormone.

Chapter 4. Nanostructured gold-based plasmonic *ex-situ* platforms, fabricated and tested for detection of EVs

This chapter is reproduced from the article published in *ECS Trans*. 75,17 11-17, 2016: This chapter covers objective 1 of the "Thesis Objective and Scope" in Section 1.5.

4.1. Outline

As discussed in detail in Chapter 3, gold and silver are the two most important metals displaying plasmonic properties that can be used for analytical purposes. The plasmon band, a strong extinction band in the visible range of the spectrum is sensitive to the environment surrounding the gold (silver) nanoparticles and shifts to longer wavelengths when biomolecules get absorbed on their surface. Because the shift of the plasmon band is proportional to the concentration of biomolecules, plasmonics can be used, successfully, for quantitative work. Our group earlier, utilized this property to develop a novel plasmonic method to detect bovine somatotropin (bST), the bovine growth hormone by utilizing gold nano-islands and an immunoassay format. Later, the method was transferred to a microfluidic environment, where an improvement in the performance of the method was obtained, with a detection limit of bST of 5 ng/mL. [144].

The knowledge and expertise acquired during this work have proven to be invaluable for carrying out further analytical work in the field of the detection of biological nanoparticles called extracellular vesicles (EVs) /exosomes. As mentioned in Chapter 1, EVs/exosomes, a class of extracellular (EV) vesicles, are unique nano-sized cargo-bearing biological vesicles, secreted by almost all normal and cancer cells into the extracellular space. Exosomes are the smallest of the extracellular vesicles with their size in the range of 30 -100 nm, they are highly heterogeneous and are present in all body fluids. It must be mentioned that, because of the heterogeneity of exosomes and the overlap of physicochemical properties of different extracellular vesicles, the separation and purification of exosomes are still difficult.

Exosomes contain disease biomarkers for cancer and other pathological conditions. They are groups of nano-scale extracellular communication organelles that dynamically transport cargoes of molecules and genetic materials between cells. Exosomes circulating in our body fluids

provide a snapshot in real-time for virtually all aspects of our physiology. Isolation detection and quantification methods of exosomes from various bio-fluids are challenging for clinical applications, like liquid biopsy. This chapter presents a simple label-free technique to capture and detect exosomes integrating an exosome-capturing synthetic polypeptide (called Vn96). This exosome capture can efficiently quantify exosomes present in a fluid and will be used for subsequent molecular analysis (protein and nucleic acid) to facilitate liquid biopsy.

4.2. Introduction

Exosomes are another type of cell-derived vesicles that are present in all biological fluids, including urine, blood, ascites, and cerebrospinal fluid fractions of body fluids such as serum and plasma, and cultured medium of cells [161]. They are formed through the endocytic pathway. In the latter case, the plasma membrane buds into multivesicular bodies (MVBs) in the cytosol, leading to the formation of intraluminal vesicles (ILVs) within MVBs. Further, MVBs fuse with the plasma membranes resulting in the release of ILVs, which are then secreted as exosomes into the extracellular space. They are usually smaller in size and more homogenous than microvesicles. The identified diameter is approximately 30 -120 nm and their size approximately overlays with the size of viruses. Their density is ranging between 1.13 - 1.19 g/ml on sucrose gradients [48]. These vesicles are cup-shaped as shown by SEM [8,36]. In this work, we have developed a novel method to detect exosomes by using a label-free LSPR method based on the sensitivity of the gold plasmon band to the environment of the gold nanoparticles.

Over the past few decades, the fabrication of different nanostructures has been a challenging active area of research in the field of chemical and biological sensing. The properties of noble metals can be customized for several applications such as biosensors, diagnosis, imaging, etc. by tuning the size and shape of the nanoparticles. The resonance frequency of the gold local surface plasmonic resonance (LSPR) band can be shifted by varying the size and morphology of the nanoparticles. In general, during the steps of a sensing protocol, the local refractive index changes at each stage of binding of various bio-molecules to the immobilized nanoparticles, resulting in the shift towards longer wavelengths [162–171].

In the past, LSPR research was based on the two-dimensional (2D) nanostructures that were fabricated, generally, by layer-by-layer deposition method [172,173] which was tedious. The various methods available for the fabrication of gold nanostructures are described in the work by

our group [144].

To capture and detect the exosomes, in the present study, three-dimensional (3D) gold (Au) nanostructures were fabricated by convective assembly [144]. In this deposition method, gold nanoparticles from a colloidal suspension evaporate at the interface of substrate and solution. The formation of ordered Au nanoparticles depends on the interaction forces between the particles and the glass surface, temperature, concentration of the Au particles, and their diameter as shown in Figure 4-1. Multilayer gold nanoparticles will be formed on the substrate and a conventional UV-visible spectrophotometer can be used for the spectral transmission measurements.

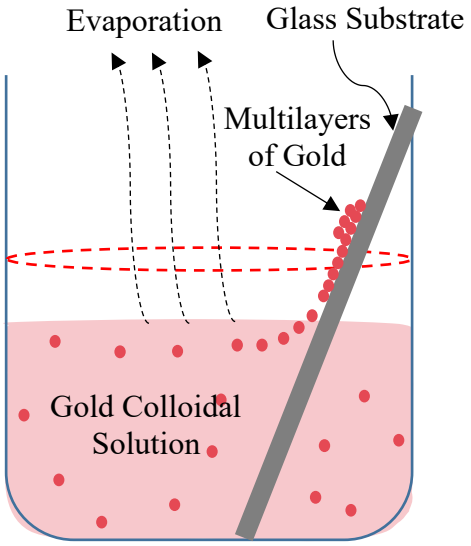

Figure 4-1: Sketch for the convective assembly process of gold nanoparticles.

The current study is aimed at the bio-sensing of exosomes by gold nano-island structures formed by annealing of gold multilayers, deposited by the convective self-assembly method. The sensing platforms developed by this method are tested for the detection of exosomes based on their interaction with biotin-Vn96. Vn96 is a peptide (27 amino acids) designed and validated to capture exosomes [60]. A calibration curve that correlates the shift of the Au-LSPR band with the concentration of exosomes captured by Vn96 grafted on gold nano-island is depicted.

4.3. Experimental Design

Three-dimensional (3D) gold nanostructures were fabricated by the thermal convection method based on the evaporation of the gold colloidal solution at the interface of substrate and solution.

4.3.1. Materials

Gold (III) chloride trihydrate ($HAuCl_4.3H_2O$), Sodium citrate, 11- mercaptoundecanoic acid in ethanol (Nano Thinks Acid 11), phosphate-buffered saline (PBS), N-(3-dimethylaminopropyl)-N'-ethyl carbodiimide hydrochloride (EDC) and N- hydroxy succinimide (NHS) were obtained from Sigma-Aldrich, Canada. Streptavidin from IBA GmBH and Biotin-PEG-Vn96 and exosomes-MCF7A are from Atlantic Cancer Research Institute (ACRI), Moncton, Canada.

4.3.2. Synthesis of NPs

Spherical gold nanoparticles were prepared using the reduction of gold chloride trihydrate ($HAuCl_4.3H_2O$) acid by sodium citrate, following Turkevich's method [174]. 15mg of gold (III) chloride trihydrate ($HAuCl_4.3H_2O$) is dissolved in 100 ml of DI water in a beaker and boiled until it reaches its boiling point of the solution. Then, 5 ml of a solution of sodium citrate (2%) is added to the boiling solution. After the addition of the sodium citrate solution, a change in color to transparent purple can be observed, showing the presence of gold nanoparticles.

4.3.3. Deposition of Gold Nanoparticles on Glass

In this deposition process, the glass substrate was cleaned with soap solution, and deionized water, then rinsed with acetone, dried, and rinsed with 2-propanol (IPA), and air dried. Then the substrate was heated in an oven at 100 °C for 1 hour to remove any moisture present, before the deposition process.

The glass substrate was immersed in a beaker containing gold colloidal solution at an angle of approximately 30 ° and kept inside the oven at temperatures between 50 °C to 60 °C until the whole amount of colloidal solution evaporated, depositing the multilayers of gold nanoparticles on the glass substrate as shown in Figure 4-1.

4.4. Sensing Protocol

The substrate is immersed in the linker solution, which is Nanothink (11-mercaptoundecanoic acid in ethanol). The linker is utilized to form self-assembled monolayers on the gold substrate. Then, the linker is activated by adding a few drops of cross-linker solution containing N-(3-dimethylaminopropyl)-N'-ethyl carbodiimide hydrochloride (EDC) and N-

hydroxy succinimide (NHS) mixed in the ratio of 1:1, on the whole surface of the sample and it is allowed to dry after incubation. EDC is a water-soluble condensing reagent that has been utilized as a carboxyl activating agent for amide bonding with primary amines and NHS is an additive used in the carbodiimide method for improved amidations and peptide couplings. In the next step, streptavidin is deposited on the activated linker and then the biotin-PEG-Vn96 is added to streptavidin. In the last step, exosomes will be captured by Vn96, a synthetic peptide, specifically designed to capture exosomes. A schematic, explaining the various steps in the biosensing protocol is shown in Figure 4-2.

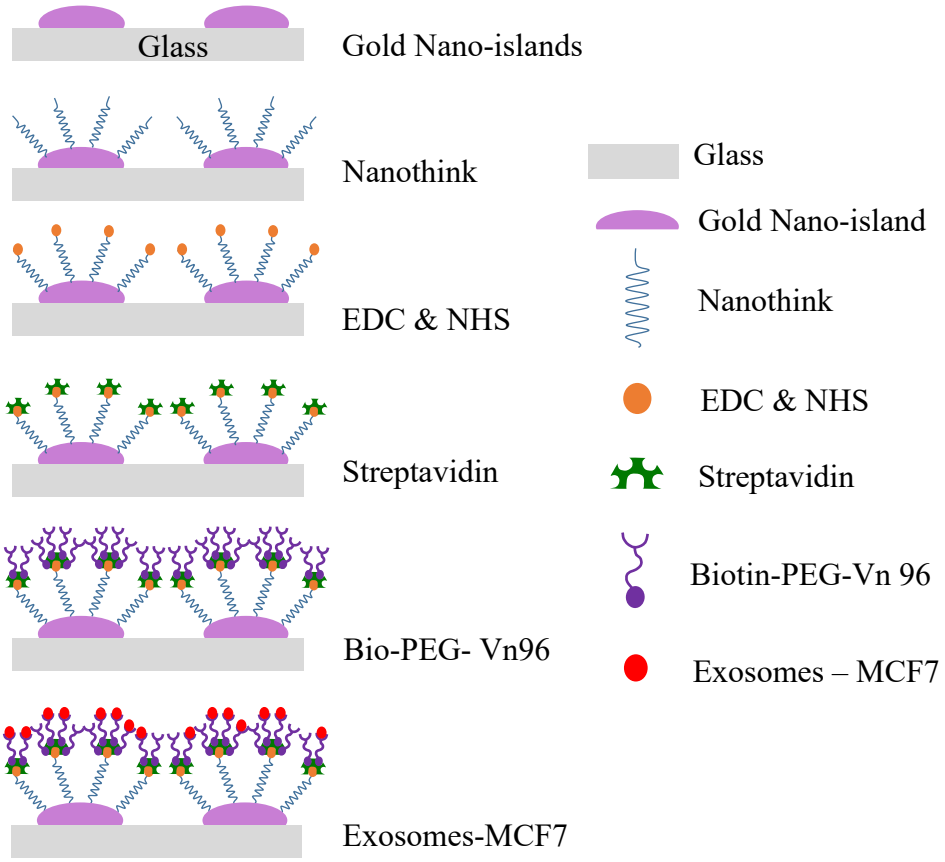

Figure 4-2: Biosensing protocol using gold nano-islands as a sensing platform.

4.5. Results and Discussion

4.5.1. Morphological tuning of 3-D Gold Nanostructure.

The substrates, before annealing, appear to be dark blue, whereas post annealing at 560 °C, they appear to be pinkish as shown in Figure 4-3 (a). The schematic of morphological tuning of 3-D gold nanostructures from nano-aggregates to nano-islands is shown in Figure 4-3 (b).

The scanning electron microscope (SEM) images for the substrates, before and post annealing, are shown in Figure 4-4 (a) and Figure 4-4 (a), from the SEM images it is noticeable that before annealing, the nanoparticles appear as aggregates, with many layers one above the other, due to the strong attractive van der Waals forces between gold nanoparticles [175], whereas the annealed samples show well separated nano-island structures with an average diameter of around 110 nm with fewer smaller particles.

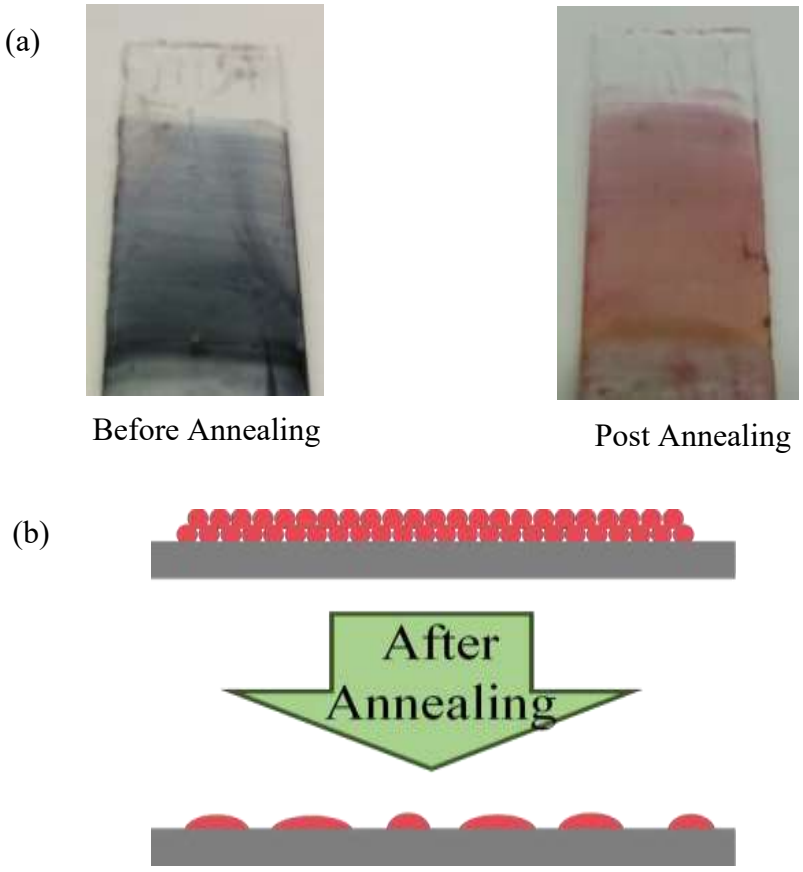

Figure 4-3: Morphological tuning of 3-D Gold Nanostructure. (a) Images of the substrate before annealing and post annealing (b) Schematic of the morphological tuning of 3-D Gold Nanostructure.

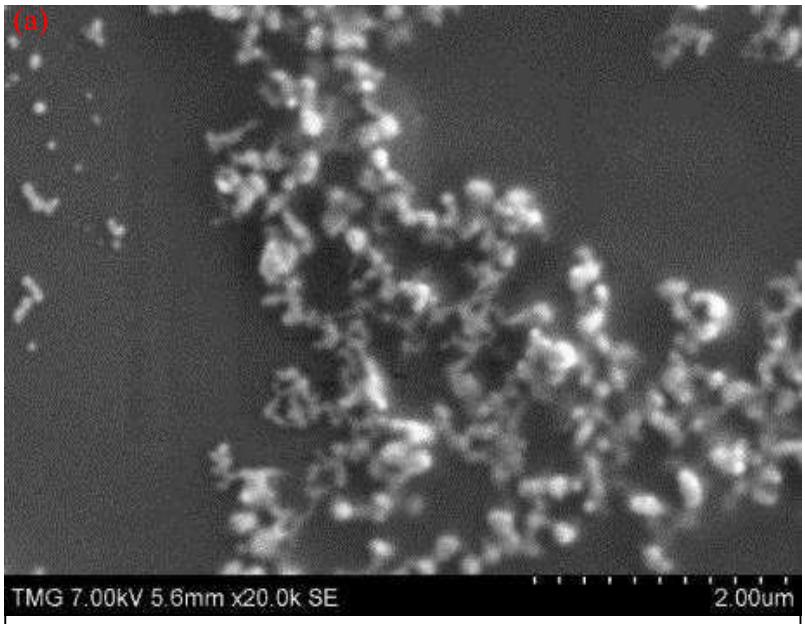

GNPs - Before Annealing

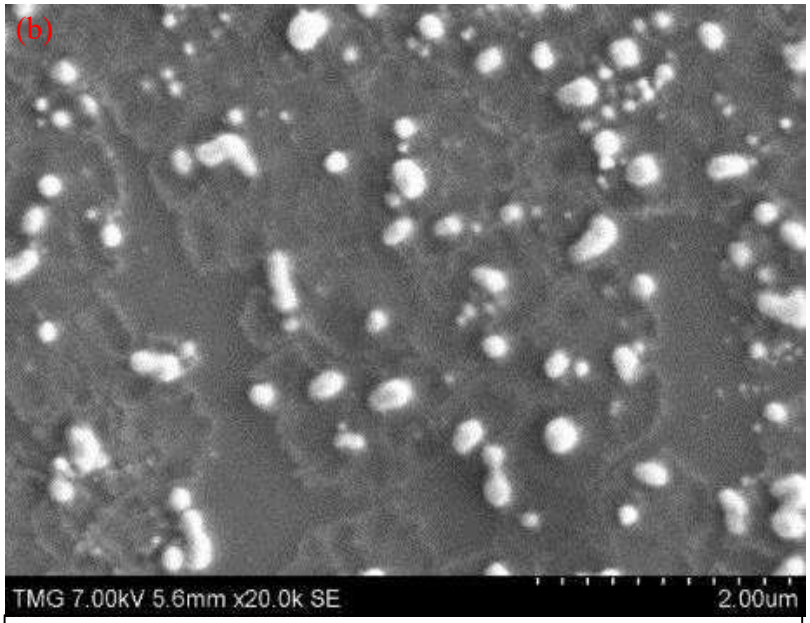

Gold nano-islands - Post Annealing

Figure 4-4: SEM images of 3-D gold nanostructures. (a) before annealing. (b) post annealing.

4.5.2. Detection of Exosomes

The absorbance spectrum of the sample is recorded at each stage of the sensing protocol, using the lambda 650 UV-Visible spectrophotometer. The Au-LSPR band is recorded after the functionalization of the nanoparticles with the linker, followed by attaching the cross-linker, the streptavidin, and biotin-PEG-Vn96. The spectra show a shift of the Au-LSPR band of around 7 nm upon the interaction of biotin-PEG-Vn96 and exosomes as shown in Figure 4-5.

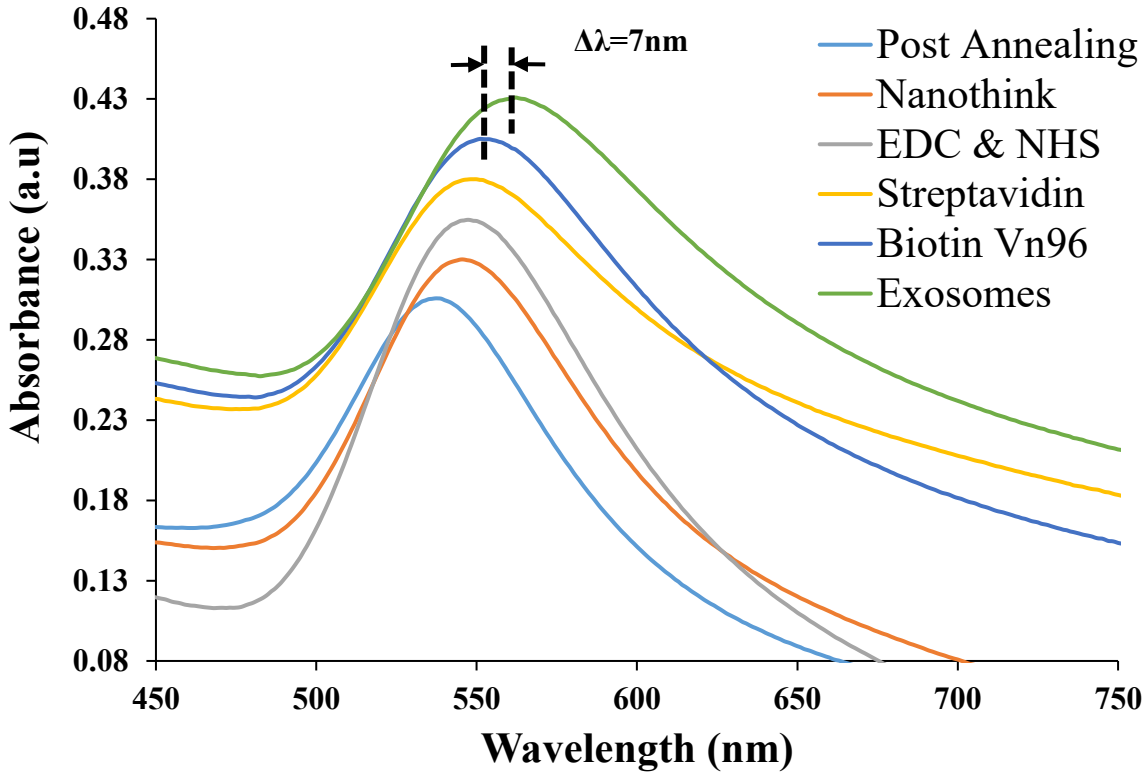

Figure 4-5: LSPR absorption spectra corresponding to each stage of the sensing protocol.

4.5.3. Calibration Curve

Various dilutions have been tested to determine the optimal dilution factor of exosomes, so that the interaction of biotin-PEG-Vn96 and exosomes could be observed with the maximum shift of the Au-LSPR band. Based on a large number of experiments, a calibration curve is established with the original concentration of exosomes (MCF 7A) of 10^6 exosomes per 100µl. Figure 4-6 shows the calibration curve, which clearly shows that with an increase in the concentration of exosomes, the shift of the Au-LSPR band (Δλ) towards the longer wavelength increases as well. It can be seen that at higher dilution factors, the slope of the curve is quite

low, showing a low sensitivity. However, dilution factors of 10 and lower, allow the detection of exosomes with a high sensitivity.

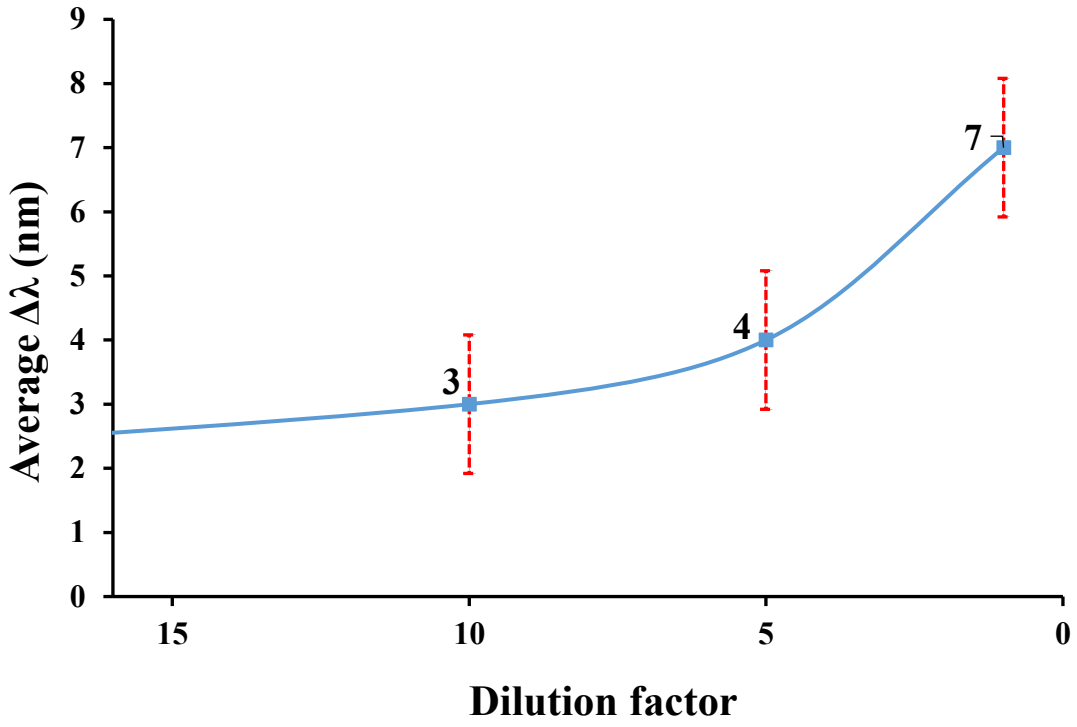

Figure 4-6: Shift in the wavelength (Δλ) versus dilution factor of exosomes (Error bars represent the standard error of 10 measurements).

4.6. Conclusion

To increase the sensitivity, the nanoparticles deposited on glass substrates by a thermal convection method were subjected to high-temperature annealing that allowed the tuning of morphology to nano-islands. The sensing protocol is based on the high affinity of biotin-PEG-Vn96 toward the exosomes. Thus, a label-free method, based on the sensitivity of the Au-LSPR band to the surrounding environment has been developed as our method does not require the use of fluorescent, radioactive, or enzymatic labels to detect the binding of the exosomes to the nano-islands. This method has to be still optimized to enhance the sensitivity toward exosomes at lower concentrations.

So, in the next chapter (Chapter 5) we will look at the fabrication of *ex-situ* based synthesis of gold nanostructured plasmonic platforms, in comparison to the *in-situ* based synthesis of silver nanostructures and evaluate it for the detection of Extracellular vesicles (EVs).

Chapter 5. Study of Detection and Capture of Exosomes by Using the Morphologies of *Ex-Situ* and *In-Situ* Nanostructures

This chapter is reproduced from the article published in *J. Electrochem. Soc.* 166 9 B3001, 2019: This chapter covers objective 2 of the "Thesis Objective and Scope" in 1.5.

5.1. Outline

The method of detection of EVs/exosomes discussed in the previous chapter is an *ex-situ* method, where a gold colloidal solution is deposited on a glass substrate, resulting in multilayers of gold. that, after annealing at a quite high temperature (560 °C) will change their morphology and form nano-islands. In this configuration, the gold nano-islands are on the surface of the glass slide, in direct contact with the reactants all along the sensing protocol. It is a well-known fact that the perfect material for plasmonic applications is the one with the least amount of loss and with the most stability in the intended application. Silver and gold are popular choices as they have unique physical, chemical, and biological properties and are thus widely used in a range of nanotechnology applications. These metal nanoparticles exhibit Localized Surface Plasmon Resonance (LSPR), which is a distinct and well-defined plasmon absorption in visible light. Therefore, gold and silver nanocomposites Ag- polydimethylsiloxane(PDMS) and Au-PDMS prepared by *in-situ* methods are tested for the LSPR detection of EVs/exosomes. However, in this chapter, Ag-PDMS is prepared and evaluated as a plasmonic platform for the detection of EVs/exosomes, and the results were compared to that of the Au nano-islands *ex-situ* synthesized platform.

5.2. Introduction

Cancer is a complex and dynamic disease. One of every four deaths in the United States and Canada is due to cancer [18]. Thus, the early diagnosis of cancer is of much significance because the chances of survival of patients would increase. This is viable only if proper methods and devices of identification of biomarkers or targets are developed. Currently, a cancer diagnosis is carried out, generally through imaging, tissue biopsy, and liquid biopsy. Biomarkers are also important in monitoring the disease.

Liquid biopsy is a minimally invasive technique in which sampling of a biological fluid

is carried out to detect the cell-derived material, indicating the presence of an underlying pathology such as cancer or other diseases. The interesting key feature of liquid biopsy is that it enables the monitoring of the diseases over the entire timeline, from healthy to advanced stages. During the last few years, the role of exosomes in cancer diagnosis has become predominant and promising due to their usefulness as valuable sources of material for liquid biopsy [8,36,48].

Exosomes are nanoscale heterogeneous vesicles in the size range of 30-100 nm, which are released by cells as shown in Figure 5-1. These vesicles play a significant role in intercellular communications, and transport of proteins, RNA, and other molecular information. In the last decade, researchers have shown substantial interest in this field as there is no specific methodology to isolate and detect them. Currently, the exact science behind the major standard techniques of isolation of exosomes is not clearly understood. Thus, the limitations due to low yield and poor quality of exosomes may compromise the molecular analysis for diagnosis. The ultracentrifugation method of isolation of exosomes is time consuming, laborious, infrastructure intensive and it may lack specificity. Therefore, a lot of challenges exist in this field to develop next-generation affinity-based technologies to capture the exosomes selectively and use them for further diagnosis at the clinical level.

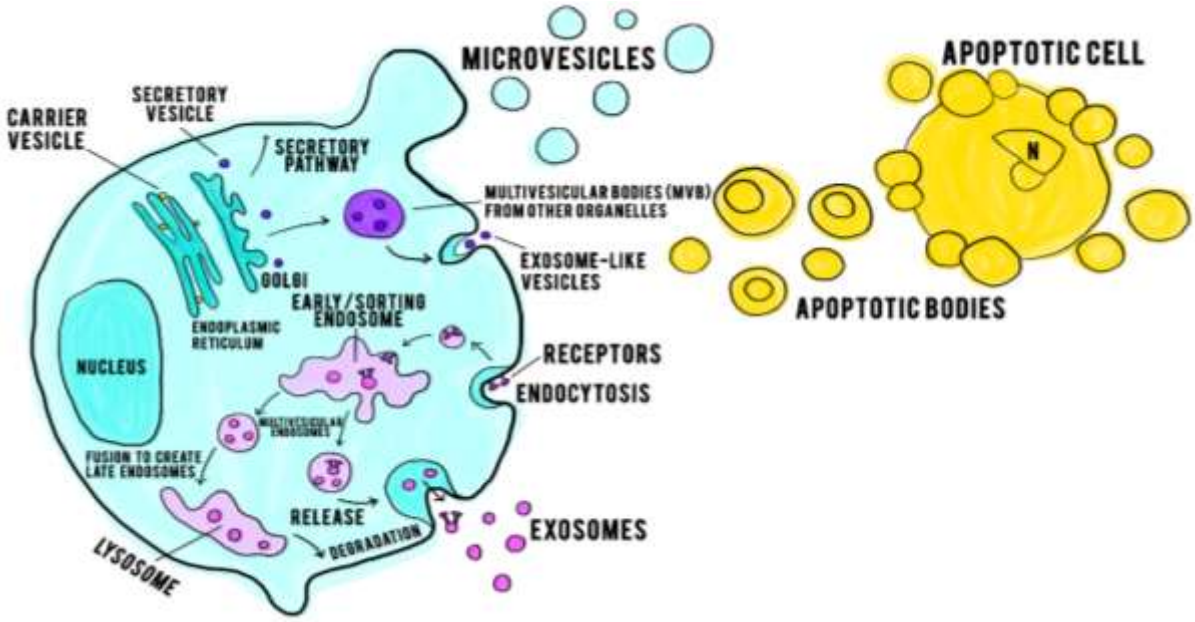

Figure 5-1: Biogenesis and Release of Extracellular Vesicles (EVs).

In the present work, two different sensing platforms, developed in our laboratory for the detection of exosomes, are compared. The two platforms are the *ex-situ* gold (Au) nano-islands

on glass substrates and the *in-situ* prepared silver (Ag) and polydimethylsiloxane (PDMS) nano-composite [137,144,176]. The first platform is fabricated by depositing colloidal Au nanoparticles on a glass substrate by the thermal convection method, followed by morphological tuning of the formed nanoparticles to nano-islands by annealing at 560 °C. The second is the nano-composite platform prepared by the *in-situ* reduction of Ag ions in the silver nitrate solution by the curing agent of the PDMS polymer. This study is carried out to choose the most sensitive platforms to detect and capture the nano-sized exosomes. The exosomes are rich sources of associated biomarkers, containing specific proteins, mRNA microRNA, rRNA[11], and DNA and thus having the potential for early cancer detection along with the information on the tissue and cell of origin.

Given the growing evidence that EVs/exosomes may be a clinically relevant biomarker source, there is a great demand for simple and efficient EV isolation from biofluids. Currently, the gold standard, the time-consuming method of isolation by ultracentrifugation is not a clinically viable method. Furthermore, polymer-based EV isolation methods are not suitable for therapeutic applications because these polymers are toxic. Most affinity-based EV-isolation methods rely on antibodies directed against EV surface marker(s).

In both the platforms developed in our laboratory, the detection and capture of exosomes are based on the strong affinity of heat shock proteins contained in exosomes to a polypeptide called Venceremin or Vn96 (27 amino acids), specifically developed and validated [60]. The Vn96 peptide targets the canonical heat shock proteins (HSPs) present on the surface of exosomes. The Vn96-based exosome detection and capture method is further validated for downstream analyses, clinical compatibility, liquid biopsy assays (biomarker and mutation detection), and platform versatility, using cell-culture conditioned media and human body fluids as sources of exosomes. Overall, Vn96 provides multiple advantages over currently-available affinity-capture methods for EVs/exosomes isolation: scalability, quality, platform versatility, and cost-effectiveness.

By using the Au nano-islands platform, a biotinylated Vn96 peptide is bounded onto the streptavidin-coated Au nano-islands, and the subsequent steps of binding of nano-sized vesicles

[11] **Ribosomal ribonucleic acid (rRNA)** is a type of non-coding RNA which is the primary component of ribosomes, essential to all cells

(exosomes) are monitored through the Localized Surface Plasmon Resonance (LSPR) band of Au nanoparticles [164,168,169,171,172,177,178]. The Ag-PDMS platform is used similarly and the shift of the Ag LSPR band is monitored after each sensing step. Generally, the magnitude of the LSPR shift depends on the size and shape of the nanoparticles and the dielectric constant (refractive index) of the surrounding environment. Following a binding event, the refractive index will change and the change will trigger a shift in the position of the LSPR band. The magnitude of the shift reflects the strength of the interaction and it is proportional to the concentration of the analyte, in our case the EVs/exosomes present in the cell culture media that are extracted from a bioreactor, filtered, and ultra-centrifuged. The platform based on gold islands is suitable for sensing various peptides and proteins by using the corresponding antibodies [137,144,176].

It is found that the results of the sensing process depend on two major things: the molar ratios of streptavidin to biotin-PEG-Vn96 and the final step, the capture of exosomes by the biotin-PEG-Vn96 complex. The morphology of Au nano-islands and Ag-PDMS nanocomposite were further investigated by SEM and LSPR techniques.

5.3. Experimental Design

5.3.1. Materials

Gold (III) chloride trihydrate ($HAuCl_4.3H_2O$), Sodium citrate, Silver nitrate, 11-mercaptoundecanoic acid in ethanol (Nano Thinks Acid 11), phosphate-buffered saline (PBS), N-(3-dimethylaminopropyl)-N'-ethyl carbodiimide hydrochloride (EDC) and N-hydroxy succinimide (NHS) were obtained from Sigma-Aldrich, Canada. Sylgard® 184 elastomer kit and curing agent for the PDMS fabrication purchased from Dow Corning. De-ionized (DI) water with a resistivity of 18MΩ is obtained from the NANO pure ultrapure water system (Barnstead). Streptavidin from IBA GmBH and Biotin-PEG-Vn96 and exosomes (MCF7) are from the Atlantic Cancer Research Institute (ACRI), Moncton, Canada.

5.3.2. Fabrication of the Platform by *ex-situ* Synthesis

In the *ex-situ* synthesis, Au nanoparticles were deposited on a glass substrate by the convective assembly of gold nanoparticles from a gold colloidal solution. The colloidal gold solution was prepared by using the Turkevich's method [174]. During the evaporation process,

the Au nanoparticles present in the colloidal suspension are deposited at the interface of the substrate and solution resulting in multi-layers of Au structures. The thickness of the layer depends on the concentration of Au particles, their diameter, and the interaction forces between the particles and the glass surface. The synthesis, as well as the convective assembly, is shown in Figure 5-2 (a). By varying the size of nanoparticles and their morphology, the peak resonance frequency of the Au-LSPR band can be shifted to other wavelengths when the refractive index of the surrounding environment is changed.

During each step of the sensing protocol, the local refractive index changes due to the binding of various biomolecules to the immobilized nanoparticles and results in a shift towards longer wavelengths. The Au nano-island structures were fabricated by annealing the deposited Au multilayers at 560 ºC for an hour.

5.3.3. Fabrication of the Platform by *in-situ* Synthesis

Nanocomposites seem to be alternative and promising substrates for label-free biosensing [137,176]. In this process, silver (Ag) ions from the silver nitrate aqueous solution are reduced by the curing agent present in the polydimethylsiloxane (PDMS) matrix, a good reducing agent of Ag ions to form the Ag-PDMS nanocomposite as shown in equation 5.1. As shown in Figure 5-2 (b) the first step is the fabrication of the PDMS substrate. The substrate is prepared by mixing the PDMS base (pre-polymer) and curing agent in a ratio of 3:1 by weight and then spin-coated on a glass substrate of 25mm x 25mm x 1mm, using the LAUREL spin coating machine at a speed of 2000 rpm, to obtain a thickness of around 10 µm. After the spin-coating, the polymer is cured at 70 °C, for about 2 hours. The cured substrates were then immersed in the Ag precursor solution, prepared by adding 1g of silver nitrate into 100 ml of DI water. The immersed substrates were kept in an oven at 50-60 °C, for about 2 days to increase the rate of the reduction reaction. The synthesized platforms were annealed at 250 ºC, for 10 minutes to tune the morphology of Ag aggregates to nanoparticles.

$$R-\underset{|}{\overset{|}{Si}}-H+AgNo_3 \rightarrow \underset{|}{\overset{|}{Si}}-O-\underset{|}{\overset{|}{Si}} \mp Ag + NO_2 + \mathrm{H_2O} \qquad 5.1$$

5.3.4. Biosensing protocol

The various steps involved in the biosensing protocol for both platforms are shown in Figure 5-3 (a) and Figure 5-3 (b). In the case of the Au nano-islands platform, initially, the Au nano-islands were functionalized by immersing the substrate into the linker solution, which is Nano think (11-mercaptoundecanoic acid in ethanol) to form a self-assembled monolayer on the top of Au nano-islands. In the next step, the structure is activated by adding a few microliters of the cross-linker which is a 1:1 mixture of 0.1M N-(3-dimethylaminopropyl)-N'-ethyl carbodiimide hydrochloride (EDC) - a carboxyl activating agent for amide bonding with primary amines and 0.05M of N-hydroxy succinimide (NHS), an additive used for the improved amidations and peptide/protein couplings. The substrate is incubated for about 3 hours.

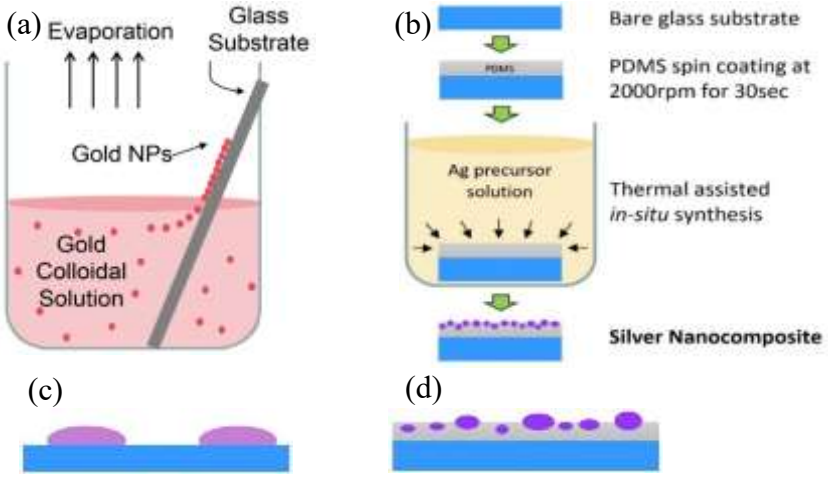

Figure 5-2: Schematics of the *ex-situ* and *in-situ* synthesis. (a) Schematic of the convective assembly for the gold nanoparticle synthesis and the multi-layer formation (*ex-situ* synthesis). (b) Schematic for the fabrication of silver nanocomposite (*in-situ* synthesis). (c) Schematic of nano-islands on a glass substrate. (d) Schematic of Ag nanoparticles on the polymer (PDMS) surface.

The streptavidin-biotin complex is the strongest known noncovalent complex (Kd = 10^{-15} mol/L). The bonding is very rapid and the bond is unaffected by extreme values of pH, temperature, organic solvents, and other denaturing agents. Streptavidin (0.01mg/ml) is immobilized onto the activated linker layer and incubated for an hour. Further, the biotin-PEG-Vn96 (0.003 mg/ml) is immobilized on the streptavidin layer and then incubated again for about 4 hours. In the last step of the biosensing protocol, the MCF 7 (breast cancer cell line) cell culture conditioned media, containing EVs/exosomes is immobilized onto the Vn96 layer, a synthetic peptide designed to capture them. in the concentration of biotin-PEG-Vn96 (0.015 mg/ml).

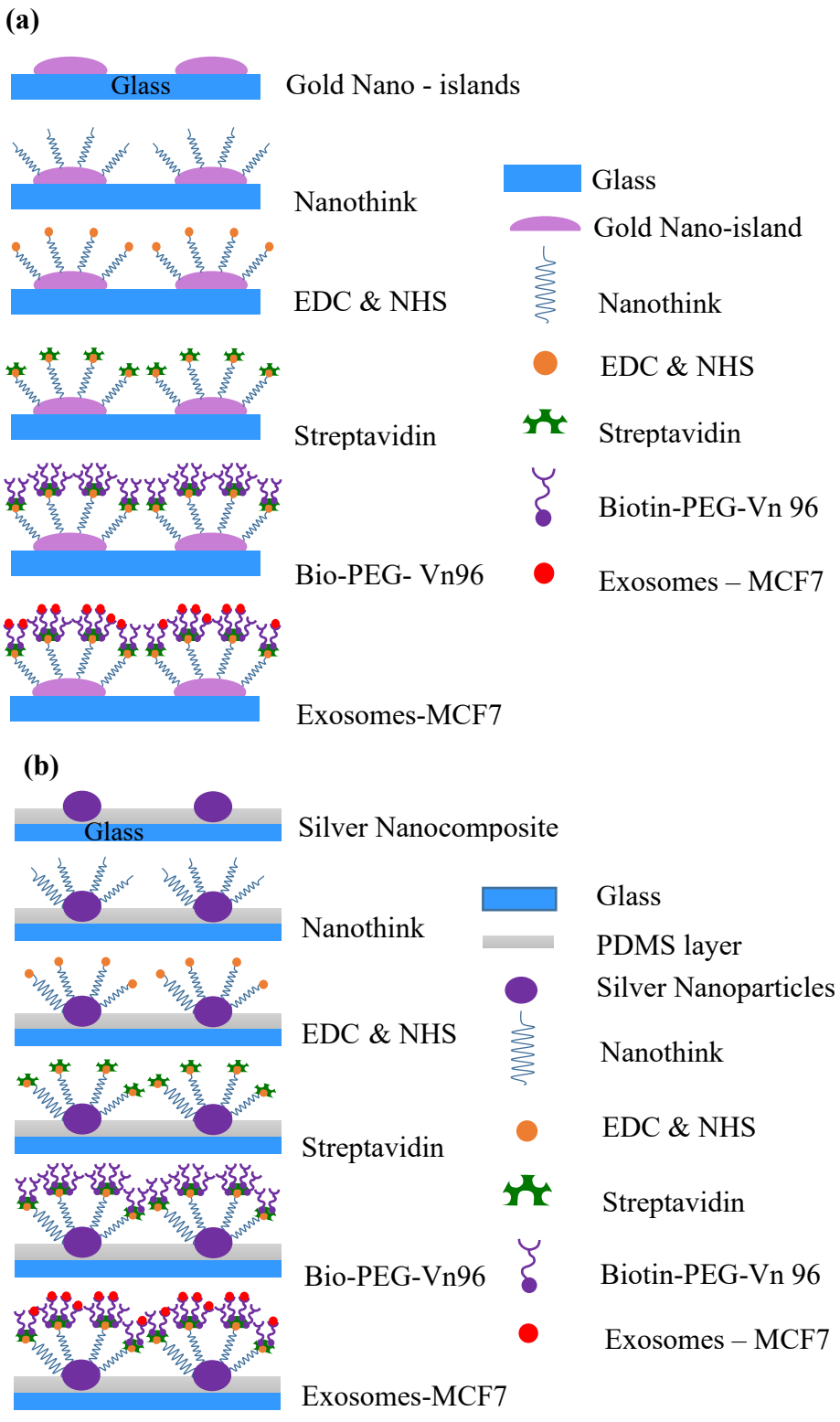

Figure 5-3: Biosensing protocol (a) For Gold nano-island (*ex-situ*). (b) For Silver PDMS nanocomposite (*in-situ*) platforms.

5.4. Results and Discussion

5.4.1. Morphological tuning and SEM characterization

To tune the morphology of the *ex-situ* synthesized substrate it was annealed at 560 °C for an hour. The scanning electron microscope (SEM) images of the gold structures, before and after annealing are shown in Figure 5-4. It is visible that before annealing, the nanoparticles appear as aggregates, with several layers of Au one above the other, due to the strong attractive van der Waals forces between gold nanoparticles [175] and the glass surface, whereas the annealed samples show well-separated nano-island structures with an average diameter of islands of around 110 nm. Because of the size of the exosomes, this size is adequate for sensing considering the depth of penetration of the plasmonic field [98].

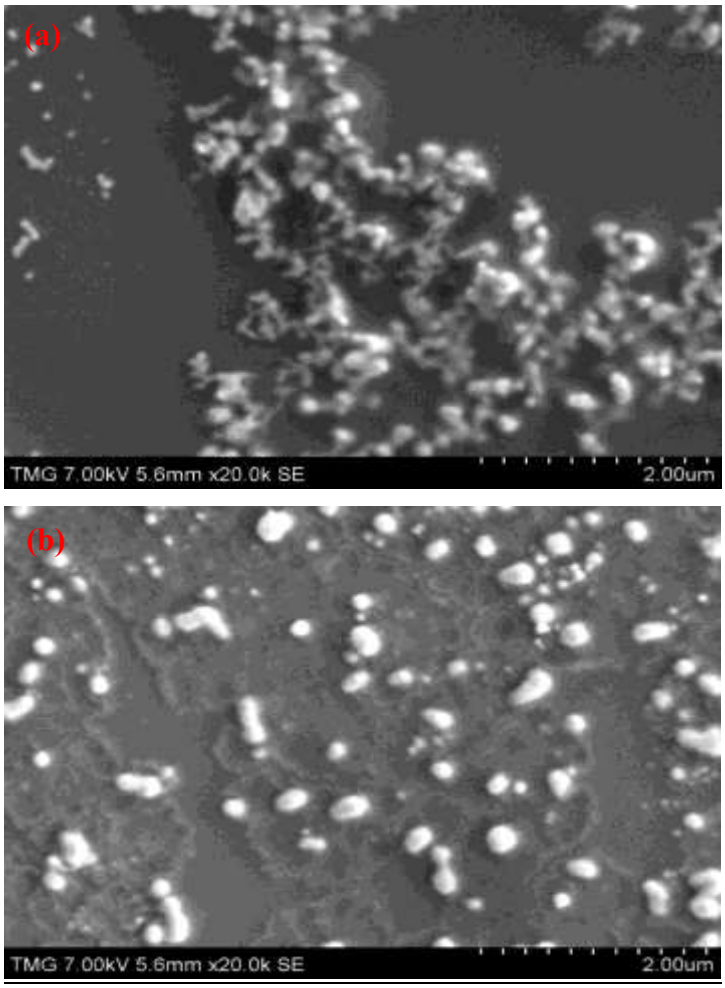

Figure 5-4: SEM images of Gold (Au) nanostructure (*ex-situ*). (a) before annealing. (b) after annealing (560 °C for 1 hour).

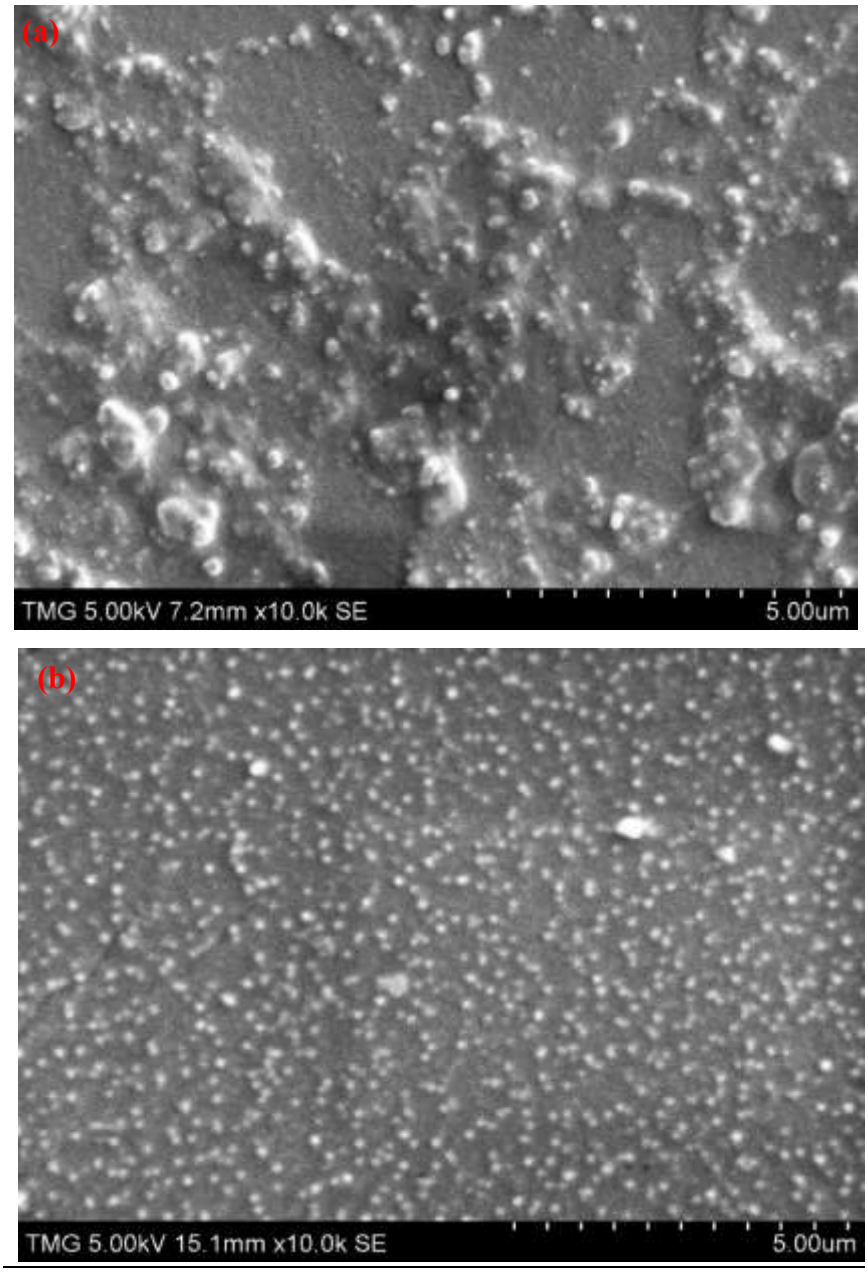

Figure 5-5: SEM image of silver (Ag) – PDMS (*in-situ*). (a) before annealing. (b) after annealing (250 °C for 10 minutes.

The *in-situ* synthesized substrates were annealed at 250 °C, for 10 minutes to tune the morphology of formed nano aggregates to particles as shown in Figure 5-5. It is evident from the SEM images that, before annealing, the synthesized Ag nanoparticles were found to be aggregates with multiple layers one over the other, well-separated particles of around only 80 nm as compared to the size of the Au nano-island.

5.4.2. Detection of Exosomes

The Au-LSPR absorbance spectrum for the *ex-situ* platform is recorded at each stage of the biosensing protocol: after the functionalization of the nano-islands with the linker, followed by the cross linker, the streptavidin, and biotin-PEG-Vn 96 using a lambda 650 UV-visible spectrophotometer. The spectra show a shift of the Au-LSPR band of around 6 nm upon the interaction of biotin-PEG-Vn 96 and exosomes (MCF7) as shown in Figure 5-6. Similarly, for the *in-situ* synthesized platform, the Ag-PDMS LSPR band is recorded at every stage of the biosensing protocol. In this case, a shift of 4 nm is noticed, between the biotin-PEG-Vn 96 and exosomes (MCF7) stage as shown in Figure 5-7.

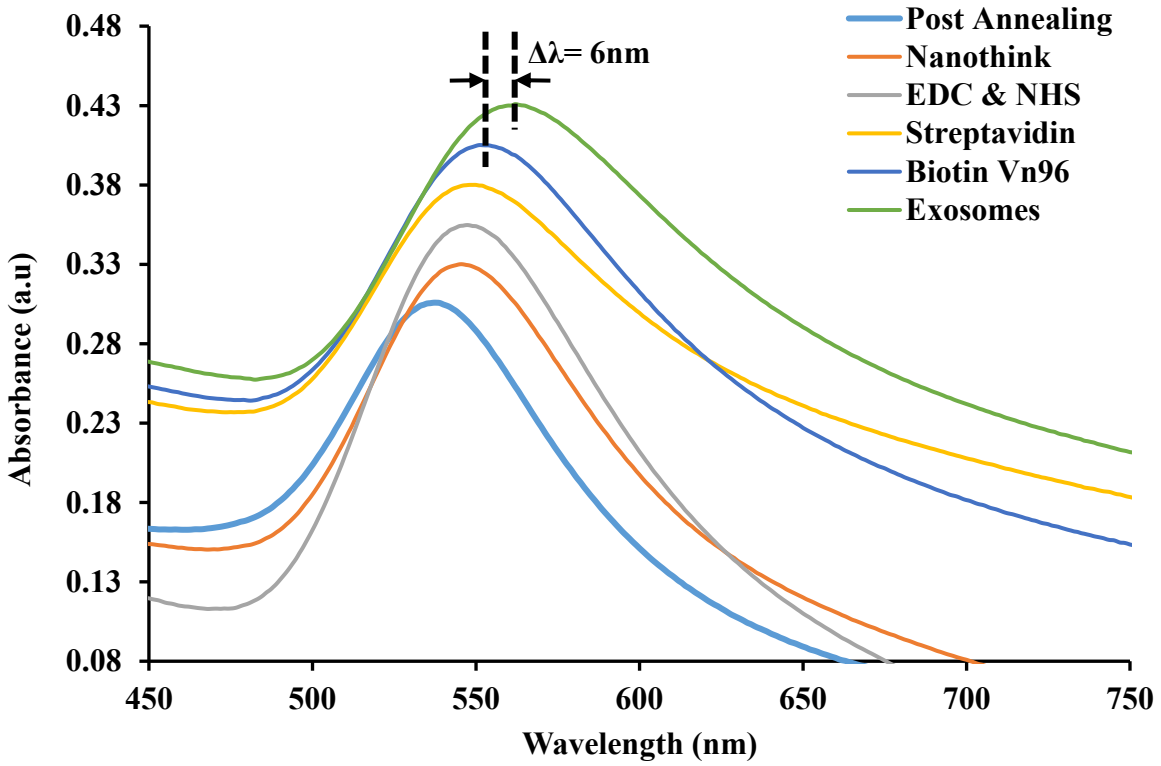

Figure 5-6: Au-LSPR absorption spectra corresponding to each stage of the sensing protocol (*ex-situ* synthesis).

5.4.3. Substrates Characterization using Confocal Microscopy

To determine whether the roughness of substrates plays any role in the sensitivity of the platforms, measurements were carried out by using an Olympus LEXT OLS 4100 laser scanning digital microscope. Further, it can be seen in Table 5.1 that, in the case of *ex-situ* synthesized Au nano-island substrates, the roughness value (Ra & Sa) increases considerably after the

immobilization of the chemicals and biomolecules, whereas, in the case of the *in-situ* synthesized Ag platform, the roughness (Ra & Sa) does not change significantly. This indicates that, in the case of the *ex-situ* synthesized Au platform, the number of Au nano-islands present on the substrate is considerably larger as shown in Figure 5-8 (a-d), than in the case of the *in-situ* synthesized Ag platform where the number of Ag nanoparticles is low as shown in Figure 5-8 (e-h). Thus, the average LSPR shift in the case of ex-situ Au platform varies considerably with the concentration of exosome but the *in-situ* synthesized Ag platform is not that sensitive. Most of the Ag NPs are completely embedded in the PDMS surface.

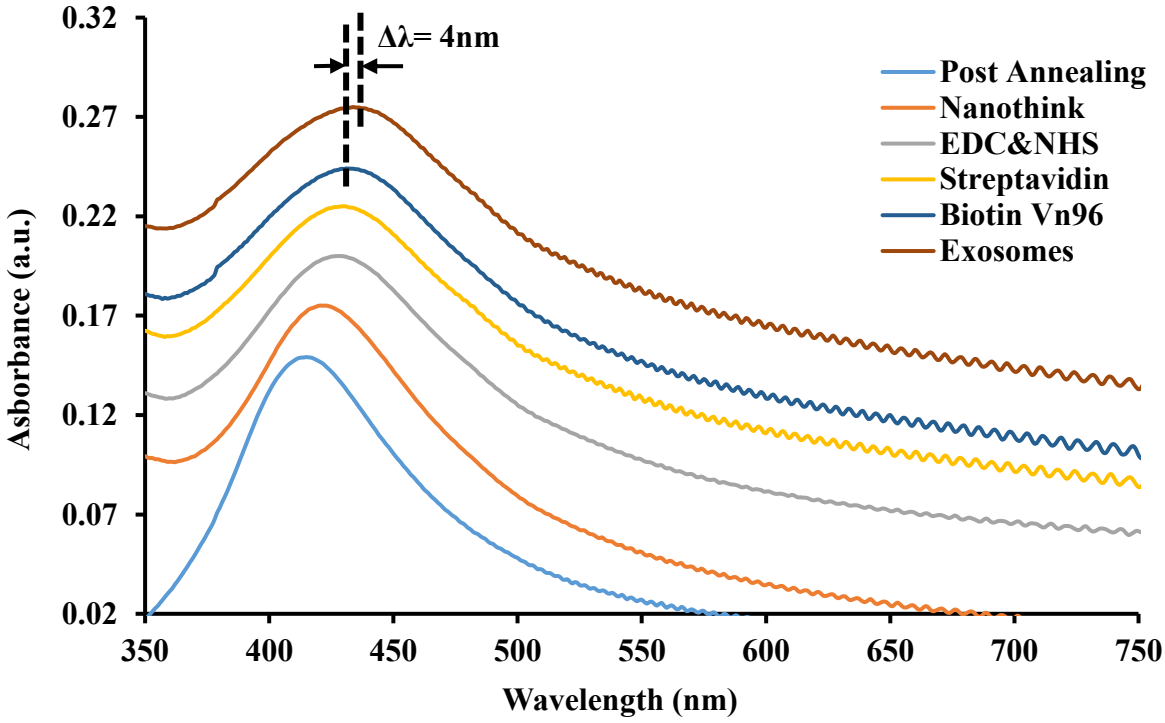

Figure 5-7: Ag-LSPR absorption Spectra corresponding to each stage of the sensing protocol (*in-situ* synthesis).

Table 5.1: Average line roughness for both the sensing platforms, before and after the immobilization of analytes.

Sample Description	Line Roughness R_a [µm]		Surface Roughness S_a [µm]
	Horizontal (X)	Vertical (Y)	
Au nano-islands substrate	0.443	0.324	0.38
Au nano-islands substrate + Biosensing analytes	2.671	0.965	3.68
Ag-PDMS substrate	0.248	0.206	0.291
Ag-PDMS substrate + Biosensing analytes	0.290	0.192	0.294

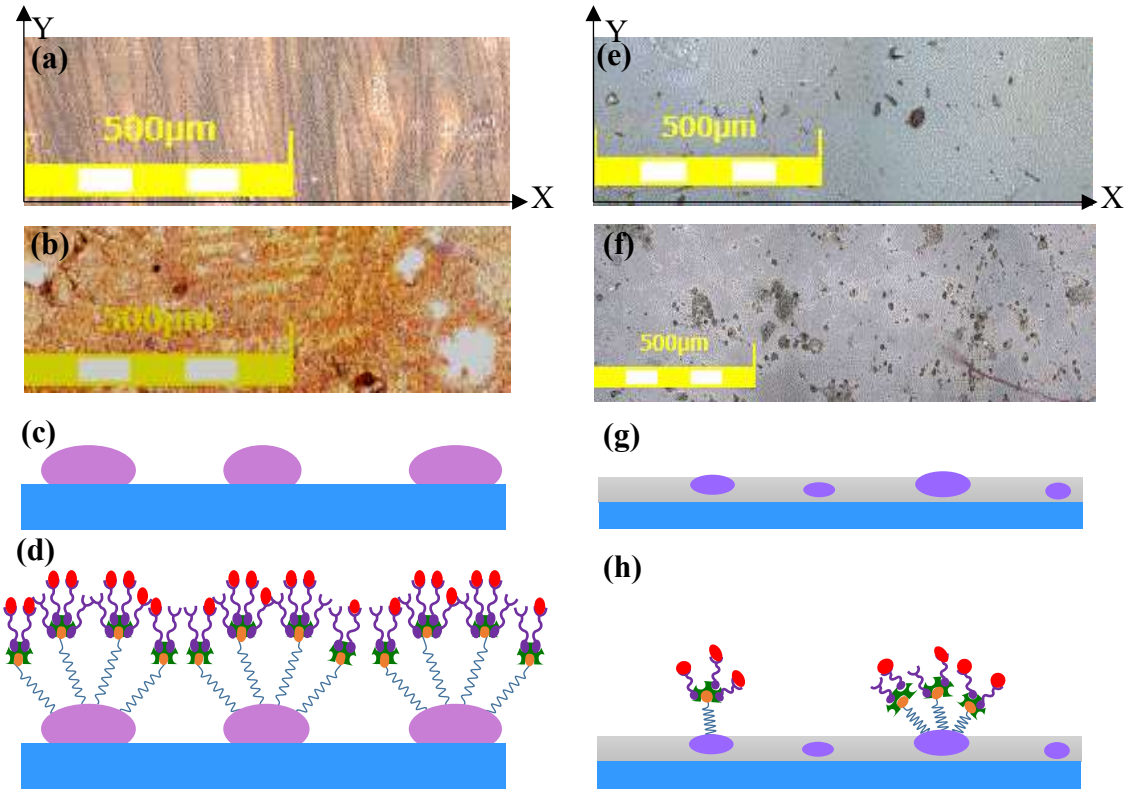

Figure 5-8: Confocal microscopy image and schematics. (a) Image of Au nano-islands on a glass substrate. (b) Image of Au nano-islands on a glass substrate with the bounded analytes. (c) Schematic of Au nano-islands on the glass substrate. (d) Schematic of Au nano-islands on a glass substrate with the bounded analytes (e) Image of Ag nanoparticles on the PDMS substrate. (f) Image of Ag nanoparticles on the PDMS substrate with bounded analytes. (g) Schematic of Ag nanoparticles on the PDMS substrate. (h) Schematic of Ag nanoparticle on the PDMS substrate with bounded analytes.

5.4.4. Dependence of the LSPR Shift on the Concentration of Exosomes

To quantify the exosomes (MCF7) by using the two platforms, five experiments were carried out for each dilution factor (D) (1x, 5x, 10x). The concentration of exosomes/particles present in the cell culture is of the order of 1.33 x 10^{10} per ml. In the present study '1x' denotes the undiluted solution. It is clear from Figure 5-9, that the sensitivity of the Au platform is higher than that of the Ag one because of the availability of Au nano-islands (*ex-situ*) on the surface of the substrate, as seen in Figure 5-2 (c). As noted before, in the case of the *in-situ* synthesis platform, Ag is embedded in the sub-surface layer, and thus the nanoparticles are not exposed to the surrounding medium as shown in Figure 5-2 (d). Further, it can be seen that the slope of the graph in the case of the Au nano-island platform is larger because this platform 'feels' much more the change of the refractive index with the concentration of exosomes than the embedded Ag.

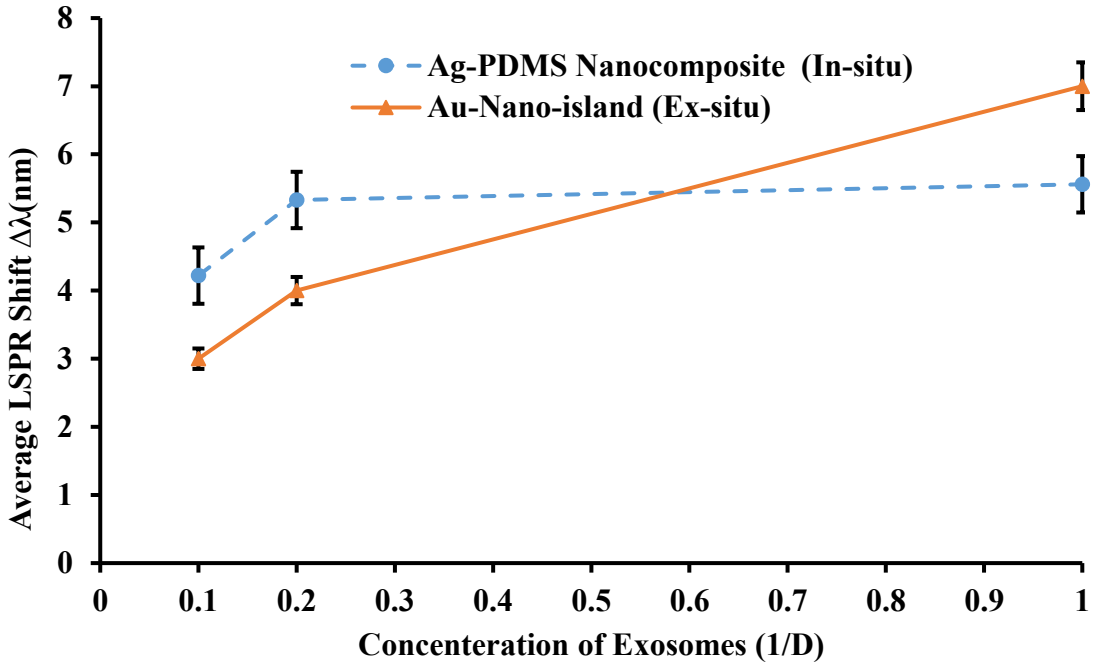

Figure 5-9: Average LSPR shift of the wavelength (Δλ) versus concentration of exosomes ((1/D) - 'D'-Dilutions), (Error bar represents the standard deviation error over 5 measurements).

5.5. Conclusions

It is found that the refractive index sensitivity of the *ex-situ* synthesized Au nano platform is considerably higher than that of the *in-situ* synthesized Ag-PDMS nanocomposite and consequently, this platform is much more performant for sensing exosomes. Two principal reasons were identified to account for this difference. It is thought that, because of the low-temperature annealing of Ag-PDMS, contrary to the Au nano-islands, a non-suitable morphology is formed. It has been demonstrated that nano-island structures have a higher sensitivity due to their morphological characteristics. On the other hand, due to the *in-situ* formation mechanism, a large proportion of the surface Ag particles will diffuse inside the polymer, sub-surface and, hence they will not be available anymore for sensing. The studies carried out on various platforms so far show that a label-free LSPR sensing method can be used for the detection of EVs/exosomes by using the Vn96 peptide to capture them through their interaction with the proteins on their surface.

So, the next chapter (Chapter 6) discusses the effect of the cross-linker of PDMS and thermal budget on plasmonic sensing and sub-surface segregation for the fabrication of an *in-situ* synthesized gold PDMS platform.

Chapter 6. Effect of Cross-Linking and Thermal Budget on Plasmonic Sensing and Sub-Surface Segregation of *In-situ* Synthesized Gold in PDMS

This chapter is reproduced from the article published in *J Nanopart Res*, 23, 21, 2021: This chapter covers objective 3 of the "Thesis Objective and Scope" in Section 1.5.

6.1. Outline

Surface gold – Poly (dimethyl siloxane) nanocomposites are a unique class of composite materials that feature gold nanoparticles concentrated in a sub-surface layer within the polymer matrix. This study involves the creation of sub-surface nanocomposites through an *in-situ* process where gold nanoparticles are synthesized within the polymer. This synthesis occurs through the reduction of gold ions using the polymer's cross-linking agent, which is a vinyl silicon compound. Subsequently, the gold nanoparticles diffuse into the poly (dimethyl siloxane) (PDMS) matrix through a heat treatment process. The investigation of this process primarily relies on various analytical techniques, including UV-Vis spectroscopy, Scanning Electron Microscopy (SEM), Atomic Force Microscopy (AFM), X-ray diffraction (XRD), and X-ray photoelectron spectrometry (XPS).

The study reveals that the newly formed gold nanoparticles become stabilized as they diffuse into the sub-surface layer of the composite, where they tend to aggregate in small clusters. The research also delves into the kinetics of the *in-situ* reduction reaction occurring at the interface between the solution and the polymer film. Moreover, the interaction between the reduction of gold ions and the continuous diffusion of the cross-linking agent toward the composite's surface is explored in detail.

Furthermore, the impact of the sub-surface segregation of gold nanoparticles and their subsequent spatial distribution on the nanocomposite's sensing capabilities is presented and discussed. This research likely contributes to our understanding of how the arrangement of gold nanoparticles within the polymer matrix affects the overall performance and functionality of these nanocomposite materials.

6.2. Introduction

Nanoparticle-polymer composites are advanced functional materials that incorporate nanoparticles into a polymer matrix. These materials combine the inherent characteristics of polymers, such as transparency and ease of processing, with the exceptional electrical, optical, and magnetic properties of the metallic components within them. This unique combination opens up a wide range of potential applications, including but not limited to ultrathin color filters, UV absorbers, tunable optical filters, optical sensors, waveguides, optical strain detectors, and thermo-chromic materials, many of which stem from the remarkable properties of nano-sized noble metals [179–187]. The design, fabrication, and characterization of conducting polydimethylsiloxane (PDMS) with metallic powder have also been explored for applications like microheaters and temperature sensors [188]. Stretchable PDMS structures doped with gold nanoparticles have been developed and proposed for use in strain sensors [189]. Furthermore, gold (Au) and silver (Ag) nanocomposites have found applications in water purification, targeted drug release, antimicrobial coatings, and the analysis of environmental pollutants [190–195].

The strong Localized Surface Plasmon Resonance (LSPR) bands exhibited by gold and silver nanoparticles in the visible spectrum, resulting from the excitation of plasmons by incident light and giving rise to characteristic absorption, make some gold-nanocomposites suitable for sensing applications. The biosensing properties of these nanocomposites depend on factors related to their preparation, particularly the distribution of metal particles within the polymer matrix. Controlling the spatial distribution of gold nanoparticles (AuNPs) is crucial in determining their biosensing properties [196].

Nanocomposites can be synthesized using either an *in-situ* method, where the polymer reacts with a precursor to create nanoparticles, or an *ex-situ* method, where pre-made nanoparticles are incorporated into the polymer. Physical methods like chemical vapor deposition, ion implantation, and thermolysis have also been employed to create nanocomposites with gold on the polymer's surface [197,198].

In some cases, depending on the polymer's softening temperature, nanoparticles can be embedded just below the polymer's surface, where they reach a metastable state with minimal Gibbs free energy [199]. The limited movement of nanoparticles from the surface to the sub-surface layer is influenced by their tendency to reduce high surface energy. Despite efforts to

prepare nanocomposites with desired morphologies and enhanced surface properties, precise control of nanoparticle spatial distribution remains an evolving area of research [200].

When nanoparticles are well-dispersed within the polymer matrix without significant interactions between them, the nanocomposite exhibits properties that are a simple combination of those of the individual components. However, if the polymer matrix is structured, entirely new properties can emerge. For instance, in the case of PDMS with a segregated layer, nanoparticles form and concentrate within the segregated layer(s), leading to unique properties [201], especially in Surface-Enhanced Raman Scattering (SERS) applications [202–205].

A structured design, like the segregated layer in PDMS, can be utilized to control the degree of nanoparticle aggregation within the polymer. PDMS is a commonly used polymer for fabricating microfluidic devices due to its ease of preparation, cost-effectiveness, transparency, and compatibility with biomolecules.

The cross-linking of PDMS is achieved through a process known as hydrosilylation. In this reaction, the vinyl groups present in one component, which is the pre-polymer, react with the hydrosilane groups in the second component, which serves as the curing agent and is typically a vinyl silicon compound. This reaction is catalyzed by platinum (Pt) [206,207], as illustrated in the equation 6.1. This hydrosilylation process with platinum catalysis plays a critical role in creating the cross-links within the PDMS structure, imparting its desired properties.

$$(Cross-linker)-Si-H\ +\ CH_2\ =\ HC-Si-(polymer)\ \underset{heat}{\overset{Pt\ catalyst}{\rightarrow}}\ -Si-CH_2-CH_2-Si-(3D\ network) \quad \textbf{6.1}$$

Numerous researchers [208,209] have investigated the kinetics of the hydrosilylation reaction catalyzed by a platinum complex. However, most of these studies have focused on the bulk reaction involving vinyl-terminated PDMS and silane cross-linkers. When dealing with thin films or coatings, the kinetics of the cross-linking reactions differ from those in bulk systems. This variation is primarily due to segregation phenomena, which can occur either at the interface with the surrounding atmosphere or at the substrate.

As a consequence of this segregation, there is a reduced concentration of the cross-linker and the platinum (Pt) catalyst within the bulk material. This localized depletion of reactants at the

surface or substrate interface leads to distinct reaction kinetics in thin films compared to those observed in bulk reactions.

Zhang et al. and Goyal et al. have proposed that, in the context of *in-situ* synthesis of gold, an excess curing agent might serve as a reducing agent for gold ions [210,211]. Zhang's work examined the impact of altering the curing (cross-linking) agent-to-monomer ratio (η), which essentially relates to the concentration of the curing agent. The diminished sensing performance observed in their study was attributed to the local deformation of the polymer surface resulting from the growth of nanoparticles and their partial embedding within the polymer matrix. Furthermore, they conducted measurements of the optical and thermoplasmonic response of the *in-situ* reduced gold nanoparticles (AuNPs) [212], and there have been various reported applications for the in-situ prepared Au-PDMS nanocomposite [213,214].

Our research group has conducted a comprehensive examination of the *in-situ* synthesis of gold and silver nanocomposites within PDMS, with a particular focus on their applications in microfluidic sensing [176,215–217]. To develop these in-situ nanocomposites for diverse applications, it is crucial to systematically investigate surface nanocomposites created by reducing gold ions with an excess of cross-linking agent in thin, self-standing PDMS films. Our specific interest lies in two key aspects:

(i) The influence of cross-linking agent concentration on the distribution and *in-situ* synthesis of gold nanoparticles after a designated synthesis period, as depicted in the schematic in Figure 6-1(a).

(ii) How the thermal conditions affect the penetration of the sub-surface layers of the polymer, as illustrated in the schematic of Figure 6-1(b).

In the case of free-standing films, precursor molecules diffuse simultaneously through all six sides of the sample. Given our focus on sensing applications, we are particularly concerned with the state of agglomeration of gold nanoparticles (AuNPs) in the surface-segregated layers due to the cross-linking agent and their diffusion into the PDMS matrix during the annealing process.

This research endeavor aims to establish how the distribution of AuNPs within the nanocomposite influences its sensing capabilities. Additionally, it contributes to the broader field

of understanding how nanoparticles diffuse within polymer films (coatings) and the resultant impact on the properties of nanocomposites.

The structure of this paper begins with the experimental section, covering the fabrication of Au-PDMS nanocomposites. Subsequently, we present the results, which encompass the kinetics of the *in-situ* reaction and the morphology of the Au-PDMS surface composites. We then delve into a detailed discussion of the distribution of AuNPs within the polymer film.

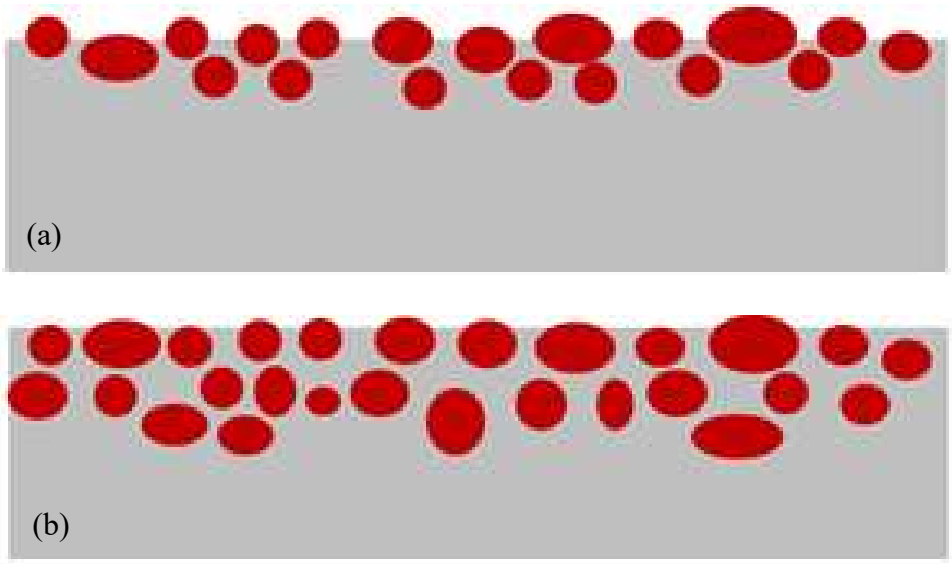

Figure 6-1: Illustration of diffusion of gold nanoparticles and effect of heat treatment on a nanocomposite sample. (a) Schematic showing AuNPs in the as-prepared sample. (b) Heat-treated sample (only the upper portion of the sample is shown for simplicity).

6.3. Experimental

6.3.1. Materials

Gold (III) chloride trihydrate ($HAuCl_4.3H_2O$), isopropyl alcohol, dimethylformamide, chloroform, toluene, and anisole were purchased from Sigma-Aldrich. The Sylgard® 184 elastomer kit for the PDMS fabrication was purchased from Dow Corning. De-ionized (DI) water with a resistivity of 18MΩ, used in all the experiments, was obtained from the NANO pure ultrapure water system (Barnstead). Ethanol was purchased from Fisher Chemicals.

6.3.2. Fabrication and synthesis of the gold-PDMS nanocomposite

In this study, the base polymer and the curing agent were mixed in the ratio of 10:1 and 4:1 by weight, respectively. After mixing them thoroughly, the bubbles formed were removed by

degasification for 30 minutes, by using a vacuum desiccator. The mixture was then poured on a clean silanized silicon wafer to obtain a smooth film. The thickness of the films can be adjusted by varying the volume of PDMS. The mold, filled with PDMS, was kept for curing in the oven at 60 °C for 12 hours. After curing, the oven was allowed to cool down and the mold was taken out only when it reached room temperature. Then, PDMS was cut into pieces with a size of 12mm x 35mm, peeled off from the mold, and immersed vertically in the gold precursor solution

The gold precursor solution is prepared by dissolving gold (III) chloride trihydrate ($HAuCl_4 \cdot 3H_2O$) in ethanol. The concentration of the precursor solution was 0.6% (wt/v). The PDMS samples were created with two different concentrations of the base to cross-linking agent, specifically, in ratios of 4:1 and 10:1. To synthesize Au-PDMS nanocomposites, the prepared PDMS films were vertically immersed in the gold precursor solution and left to incubate for approximately 48 hours. Figure 6-2 (a) depicts the film immersed in the precursor solution, and Figure 6-2 (b) illustrates the resulting nanocomposite after the completion of the reaction (the PDMS film is slightly slanted for clarity). In the subsequent sections, this nanocomposite will be referred to as the "as-prepared sample," indicating that the sample was removed after a synthesis time of 48 hours at room temperature and was not subjected to any heat treatment (t_{synth}= 48hrs, no heat-treatment).

Following the *in-situ* synthesis, the morphology of the gold nanoparticle aggregates in the as-prepared sample is modified by subjecting the Au-PDMS nanocomposite samples to a heat treatment at 200 °C for 30 minutes. These treated samples will be referred to as "heat-treated samples" (t_{synth}= 48hrs, Temp = 200 °C, 30min heat-treatment).

6.3.3. Characterization methods

The Au-PDMS nanocomposites were characterized by UV-visible spectroscopy, Scanning Electron Microscopy (SEM), Atomic Force Microscopy (AFM), X-ray diffraction (XRD) and X-ray Photoelectron Spectroscopy (XPS). Perkin Elmer lambda 650 UV-visible spectrometer was used for all the spectral measurements. SEM images were captured using Hitachi S 3400N. AFM images were captured in tapping mode by scanning an area of 20x20 μm, using scanning probe microscopy. XRD measurements were obtained using a PANalytical X'Pert PRO system. XPS characterization was performed using a VG Scientific ESCALAB MKII spectrometer with an Ar^+ sputtering energy of 1keV and an estimated sputtering rate of 3.4 nm/min. A surface area of 2mm

x 3mm is sputtered and analyzed until a depth without gold signal. The sensitivity of the synthesized nanocomposite for sensing was measured, using solvents with different refractive indices. The measurements were performed by measuring the absorption spectra, after immersing the nanocomposite sample in a quartz cuvette, filled with the solvent, for 1 hour.

6.4. Results and Discussion

6.4.1. Assessment of the distribution of AuNPs

For visual analysis of the distribution of AuNPs after the *in-situ* synthesis, a portion along the thickness of a 4:1 ratio sample of 1mm thickness was sliced, using a sharp blade. Out of all six faces of the sample, four faces were sliced, except the top and the bottom face as shown in the schematic of Figure 6-2 (c).

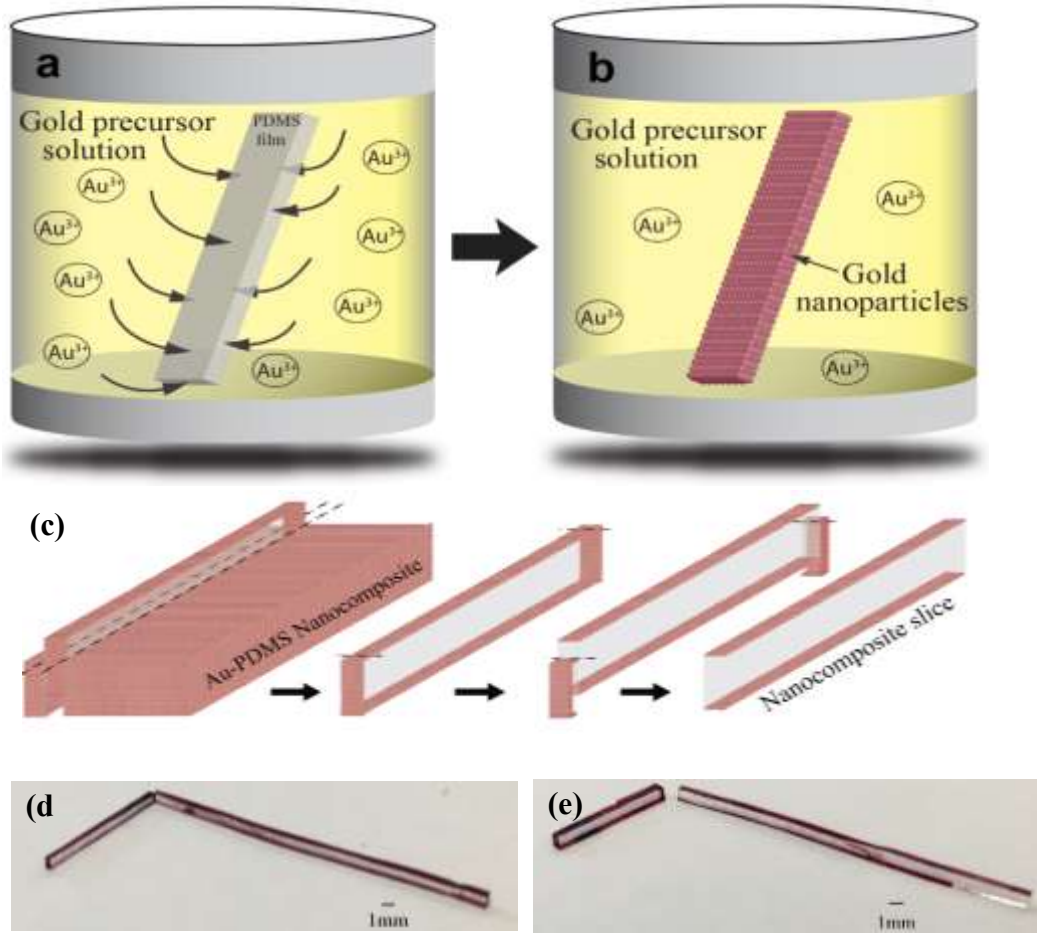

Figure 6-2: *In-situ* synthesis and slicing of the sample. (a) Schematic of *in-situ* synthesis, the PDMS film, immersed in the gold precursor solution. (b) Au-PDMS nanocomposite (red), after 48 hrs. (c) Schematic of slicing the Au-PDMS nanocomposite sample. (d) Image of sliced 1mm thick heat-treated sample at 200 °C for 30 minutes.

For a qualitative assessment of the way AuNPs are distributed in the polymer matrix, the samples were cut as described in the experimental part Figure 6-2 (d) and Figure 6-2 (e) show the images of the sliced 1mm Au-PDMS nanocomposites for both the as-prepared and heat-treated samples. The same qualitative assessment has been done for nanocomposites prepared with an even higher concentration of the precursor and the results were found the same. They confirmed that, under the conditions of the experiment, no matter the concentration of the gold precursor, nanoparticles are *in-situ* formed and concentrated only at the interfaces. This qualitative observation prompted us to undertake a detailed investigation of Au-PDMS nanocomposites, by using a variety of methods, suitable for their characterization to quantify the influence of cross-linking agent and thermal budget.

6.4.2. *In-situ* synthesis of AuNPs on the surface of the polymer

During the *in-situ* synthesis, the gold ions in the precursor solution are reduced to AuNPs by the excess curing agent in PDMS. The amount of curing agent present in PDMS as well as the concentration of the precursor solution will determine the rate of AuNP formation. In other words, by increasing the amount of curing (cross-linking) agent in PDMS, by keeping the concentration of the precursor molecule constant, more AuNPs will be formed at the interface(s) of the polymer. Therefore, it is expected to have more gold ions reduced in 4:1 PDMS samples where the reductant is in a higher concentration than in the 10:1 sample. In our previous work, we found that the *in-situ* synthesis of nanoparticles in the PDMS matrix by using the ethanol solution of the precursor is faster than in the aqueous solution [218]. This was accounted for by the high rate of permeation of ethanol-based precursor solution. To study the kinetics of the reaction, the evolution of the absorption spectra of nanocomposites prepared in ethanol solution (0.6% wt./v) have been examined and shown in Figure 6-3 (a) and Figure 6-3 (b). The reaction of the formation of gold nanoparticles is shown in the equation 6.2.

$$3\,\begin{array}{c}|\\Si-H\\|\end{array}+\frac{3}{2}H_2O+2AuCl_4^-\rightarrow\frac{3}{2}-\begin{array}{c}|\\Si\\|\end{array}-O-\begin{array}{c}|\\Si\\|\end{array}-2Au+8Cl^-+6H^+$$

6.2

To better understand the kinetics of the *in-situ* reduction, the variation of absorbance values of the Au-LSPR bands at each time interval is shown in Figure 6-3 (a) and Figure 6-3 (b). From these progresses of synthesis, under the conditions of the experiment, the reduction process seems

to be completed after 80 hours in the case of a 4:1 sample. It can also be seen that more gold results when the concentration of the curing agent is higher (4:1 samples).

The maximum absorbance of the Au-LSPR band is shown against the time, for the concentrations of cross-linking agents namely 4:1 and 10:1. Figure 6-4 (a) shows the three phases that describe the progress of kinetics: induction, the actual formation step, and, saturation. As shown in Figure 6-4 (a) the induction step is around 5 hours in both cases, while the actual formation step takes around 100 hours in the case of the 4:1 sample and 140 hours for the 10:1 sample. After this time, very less new gold nanoparticles are formed (saturation). The shorter time of saturation, in the case of the 4:1 ratio sample, is due to the higher reaction rate, because of the relatively higher concentration of the reductant.

From the evolution of plasmonics, it can be presumed that the precursor solution continues to enter the PDMS film, and the gold ions are reduced, forming AuNPs, until the whole surface area is filled. After this, AuNPs start to aggregate inside the film, giving rise to a broad absorption peak in the UV-visible spectrum. The aggregated state of the nanoparticles is reflected by the broadening of Au-LSPR bands, after around 100 hours of reaction. The evolution of the aggregation of gold nanoparticles is shown in Figure 6-4(b). It can be seen that, in the case of the 4:1 sample, where the rate of the reduction is faster, the width of the band shows a steady increase but this is not the case for the10:1 sample, where the amount of the reductant is significantly lower.

6.4.3. Morphology of the Au-PDMS Surface Composites

The SEM images shown in Figure 6-5 (a) to Figure 6-5 (f) confirm that the gold nanoparticles start to aggregate as the synthesis progresses, in agreement with the evolution of the plasmonic absorbance and width of the band, as seen in Figure 6-4 (a), and Figure 6-4 (b). At the same time, the formation of large aggregates is reflected in the widening of the absorption bands, as shown in the images. The SEM images of the 10:1 sample at 48hrs and 96hrs do not show any particles on the surface of PDMS, but at 216hrs, a few nanoparticles can be seen. From the images, it can be inferred that the rate of *in-situ* synthesis is considerably slower in the 10:1 sample than in the 4:1 sample, as the amount of the reducing agent is less in the 10:1 sample. The SEM images confirm the formation of significantly more AuNPs in the case of the samples prepared with a

higher concentration of curing agent (4:1; Figure 6-5 (a) to Figure 6-5 (c)) as compared to the (10:1; Figure 6-5 (d) to Figure 6-5 (f)) samples.

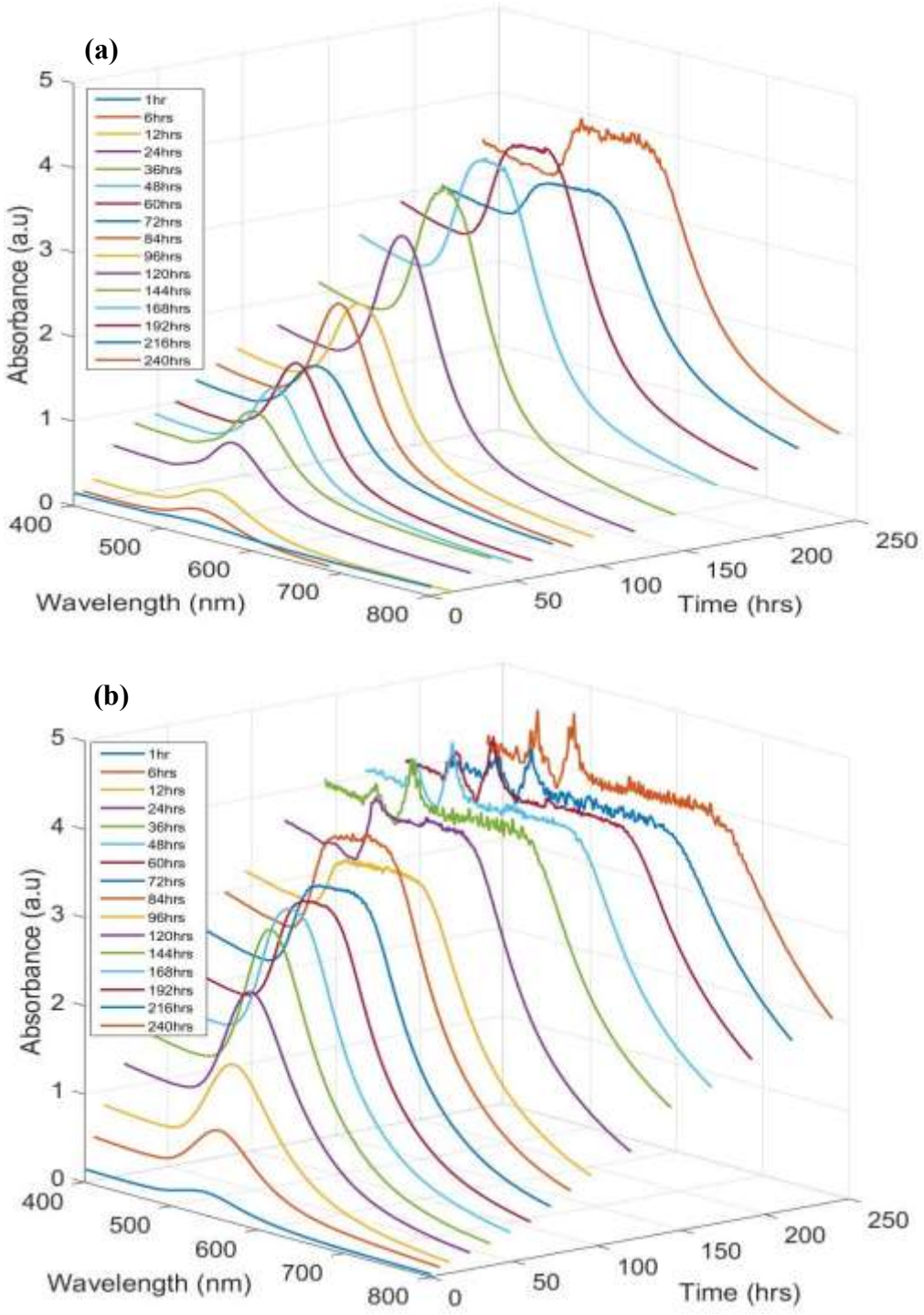

Figure 6-3: The Au-LSPR bands at each time interval are plotted against the synthesis time. (a) 10:1 PDMS sample. (b) 4:1 PDMS sample.

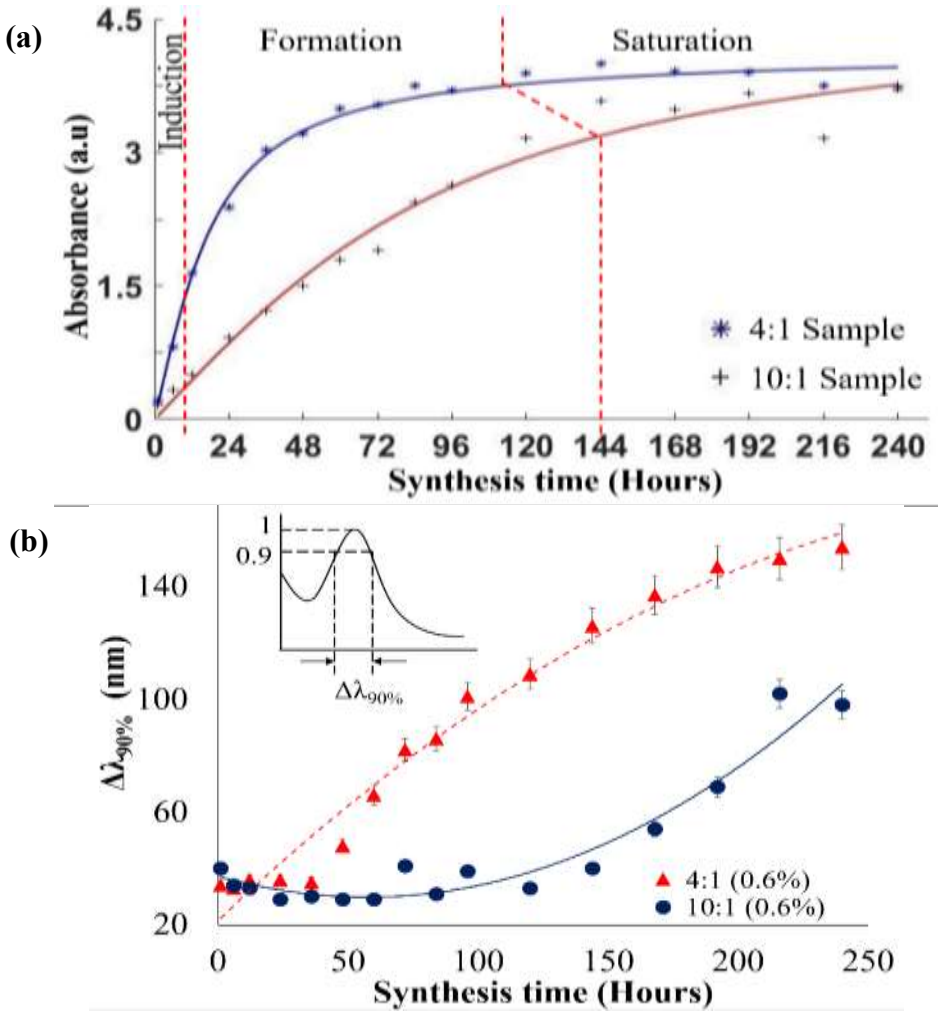

Figure 6-4: Evolution of the *in-situ* reduction reaction for two concentrations of the cross-linking agent. (a) Evolution of absorbance around 540nm against synthesis time (t_{synth}). (b) The bandwidth measured at 90% of the spectral peak corresponds to two concentrations of the cross-linking agent.

In previous work by our group members, several gold-polymer surface nanocomposites were prepared and characterized [176]. Morphology investigations of these samples have revealed that as-prepared nanocomposites always had gold aggregates on the surface. The heat treatment, in general, reduced the size of the aggregates, or even disaggregated them completely, releasing individual nanoparticles. To better observe nanoparticle aggregates morphological changes AFM studies have been carried out on both the as-prepared and heat-treated nanocomposite samples of 10:1 and 4:1 composition. In the case of the *in-situ* prepared Au-PDMS nanocomposites, by comparing the AFM images of as-prepared and heat-treated samples in Figure 6-6 (a) and Figure

6-6 (b), it can be seen that the aggregates are present in the surface and a complete disaggregation through the heat treatment process does not happen.

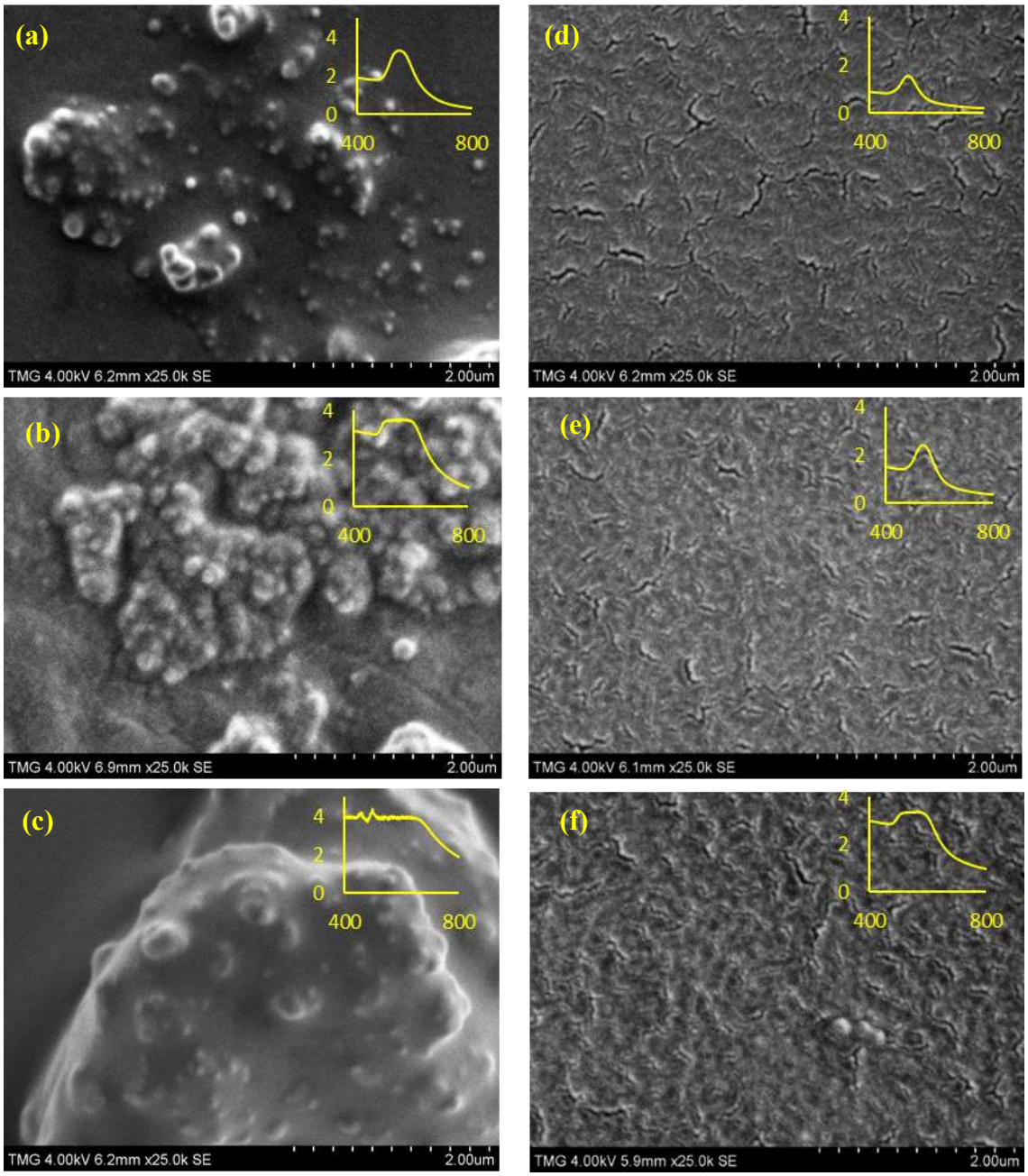

Figure 6-5: SEM images of 1mm thick samples at different synthesis times, along with their absorption bands (inset) (Images (a-c) 4:1 sample at 48 hrs, 96 hrs, and 216 hrs, and images (d-f) 10:1 sample at 48 hrs, 96hrs and 216 hrs, respectively).

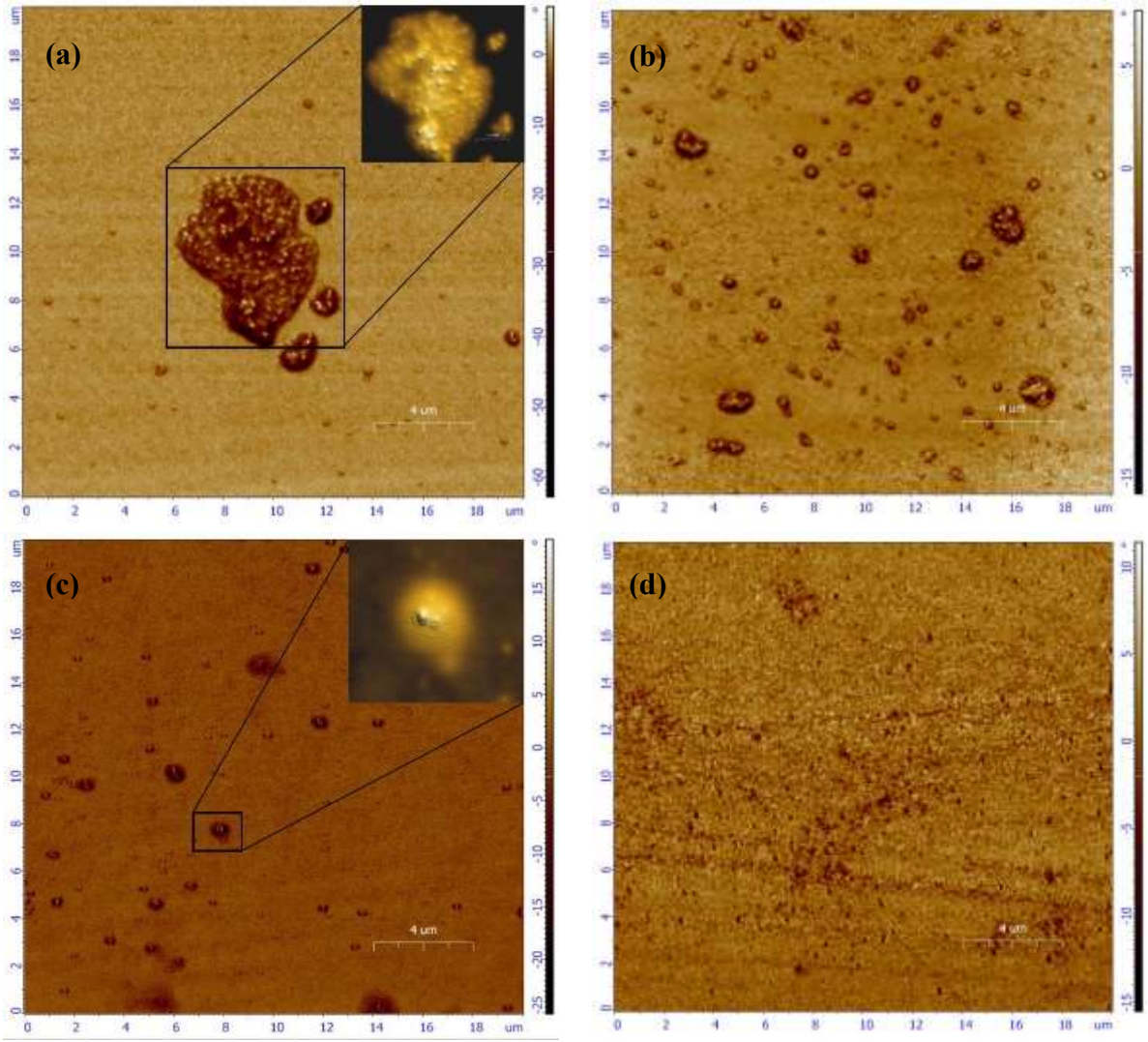

Figure 6-6: AFM Phase contrast images: (a-b) 10:1 as-prepared (t_{synth}= 48hrs, no heat-treatment) along with the topography image (inset) and heat-treated (t_{synth}= 48hrs, T = 200 °C, 30min heat-treatment) PDMS sample (c-d) 4:1 as-prepared, along with the topography image (inset) and heat-treated PDMS sample.

Figure 6-6 (a) shows the phase contrast image with its topography image (inset) of 10:1 as-prepared aggregated samples with particle sizes ranging from hundreds of nanometers to several microns on the surface of the nanocomposite. However, the topography image clearly shows that the aggregates seem to be covered with a thin layer of PDMS. As the process of heat treatment changes the morphology, the aggregates appear to be re-organized and distributed on the surface as shown in Figure 6-6 (b). Figure 6-6 (b) shows the presence of smaller aggregates, even after the heat treatment. The same tendency, but with a higher amount of gold nanoparticles, is observed in the phase contrast and topography images of the 4:1 PDMS sample as shown in Figure 6-6 (c) and Figure 6-6 (d).

6.4.4. Sensitivity Measurements of the Platforms

The refractive index sensitivity of 1mm thick 10:1 and 4:1 nanocomposite samples, both in as-prepared and heat-treated (at 200°C) conditions, was measured using various solvents, as outlined in the experimental section. Figure 6-7 displays the sensitivity plots corresponding to these measurements. It is evident from the plots that the sensitivity of all the nanocomposite platforms is notably low.

The low refractive index sensitivity observed in the Au-PDMS nanocomposite samples confirms that the majority of nanoparticles are located beneath the surface, covered by a thin polymer layer. In other words, they are not readily available for sensing, as depicted in the topography image (inset) in Figure 6-6 (a) and Figure 6-6 (c). When gold nanoparticles are prepared through *ex-situ* synthesis or physical deposition methods such as chemical vapor deposition, ion implantation, and thermolysis, they are typically situated on the surface of the film [197,198].

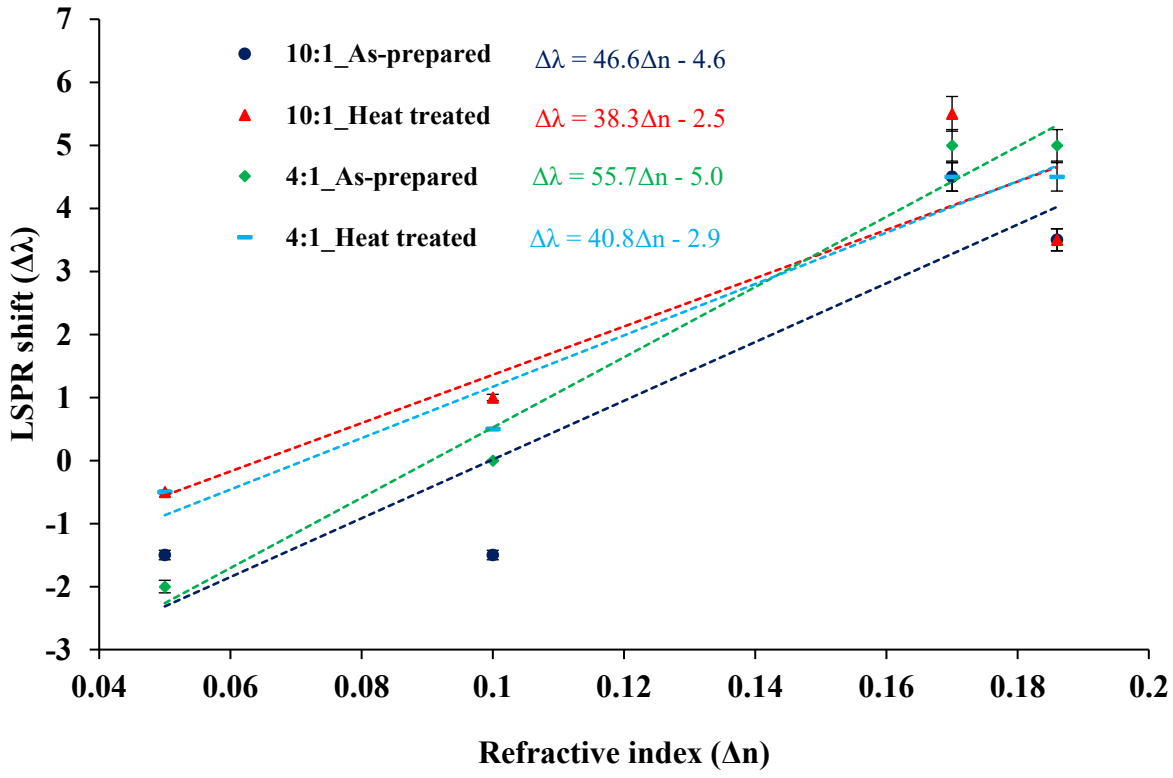

Figure 6-7:Sensitivity measurements of a 1mm thick 10:1 and 4:1 nanocomposite sample, as-prepared (t_{synth}= 48hrs, no heat-treatment) and heat-treated (t_{synth}= 48hrs, T = 200 °C, 30min heat-treatment).

However, in the case of *in-situ* synthesis, the Au nanoparticles are submerged beneath the surface, surrounded by polymer chains, and thus, they do not come into direct contact with the analyte. Even after heat treatment, during which more nanoparticles diffuse into the polymer, they remain beneath the surface and do not appear on the surface. This phenomenon accounts for the low sensitivity of the platform when *in-situ* synthesis of Au NPs is employed.

Furthermore, for this platform, the FOM has been calculated, and it is in the order of 13.31, and 10.94 for 10:1 as-prepared, and heat-treated samples, respectively. In contrast, for the 4:1 as-prepared and heat-treated samples, it is 11.14 and 9.06, respectively.

6.4.5. Distribution of AuNPs in the Polymer Film

The distribution of AuNPs in the depth of the Au-PDMS nanocomposite was analyzed by XPS. Figure 6-8 (a) shows the elemental composition of the as-prepared ethanol nanocomposite sample (4:1 ratio), plotted against the binding energy of the corresponding atomic orbital. The distribution of AuNPs, along the depth of the nanocomposite sample was analyzed. The gold atomic percentage was plotted against the depth as shown in Figure 6-8 (b) and Figure 6-8 (c) for the as-prepared and heat-treated samples, respectively.

It can be observed from the XPS analysis in Figure 6-8 (a), Figure 6-8(b), and Figure 6-9 that most of the reduced gold nanoparticles are just below the surface layer, concentrated in a strip of around 100 nm, in the case of both as-prepared and heat-treated samples. However, gold at an atomic concentration of about 0.9% was found in the heat-treated 10:1 sample until a depth of around 1 μm while, in the case of the 4:1 sample, the concentration of gold, right under the surface was found higher (around 3.5%) but decreased abruptly with depth. In the heat-treated sample, the strip of AuNPs is found deeper and some more AuNPs can be seen in the depth of the sample.

A part of the AuNPs has diffused to a depth of almost 700 nm in the as-prepared samples of 10:1 and 4:1 ratios and to a depth of more than 1200 nm in the heat-treated samples of 10:1. The XPS measurements show that the morphology is changed when the samples are heat-treated at 200°C, (see the AFM images Figure 6-6 (b) and Figure 6-6(d)). The aggregates become smaller and the nanoparticles are re-distributed over the surface and in the depth. Figure 6-9 shows the schematic of the re-distribution of AuNPs and the gold atomic percentage in the sub-surface of the as-prepared and heat-treated samples with 10:1 and 4:1 composition.

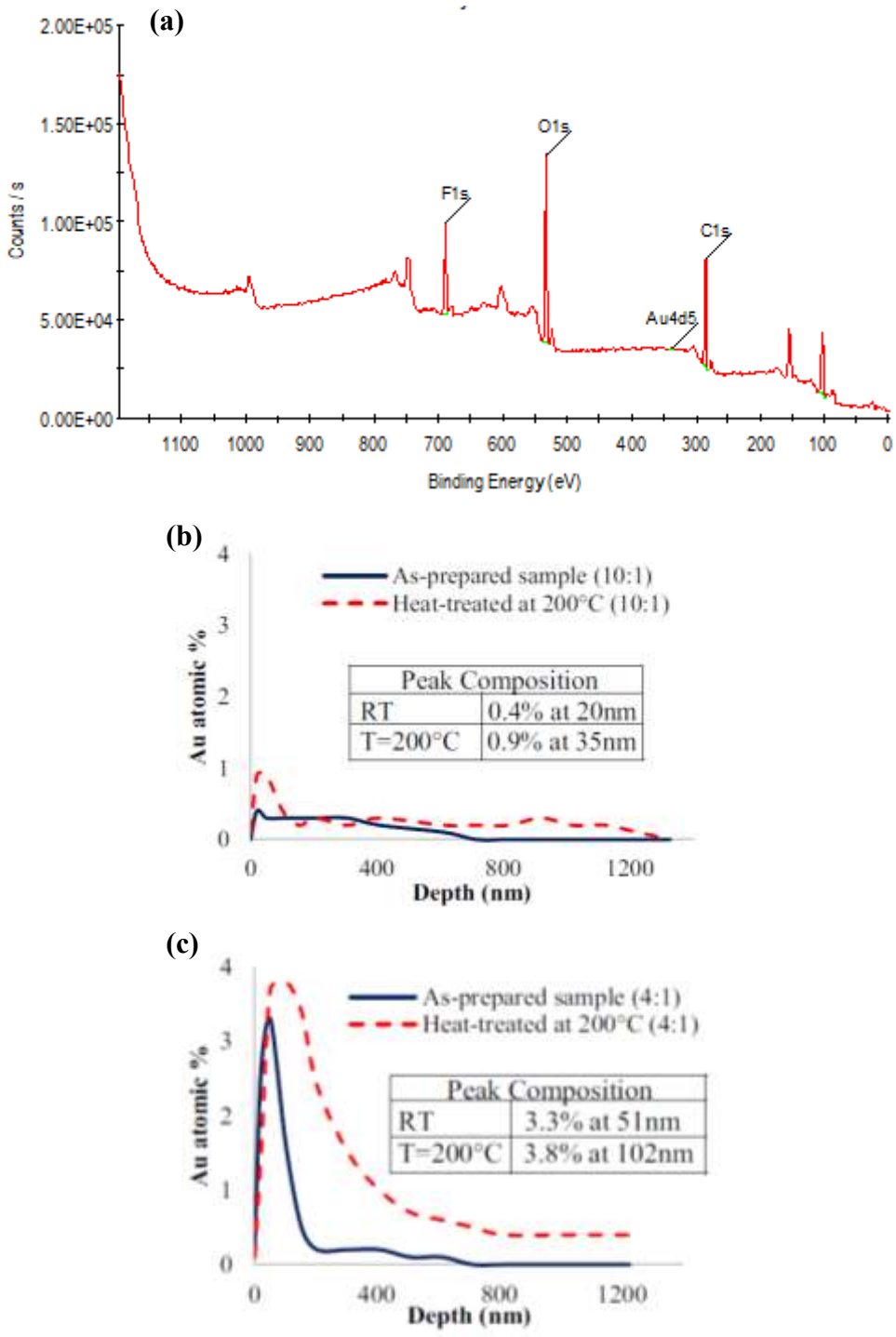

Figure 6-8: Analysis of gold atomic percentage as a function of depth, in the case of as-prepared (t_{synth}= 48hrs, no heat-treatment) and heat-treated (t_{synth}= 48hrs, Temp = 200 °C, 30min heat treatment) samples. (a) XPS spectrum showing the elements present in the Au-PDMS nanocomposite. (b) 1mm thick 10:1sample. (c)1mm thick 4:1sample.

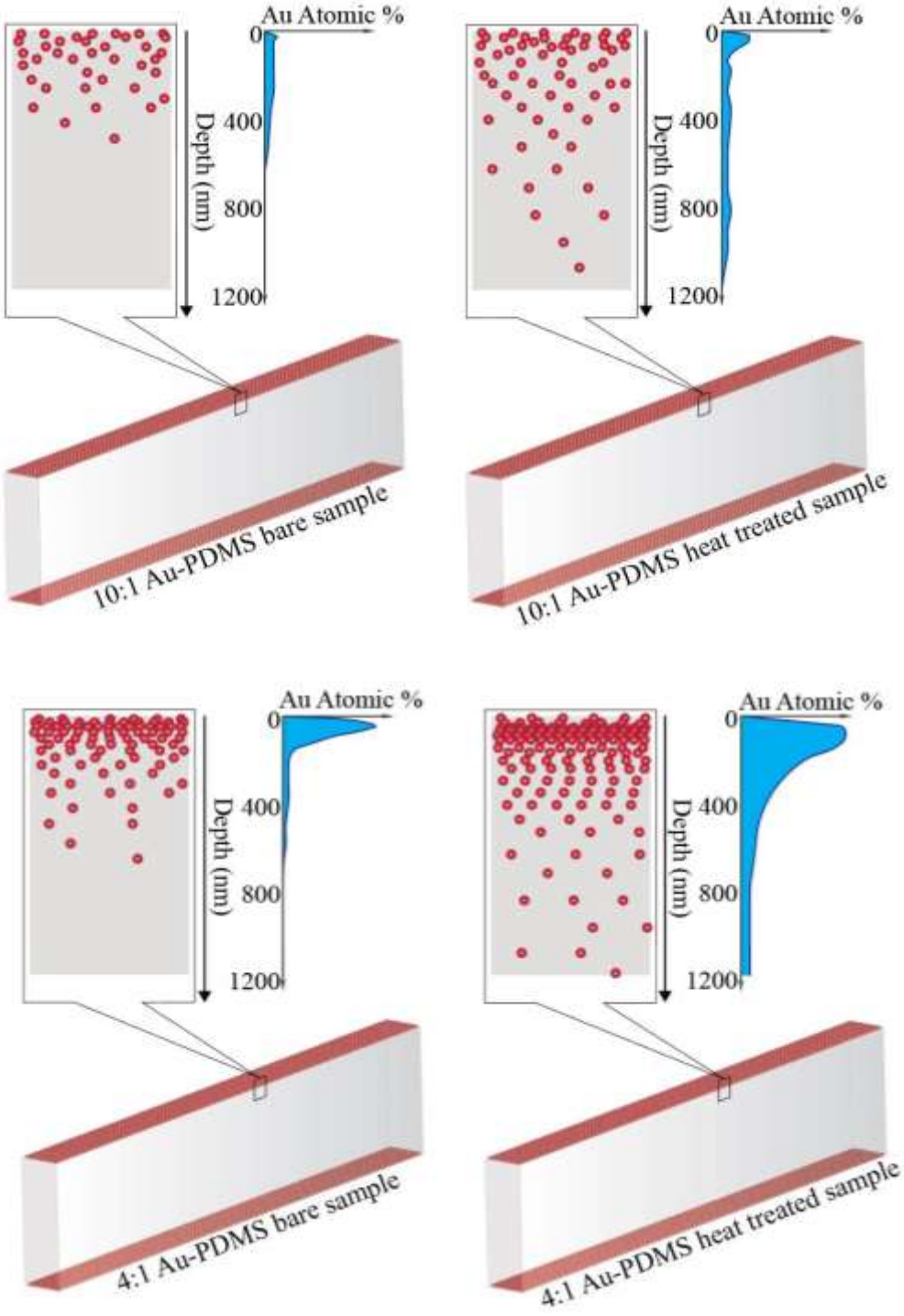

Figure 6-9: Schematic showing the distribution of AuNPs and gold atomic percentage in the sub-surface of samples.

The schematic shows the diffusion of AuNPs into the depth of the sample when their kinetic energy is increased by heating. The schematic is a simplified view of diffusion from only the top of the sample. In reality, as AuNPs are formed at each interface of the free-standing sample, the diffusion is not unidirectional, and the trajectories of AuNPs may intersect with those of the particles in the vicinity, coming from the sides of the sample. The schematic shows the diffusion of AuNPs into the depth of the sample when their kinetic energy is increased by heating. The schematic is a simplified view of diffusion from only the top of the sample. In reality, as AuNPs are formed at each interface of the free-standing sample, the diffusion is not unidirectional, and the trajectories of AuNPs may intersect with those of the particles in the vicinity, coming from the sides of the sample. The results show that the AuNPs from the sub-surface layers are redistributed upon heat treatment. It can be inferred that the curing agent in self-standing thin films is concentrated on the surfaces of the films (in contact with the atmosphere) and that the reduction reaction is taking place exclusively there and not inside the film.

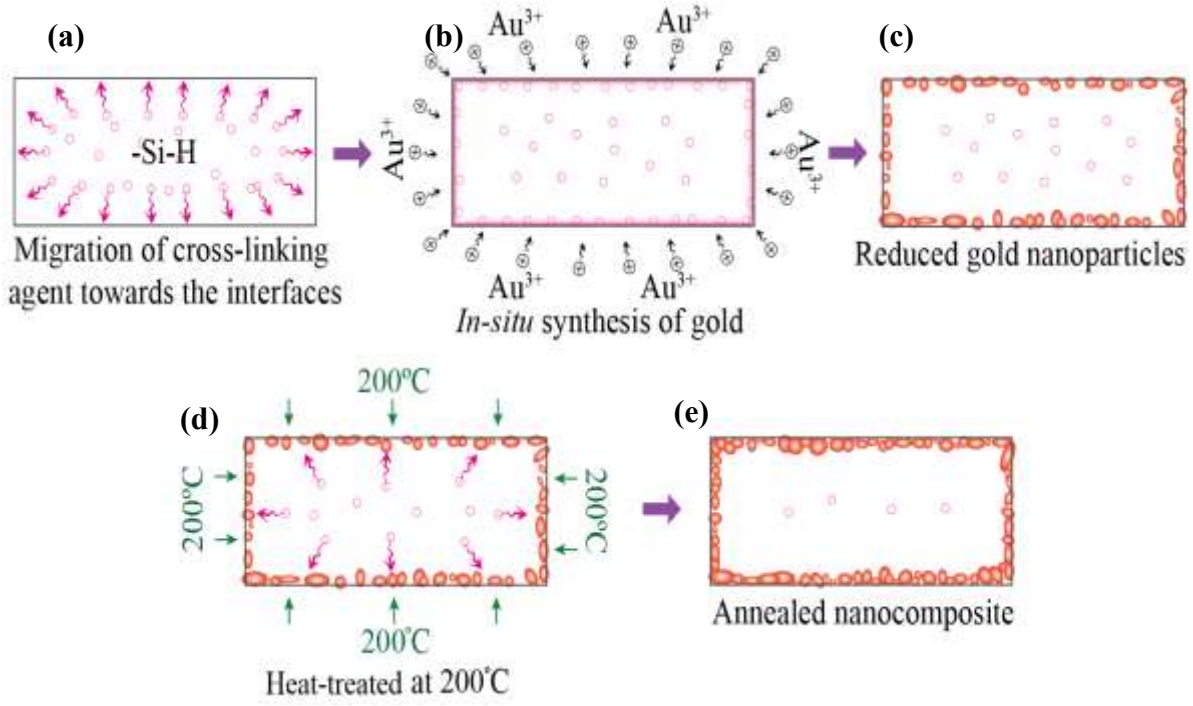

Figure 6-10: Schematic of *in-situ* formation, sinking, and re-distribution of AuNPs. (a) The excess of cross-linking agents migrates to the interfaces. (b) Reduction of gold ions (Au^{3+}). (c) *In-situ* formed AuNPs sink under the surface. (d) New cross-linking molecules migrate toward the interfaces and reduce the remaining gold precursor molecules during heat treatment at 200 °C for 30min. (e) A larger amount of (additional) AuNPs are formed in the sub-surface and some migrate inside the polymer as well due to the migration of cross-linking agents during heat treatment.

To better understand the synthesis of AuNPs on the surface of the PDMS sample, a schematic of the *in-situ* synthesis of AuNPs on the surface of the polymer is shown in Figure 6-10 (a) to Figure 6-10 (e). The excess of the free cross-linking agent migrates toward the interfaces and reduces the incoming gold precursor molecules. After the nucleation, the growth of AuNPs, and the formation of aggregates, the gold structure will be embedded in the polymer. Heat treating, the nanocomposite sample at 200 °C for 30 minutes, would drive more cross-linker molecules to the surface and additional AuNPs will be formed at the interfaces.

Table 6.1: Relation between the concentrations of cross-linker, the atomic percentage of synthesized gold, and their sensitivity

Nanocomposite sample type	Total gold synthesized (Au_{total} %)	Normalized amount of gold (%)	Sensitivity (nm/RIU)
10:1 as-prepared sample (t_{synth}= 48hrs, no heat-treatment)	158.83	100	46.6
10:1 heat-treated sample (t_{synth}= 48hrs, T = 200 °C, 30min heat-treatment)	327.10	206	38.3
4:1 as-prepared sample (t_{synth}= 48hrs, no heat-treatment)	400.63	252	55.7
4:1 heat-treated sample (t_{synth}= 48hrs, T = 200 °C, 30min heat-treatment)	1374.52	865	40.8

t_{synth}- synthesis time; T- heat treatment temperature, Au_{total} – Gold nanoparticles synthesized over 1200 nm in %

When the nanocomposite's sensitivity is compared with the XPS results, it is very clear that the sensitivity of the nanocomposite depends on the amount of gold present in the sample. Table 6.1 shows the amount of gold synthesized represented by the area under the curves for the as-prepared and heat-treated samples of the composition 10:1 and 4:1. If the Au_{total} of 10:1 as-prepared is set as reference, considering the curves from Figure 6-8 (b), and Figure 6-8 (c) and normalized to 100%, the process of heat-treatment at 200 °C for 30 minutes results in the formation of more gold, that is, 2.06 times more than in the as-prepared sample. By analyzing the Au_{total} and

the XPS curve pattern, it is clear that the heat treatment is not only increasing the amount of gold synthesized, but it is driving the gold nanoparticles deeper into the surface of the nanocomposite. For this reason, the sensitivity of the 10:1 heat-treated sample is reduced when compared to the 10:1 as-prepared. A similar trend is observed in the case of the 4:1 as-prepared and heat-treated samples. Also, the normalized Au_{total} shows that the 4:1 as-prepared sample has a 2.52 times higher percentage of gold than that of the 10:1 as-prepared sample, because of the higher amount of cross-linking agent present in the 4:1 sample. Thus, due to the higher percentage of gold in the 4:1 as-prepared sample, the sensitivity is higher, than the 10:1 as-prepared sample. Therefore, if a given application requires a higher sensitivity, the cross-linking agent to base ratio in the PDMS has to be 4:1 or more. If the application requires further distribution of nanoparticles in the nanocomposite, heat treatment could be considered as well.

In addition to sensing applications, Au (Ag)-PDMS nanocomposites, with the addition of carbon nanotubes, can be used for shielding from electromagnetic interference [145,155].

6.4.6. Identification of Gold by XRD

To identify the gold nanoparticles in the nanocomposite samples and to assess their crystallinity, X-ray diffraction (XRD) analysis has been utilized. Figure 6-11 (a), Figure 6-11 (b), and Figure 6-12 (a), Figure 6-12 (b) shows the XRD pattern of the gold from 10° to 80°. Four diffraction peaks can be observed in the plots, which can be indexed to (111), (200), (220), and (311) crystal faces of gold, revealing that the nanoparticles synthesized at the interface of the polymer are composed of crystalline gold [JCPDS No. 04-0784]. The intensities of the 4:1 nanocomposite sample are relatively higher than that of the 10:1 sample, which confirms the formation of more gold in the case of the 4:1 sample. As the peak corresponding to the (111) plane is more intense than the other planes, it seems that the (111) plane is the predominant orientation of the synthesized gold nanoparticles.

6.4.7. Mechanism of Formation of Sub-surface Segregated AuNPs

Unusual sub-surface structures, prepared by vacuum deposition onto heat or solvent vapor-softened thermoplastic polymer substrates, have been reported [219–221]. For example, silver crystalline aggregates as well as other metal structures, have been observed by SEM at a depth of several particles below the polymer surface. The detailed calculation of surface and interfacial tension forces demonstrated that the completely embedded sub-surface structures are

thermodynamically the most stable. We hypothesized that the gold nanoparticles formed at the surface by *in-situ* synthesis, would also diffuse and completely embed in PDMS.

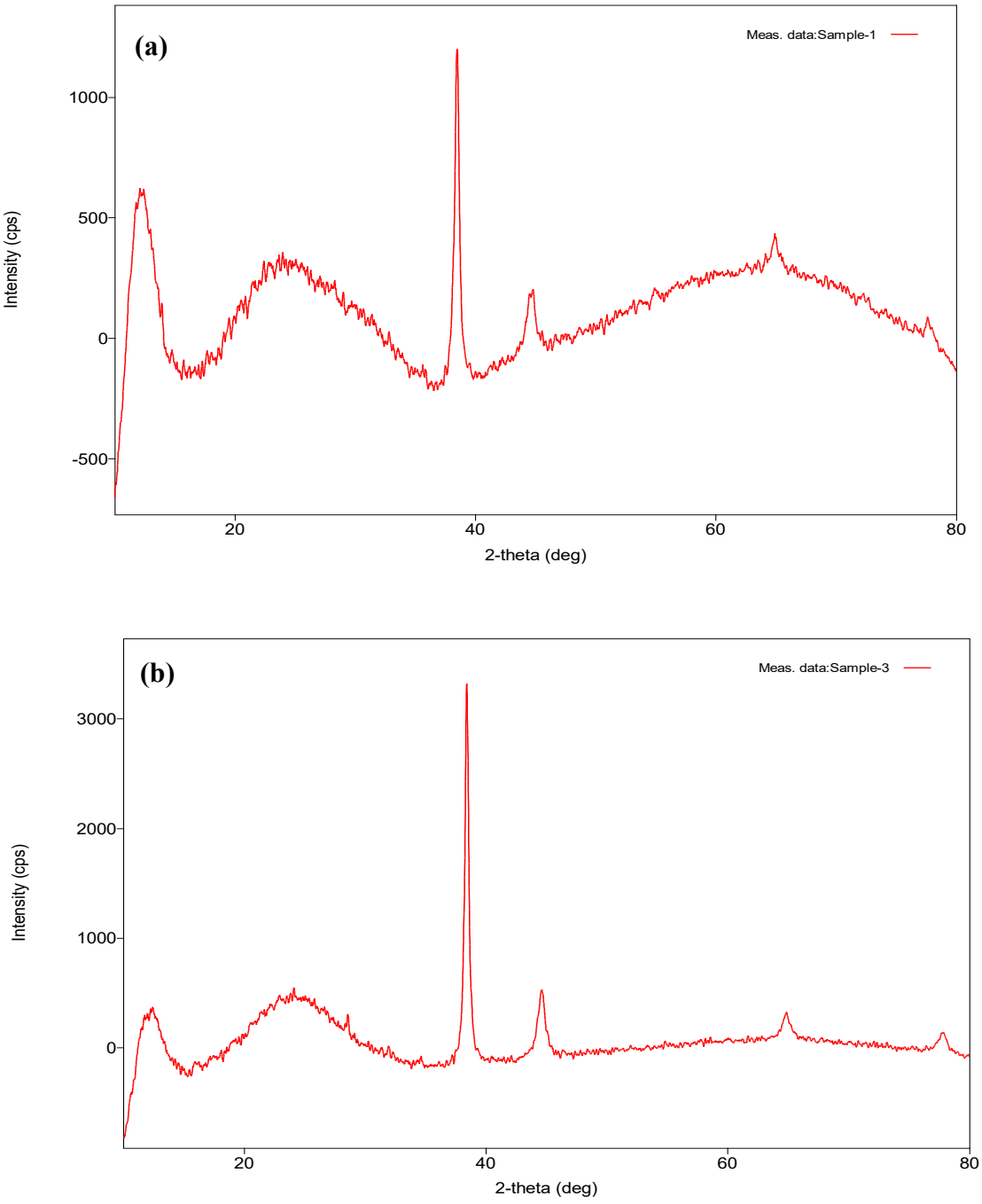

Figure 6-11: Indexed XRD pattern of gold synthesized in 1mm thick samples. (a) 10:1 as-prepared. (b) 10:1 heat-treated at 200°C for 30 minutes.

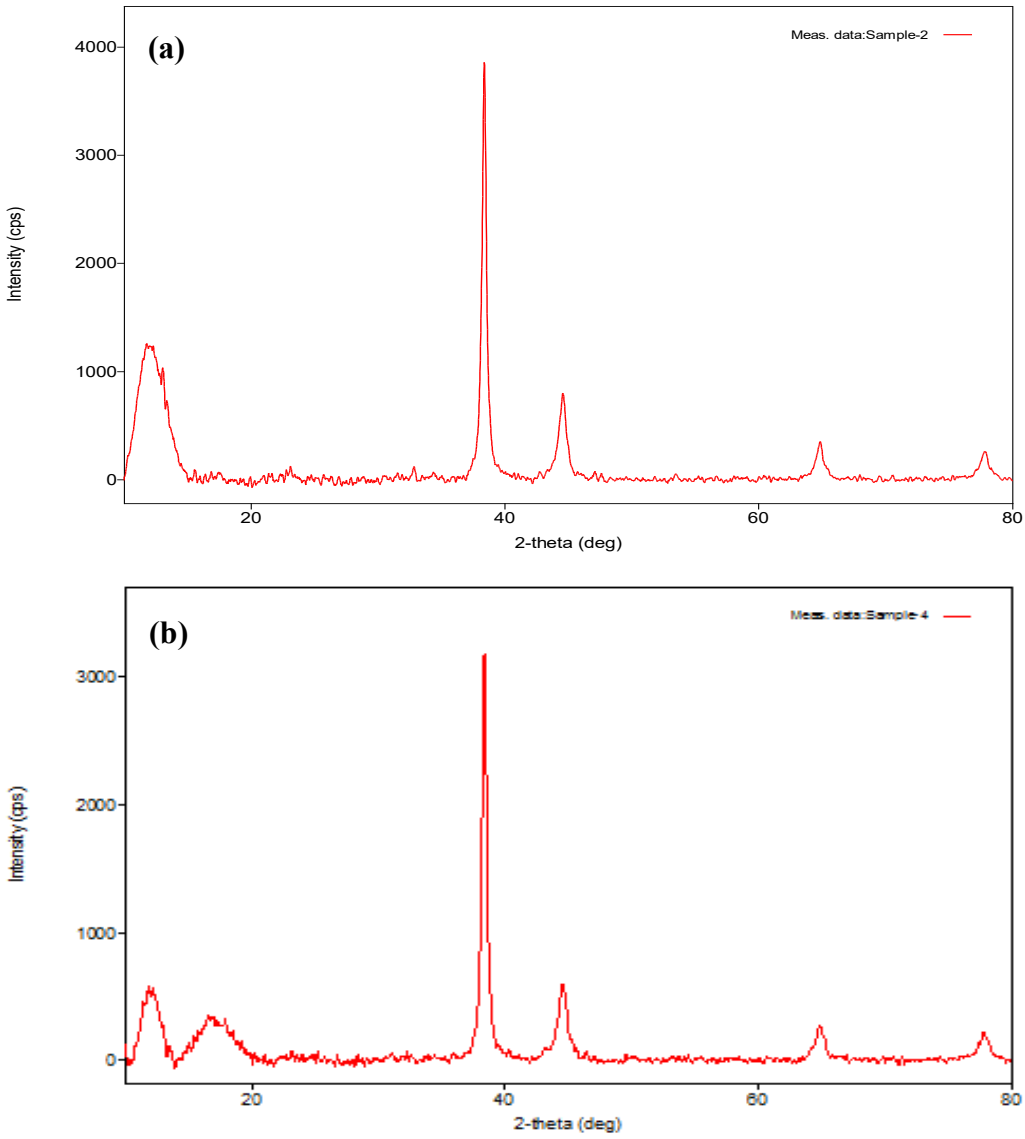

Figure 6-12: Indexed XRD pattern of gold synthesized in 1mm thick samples. (a) 4:1 as-prepared. (b) 4:1 heat-treated at 200°C for 30 minutes.

The surface free energy associated with a particle is:

$$F_s = A\,\gamma_1 \qquad \textit{6.3}$$

Where γ_1 is the surface tension of the particle and A is its surface area

When the particle is embedded, the surface free energy change will be:

$$\Delta F_s = A\,(\gamma_{12} - \gamma_1) \qquad \textit{6.4}$$

Where γ_{12} is the interfacial tension and A$\gamma_{12}$is the interfacial free energy

Embedding is favorable, that is, $\Delta Fs < 0$ when the surface tension of the particle is larger than the interfacial free energy so that the sinking process is energetically favorable.

The interfacial tension (γ_{12}) between PDMS and the gold nanoparticles has been reported to be around 4.0 mN/m [222]. In comparison, the surface tension of AuNPs (γ_1) was calculated to be 8.78 N/m [223] and γ_1= 6.3 N/m for AuNP in a polymer matrix [224]. According to these data, the interfacial tension is inferior to the surface tension of the gold nanoparticles (weak Au-PDMS interactions) and, consequently, the thermodynamic criterion for sinking is fulfilled.

6.5. Conclusion

The distribution of *in-situ* prepared AuNPs on the surface of PDMS self-standing films has been investigated by SEM, AFM, XRD, XPS, and UV-visible spectroscopy. It was found that nanoparticles are formed by the *in-situ* reduction of gold ions on the surface of the film by the curing (crosslinking) agent and, right after formation, they are segregated in the sub-surface layer of PDMS, and only a few nanoparticles in the depth. The pattern of distribution at room temperature and after heat treatment at 200°C was studied concerning the amount of the curing agent in the PDMS composition. It is inferred that in thin self-standing PDMS films, the excess curing agent migrates toward the interfaces with the atmosphere and reduces the incoming gold ions. The influence of the amount and distribution of AuNPs in PDMS on the refractive index sensitivity of the nanocomposite platform is discussed. The results show that the sensing capability of Au-PDMS surface nanocomposite film is low due to the polymer layer covering the AuNPs. The formation of the sub-surface structure in a thin self-standing nanocomposite film is accounted for by the weak Au-PDMS interfacial interactions, permitting the gold to sink under the surface and embed in the polymer.

6.6. Evaluation of the tested plasmonic platforms for future perspectives

The platforms tested in the first part of this work, that is, gold nano-islands, fabricated from a colloidal solution (*ex-situ* method), and gold-PDMS nanocomposite as well as silver-PDMS, fabricated through an *in-situ* method have not shown a high refractive index sensitivity for analytical purposes. However, the sensitivity of the gold nano-islands fabricated on glass by an *ex-situ* method has proved to be considerably higher than the sensitivity of the gold (Au) and silver (Ag) nanocomposite platforms prepared by an *in-situ* method. The reason(s) for this behavior have

been accounted for by the sub-layer segregation of gold in the nanocomposite, making the gold inaccessible for sensing purposes. The redistribution of gold by a subsequent heat treatment further lowered the sensitivity of the Au-PDMS nanocomposite. These results, however interesting and useful for different purposes, do not completely answer the problem of developing a highly sensitive detection method for EVs in varying environments. For this reason, it was found necessary to orient the work in another direction, that is, using physical vapor deposition methods for the deposition of gold.

So, the next chapter (Chapter 7) discusses one of the possible applications to use the LSPR of the silver (Ag)-PDMS nano-composite platform suitable for the detection of extracellular vesicles (EVs) and which could be potentially used for sensor networks. This work is an attempt to adapt a biosensing method to the future requirements of Industry 4.0.

Chapter 7. LSPR detection of extracellular vesicles using a silver-PDMS nano-composite platform suitable for sensor networks

This chapter is reproduced from the article published in *Enterprise Information Systems*, 14, 4, 532–541, 2020.

7.1. Outline

A novel method for the detection of exosomes in body fluids and cell cultures has been developed. The method is an optical method, based on LSPR of silver nanoparticles. The method was extended to a microfluidic environment, amenable to be integrated into a sensor network. However, their isolation, detection, and quantification methods in bio-fluids are challenging for clinical applications. Herein, we present a simple label-free method based on the LSPR technique to capture and detect the EVs quantitatively using a synthetic peptide, called Vn96. This work is an attempt to adapt a biosensing method to the future requirements of Industry 4.0.

7.2. Introduction

Industry 4.0 enables sensors actuators, and control systems to interact with one another through a data infrastructure such as the Internet. The convergence of industrial systems with the power of advanced computing, low-cost sensing, and high levels of connectivity permitted by the internet, is making Industry 4.0 the next great step in industrial advancement. The concept of networking and data storage is infiltrating areas such as sensors, which are now on the front line of the fourth industrial revolution, and they must advance further to make Industry 4.0 effective. Advances in chip technology have made the sensors themselves smarter as they become both the data collectors and analysts that share, in real-time, their knowledge through IO-Link.

Sensors are devices that detect physical, chemical, and biological signals that can be measured and recorded. In healthcare, sensors can monitor temperatures, pressures, chemical, and biological levels of users and/or patients. Thanks to digitalization electronics, conventional chemical, and physical sensors are now ready for Industry 4.0 and underline the need for better quality and quantity of data, intelligently communicated by using the power of IO-Link communication protocol. This is a universal, point-to-point open communication system that

links sensors and actuators, an interface between the control system and the sensors or actuators. Sensor data is provided on a serial communication channel and the monitoring and adjusting of the sensor itself is possible. Remote configuration and monitoring and increased data availability allow sensors and actuators to carry out additional functions such as, for example, remote monitoring.

Medical applications are rapidly coming to the forefront, by combining communications and sensor output to deliver new functions. Devices can gather and share information and the cloud so that data can be collected and analyzed accurately.

In the future, the global system of medical devices will comprise a multitude of devices and applications using sensors, actuators, microcontrollers, mobile communication devices, and healthcare will be delivered more effectively and at lower cost. It will include not only the collection of patient data for preventive care but also diagnostics and treatment results. Automation and real-time aspects will reduce errors and improve quality and efficiency. Today, wireless sensor-based systems gather medical data that were never before accessible and deliver care directly to patients. Healthcare is based now on a network of devices that connect directly with each other to capture and share data through a server in the cloud and then on to caregivers. Data is captured via sensors, and analyzed, and medical professionals can wirelessly access the information and make treatment recommendations. Remote monitoring means that more patients will have access to adequate healthcare. Progress in sensor technology will in this way change the role of hospitals, outpatient sites, and homes. Within the medical world, there is an intersection between information technology and biotechnology, and increasingly the role of sensors, signal transducers, actuators will broaden too. Some examples of new-generation medical sensors indicate new roles that these devices will have in many areas of health care.

In many cases, the quality of care will be improved patients can be managed in their homes and hospitals will operate differently, more safely, and efficiently. Low-cost sensing, and new levels of connectivity enabled through the Internet. Some of the technologies supporting this revolution are cloud services, big data analytics, and, intelligent, sensing technologies.

Over the last few years, continuous efforts have been made by researchers to develop integrated point-of-care (POC) biosensor networks, capable of automatically delivering results. Biosensor networks are generally a multidisciplinary technological work, based on Biological

Micro Electromechanical Systems (BioMEMS). This field seems to be gaining momentum for biosensing applications to meet the requirements of ultra-fast label-free detection, shrunken sensor size, and portability.

To meet the needs of the biosensor market, currently, researchers in BioMEMS field across the world are focusing on the development of complete lab-on-a-chip (LOC) devices, taking advantage of laminar flow, low sample volume requirement, reduction in reaction time to achieve high-throughput and low cost.

Therefore, as the health care costs are going up tremendously with the current world population, biosensor networks will provide the platform for patient real-time and remote health monitoring. Offering real-time feedback is achievable with biosensors networks through the wireless links so that the transmission of collected clinical data can be transferred to the health care provider and medical station. Thus, the medical needs of the future can be met by using a combination of wireless MEMS and biosensor networks as shown in Figure 7-1.

In the last couple of years, active research has been going on to develop biosensor networks, using noble metal nanocomposites. Metal nanocomposites can be customized for many applications such as biosensing, diagnosis, imaging, etc. by tuning the size and shape of the formed nanoparticles. The use of polymers for the fabrication of nanocomposite is growing rapidly since the polymers have good optical and mechanical properties, cost effectiveness, and they are, generally, biocompatible. When compared to other polymers, poly (dimethyl siloxane) (PDMS) proved to be one of the best polymers for the fabrication of gold and silver nanocomposites [225] due to the ease of fabrication, low cost, elasticity, moldability, chemical inertness, optical transparency, and bio-compatibility. In addition, it has a low glass transition temperature. Silver (gold)-PDMS nanocomposites are useful materials with interesting optical properties and applications as sensing platforms.

All biological fluids, including urine, blood, ascites, and cerebrospinal fluid fractions of body fluids such as serum and plasma, as well as cultured medium of cells have in their composition cell-derived vesicles (EVs). They are heterogenic, mostly spherical particles and are enclosed by a phospholipid bilayer. The typical diameter of these vesicles ranges from 30 nm to 1μm, which is about a hundred times smaller than the smallest cell [4–6,226]. EVs are formed by budding and the subsequent splitting of the plasma membrane through an endocytic

pathway and are generated when the cells undergo apoptosis. Their density ranges between 1.1 and 1.19 g/ml on sucrose gradients [227]. Currently, very few techniques are in practice for the isolation, purification, and characterization of EVs. Thus, a versatile, easy-to-use technique is required to quantify and characterize EVs for further diagnosis at the clinical level.

Figure 7-1: Biosensing network for healthcare, providing diagnosis results in multiple places where they are needed.

7.3. Experimental

7.3.1. Material

Sylgard® 184 elastomer kit and curing agent for the PDMS fabrication were purchased from Dow Corning, Silver nitrate, 11-mercaptoundecanoic acid (Nano Thinks Acid 11), phosphate buffered saline (PBS), N-(3-dimethylaminopropyl)-N'-ethyl carbodiimide hydrochloride (EDC) and N-hydroxy succinimide (NHS) were obtained from Sigma- Aldrich, Canada. De-ionized (DI) water with a resistivity of 18MΩ, used in all the experiments is obtained by using the NANO pure ultrapure water system (Barnstead). Streptavidin was purchased from IBA GmBH and Biotin-PEG-Vn96 and MCF10A exosomes were obtained from Atlantic Cancer Research Institute (ACRI), Moncton, Canada.

7.3.2. Fabrication of Silver -PDMS Nanocomposite

The nanocomposite is formed by *in-situ* synthesis of silver (Ag) in the polydimethylsiloxane (PDMS) matrix by the reduction of silver ions from the silver nitrate aqueous solution. The *in-situ* reaction is performed by keeping in an oven between temperatures 50 °C to 60 °C to increase the rate of the reaction [218]. The curing agent present in the PDMS matrix is found to be a good reducing agent of Ag ions. Thus, the PDMS substrate embedded with silver nanoparticles (yellowish-brown) has good structural properties, important for future microfluidic applications. In addition, PDMS has excellent optical properties such as transparency in UV and visible light thus making it, an ideal candidate for the fabrication of optical Lab-on-chip (LOC). The fabrication of nanocomposites involves the preparation of silver precursor solution by adding 1g of silver nitrate in 100ml of DI water. Before this, the PDMS base (pre-polymer) and curing agent are mixed in a ratio of 3:1 by weight. The PDMS mixture was placed in a vacuum desiccator and degassed to remove the air bubbles. Then, PDMS was spun on a glass substrate of dimensions (25 mm × 25 mm × 1 mm) using a LAUREL spin coating machine to obtain a film thickness of 10 µm. The uniformly spread PDMS was cured at 70 °C for about 2 hours. Then, the glass substrate with the cured PDMS is immersed in the silver precursor solution and kept in the oven between temperatures 50 °C to 60°C for about two days. The silver nanocomposite is annealed at 250 °C for 10 minutes. The sensing process is then carried out as shown in Figure 7-2. The detection of exosomes is based on their affinity interaction with biotin-polyethylene glycol (PEG) Vn96.

7.3.3. Sensing Protocol

To carry out the sensing protocol, the substrate is first immersed completely in the linker solution, which is 5mM Nano Thinks (11-mercaptoundecanoic acid in ethanol) that forms the self-assembled monolayers (SAMs) around Ag nano-islands. SAMs are activated by adding a cross-linker solution and incubating for 3 hours. The cross-linker is N-(3-dimethylaminopropyl)-N'-ethyl carbodiimide hydrochloride (EDC) of 0.2M concentration and N-hydroxy succinimide (NHS) of 0.05M concentration, mixed in the ratio of 1:1. After incubation, a streptavidin solution (0.1mg/ml) is deposited on top of the activated linker layer and incubated for an hour. Further, the biotin-PEG-Vn96 solution is deposited on top of the streptavidin layer and incubated for 4 hours. As the final step of the bio-sensing protocol, the

MCF-7A exosomes solution is deposited onto the top of Vn96, a synthetic peptide that is specifically designed to capture them.

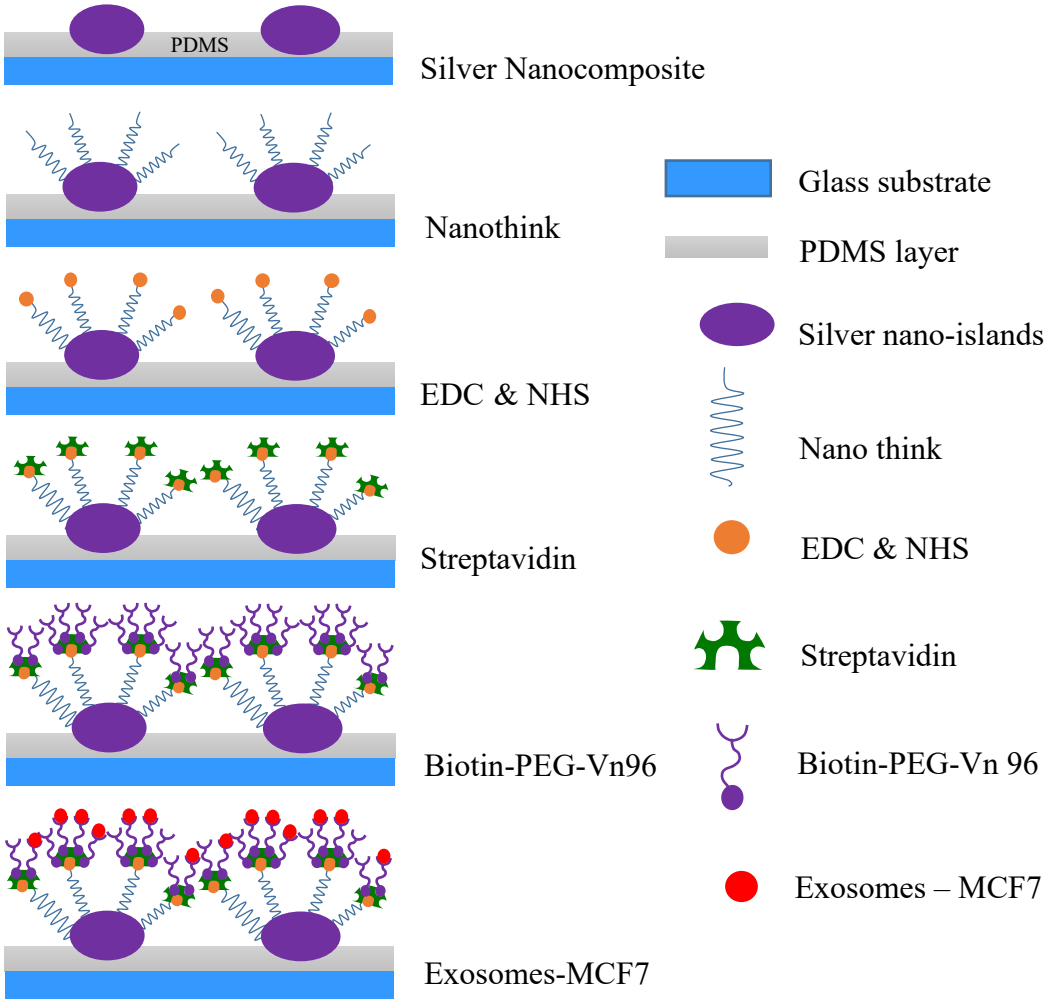

Figure 7-2: Schematic representation of the steps involved in the biosensing protocol of silver nanocomposite

7.4. Results and Discussion

7.4.1. Morphological tuning of Ag nanoparticles

The substrates appear to be transparent, before synthesis as seen in Figure 7-3 (a), and light yellowish-brown, after the *in-situ* synthesis as seen in Figure 7-3 (b). The substrates were annealed at 250 °C, for 10 minutes to tune the morphology of the silver aggregates to nano-islands [228,229]. Scanning electron microscope (SEM) images for the silver nanocomposite, before and after annealing, are shown in Figure 7-4. From the SEM images, it is noticeable that before annealing, the nanoparticles are aggregated, whereas the annealed samples show well-

distributed individual particles/islands in the range of 80 - 100 nm. The morphology of the Ag nanoparticles is tuned during the process of annealing. Annealing will change the aggregates to nano-islands well-distributed in PDMS. They are known as highly sensitive entities [165,228]. The absorption band of the Ag nanocomposite, before and after annealing, is shown in Figure 7-5. It can be seen that the broad band of the Ag-LSPR peak is converted to a narrow band through the annealing process, indicating the presence of individual Ag particles/nano-islands. Therefore, this narrow band is much more suitable for sensing purposes and the spectral shifts due to the binding of molecules can be observed more precisely than in the case of a broad band.

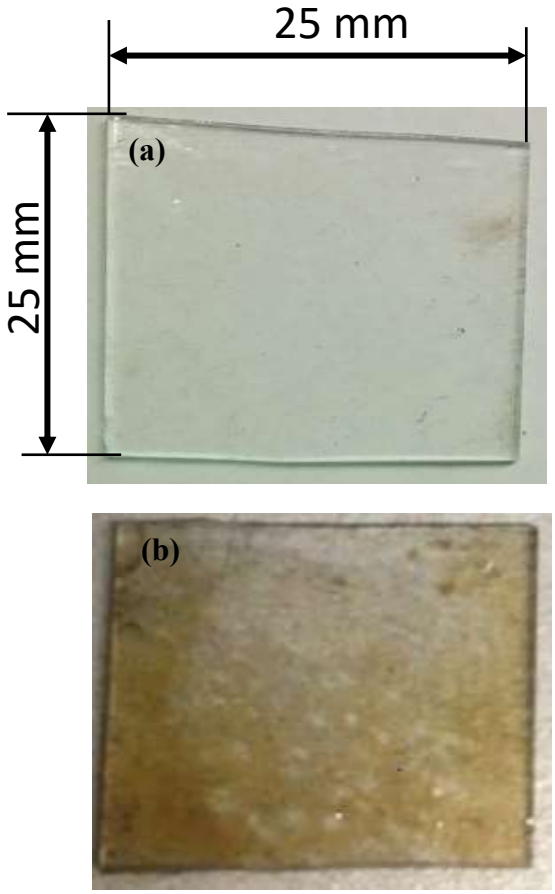

Figure 7-3: Photo of the samples. (a) Before the synthesis. (b) After the *in-situ* synthesis.

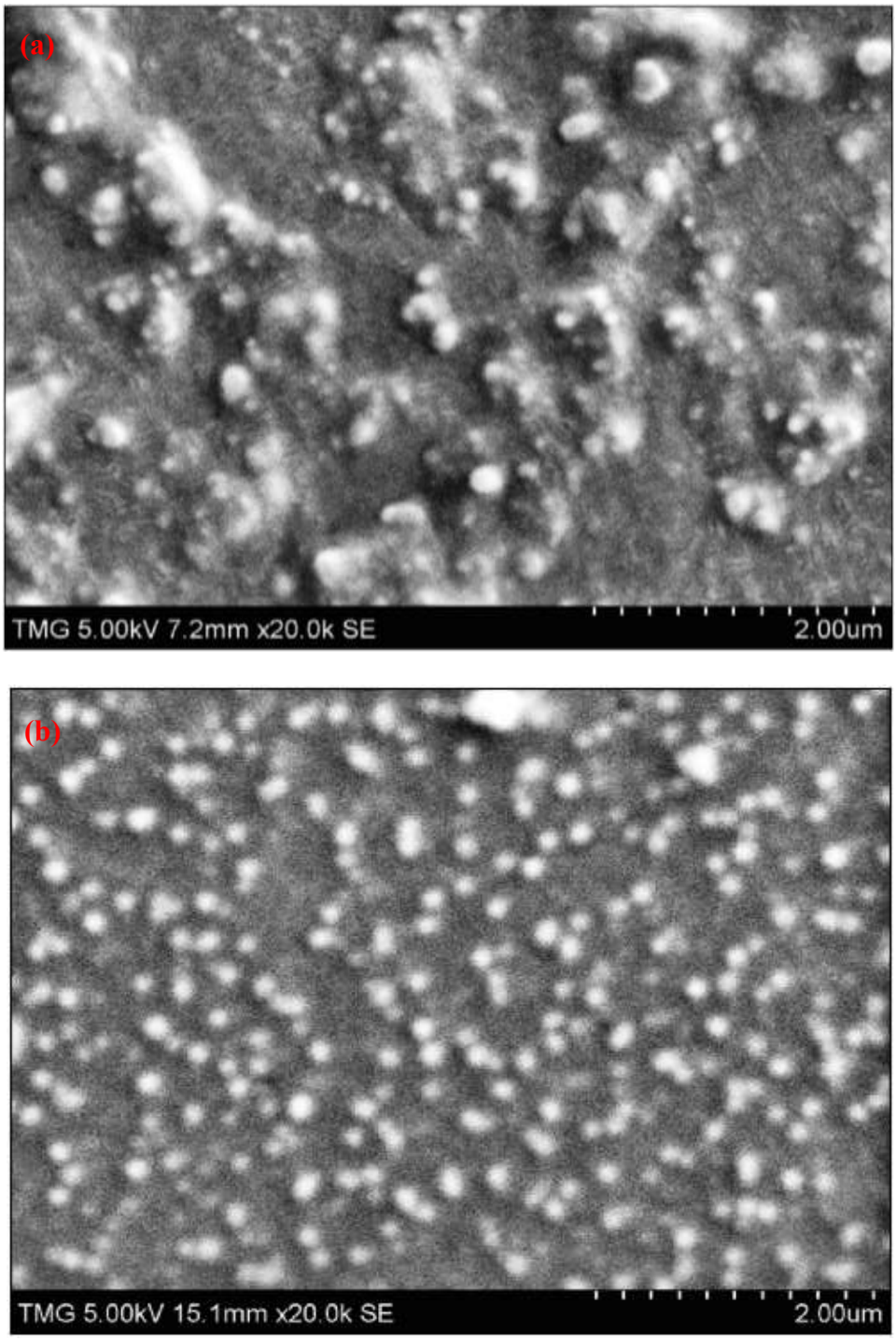

Figure 7-4: SEM images. (a) Silver (Ag) nanocomposite before annealing (aggregates). (b) Silver (Ag) nanocomposite after annealing at 250 °C for 10 min (distributed).

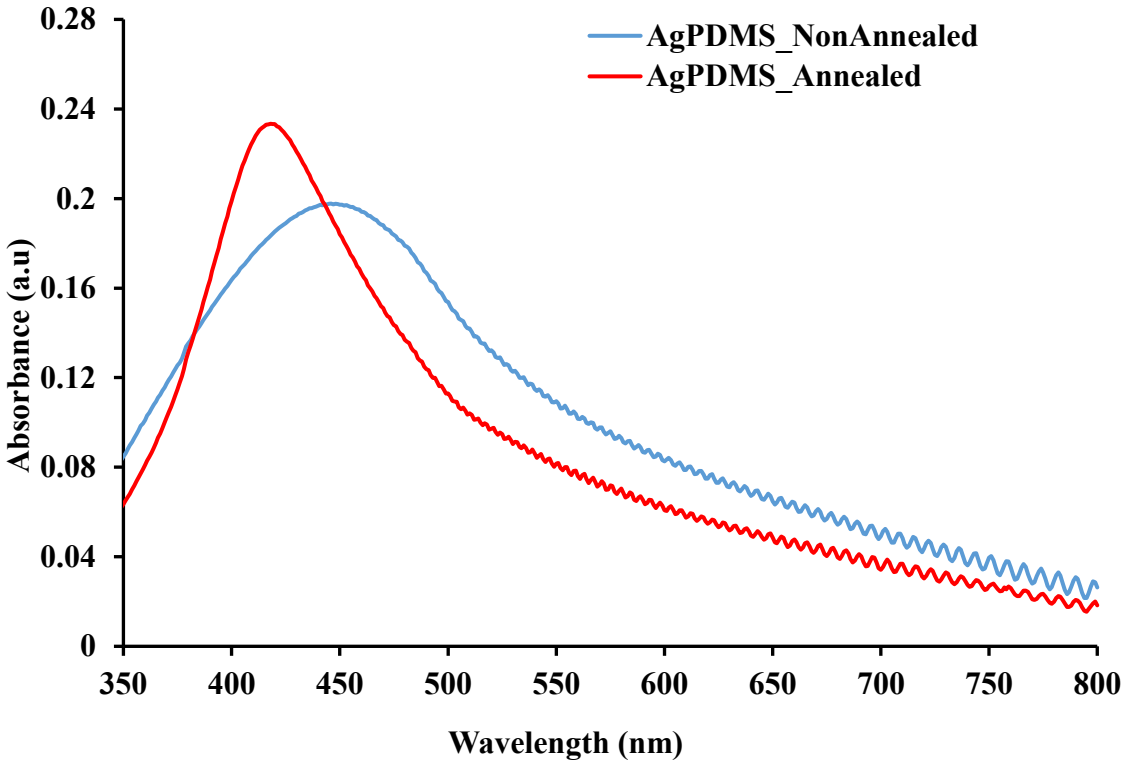

Figure 7-5: Ag-LSPR absorption spectra of non-annealed and annealed Ag nanocomposite.

7.4.2. Characterization of Exosomes

The characterization of the MCF- 7 exosomes is done in an SEM as shown in and from the micrograph, it is noticeable that the typical diameter is of the order of 120 – 150 nm which is within the range of the sizes of exosomes reported in the literature [4].

7.4.3. Detection of Exosomes

The absorbance band of silver is recorded at each stage of the biosensing protocol, using the UV-visible spectrophotometer (PerkinElmer lambda 650). The measured Ag-LSPR band at each stage is plotted and the shift is measured upon the interaction of Biotin-PEG-Vn96 and the diluted MCF-7A exosomes from the stock solution as shown in Figure 7-7. From this figure, it is noticeable that the shifts of the Ag-LSPR band all along the sensing protocols are larger for the first steps and decrease for the last steps. This may be due to the thickness of the layers formed around the silver nanoparticles. For detection purposes, only the shift in wavelength due to the binding of Biotin-PEG-Vn96 and the MCF-7A exosomes is considered and which is around 4 nm as shown in Figure 7-7.

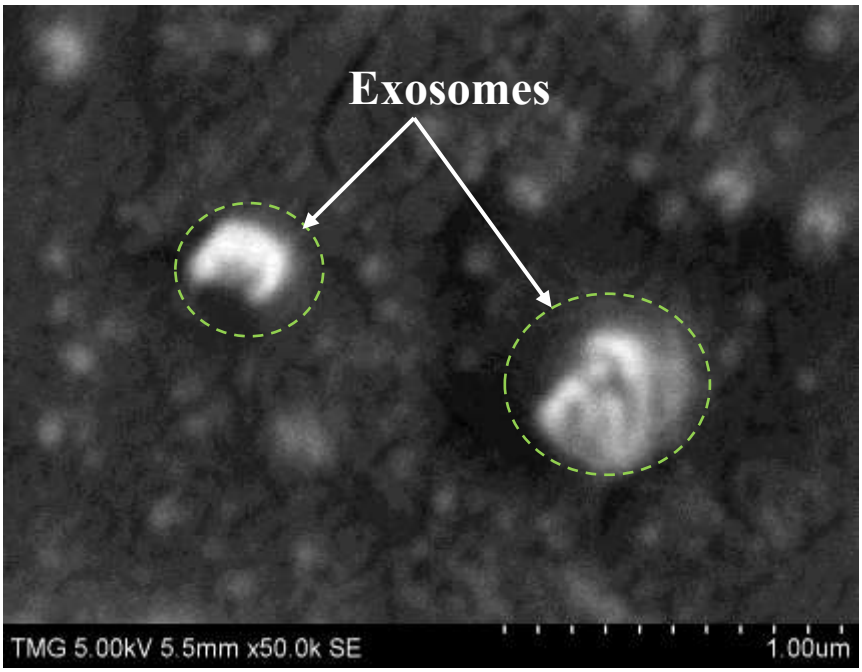

Figure 7-6: Figure 7.6: SEM image of MCF-7A exosomes

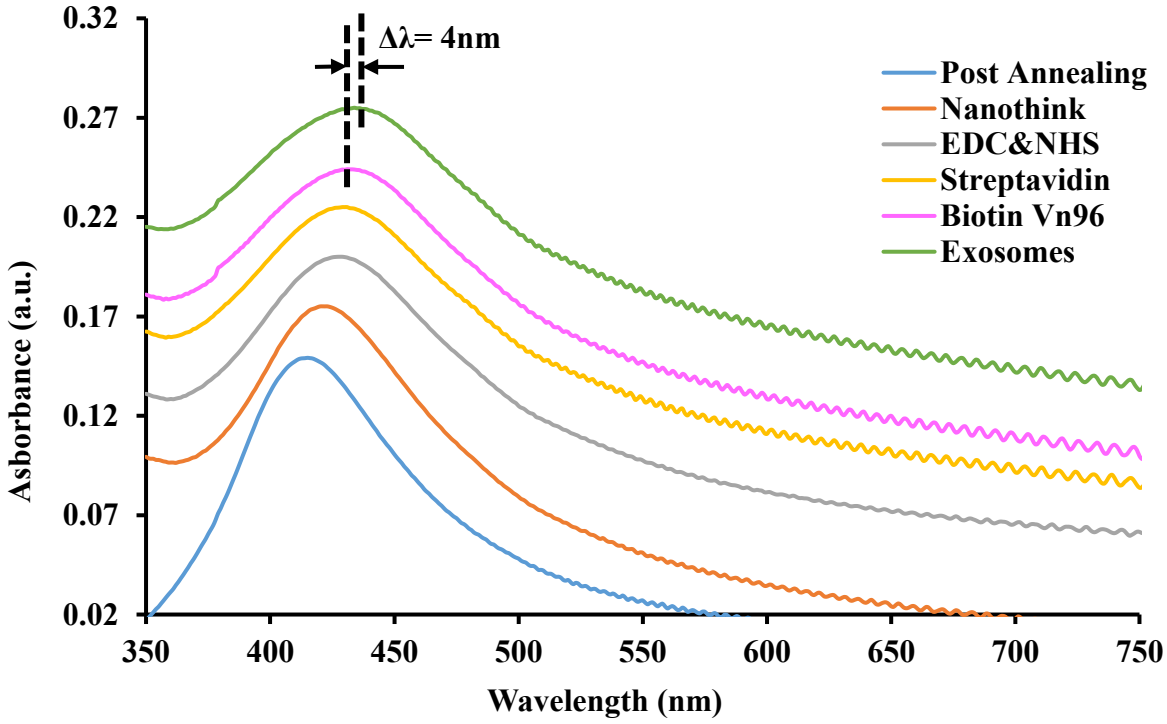

Figure 7-7: Ag-LSPR absorbance spectra showing the LSPR shift corresponding to the different steps of the biosensing protocol.

The next step is the transfer of the sensing protocol to a microfluidic environment. The

device as shown in Figure 7-8 is composed of PDMS polymer with an embedded channel, an inlet, and an outlet tube, respectively. Typically, the channel is 500 µm wide, its depth is 200 µm, and the collection chamber has a diameter of 5 mm. This diameter is considered relatively large, so that the fluid covers the entire region with considerably low velocity, enabling the binding of the compounds flowing in the channel to the gold nano-islands.

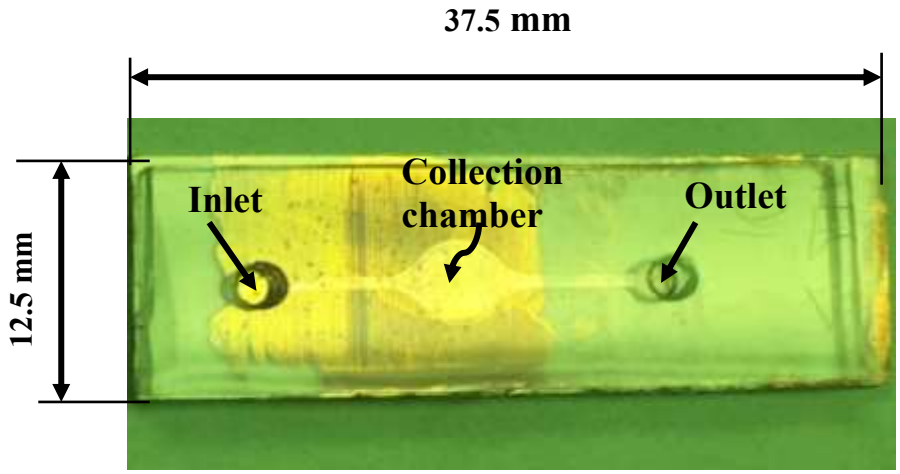

Figure 7-8: Nano-integrated microsystem for bio-sensing.

Devices with more channels have also been developed and tested. In the final stage of the work, several microfluidic devices will be connected to form a network. Microfluidic devices need only very small amounts of samples and reagents and the overall analysis time is much shorter than in the case of the `substrate detection method. Due to the continuous process, the devices can be connected easily and integrated into a network and the results can be analyzed and transmitted to the interested parties. This process will take only a short time and the accuracy of the results will be higher than those of a discontinuous detection.

7.5. Conclusion

A new method to detect exosomes in cell cultures has been developed, first in a discontinuous manner and later on in a microfluidic environment that is directly amenable to be integrated into a network of sensors. The preliminary results showed that a label-free technique, based on the sensitivity of the Ag-LSPR band to the surrounding environment, is promising for the detection of exosomes. Instead of an immune affinity approach, this work makes use of the affinity of exosomes toward the Vn96 polypeptide. As the shift of the Ag-LSPR band is proportional to the concentration of exosomes, the method can be used for their detection in

varying environments. This method, once completely optimized, can be easily performed in a microfluidic environment as well. By integrating the microfluidic sensor into a network, the results of the analysis will be widely distributed. This work is an attempt to bring a plasmonic biosensing method to a superior level, in line with Industry 4.0's requirements.

So, the next chapter (Chapter 8) discusses the Development of gold nano-island platforms prepared through dewetting of e-beam-deposited films for the detection of extracellular vesicles (EVs).

Chapter 8. Development of Gold Nano-island Platforms Prepared Through Dewetting of e-beam Deposited Films for the Detection of Extracellular Vesicles (EVs)

This chapter is to be submitted to a journal: This chapter covers objective 4 (a-e) of the "Thesis Objective and Scope" in Section 1.5.

8.1. Outline

The platforms tested in the first part of this work, that is, gold nano-islands, that are fabricated from a colloidal solution (*ex-situ* method), and gold-PDMS nanocomposite as well as silver-PDMS nanocomposite, fabricated through *in-situ* method have not shown a refractive index sensitivity high enough for detection of EVs. Therefore, it was necessary to orient the work in a new direction using physical vapor deposition (PVD) methods for the deposition of gold.

The main advantage of PVD methods, such as thermal evaporation, sputtering, and e-beam deposition, is the excellent uniformity of the film. A large area of highly uniform films can be obtained in a relatively short time because a high rate of deposition can be kept constant during deposition. In addition, in the physical methods of deposition, especially, e-beam deposition, it was possible to use adhesion layers between the substrate and the gold film, considerably increasing the stability of the system. For all these reasons, it was decided to investigate the behavior of e-beam-deposited thin gold films, consolidated by the presence of adhesion layers, as starting points for the fabrication of nano-island platforms, intended for the detection of EVs.

8.2. Introduction

Nanostructured noble metallic films deposited on transparent substrates exhibit fascinating optical properties resulting from the interaction of light with the collective oscillations of the conduction electrons located at the metal-dielectric interfaces. This interaction leads to the excitation of localized surface plasmon resonance (LSPR) in the ultraviolet (UV) to visible (Vis) spectral range, which amplifies the local electromagnetic field and enables the manipulation of optical energy at the nanoscale. The plasmonic properties of these materials

depend on several factors such as the size and shape of nanoparticles, their interparticle distance, and the surrounding medium's dielectric properties. Experimental evidence has revealed that the binding of organic or biomolecules to the nanoparticle's surface increases the local refractive index, resulting in a red shift of the LSPR band, allowing for the monitoring of molecular interactions. The spectral response is described by equation 8.1

$$R = m\Delta\eta[1 - exp(-d/l)] \quad \textbf{8.1}$$

where 'R' is the sensor response (shift of the plasmon band or/and change in the absorbance); 'm' is the refractive index sensitivity (RIS) that is, spectral intensity change per refractive index unit (RIU) change; 'Δη' is the change in the refractive index of the surrounding medium due to the binding of the adsorbate, 'd' is the thickness of the adsorbate(dielectric) layer, and 'l' is the plasmon effective decay length.

The field of nanoplasmonic platforms for sensing is an active area of academic research. The recent focus has been on the development of gold nanostructures, specifically nano-islands, for use as plasmonic platforms for label-free sensing applications [103,120,230–233]. Nano-islands are highly stable nanostructures that are created through the thermal dewetting of flat continuous metal films, deposited by physical methods such as thermal or e-beam evaporation and sputtering. This process, known as solid-state dewetting, occurs at temperatures below the melting point of the film, and an ensemble of distinct objects, such as droplets, stripes, and pillars, may form through ruptures on the surface. Nano-islands are formed via hole nucleation and subsequent growth. They are convenient sensing platforms and have been successfully employed in numerous applications [113,234,235].

Gold exhibits a high surface diffusivity and is capable of dewetting to form nano-islands but its chemical inertness results in poor adhesion, which can lead to film delamination and peeling during sensing protocols. To enhance adhesion, 2-10 nm of Cr, Ti, Ni, Pt, or Ge adhesion (seed) or "glue" layers, organic (amino- or mercapto-silane) coupling layers, or polymers can be evaporated on the substrate before depositing the gold film [132,236–239]. Gold is a widely used metal in plasmonic platforms due to its favorable electrical, optical, and chemical properties. Moreover, gold can be easily functionalized owing to its strong bonding with thiol functional groups. However, its chemical inertness results in poor adhesion, which can lead to

film delamination and peeling during sensing protocols in an aqueous environment. The growth of continuous ultra-thin (1.0 -5.0 nm) gold films on bare glass and other oxide substrates using standard deposition methods was challenging due to the poor wetting of gold in these materials. Light absorption by metal and metal oxide adhesion layers can significantly impact the field enhancement and optical interferences, making it difficult to measure accurately and can decrease the sensitivity of plasmonic systems due to changes in refractive index due to the evanescent field's exponential decay. While research on the impact of adhesion layers on various plasmonic systems is limited, previous studies have found that they cause the plasmon band to shift towards longer wavelengths and significantly reduce its extinction (plasmon damping). Rubinstein's [129] team has developed a highly stable nanostructure, without adhesion layers to address these issues. They achieved this by thermally embedding gold island films in glass or post-coating them with an ultrathin sol-gel-derived silica film. This film has also been recommended as an alternative method to stabilize gold nanostructures on silanized glass [113,240–242].

Ultra-thin films have yet to meet the requirements of creating atomically smooth uniform metal surfaces, essential for contemporary electronic and photonic systems. This was primarily due to the rough surface topography that results from the deposition techniques commonly employed, including thermal or e-beam evaporation, ion-beam-assisted deposition, and RF/DC sputtering, as confirmed by AFM measurements. These rough surfaces cause scattering loss and are not appropriate for manufacturing plasmonic circuits and devices that manipulate optical information [243,244]. One of the key reasons for this issue was the empirical approach taken when selecting adhesion layers. Only a few adhesion layers used with ultra-thin films have been evaluated, specifically for sensing applications. Metallic adhesion layers may diffuse both in the substrate and the gold film, with the formations of inter-metallic compounds or alloys. This may happen during the fabrication or/and post-fabrication annealing, chromium, one of the most used adhesion layers, may also be oxidized at high annealing temperatures, inducing an additional interface plasmon damping. Even though it has excellent transparency and very high conductivity, there are only very few studies on Indium Tin Oxide (ITO) and fluorine-doped tin oxide (FTO) as substrates for gold nano-islands (not adhesion layers) as well as ITO/Au/ITO sandwich structures [125,131,245,246].

The objective of the current study is to develop two novel platforms utilizing the nano-islands that are obtained from dewetting ultra-thin gold films for biosensing applications. These platforms comprise borosilicate substrates, with a 1.5 nm adhesion layer of Indium Tin Oxide (ITO) or Chromium (Cr), and a 2 nm gold (Au) layer, deposited via e-beam evaporation. The platforms were subjected to varying temperature and duration conditions to create stable and long-lasting nano-island plasmonic platforms for sensing applications. The plasmonic performance of these platforms was compared to those with pure ultra-thin gold layers and no adhesion layers, allowing us to quantify the interface plasmon-damping effects of the adhesion layers. To characterize the platforms, Field Emission Scanning Electron Microscopy (FESEM), Energy Dispersive Spectroscopy (EDS), Atomic Force Microscopy (AFM), and X-Ray Diffraction (XRD) were used to analyze their structure, morphology, and elemental composition. Furthermore, the refractive index sensitivity of both platforms was determined based on the results of the characterization and sensitivity study. An optimal platform was chosen for the quantitative LSPR detection of EVs/exosomes.

Recently Qiu et al. [247] developed an LSPR-based biosensor. They used randomly distributed self-assembled gold nanoislands (SAM-AuNIs), prepared by thermal annealing. The authors used a spectral phase detection LSPR interferometer, a highly sensitive optical biosensing [247–249] instead of using the shift of the plasmon band. In their study, they have reported that the two different tumor-derived EVs; exosomes and Microvesicles (MVs), can be distinguished using SAM-AuNIs LSPR without functionalization with an antibody. In their study, they have reported that the two different tumor-derived EVs; exosomes and Microvesicles (MVs), can be distinguished using SAM-AuNIs LSPR without functionalization with an antibody. Therefore, in our present study with the optimized Cr-Au platform, the shift of the Au-LSPR plasmon band was calculated by directly immobilizing the CCM MCF 7 EVs/exosomes onto the nanoplasmonic platform, without any surface chemistry modification for two different dewetting temperatures. Furthermore, the obtained results were compared with the detection results of our previous method which uses the immunoaffinity approach [98,137].

8.3. Methods and Materials

8.3.1. Principle of Operation of Electron Beam Deposition System

During the electron beam (e-beam) evaporation process, a tungsten filament was first

subjected to current, leading to joule heating and the emission of electrons. A high voltage was then applied between the filament and the hearth to accelerate these emitted electrons toward the crucible containing the material to be deposited, as described in Figure 8-1. A strong magnetic field focuses these electrons into a unified beam, which, upon reaching the crucible, transfers its energy to the deposition material, causing it to evaporate or sublimate and deposit onto the substrate. Introducing reactive gas, such as oxygen or nitrogen, into the chamber during evaporation enables the reactive deposition of non-metallic films.

e-beam evaporation claims several advantages over resistive thermal evaporation. Firstly, the e-beam source can heat materials to significantly higher temperatures than what was achievable using a resistive boat or crucible heater. This facilitates very high deposition rates and the evaporation of high-temperature materials and refractory metals like tungsten, tantalum, or graphite. Secondly, films deposited through electron beam evaporation can better maintain the purity of the source material; water cooling of the crucible confines the electron beam heating solely to the area occupied by the source material, preventing any undesirable contamination from neighboring components.

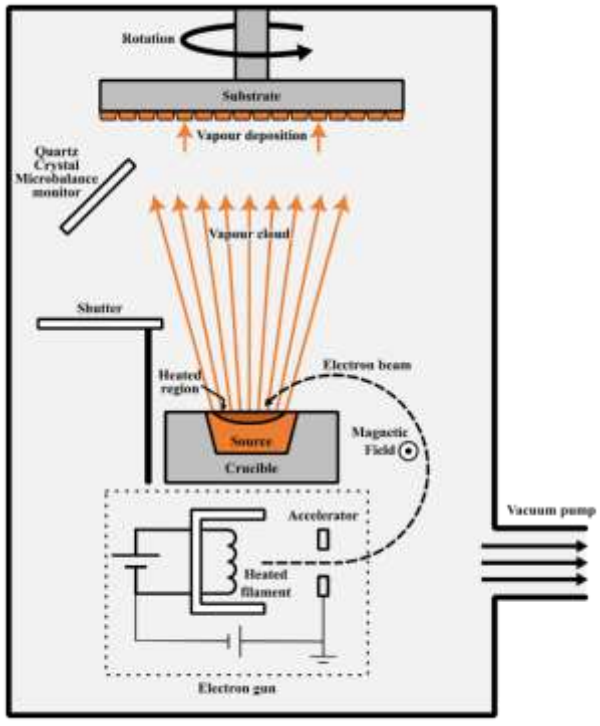

Figure 8-1: Schematic of the e-beam deposition system.

8.3.2. Structure of the Plasmonic Platforms

In the present study, the behaviour of two distinct adhesion layers was investigated, specifically, Cr and ITO onto the substrates before the deposition of the gold layer. Figure 8-2 shows the configuration of the samples. Films of 1.5 nm thickness (Cr or ITO) were deposited on top of the borosilicate glass substrate and then a 2 nm thin film of gold was deposited. These two configurations were, compared with the substrate with the deposition of only 2 nm gold film. Specialized equipment and custom-made deposition samples were required. The deposition was done by Angstrom Engineering, Inc. using a Nebula mixed e-beam evaporation and sputtering system for all the depositions as shown in Figure 8-3.

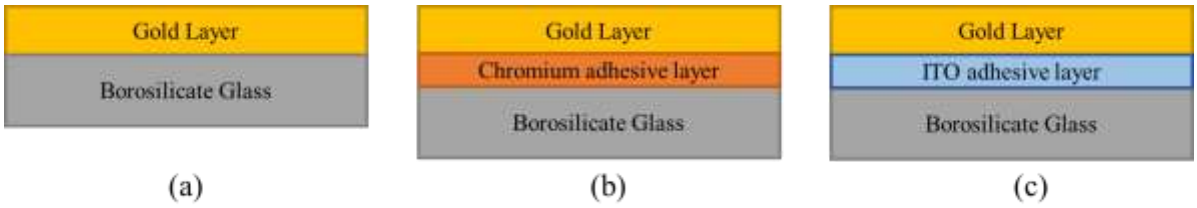

Figure 8-2: The configuration of the substrates. (a) Au layer alone. (b) Cr-Au layer. (c) ITO-Au layer.

8.3.3. Specification of Substrate and Deposition System

A 1 mm thick, 25 × 75 mm Nexterion® borosilicate glass B was used as substrate. The adhesion (Cr or ITO) and gold layers were deposited using electron beam evaporation, a type of physical vapor deposition. In the case of the ITO layer, deposition was carried out using an RF sputtering process. The chromium and gold layers were deposited using an e-beam evaporation process.

The deposition of the layers was carried out on glass slides attached to an 8-inch diameter sample holder. Throughout the deposition process, the thicknesses of deposited layers were monitored using a quartz crystal microbalance (QCM) incorporated into the system.

8.3.4. Pre-treatment Process

As the first step of the deposition process the chamber was set for ion cleaning by keeping the discharge voltage at 300 V, the discharge current at 1 A, the emission current at 1 A, and the ion clean time 300 seconds before depositing either the adhesion layer or the metal layer.

8.3.5. Deposition Process of the Cr and Au on the Substrates

After the completion of the ion cleaning step, the chamber was pumped down keeping the substrate shutter closed, and once the chamber pressure reached 1 x 10^{-6} Torr the substrate shutter will open. Throughout the process of deposition, the substrate was set to a rotation of 10 rpm, such that the layers were uniformly deposited onto the substrate. As mentioned earlier the Cr adhesion layer was deposited using an electron beam evaporation process. For the Cr adhesion layer to get deposited, the target power was set to 240 W. Once the stated target powers reached the substrate, the shutter will be opened and the Cr layer deposited at the rate of 0.2 Å/s until the target thickness of 15 Å attained. Once the adhesion layer was deposited, the Au layer was deposited at the rate of 0.2 Å/s till it reached the target thickness of 20 Å by setting up the target power to 700 W.

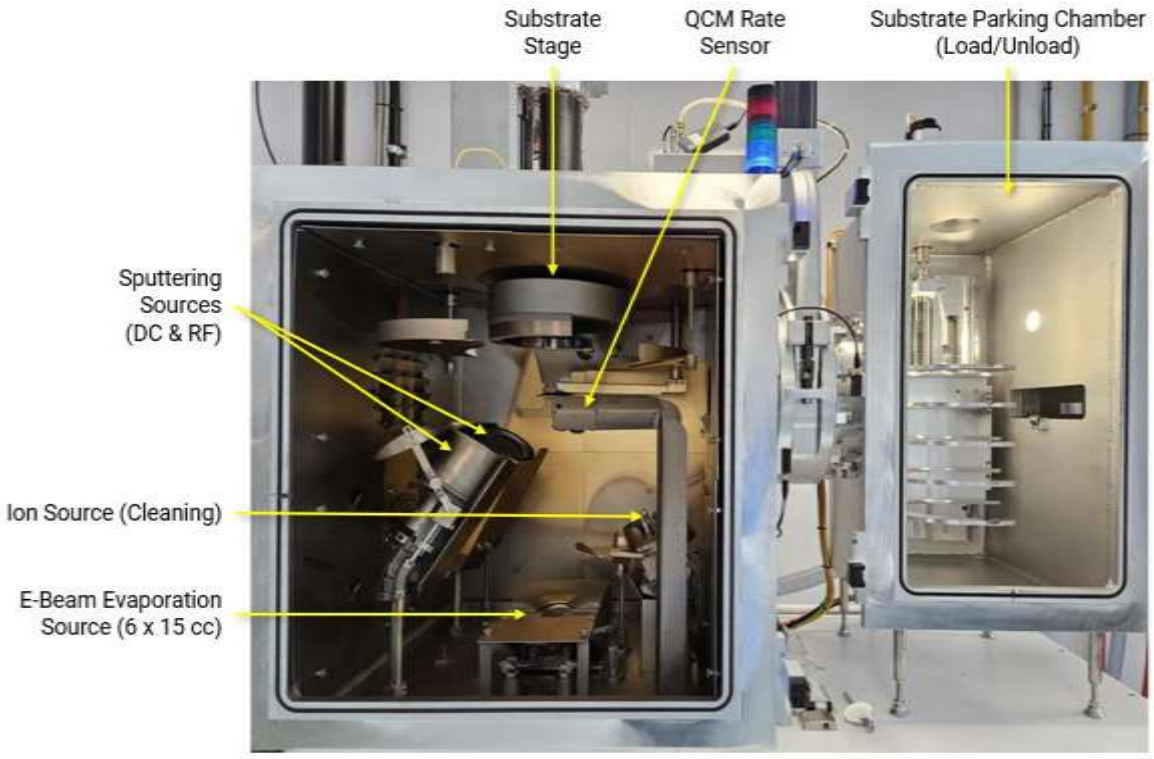

Figure 8-3: Picture of the electron beam evaporation and sputtering system [Picture courtesy Angstrom Engineering Inc].

8.3.6. Deposition Process of the ITO and Au on the Substrates

Once the ion cleaning step was completed the chamber was pumped down keeping the substrate shutter closed and once the chamber pressure reaches 1 x 10^{-6} Torr the substrate shutter

will be opened. During the entire process of deposition, the substrate was set to a rotation of 10rpm so that layers get deposited uniformly onto the substrate. As mentioned earlier the ITO adhesion layer was deposited using a RF sputtering process. Therefore, the Argon and Oxygen gases are flown into the chamber at a rate of 15 sccm and 5 sccm, respectively. The RF power was ramped up to 125 W. Once the mentioned target powers are reached the substrate shutter will be opened and the ITO layer was deposited at the rate of 0.11 Å/s until the target thickness of 15 Å was attained by setting up the target power to 125 W RF for a duration of 140s. Once the ITO layer was deposited the samples were immediately exposed to the electron beam evaporation process which was housed within the same high vacuum chamber to further deposit the layer of Au. The Au layer was deposited at the rate of 0.2 Å/s until it reached the target thickness of 20 Å by setting up the target power to 700 W.

8.3.7. Characterization of the Platforms

The platforms were characterized using UV-Vis spectroscopy, FESEM, EDS, AFM, and XRD. All the LSPR spectral measurements were carried out using the Perkin Elmer lambda 650 UV-Vis spectrophotometer. The SEM images were taken using the Hitachi SU8230 Field Emission Transmission Electron Microscope (FE-STEM) equipped with Oxford Electron Backscatter Diffraction (EBSD) and INCA EDS from the Facility for Electron Microscopy Research, McGill University. The AFM measurements were acquired in ambient conditions using a NanoscopeV- Dimension ICON Atomic force microscope (Bruker, Santa Barbara, CA, USA) from the Laboratoire de Caractérisation des Matériaux-AFM, Département de chimie/Université de Montréal. All images were acquired using the PeakForce Tapping mode (PeakForce QNM®) using RTESP probes (aluminium coated etched silicon probes with tip radius ranging between 5-12 nm and nominal spring constant of 40 N/m. XRD measurements were obtained using the 3rd generation Empyrean, Malvern Panalytical instrument from the Département de Chimie, Université de Montréal. All the measurements were carried out in the grazing angle mode with a fixed Omega angle of 1°. X-ray diffraction works in the 2θ mode with the CuKa radiation at a wavelength of 1.54 Å. Also, the sensitivity of the substrates was measured using various solvents with different refractive indices using the Perkin Elmer lambda 650 UV-Vis spectrophotometer.

8.4. Results and Discussion

8.4.1. Morphology of the as-deposited thin films

The morphology of the as-deposited samples can be seen in the SEM images as shown in Figure 8-4. The images show that the morphology of the as-deposited ultra-thin Au films was different when gold was deposited directly to the glass substrate as compared to the gold that was deposited on top of the adhesion layers, under similar conditions. While on the chromium(Cr) adhesion layer, the gold (Au) layer shows a chain-like morphology as could be seen in the inset image, similar to the ones when using the gold colloidal solutions to form the nano-islands on the glass substrate as previously studied by our group [98,137]. Whereas in the case of the Indium Tin Oxide (ITO) adhesion layer, quite uniformly distributed small nanoparticles of gold (Au) could be seen in the inset image. The different morphologies were attributed to the different physical and chemical properties of the Cr and ITO adhesion layers, in addition to the different deposition processes used.

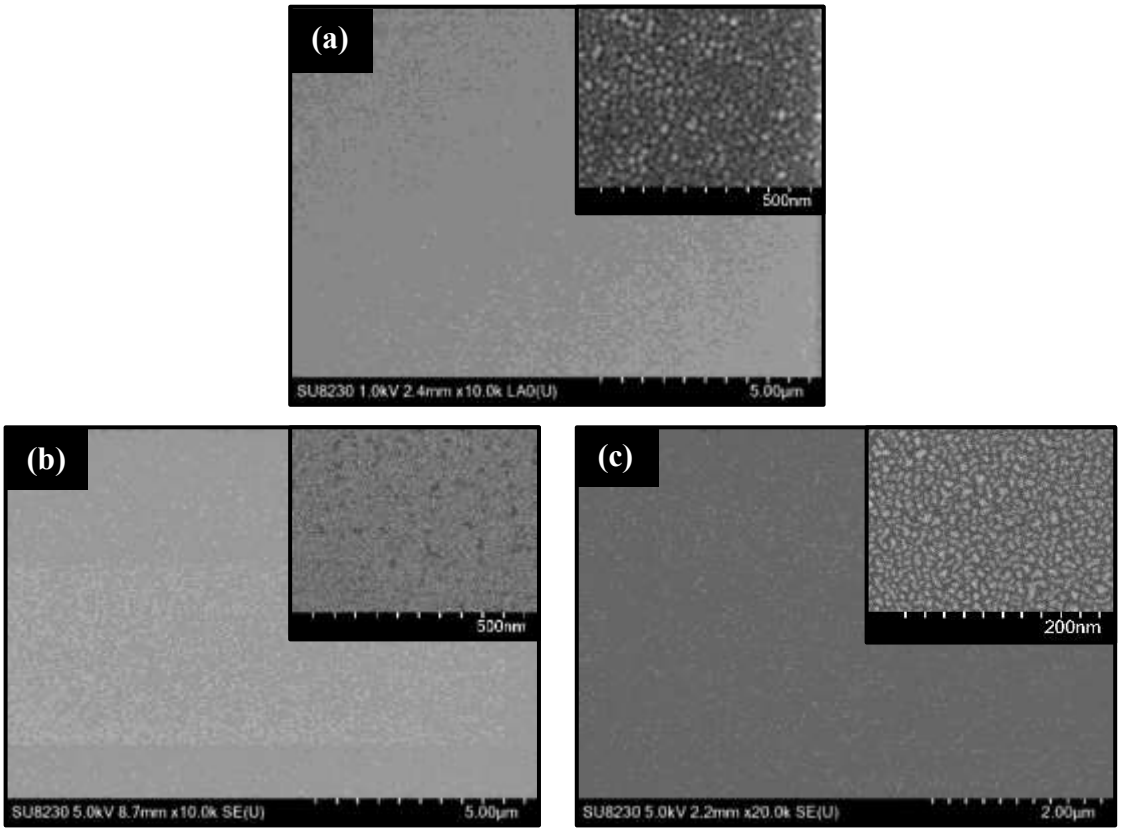

Figure 8-4: SEM Image of non-annealed substrates. (a) Au layer of 2 nm without the adhesion layer. (b) Au layer of 2 nm with Cr adhesion layer of 1.5 nm. (c) Au layer of 2 nm with ITO adhesion layer of 1.5 nm.

8.4.2. Plasmonic Properties of as-deposited thin films

The plasmonic properties of the samples were evaluated using UV-Vis spectroscopy as shown in Figure 8-5. It could be noticed in Figure 8-5 that for the platform with only the Au layer and the platform with the ITO adhesion layer and the gold (Au) layer on top, the Au-LSPR band could be noticed even before annealing. On the other hand, the platform with the Cr adhesion layer and the gold (Au) layer on top of it doesn't show any Au-LSPR band.

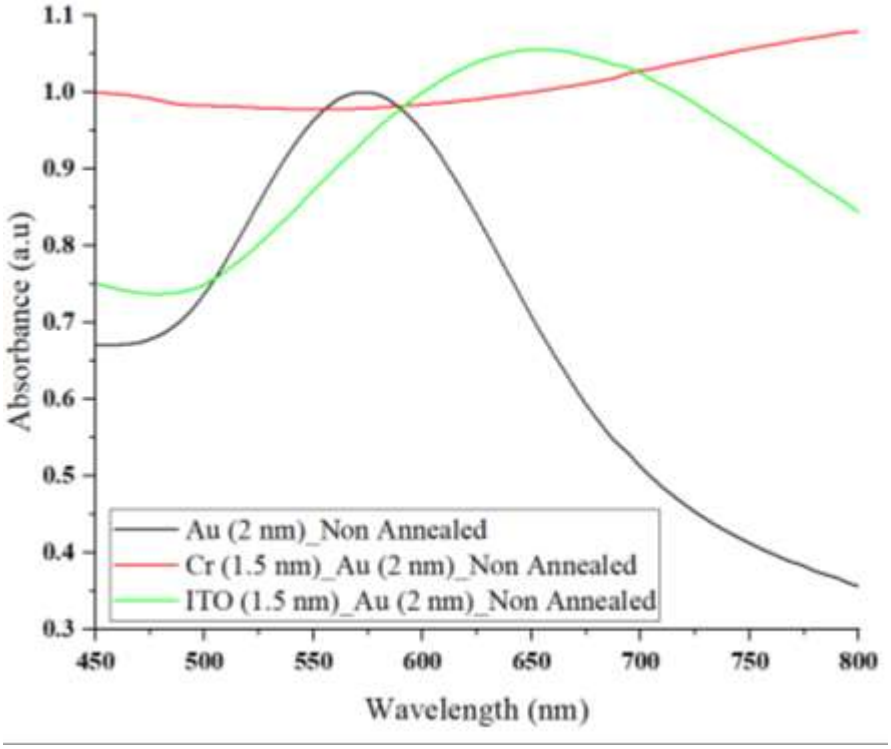

Figure 8-5: Au-LSPR spectral characteristics of the Non-Annealed (as-deposited films) for the Au layer, Cr-Au layer, and ITO-Au layer.

8.4.3. Visual Inspection and Adhesion Quality of the as-deposited thin films

The glass slides for each of the studies in this work were cut to the size of around 12.5 mm x 18 mm from a 1 mm thick, 25 × 75 mm Nexterion® borosilicate glass B. The visual inspection of the as-deposited film for all three configurations is shown in Figure 8-6. From Figure 8-6 (a) it is noticeable for the configuration with only a thin layer of Au (2nm) that the adhesion of the gold is very poor and the Au layer has partly detached while handling the sample, as compared to the other two configurations Figure 8-6 (b) and Figure 8-6 (c). Therefore, the substrates with the Au

layer alone may not be suitable for the sensing application. Thus, the substrates with Cr and ITO adhesion layers were considered for further characterization studies.

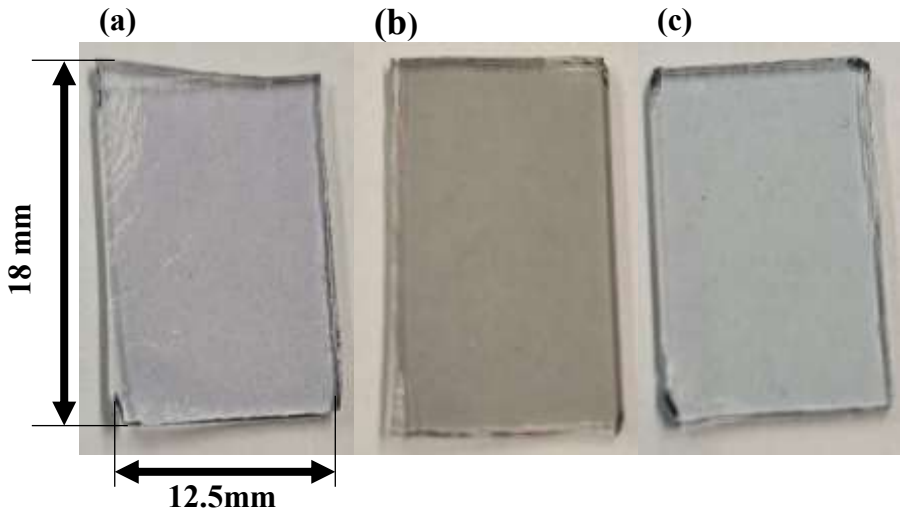

Figure 8-6: Picture of the As-deposited film for all three configurations. (a) Au layer. (b) Cr-Au layer. (c) ITO-Au layer.

8.4.4. Plasmonic Properties of the Cr-Au and ITO-Au Platforms

Gold nano-islands, which are sensitive plasmonic platforms, were produced through the annealing process at different temperatures (250°C to 650°C) and durations (15 minutes, 1 hour, and 5 hours). The plasmonic properties of the samples were evaluated using UV-Vis spectroscopy as shown in Figure 8-7 and their visual characteristics, specifically, their colour transformation could be observed as shown in Figure 8-8.

To properly assess the results of annealing, it was crucial to closely examine the samples for the emergence of nano features and the characteristic plasmon band in the visible spectrum. This can be identified by the pink colour, as seen in Figure 8-8.

The spectra of the lower-temperature annealed samples, conducted at 250 °C and 300 °C did not exhibit any distinct features and were similar to those found in continuous thin films. When the samples were subjected to an hour of annealing at 500 °C, a broad band at 600 nm emerged, which corresponds to the Au-LSPR band. Further increasing the annealing temperature to 550 °C, 600 °C, and 650 °C resulted in a blue shift of the broad Au plasmon band to 580 nm, 560 nm, and 555 nm, respectively, and the narrowing of the bands. The evolution of the spectra of the samples, containing the Cr adhesion layer that was annealed for 1hr for various temperatures is depicted in

Figure 8-9 for a better understanding of the Au plasmon band shift towards the shorter wavelength as the temperature was increased. From Figure 8-9 it can be observed that the nano-islands formation starts at an annealing temperature of 500 °C for the platform with the Cr adhesion layer.

Conversely, annealing does not change the pattern of the Au-LSPR spectrum of the samples with an ITO adhesion layer as shown in Figure 8-10. Additionally, it could be seen that the spectral pattern doesn't change with the increase in temperature of annealing as it does in the case of the substrate with the Cr adhesion layer. This was due to the presence of nanoparticles instead of nano-islands which was noticeable from Figure 8-11 that the pink colour started appearing even when the samples were annealed at, 250 °C for 15min. The evolution of the spectra of the samples, containing the ITO adhesion layer that was annealed for 1hr for various temperatures is shown in Figure 8-12 for a better understanding of the Au plasmon band shift as the temperature was increased. From Figure 8-12 it can be observed that the formation of nanoparticles starts at an annealing temperature of 250 °C for the platform with the ITO adhesion layer.

8.4.5. Calculating the Au-LSPR Peak Wavelength Bandwidth for the Cr-Au & ITO-Au Platforms

Further, to the study of plasmonic properties of both the platforms, it was decided to find out the Au-LSPR peaks bandwidth at 90% ($\lambda\Delta_{90\%}$) of the maximum peak (λ_{max}) for both the platforms for the times and temperatures at which the Au-LSPR peaks can be noticed. For the Cr-Au platform for 15min of annealing time, a well-defined Au-LSPR peak will be noticed starting from 550ºC as seen in Figure 8-7 (e) whereas for 1hr annealing time, a well-defined Au-LSPR peak will be noticed starting from 500ºC as seen in Figure 8-7 (f) and for 5hr annealing time, a well-defined Au-LSPR peak will be noticed starting from 400ºC. as seen in Figure 8-7 (g) However, for the ITO-Au platform, the Au-LSPR peak was noticeable for all the annealing times (15 min, 1hr and 5hr) and temperatures considered for the study (250 °C, 300 °C, 400 °C, 500 °C, 550 °C, 600 °C, 650 °C) as shown in Figure 8-10. The schematics for the calculation of the Au-LSPR peak are shown in Figure 8-13 (a). The plots in Figure 8-13 (b) and Figure 8-13 (c) show the calculated Au-LSPR peak average wavelength bandwidth of 90% of the maximum peak for the Cr-Au and ITO-Au platforms respectively.

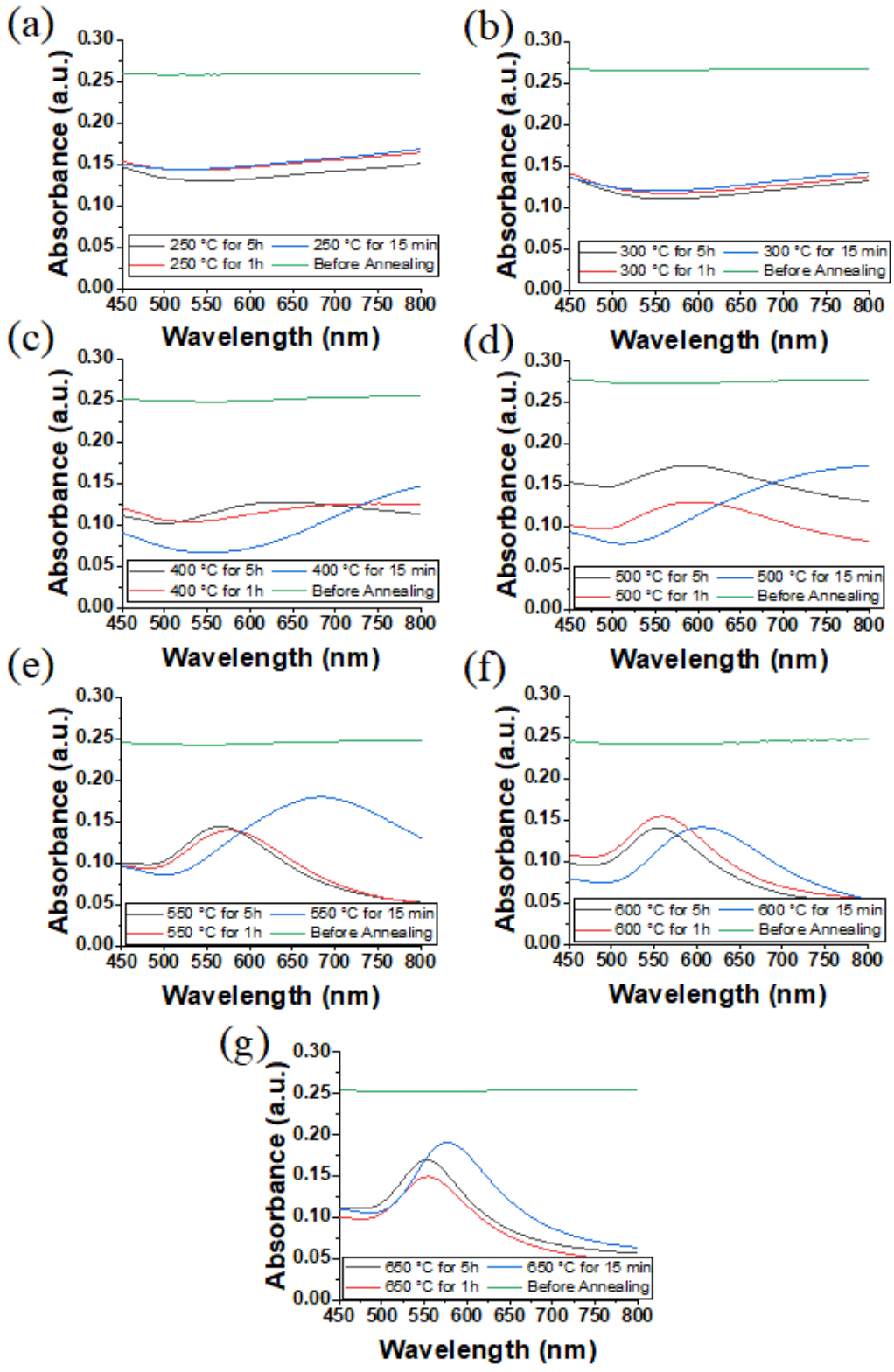

Figure 8-7: Evolution of the Au-LSPR spectral characteristics with different annealing temperatures for the platform with the Cr adhesion layer. (a) 250 °C. (b) 300 °C. (c) 400 °C. (d) 500 °C. (e) 550 °C. (f) 600 °C. (g) 650 °C.

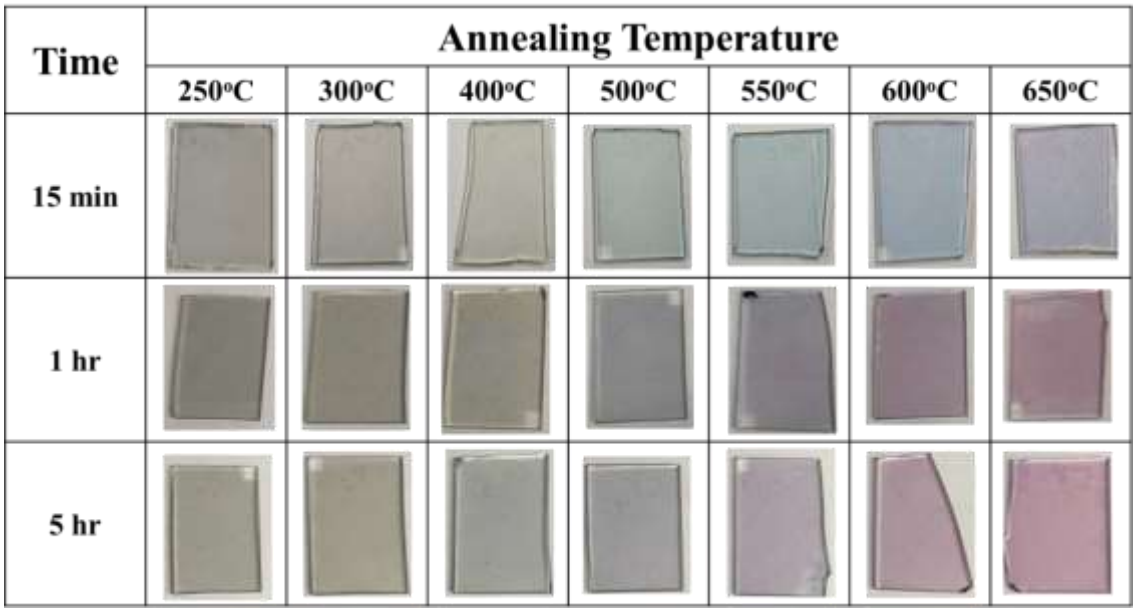

Figure 8-8: Evolution of the color change with the annealing temperature and time for the platform with the Cr adhesion layer.

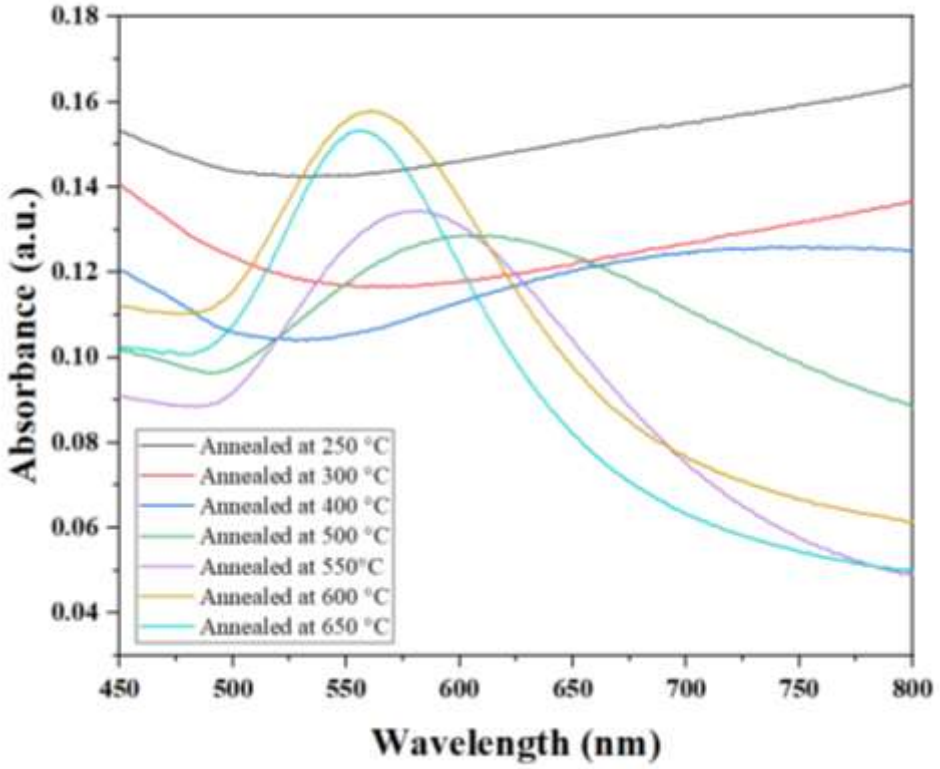

Figure 8-9: Evolution of the Au-LSPR spectral characteristics for the platform with the Cr adhesion layer for the different annealing temperatures annealed at 1hr.

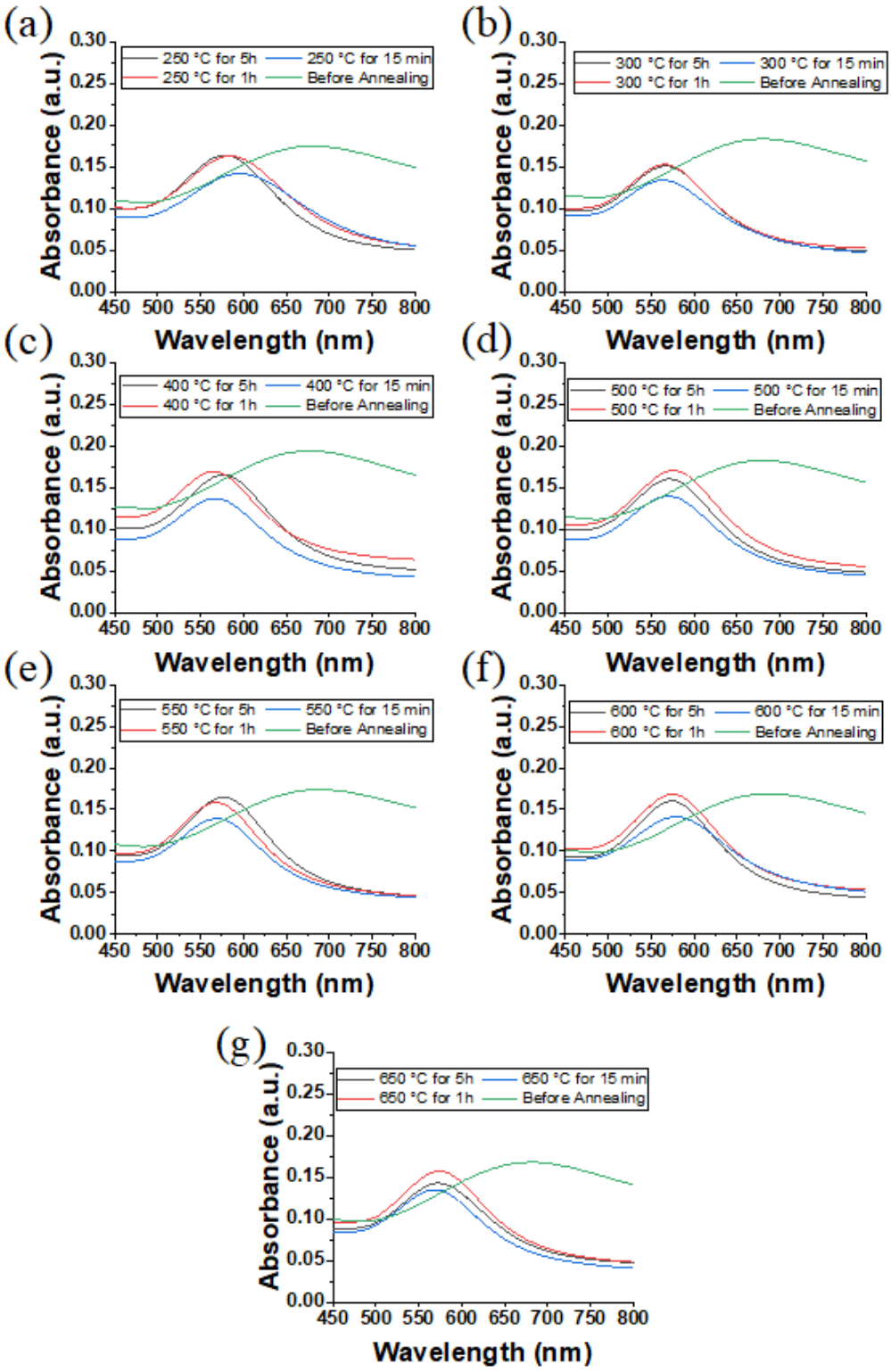

Figure 8-10: Evolution of the Au-LSPR spectral characteristics with different annealing temperatures for the platform with the ITO adhesion layer. (a) 250 °C. (b) 300 °C. (c) 400 °C. (d) 500 °C. (e) 550 °C. (f) 600 °C. (g) 650 °C.

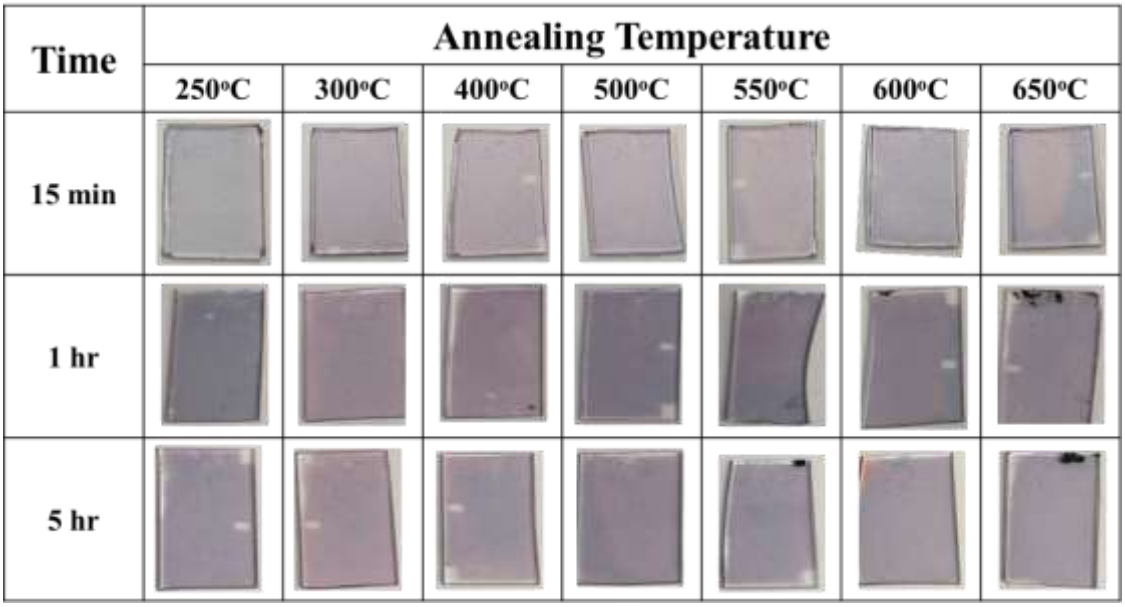

Figure 8-11: Evolution of the color change with the annealing temperature and time for the platform with the ITO adhesion layer.

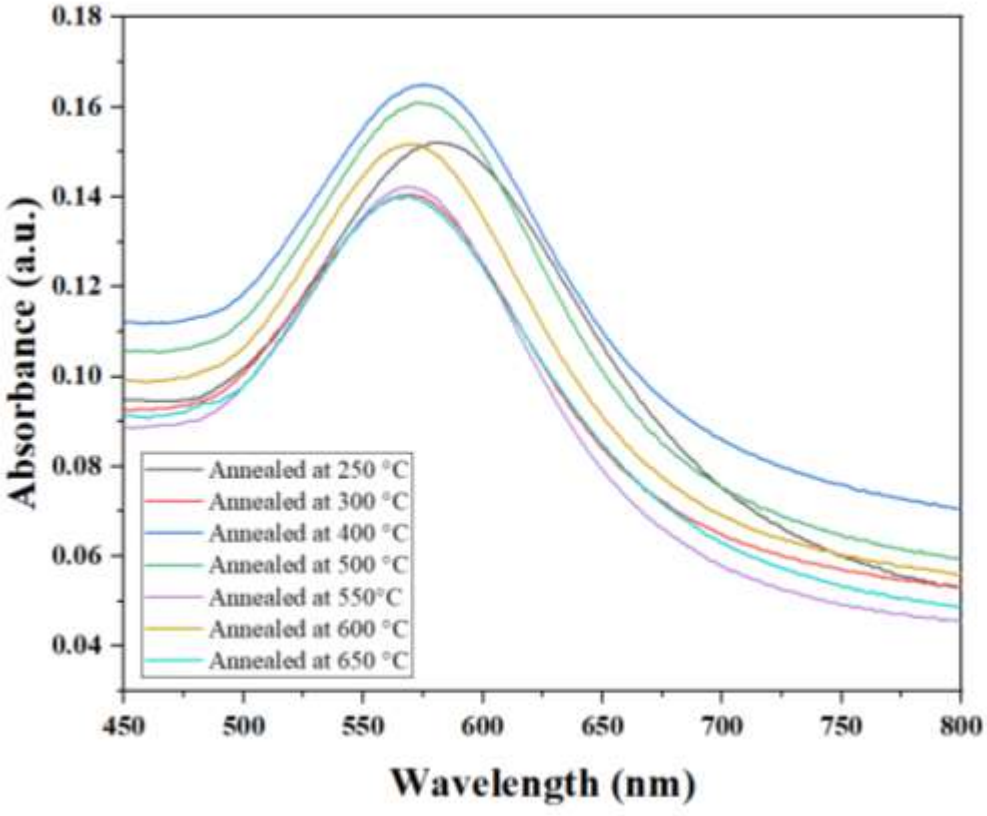

Figure 8-12: Evolution of the Au-LSPR spectral characteristics for the platform with the ITO adhesion layer for the different annealing temperatures annealed at 1hr.

It was noticeable from Figure 8-13 (b) that the average Au-LSPR peaks wavelength bandwidth were around 75 nm, 58 nm, and 49 nm for the Cr-Au platform when annealed at 550 °C, 600 °C, and 650 °C for 1hr respectively. However, from Figure 8-13 (c) the average wavelength bandwidth was around 54 nm, 56 nm, and 56 nm for the ITO-Au platform when annealed at 550 °C, 600 °C, and 650 °C for 1hr respectively. Therefore, based on the Au-LSPR peaks average wavelength bandwidth study at 90% of the maximum peak it was decided to consider the annealing temperatures of 550 °C, 600 °C, and 650 °C time for 1hr for further characterization studies of both the platforms.

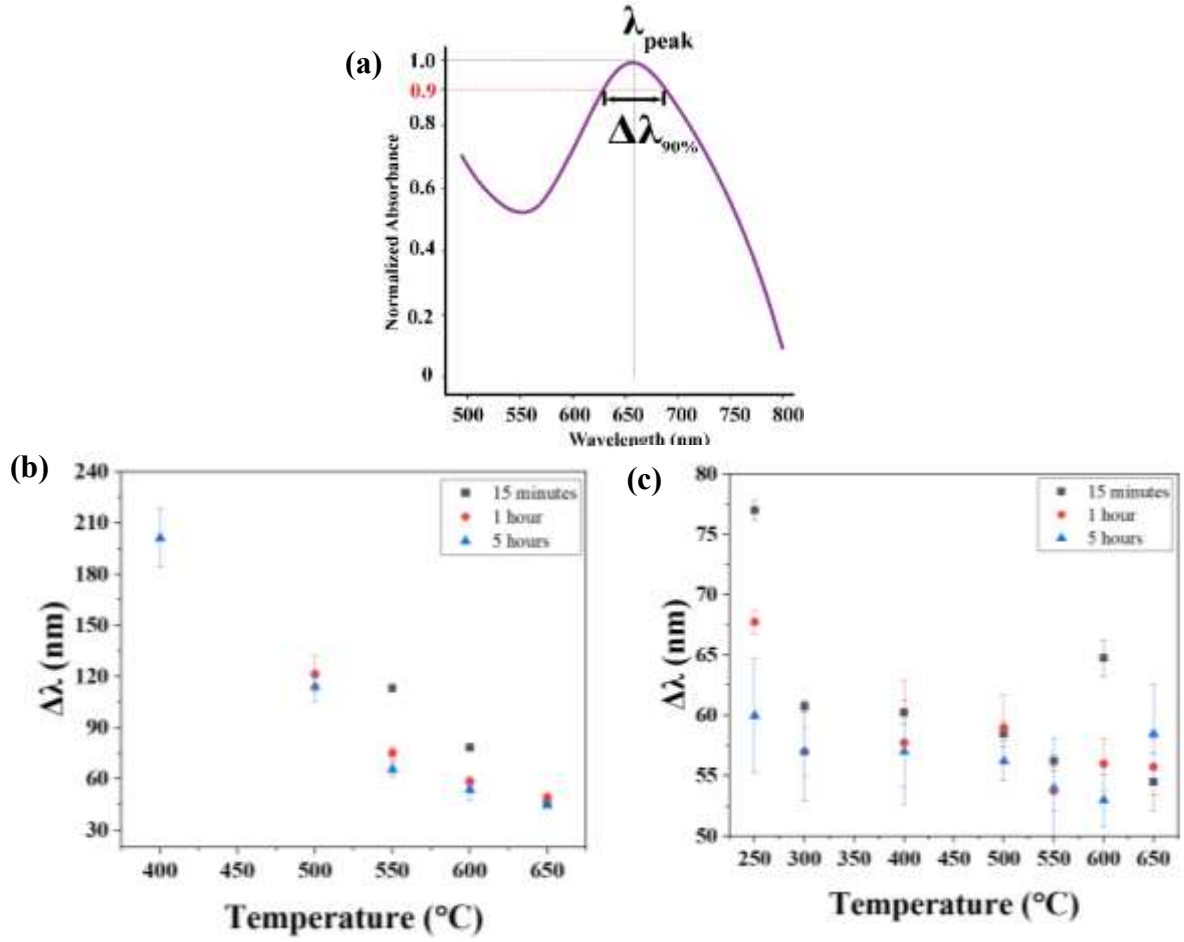

Figure 8-13: Au-LSPR peak at 90% Bandwidth of the maximum peak. (a) Schematics for the calculation of the Au-LSPR 90% bandwidth. (b) Cr-Au platform. (c) ITO-Au platform.

8.4.6. SEM and AFM Characterization of the Cr-Au and ITO-Au Platform

For both platforms, the SEM characterization was carried out for the annealing temperatures of 550 °C, 600 °C, and 650 °C for 1hr. The SEM images for the annealing

temperatures of 600 °C and 650 °C for 1hr are included in Appendix A. Whereas the AFM characterization for both the platforms was done for the samples that were annealed at 550 °C for 1hr. This was because at this temperature only for both platforms there was a well-formed Au-LSPR peak. Additionally, the SEM and AFM characterization was carried out for both platforms at 250 °C for 1hr to understand the formation of nano-islands and nanoparticles. The SEM and AFM images for the same are included in Appendix B.

It was apparent from Figure 8-14 (a) and (b) for the platform with the chromium (Cr) adhesion layer and gold (Au) layer annealed at 550 ^{o}C for 1hr that the formed nano-islands are of wide shape and size.

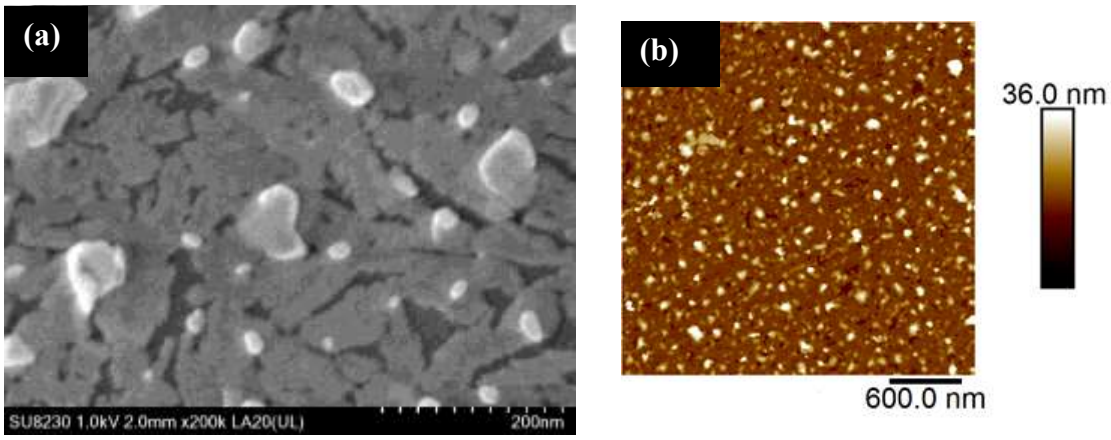

Figure 8-14: SEM and AFM image for the platform with the Cr adhesion layer and gold layer annealed at 550°C for 1hr. (a) SEM image. (b) AFM image.

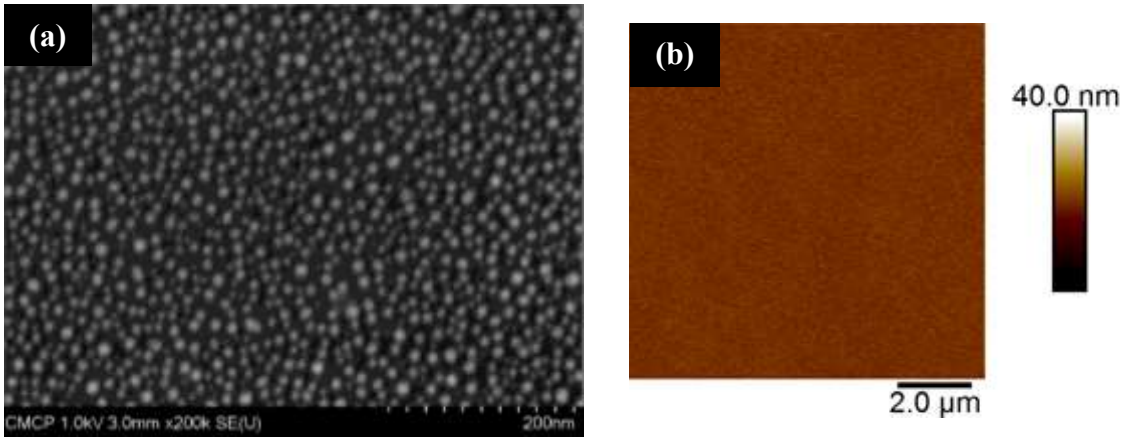

Figure 8-15: SEM and AFM image for the platform with the ITO adhesion layer and gold layer annealed at 550°C for 1hr. (a) SEM image. (b) AFM image.

It is clear from Figure 8-15 (a) and Figure 8-15(b) that the platform with the ITO adhesion layer and gold (Au) layer annealed at 550 °C for 1hr nanoparticles are formed with a wide size range.

8.4.7. Particle Size Distribution Analysis for the Cr-Au and ITO-Au Platform

The particle size distribution for the platforms was carried out using the ImageJ software. an opensource software that is available to, quantify, and validate scientific image data that was created at the National Institutes of Health. The obtained SEM images were used to do the particle size distribution analysis for each of the platforms. The step-by-step procedure to perform the particle size distribution analysis in ImageJ software is provided in Appendix C. Figure 8-16 (a) to Figure 8-16 (c) shows the presence of nano-islands of wide size with an average size of around 35.21 nm, 30.30 nm, and 30.46 nm respectively for the Cr-Au platform when the samples annealed at 550 °C, 600 °C and 650 °C. The size of the nano-islands is significantly smaller than those obtained from gold colloidal solutions, and the density of nano-islands is higher than the ones that have been previously reported using the colloidal solution deposition process [98,137]. The small diameter of the nano-islands is attributed to the low amount of gold available due to only depositing a very thin film of gold (Au). Also, from Figure 8-16 (d) the cumulative percentage of distribution of the nano-islands for the Cr-Au platform when the samples were annealed at 550 °C, 600 °C, and 650 °C 50% of nano-islands are within the size of 32.89 nm, 26.95 nm, and 27.64 nm respectively.

Table 8.1: Particle size distribution statistical data of the nano-islands for the Cr-Au platform at different temperatures annealed for 1hr.

Sample	Mean (nm)	Standard Deviation	Minimum (nm)	Maximum (nm)	Median (nm)
Cr- Au Annealed at 550 °C	**35.21**	**17.13**	**5.44**	**79.96**	**32.89**
Cr- Au Annealed at 600 °C	**30.30**	**16.72**	**8.09**	**80.20**	**26.95**
Cr- Au Annealed at 650 °C	**30.46**	**17.16**	**5.56**	**83.33**	**27.64**

Table 8.1 presents the statistical data of the nano-islands for the Cr-Au platform at different annealing temperatures annealed for 1hr. From the data, it is clear that the minimum size of the nano-islands is in the range of 5 to 8 nm whereas the maximum size is in the range of 80 to 83 nm for the different annealing temperatures.

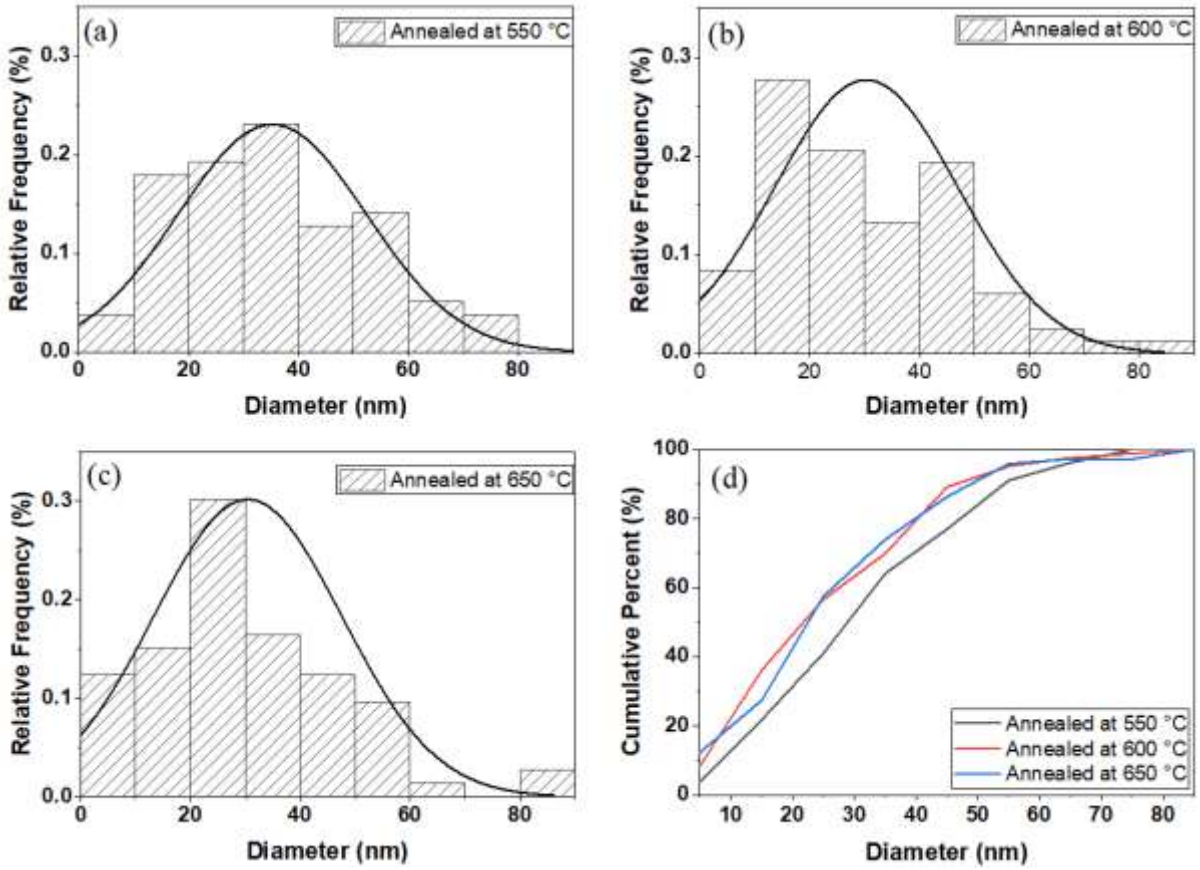

Figure 8-16: Particle size distribution for the substrate with the Cr adhesion layer and gold layer annealed for 1hr. (a) 550 °C. (b) 600 °C. (c) 650 °C. (d) cumulative distribution for all the temperatures.

Table 8.2: Particle size distribution statistical data of the nanoparticles for the ITO-Au platform at different annealing temperatures for 1hr.

Sample	Mean (nm)	Standard Deviation	Minimum (nm)	Maximum (nm)	Median (nm)
ITO-Au Annealed at 550 °C	7.81	1.89	3.64	12.94	7.86
ITO-Au Annealed at 600 °C	7.92	2.00	3.63	14.34	8.00
ITO-Au Annealed at 650 °C	7.01	1.74	3.58	12.04	6.97

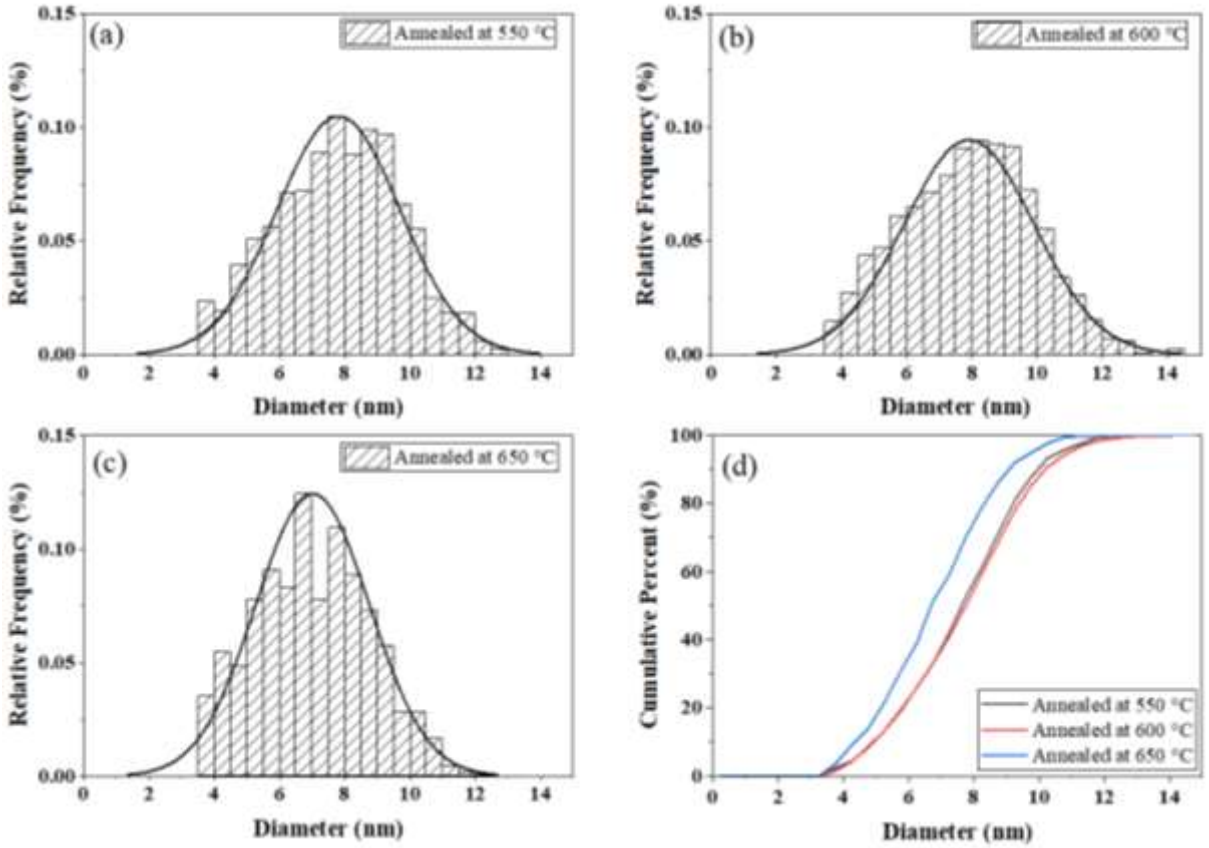

Figure 8-17: Particle size distribution for the substrate with the Cr adhesion layer and gold layer annealed for 1hr. (a) 550 °C. (b) 600 °C. (c) 650 °C. (d) cumulative distribution for all the temperatures.

Moreover, for the ITO adhesion layer from the plasmonic properties and SEM characterization, it could be concluded that the gold layer does not form nano-islands when deposited on the ITO adhesion layer. The presence of gold nanoparticles on ITO has been accounted for by the formation of nano-islands and subsequent breaking due to the long duration of annealing at high temperatures [250,251]. An alternative explanation would be assuming that the gold atoms enter the ITO surface layer during the deposition. Due to the sub-surface segregation, dewetting would be impossible.

Figure 8-17 (a) to Figure 8-17 (c) shows the presence of nanoparticles of varied size with an average diameter in the range of 7 to 8 nm for the ITO-Au platform when the samples were annealed at 550 °C, 600 °C, and 650 °C. Also, from Figure 8-17 (d) the cumulative distribution percentage of distribution of the nanoparticles for the ITO-Au platform when the samples annealed at 550 °C, 600 °C, and 650 °C are 50% nanoparticles within the size range of 7 to 8 nm.

Table 8.2 presents the particle size distribution statistical data of the nanoparticles for the ITO-Au platform at different annealing temperatures. From the data, the minimum size of the nanoparticles is in the range of around 3.6 nm whereas the maximum size is within the size range of 12 to 14 nm for the different annealing temperatures.

8.4.8. Refractive Index Sensitivity Study for the Cr-Au and ITO-Au Platform

The spectral sensitivity of the platforms can be calculated, using solvents with different refractive indices to understand their usefulness for sensing application. For any sensing platform, the spectral sensitivity is denoted by S, and it is defined as $S= \Delta\lambda/\Delta n$ where '$\Delta\lambda$' is the shift of sensor resonance in nm, and 'Δn' is the change in refractive index between the solvents. Therefore, the measurements were performed by immersing the sample in a quartz cuvette, filled with each of the solvents as listed in Table 8.3 for 1 hour and then measuring the absorption spectra using the PerkinElmer (Lambda650) spectrophotometer.

Table 8.3: Refractive indices of the solvents used for the sensitivity measurements

S. No	Solvent	Refractive Index
1	DI water	1.33
2	Ethanol	1.36
3	Isopropyl alcohol (IPA)	1.38
4	50% Glycerol	1.40
5	Dichloromethane	1.42
6	Dimethylformamide (DMF)	1.43
7	100% Glycerol	1.47
8	Toluene	1.49
9	Anisole	1.52

Measurements of the sensitivity of the Cr-Au platform annealed at 550 °C, 600 °C, and 650 °C showed a slight reduction in the RIU/nm as shown in Figure 8-18 (a). It is noticeable from Table 8.4 that with the increase in annealing temperature, there is a reduction of the particle size as well.

Further, the refractive index sensitivity of the platform with the ITO adhesion layer revealed a lack of sensitivity as illustrated in Figure 8-18 (b). It is also clear from Table 8.5 that with the increase in annealing temperature, there is not much noticeable reduction in the size of the particle. Thus, from the refractive index study, it could be concluded that the platform with the Cr adhesion layer exhibits a moderate sensitivity.

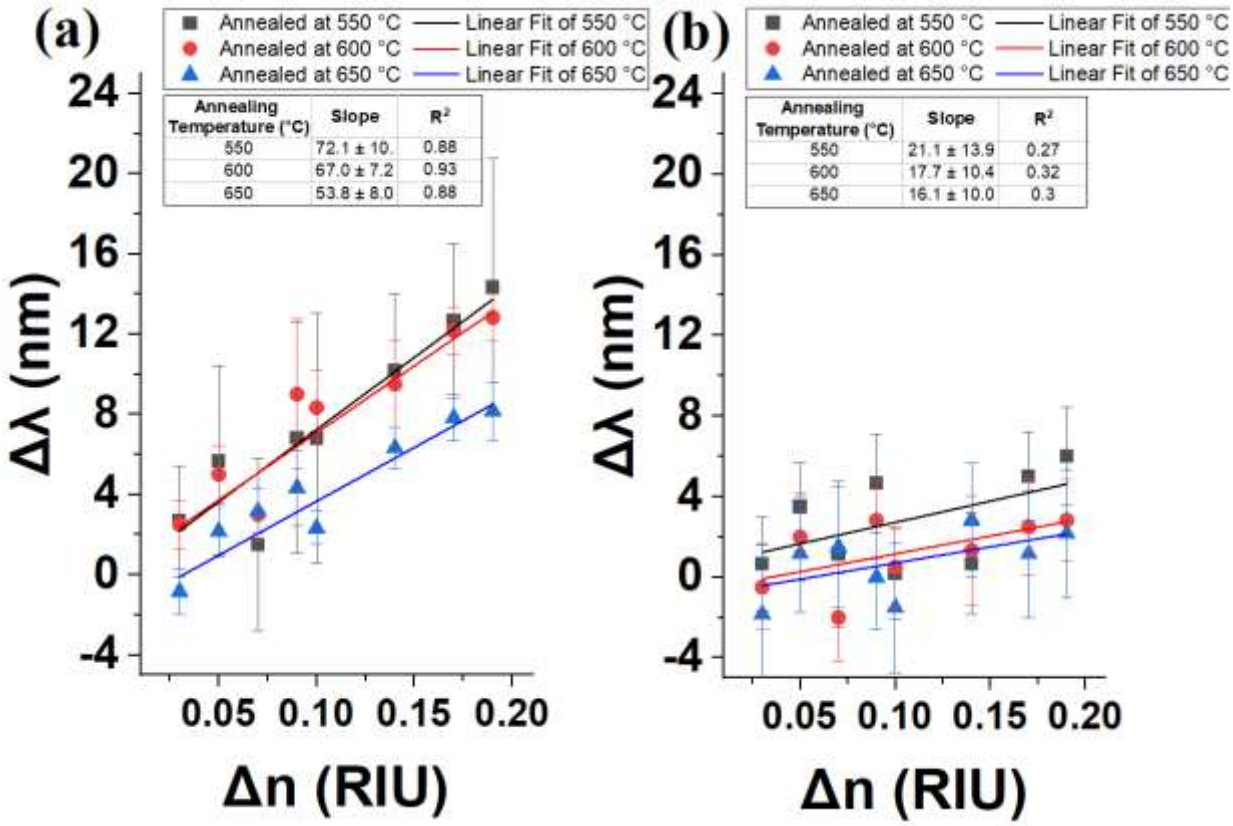

Figure 8-18: Refractive index sensitivity of the platforms annealed for 1hr at 500 °C, 600 °C and, 650 °C. (a) Cr adhesion layer. (b) ITO adhesion layer.

Table 8.4: Dependence of the sensitivity on the annealing temperature for the Cr- Au platform

Annealing temperature (°C)	Cr-Au LSPR peak (nm)	Average particle size (nm)	RIU/nm
550	637	35.21	72.1 ± 10.5
600	588	30.30	67.0 ± 7.2
650	572	30.46	53.8 ± 8.0

Table 8.5: Dependence of the sensitivity on the annealing temperature for the ITO-Au platform

Annealing temperature (^{0}C)	ITO - Au LSPR peak (nm)	Average particle size (nm)	RIU/nm
550	562	7.81	21.1 ± 13.9
600	573	7.92	17.7 ± 10.4
650	578	7.01	16.1 ± 10.0

8.4.9. Elemental Mapping and Compositions

The elemental mapping and its composition graphs are generated from the SEM-EDS (Energy Dispersive Spectroscopy) measurements. These graphs reflect, globally, the presence of the elements in the samples, no matter the place they are. Because of the limitation of sensitivity of the SEM used for this study, the elemental mapping and compositions of the platforms with the ITO layers could not be investigated. Therefore, the elemental mapping has only been conducted for the platforms with the chromium (Cr) adhesion layer that was used for detection experiments.

The elemental mapping and its corresponding compositions for the Cr - Au platforms annealed at 250 °C, 400 °C, 550 °C and, 650 °C are shown in Figure 8-19, Figure 8-20, Figure 8-21, and Figure 8-22, respectively. For each of the annealing temperatures for simplicity, the mapping of only Si, Cr, and Au elements are shown in the figure while the elemental compositions are shown for all of the elements present in the samples with their spatial distribution. It has to be mentioned that, in agreement with the SEM and spectral results, the nano-islands start forming at 400 °C but they are very well noticeable only in the SEM images of the samples annealed at 550 °C and above.

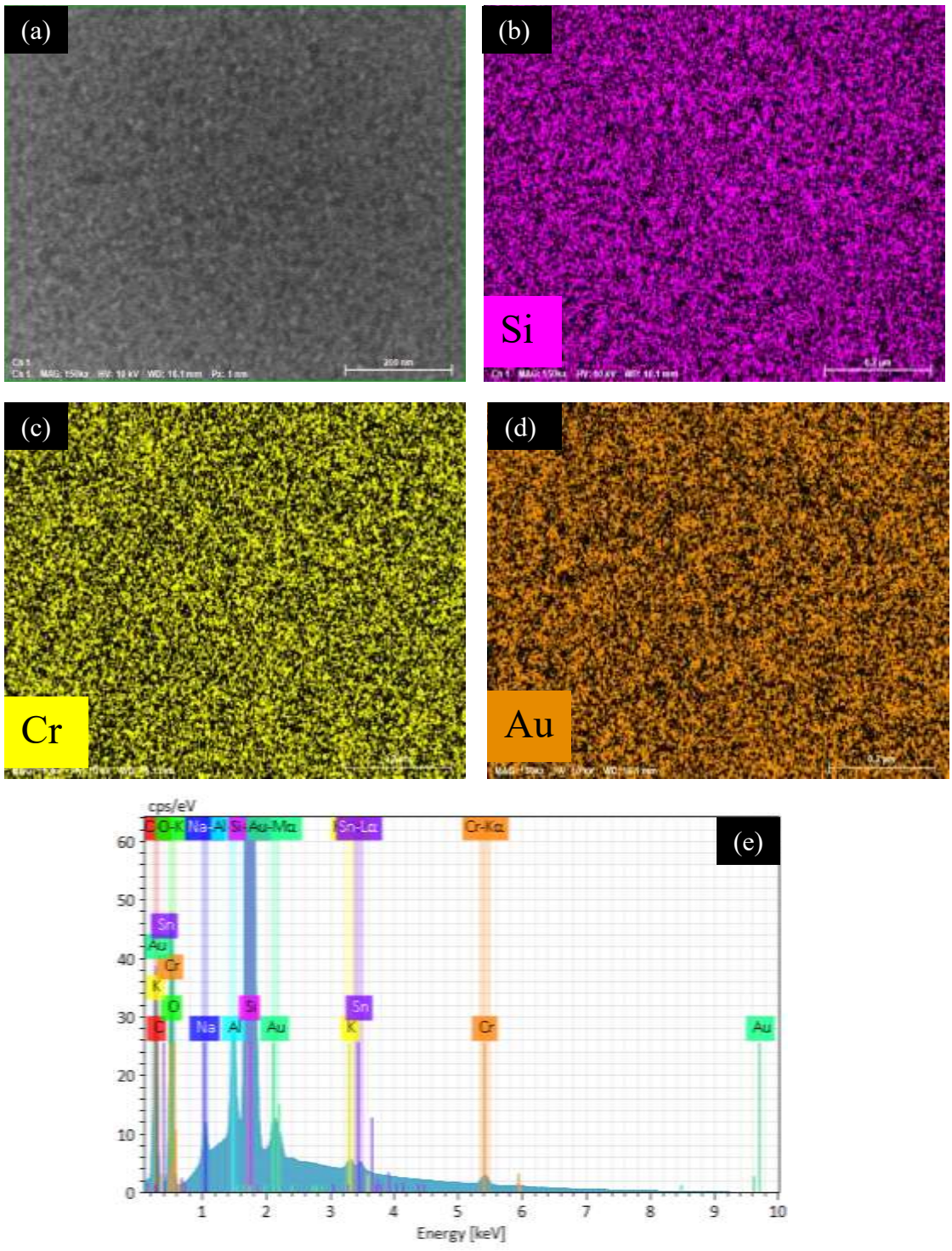

Figure 8-19: Elemental mapping and the composition plots of platforms with Cr adhesion layer annealed for 1h at 250 °C. (a) SEM image. (b) Mapping of Si element. (c) Mapping of Cr element. (d) Mapping of Au element. (e) Elemental composition.

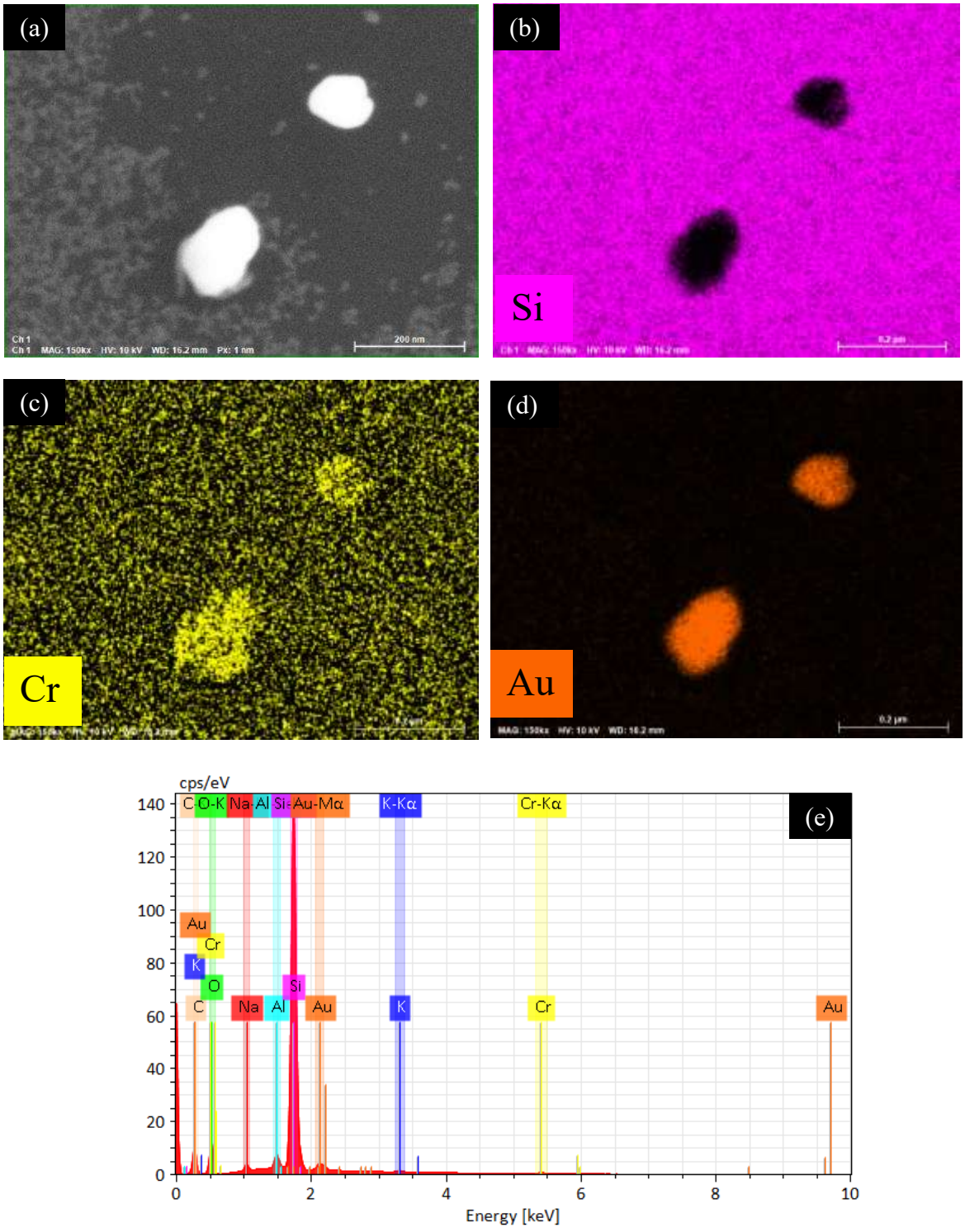

Figure 8-20: Elemental mapping and the composition plots of platforms with Cr adhesion layer annealed for 1h at 400 °C. (a) SEM image. (b) Mapping of Si element. (c) Mapping of Cr element. (d) Mapping of Au element. (e) Elemental composition.

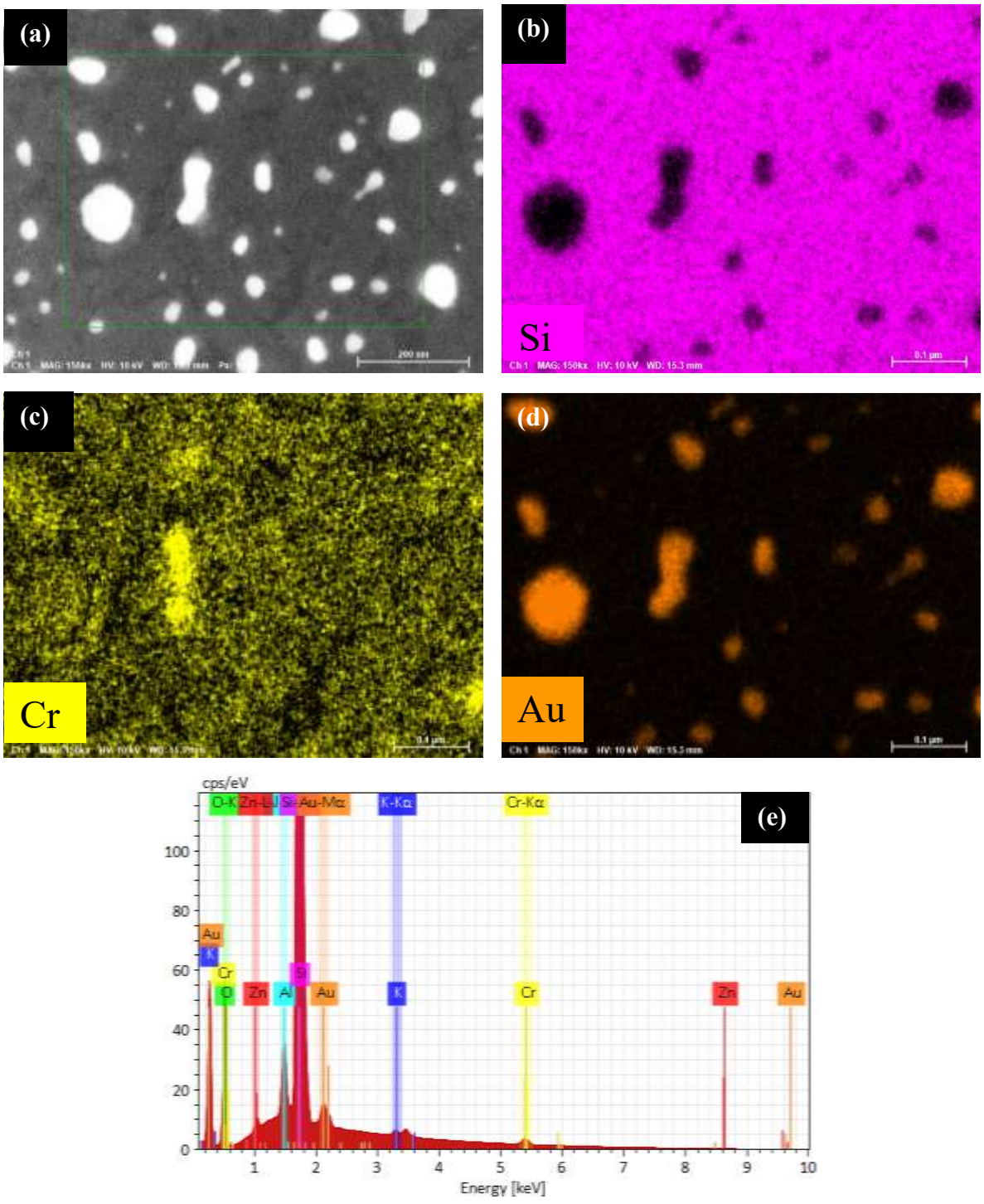

Figure 8-21: Elemental mapping and the composition plots of platforms with Cr adhesion layer annealed for 1h at 550 °C. (a) SEM image. (b) Mapping of Si element. (c) Mapping of Cr element. (d) Mapping of Au element. (e) Elemental composition.

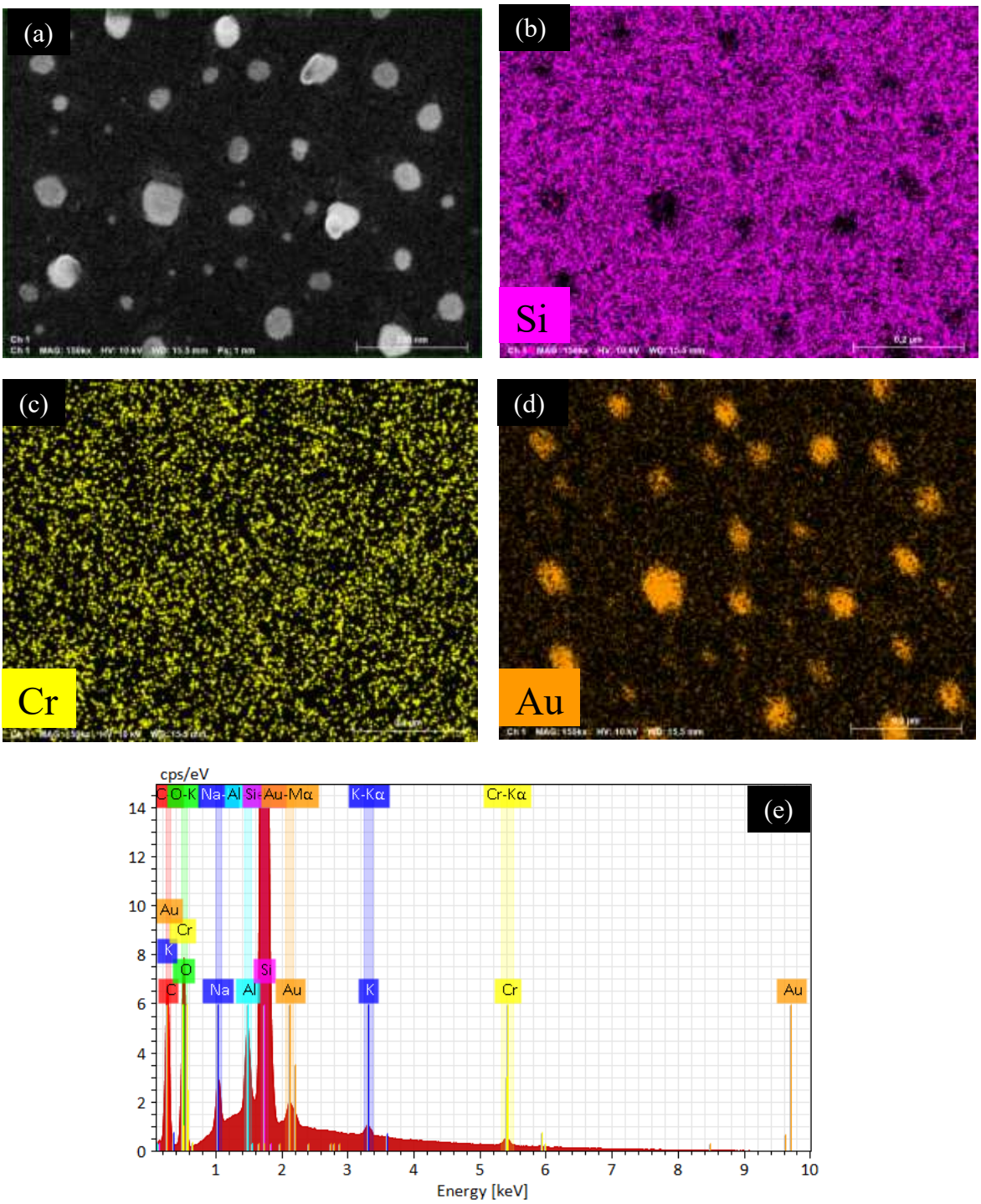

Figure 8-22: Elemental mapping and the composition plots of platforms with Cr adhesion layer annealed for 1h at 650 °C. (a) SEM image. (b) Mapping of Si element. (c) Mapping of Cr element. (d) Mapping of Au element. (e) Elemental composition.

In the EDS application, different areas of the SEM image can be chosen and the elemental composition, as normalized mass concentration, was found for each area. From the elemental

mapping, it was noticeable that nano-islands are well noticeable when the samples are annealed at 550 °C for 1hr. Thus, to better understand the elemental compositions at different areas within the single SEM image of the sample that was annealed at 550 °C for 1hr as shown in Figure 8-23 was carried out. Therefore, on this image four different areas/points were chosen that are considered to be spectrum 1, 2, 3, and 4. Figure 8-23 (b) to Figure 8-23 (e) corresponds to the elemental composition for each of the spectrums respectively.

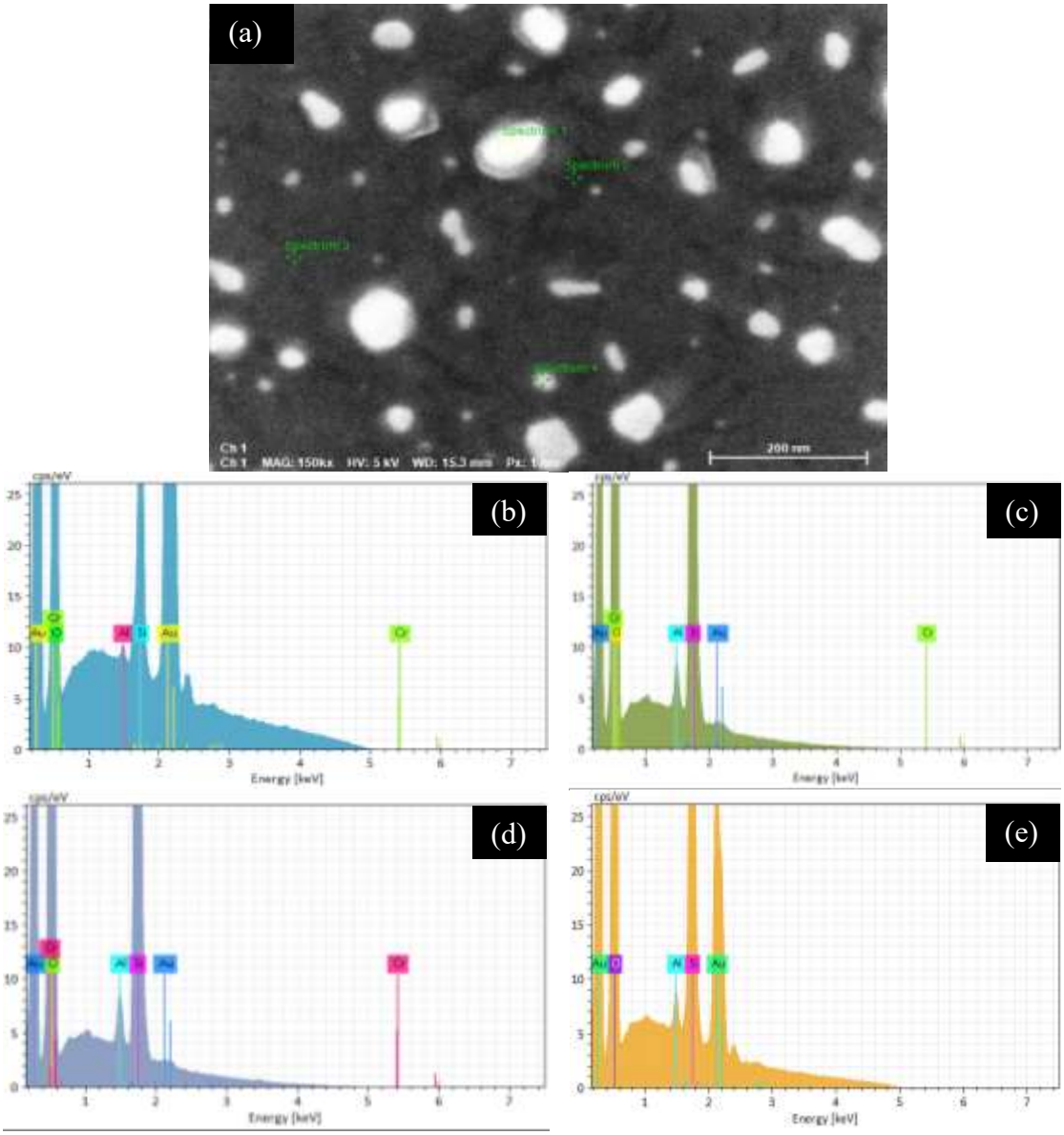

Figure 8-23: Elemental composition at different areas of the SEM image for the platform with Cr adhesion layer annealed for 1h at 550 °C. (a) SEM image. (b) Spectrum 1 elemental compositions. (c) Spectrum 2 elemental compositions. (d) Spectrum 3 elemental compositions. (e) Spectrum 4 elemental compositions.

Table 8.6 shows the dispersion of Chromium (chromium oxide) and of all the other elements, including gold, along the different selected areas/points of the annealed sample. That means that the spatial identity of the chromium adhesion layers was not preserved anymore during the high-temperature annealing process.

Table 8.6: Normalized mass concentration (%) corresponding to different areas of the platform

Spectrum	Oxygen	Aluminium	Silicon	Chromium	Gold
Spectrum 1	4.38	0.50	4.06	2.37	88.69
Spectrum 2	27.70	2.43	54.63	10.00	5.23
Spectrum 3	27.97	2.51	54.34	10.72	4.46
Spectrum 4	13.83	1.05	18.47	--	66.65
Mean	18.47	1.63	32.88	7.70	41.26
Sigma	11.49	1.00	25.64	4.63	43.00

The elemental composition graphs for each area/ point show the presence of significant amounts of gold, chromium, and elements from the borosilicate substrate. The existence of chromium may diminish the sensitivity of platforms that incorporate chromium due to the lack of its plasmonic properties. Overall, the findings suggest the need for careful consideration of the impact of inter-diffusion on the sensitivity of the detection. The images demonstrate that gold and chromium coexist within nano-islands, implying their inter-diffusion during the nano-island formation. Further investigation was crucial to explore this phenomenon as it could potentially affect the sensitivity of detection in samples with chromium.

8.4.10. Characterization of the Substrates by XRD

The XRD patterns of the Cr-Au platform are shown in Figure 8-24. From the figure, it could be noted that in the as-deposited (non-annealed) platform, the peaks are very broad and suggest very small nanocrystalline domains. When the platform is annealed at 550 °C, distinctive peaks of Au at 38° and 64°, corresponding to (111) and (220) orientations observed respectively (along with smaller peaks at 44.5° and 74.5°) accompanied by distinctive peaks for the Cr_2O_3 at 34° corresponding to (210) orientation (a second peak is observable at 54.8°).

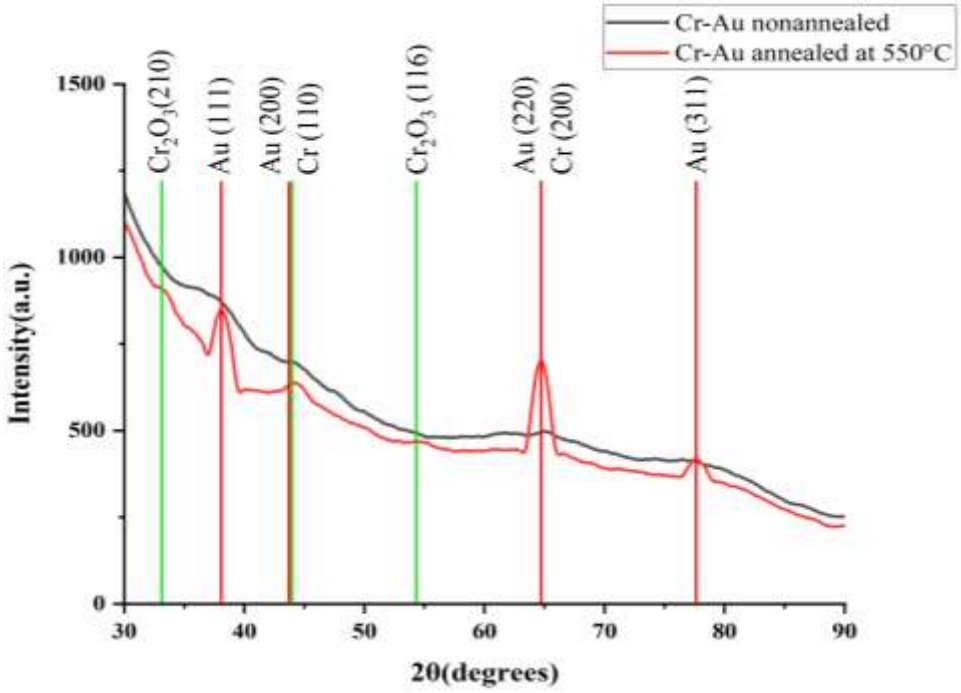

Figure 8-24: XRD patterns of the Cr-Au platform, as-deposited (non-annealed) and annealed at 550 °C for 1hr.

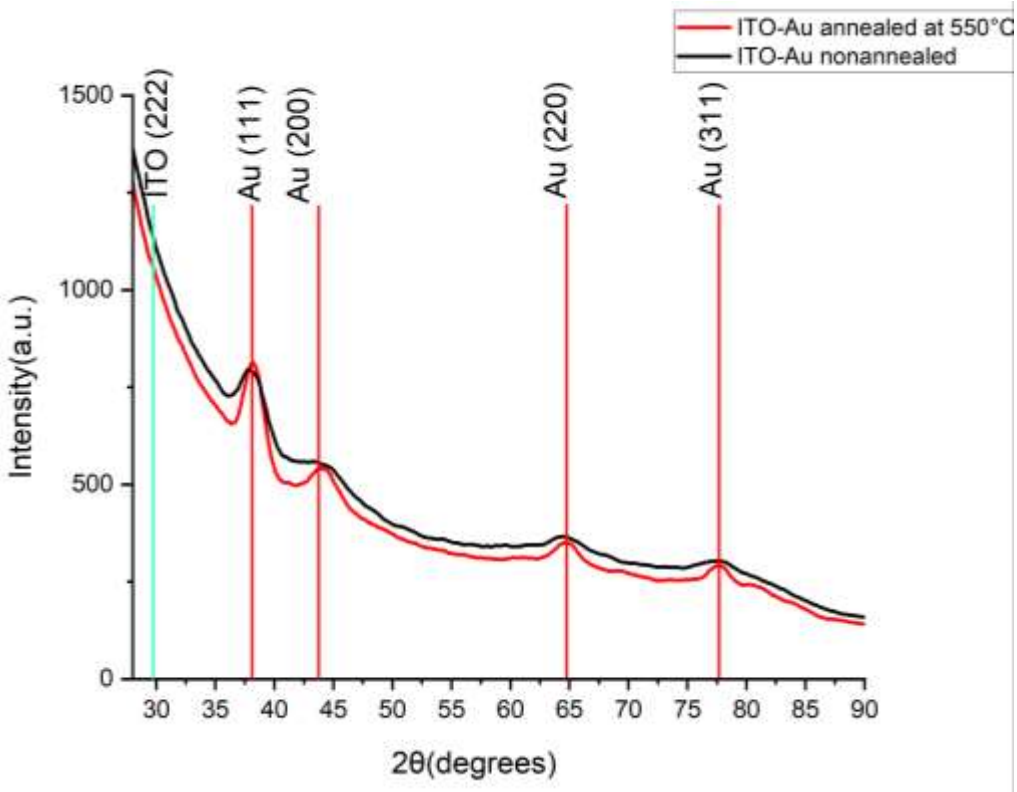

Figure 8-25: XRD patterns of the ITO-Au platform, as-deposited (non-annealed) and annealed at 550 °C for 1hr.

However, for the ITO-Au platform from Figure 8-25, a distinct peak could not be noticed for both the ITO-Au non-annealed and annealed samples for the ITO at 29.9° corresponding to (222) orientation. Indeed, Alsultany et al. [246] investigated the structure of thin ITO films. These films were annealed at temperatures 250 °C, 350 °C, and 450 °C in the air for 20 minutes using different laser power They found that annealing ITO at 350 °C, ITO crystallized with a strong (222) preferred orientation and annealed at 450 °C, the grain size increased further. It can be safely assumed that the ITO-Au platform with a very thin ITO layer (1.5 nm), annealed in air at high temperatures (550 °C - 650 °C) as in our work, will crystallize with increased grain size and will have good optical and electrical properties.

Table 8.7: Main XRD peak position and its orientation for the Cr-Au and ITO-Au platforms

Observed peaks (degree 2 theta)	**Corresponding phase**	**Direction (h, k, l index)**	**Crystallite size (nm)**			
			Cr-Au		**ITO-Au**	
			Non-annealed	**Annealed at 550 °C**	**Non-annealed**	**Annealed at 550 °C**
29.9	ITO	222	-	-	-	-
33.5	Cr_2O_3	210	-	12.1	-	-
38.2	Au	111	0.9	17.1	4.0	5.8
44.5	Au/Cr	200/110	Too weak	Too weak	Too weak	Too weak
54.8	Cr_2O_3	116	-	Too weak	-	-
64.5	Au/Cr	220/200	0.9	12.1	1.7	1.9
77.5	Au	311	Too weak	Too weak	Too weak	Too weak

As the layers of the Cr, ITO, and Au are extremely thin for the Cr-Au and ITO-Au platforms, not all expected peaks are observable as they are too broad and weak to be discerned from the substrate background signal despite the grazing angle configuration. Table 8.7 presents the dominant peak positions and the corresponding orientation for both platforms non-annealed

and annealed samples. Dominant peaks of gold are observable in all samples, with various crystallite domain sizes, always higher after annealing. As can be observed from the expected position of Cr peaks, Cr cannot be discerned from Au, since all the observed peaks of Cr are also present in the Au phase diagram. Although it is not possible to quantify if there is any quantity of metallic chromium present due to the absence of the clear signal, the pattern of the annealed sample based on the chromium adhesion layer shows the presence of chromic oxide (Cr_2O_3), formed by oxidation of the chromium adhesion layer during the high-temperature annealing.

8.5. Direct Detection of EVs/exosomes

Based on the results of characterization methods and the refractive index sensitivity studies it was decided to use the Cr - Au platforms for the detection of EVs/exosomes derived from the MCF 7 breast cancer cell line that was extracted from a bioreactor, filtered, ultra-centrifuged and suspended in the cell culture media. So far, with the different substrate matrixes that were developed viz the *ex-situ* and *in-situ* the detection of MCF 7 EVs/exosomes was carried out by functionalizing the formed nano-islands through linkers and then activating it through cross-linkers; then the interaction of the polypeptides with the crosslinkers and then finally binding the exosomes to the polypeptides. Thus, detecting the EVs/exosomes with the previously developed substrate matrixes involves several reagents and steps which eventually increases the time taken for detection and cost. Also, in a recent study [249] it was proven that with bare SAM-AuNIs chip without any functionalization could generate LSPR phase responses to the exosomes and microvesicles (MVs) in a concentration-dependent manner, like the response via an antibody-functionalized SAM-AuNIs LSPR sensor, signifying the biophysical interaction of exosomes and MVs.

Therefore, to reduce the time taken to detect the EVs/exosomes and to cut down the cost associated with the chemical reagents, it was decided to directly immobilize the EVs/exosomes to the Au nano-islands using the van der Waals force of attraction (charge-based affinity). Thus, in the current study, the detection performance of the substrates annealed at two different temperatures 600 °C and 650 °C were compared with the performance of the substrates that were developed and studied earlier using the gold colloidal solution and the immunoaffinity method [98,149].

8.6. Biosensing Protocol for the Direct Detection of EVs/exosomes

The schematic of the biosensing protocol explaining the steps involved with immobilizing the MCF7 EVs/exosomes to the Au nano-islands is demonstrated in Figure 8-26 (a) to Figure 8-26 (c). At each stage of the biosensing, steps 6 to 7 measurements were done on the same substrate and the schematic of the measurements carried out at each stage on the prepared substrates is shown in Figure 8-26 (d).

The pictures of the substrates with the steps involved as per the biosensing protocol are shown in Figure 8-27 (a) to Figure 8-27 (c). The first step involves measuring the Au-LSPR absorption spectrum of the prepared substrates as shown in Figure 8-27Figure 8-26 (a) using the Perkin Elmer spectrophotometer (Lambda650). The second step is immobilizing the MCF7 EVs/exosomes onto the Au nano-islands by depositing 50µl of the CCM containing the EVs/exosomes is immobilized onto the substrates, as shown in Figure 8-27 (b). Then the substrates are incubated for about 1 hour as shown in Figure 8-27 (c). After this step, the absorption spectrum is measured as shown in Figure 8-26 (d), the schematic of the biosensing protocol.

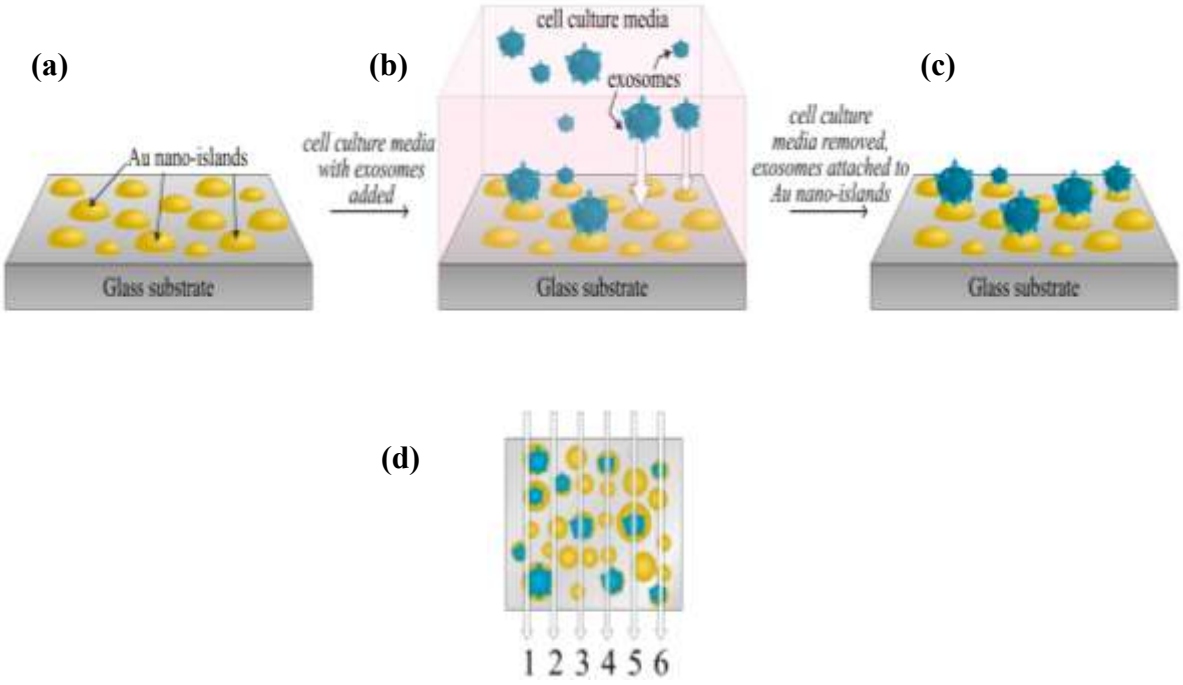

Figure 8-26: Schematic of the biosensing protocol and the LSPR measurements. (a) Glass substrate with the nano-islands. (b) Immobilization of the MCF 7 EVs/exosomes to the nano-islands. (c) Binding of the MCF 7 EVs/exosomes to the nano-islands. (d) Schematic for the LSPR measurements carried out on the prepared substrates, before and after the immobilization of the MCF 7 EVs/exosomes.

8.7. Direct Detection of EVs/exosomes and Optimization of DI Water Rinsing

The Au-LSPR absorbance band for each of the substrates is recorded after the incubation step. The shift of the Au plasmon band towards longer wavelengths (redshift) confirms the immobilization of the EVs/exosomes onto the surface of nano-islands as shown in Figure 8-28. However, the substrates were rinsed with DI water and after that, the measurements were repeated for each of the substrates. This step was carried out to remove any of the nonspecific binding of the MCF 7EVs/exosomes to the Au nano-islands. The DI water rinsing step was repeated thrice to determine the numbering of times the rinsing is required to remove the nonspecific binding such that a further blueshift is not noticed. The measured Au-LSPR band on the substrate before, after immobilizing the MCF7 EVs/exosomes, and after rinsing the substrate with the DI water is shown in Figure 8-28. It is clear from Figure 8-28 that there is no noticeable blue shift of the Au- LSPR spectra between the first rinsing of the substrate and the third rinsing of the substrate with DI water as compared to the Au-LSPR spectra before rinsing the substrate with the DI water. Therefore, it might be concluded that the rinsing of the substrates once with DI water would be sufficient to remove the nonspecific binding of the MCF 7EVs/exosomes to the Au nano-islands.

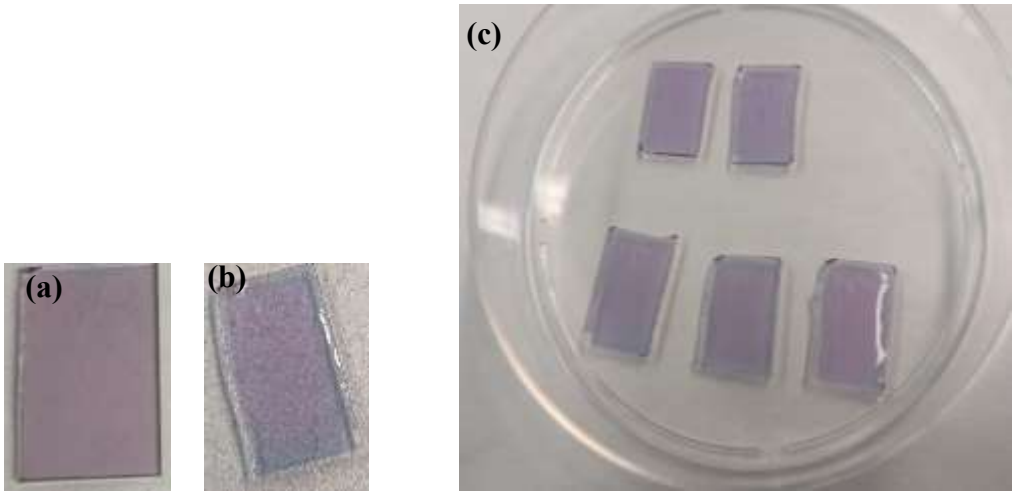

Figure 8-27: Pictures of the prepared substrates for the detection of MCF 7 EVs/exosomes. (a) Substrate before immobilizing MCF 7 EVs/exosomes. (b) Substrate after immobilizing MCF 7 EVs/exosomes. (c) Incubation of the samples after immobilizing MCF 7 EVs/exosomes onto the substrates.

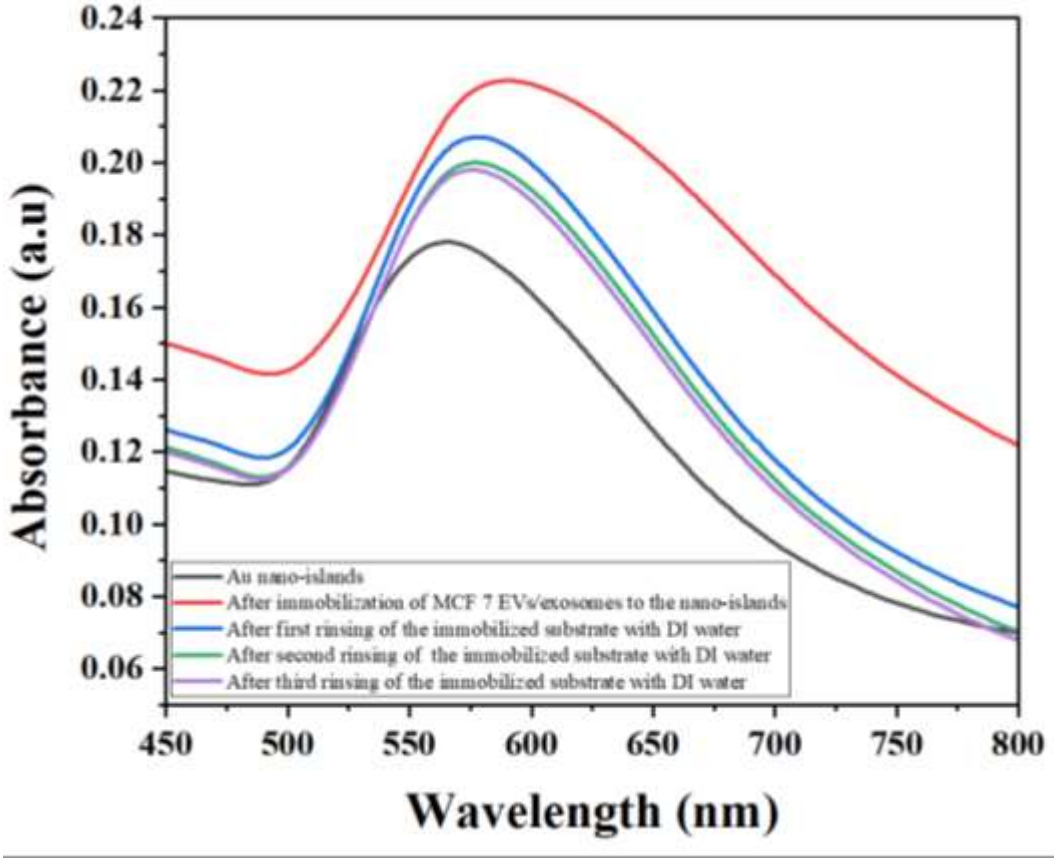

Figure 8-28: Au-LSPR band absorbance spectra at each stage - before immobilizing the MCF7 EVs/exosomes onto the substrate, after immobilizing the MCF7 EVs/exosomes to the substrate, and then after rinsing it with DI water (first, second, and third).

8.8. FESEM Characterization of EVs/ exosomes

The characterization of the MCF 7 EVs/ exosomes was done in an FESEM and it is shown in Figure 8-29 (a) and Figure 8-29 (b). It is noticeable from Figure 8-29 (b) that the MCF 7 EVs/ exosomes are immobilized onto the Au nano-islands and hence those nano-islands appear to be a brighter spot as compared to Figure 8-29 (a) that corresponds to the substrate with only the Au nano-island. Hence this confirms that the direct detection of the MCF 7 EVs/ exosomes using the newly developed platform is possible.

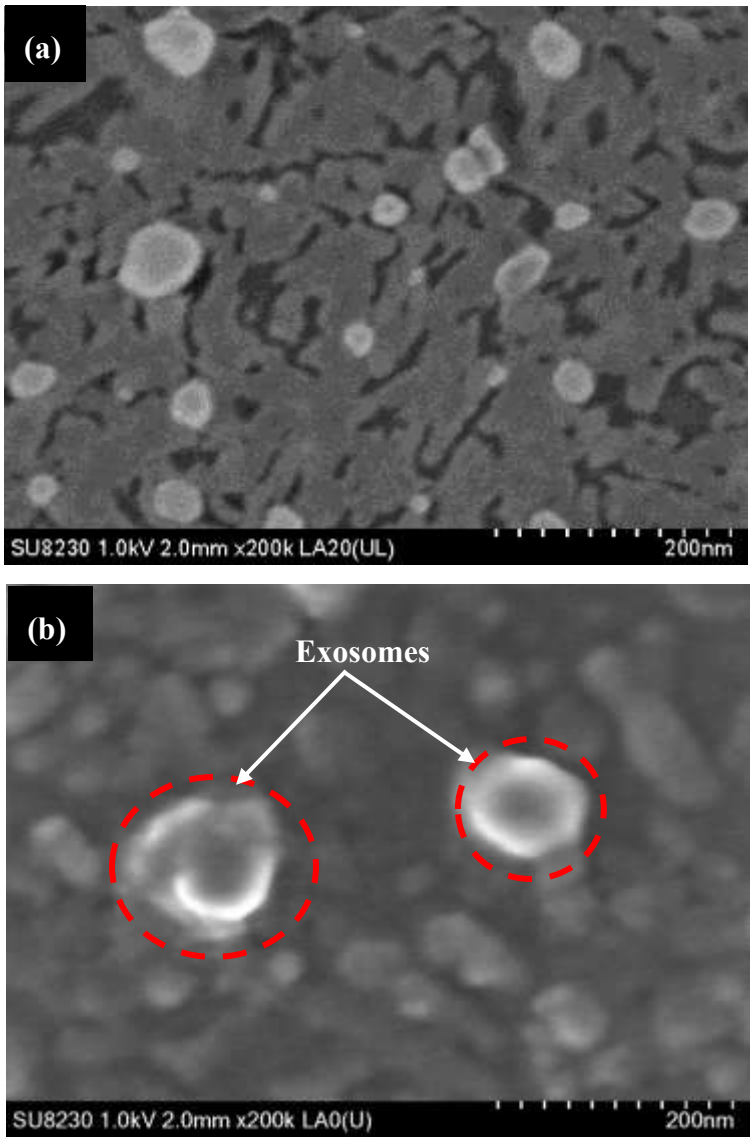

Figure 8-29: SEM image of the gold nano-islands with and without MCF7 EVs/ exosomes. (a) SEM image of the gold nano-islands without MCF7 EVs/ exosomes. (b) SEM image of the gold nano-islands with MCF7 EVs/ exosomes.

8.9. Dependence of the LSPR Shifts on the Concentration of MCF7 EVs/ exosomes and the Annealing Temperature

To quantify the MCF7 EVs/ exosomes, experiments were carried out for different concentrations of exosomes that correspond to the dilution factors of 1x, 5x, 10x, 25x, and 50x. The concentration of MCF7 EVs/ exosomes present in the cell culture media is of the order of 1.33 x 10^{10} per ml. The '1x' denotes the undiluted solution. It is clear from Figure 8-30 that the average shift decreases as the dilution factor increases. In addition, from Figure 8-30, it is clear that, as the

annealing temperature increases, the average shift for the same concentration decreases. This might be due to the decrease in the size of the formed nano-islands as the annealing temperature increases.

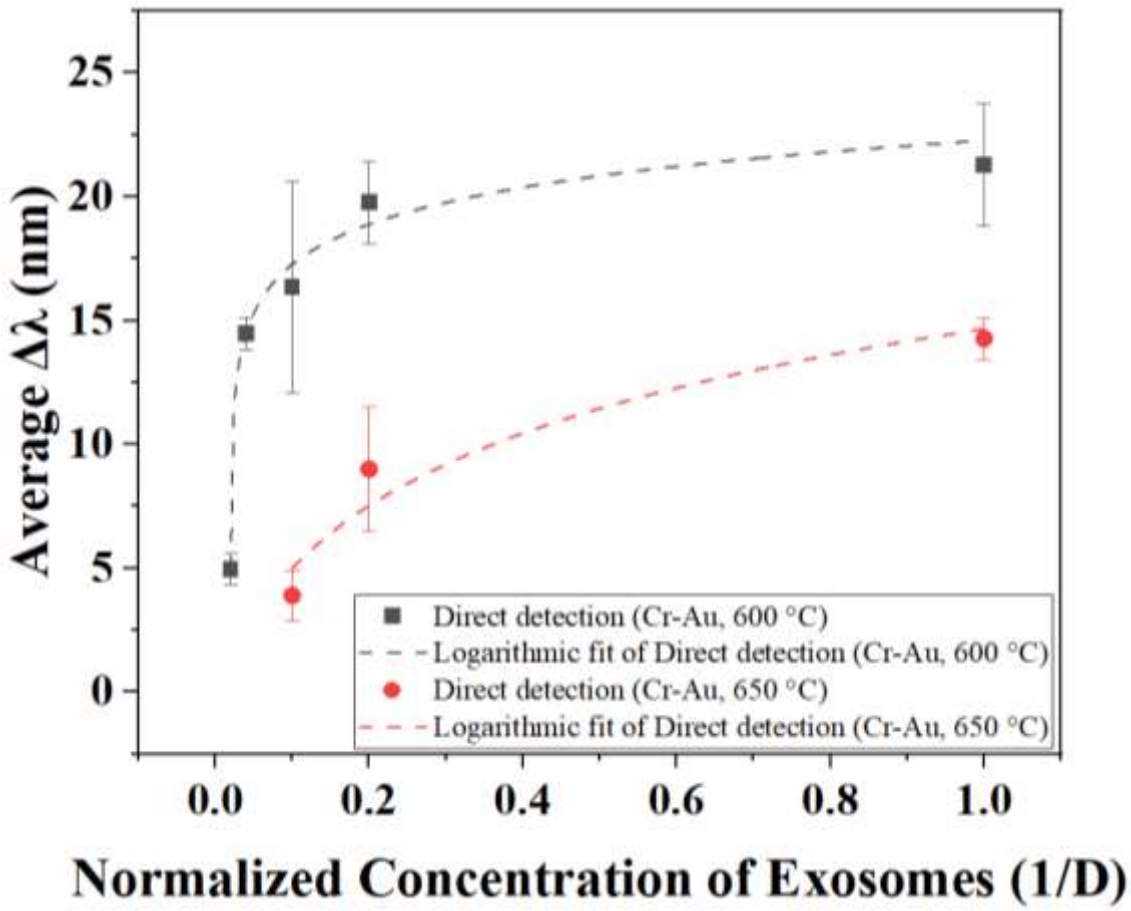

Figure 8-30: Average LSPR shift corresponding to the different concentration of MCF7 EVs/exosomes for different annealing temperatures.

8.10. Comparison of the LSPR shifts for MCF7 EVs/ exosomes Between the Methods of Direct Detection and Immunoaffinity

Figure 8.31 demonstrates that the LSPR detection of the developed platform, with direct immobilization of MCF7 EVs/exosomes onto the Au nano-islands, exhibits superior sensitivity compared to our earlier method using the immunoaffinity approach. Therefore, optimizing and utilizing the direct detection method for further studies is advantageous as it significantly reduces both the detection time for MCF7 EVs/exosomes and the costs associated with the additional chemical reagents required for the immunoaffinity method.

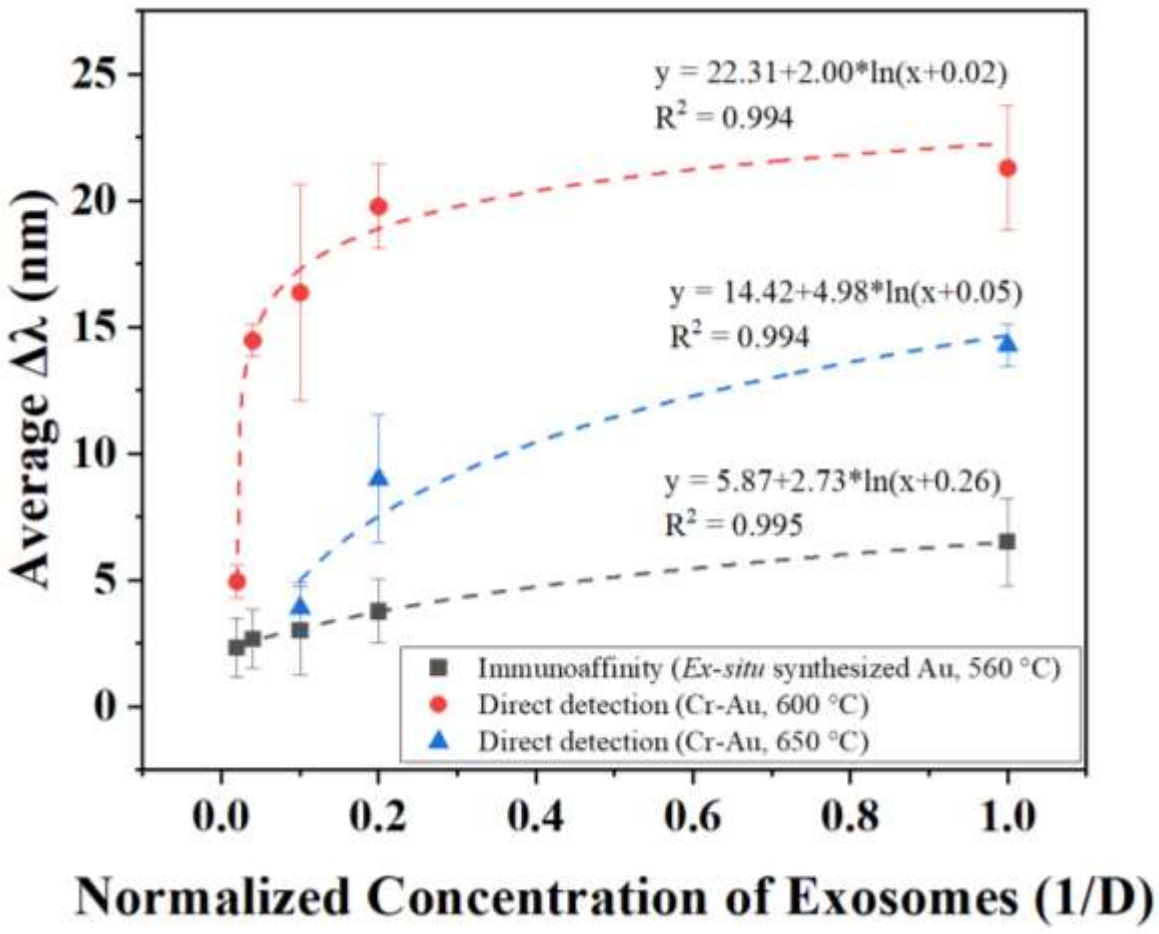

Figure 8-31: Comparison of the average LSPR shifts for MCF7 EVs/ exosomes between the method of direct detection and immunoaffinity [98].

8.11. Conclusion

In this chapter, a new plasmonic platform for the detection of EVs was developed and tested. For this purpose, a novel technique of fabrication of the thin and very thin gold films was investigated, namely e-beam deposition, that is, a physical method not prone to contamination. This method has many advantages over chemical methods and other physical deposition methods as well. The e-beam source is capable of heating materials to much higher temperatures than is possible using a crucible heater. This allows for very high deposition rates and evaporation of high-temperature materials and refractory metals. In addition, films deposited by electron beam evaporation can better maintain the purity of the source material as water cooling of the crucible tightly confines the electron beam heating to only the area occupied by the source material,

eliminating any unwanted contamination. e-beam deposited films are highly uniform and can be used for the deposition of two successive films as well.

To prepare the gold plasmonic platform for the detection of EVs, two adhesion layers, Chromium (Cr) or Indium Tin Oxide (ITO), respectively, have been e-beam-deposited on a borosilicate glass substrate, before the deposition of gold, to improve the adhesion of gold and consolidate the whole system. To prepare the nano-island films, the gold films were dewetted by annealing under varying temperatures and duration conditions. The results proved that thin nano-island gold films can be prepared from e-beam deposited films. Their morphology and plasmonic properties were thoroughly investigated and their suitability for EV detection has been evaluated in terms of refractive index sensibility. The results have revealed that the morphology of the as-deposited Au film strongly depends on the adhesion layer. Gold forms a chain-like morphology on the Chromium adhesion layer, while on ITO, SEM images revealed the presence of small Au nanoparticles, distributed uniformly. The XRD patterns of the platforms evidenced, principally, the Au peaks because of the reduced thickness of both the Au and the adhesion layers. It is presumed that the interdiffusion of Chromium into the gold layer and *vice versa* takes place even during the fabrication and, certainly, is intensified during the annealing process. Regarding the ITO layer, possibly, its XRD peaks overlap with the Au peaks. XRD data, regarding the annealed platforms demonstrated that during the annealing process, Chromium was oxidized by the air from the oven and formed chromic oxide (Cr_2O_3). The SEM images have been analyzed and the size distribution of nano-islands, in the case of utilizing the Chromium adhesion layer and nanoparticles, in the case of ITO, was determined, by using Image J software. The average size of nano-islands on the Chromium layer was found around 30 to 35 nm and that of nanoparticles (by using the ITO adhesion layer) was 6 to 8 nm. The density of the nano-islands was much higher than that of the nano-islands fabricated by thermal convection of gold colloids. These results confirm the strong dependency of the morphology of gold nanostructures on the physical and chemical properties of the substrates, in this case, the two adhesion layers. To account for this result, more experiments will have to be done in the future. The refractive index sensitivity of the two platforms has been determined experimentally and validated by simulation. The platform, having the ITO adhesion layer, has proved to be not sensitive enough for detection purposes (around 21.00 RIU/nm, compared with around 72.00 RIU/nm, the sensitivity of the platform with the Chromium adhesion layer). Because of the very low sensitivity of the ITO platform, only the

Chromium platform has been considered for quantitative measurements and has been further investigated by EDS to find out the elementary composition in different parts of the platform. The EDS results confirmed the diffusion of Chromium into the gold layer, showing that the spatial identity of the chromium adhesion layers is not preserved anymore during the high-temperature annealing process. These results show that, in the case of very thin gold films, the efficacy of adhesion layers is lower than in the case of thicker gold films.

Therefore, based on the characterization results the Cr-Au platforms annealed at, 600 °C and 650 °C were decided to use for the detection of the EVs by the direct detection method. The calibration curves were established by preparing several concentrations of EV in its dilution media, with initial known concentrations. For this purpose, accurately measured volumes of EV were diluted with dilution media, and thoroughly mixed to obtain uniform solutions. Each solution was carefully put on the surface of the platform and the experiments were carried out. It could be concluded that based on the comparison of the sensitivity the solid-state dewetted platforms are more sensitive than *in-situ* and *ex-situ* platforms that were studied for the detection of EVs/exosomes derived from the MCF7 breast cancer cell line. Also, the direct detection method seemed to be more sensitive than the immunoaffinity method that has been studied as part of this thesis work. Thus, through this developed novel platform the sensitivity has been improved by 1.5 times and the detection time has been reduced by almost one-fourth of the time as compared to the immunoaffinity method that has been studied in this thesis work.

Chapter 9. Conclusions and Future Works

9.1. Conclusions

The major goal of this doctoral research work was to identify and develop many sensing platforms for early diagnosis of breast cancer through exosomes. For the detection of EVs/ exosomes derived from the MCF-7 breast cancer cell line, the initial research was carried out on the *ex-situ* synthesis of gold and the *in-situ* and fabrication of gold (and silver)-PDMS nanocomposites to determine their potential utility as plasmonic platforms. The platforms underwent fabrication, structural analysis, and performance evaluation for the detection of EVs/exosomes. The *ex-situ gold* and *in-situ* silver-PDMS nanocomposites, respectively, were found to be sufficiently sensitive for detection. However, the *in-situ* generated gold nanoparticles were not acceptable for analytical purposes due to their uneven distribution, concentration in a subsurface layer, and lack of direct interaction with the surrounding media.

Thus, for the detection of EVs/ exosomes with better sensitivity than the *ex-situ* synthesis of gold and the *in-situ* synthesis of silver-PDMS nanocomposites platforms a new platform based on the e-beam deposition, a physical vapor deposition technique that minimizes contamination was developed. The e-beam evaporation offers several advantages, including a higher deposition rate, the ability to handle materials at high temperatures, and the preservation of material purity. This method produces highly homogeneous films that are suitable for multiple layers. Therefore, to enhance the adhesion of gold, Chromium (Cr) or Indium Tin Oxide (ITO) layers were e-beam-deposited on a borosilicate glass substrate before gold deposition. The Cr-Au and ITO-Au platforms were then annealed at different temperatures to form nano-islands or nanoparticles.

Both the platforms were characterized using UV-Vis spectroscopy, FESEM, EDS, AFM, and XRD to analyze their plasmonic properties, structure, morphology, and elemental composition. Furthermore, the refractive index sensitivity of both platforms was determined based on the results of the characterization study. The refractive index sensitivity study revealed that the Cr-Au platform is significantly more sensitive (72.00 RIU/nm) than the ITO-Au platform (21.00 RIU/nm). Thus, only the Cr-Au platform was considered suitable for the quantitative LSPR detection of EVs/exosomes. In addition, the other novelty in the present study is to directly immobilize the EVs/exosomes to the formed nano-islands using the van der Waals force of attraction (charge-based affinity) without any surface chemistry modification of the plasmonic

platform as in our earlier studies. It is important to reduce the time taken for the detection of EVs/exosomes and to be cost-effective. Further detection studies were carried out for various known concentrations of the MCF7 EVs/exosomes. By comparing the detection sensitivity results with the current method and the previously developed immunoaffinity method, it can be concluded that solid-state dewetted platforms are more sensitive than the *in-situ* and *ex-situ* platforms that were investigated to detect EVs/exosomes derived from the MCF7 breast cancer cell line.

9.2. Future works

The potential ways to expand and enhance this research work are:

(1) To further validate the direct detection method using the elution of the new platform to isolate MCF7 EVs/exosomes from the substrates and then perform the characterization of it using Nanoparticle Tracking Analysis (NTA), Tunable Resistive Pulse Sensing (TRPS) and Transmission Electron Microscopy (TEM).

(2) Studies to explore the sensitivity of the new platform using antibodies to detect and isolate the EVs/exosomes.

(3) To explore the integration of the developed new platform into Lab-on-a-Chip (LOC) technology and a part of this work has been already completed. but, it is not included in the thesis.

(4) Theoretical validation of refractive index sensitivity of the new platform and a part of this work have been already completed but not included in the thesis.

(5) *In-situ* characterization of the capture performance of the LOC for various concentrations of EVs/exosomes for different cancer cell lines and other related sample sources through imaging (TEM and SEM).

(6) Molecular analysis of captured EVs/exosomes by Droplet Digital PCR (ddPCR) based amplification and sequencing for the diagnostic purpose as a point of care device.

(7) In the future, it would be interesting to investigate other adhesion layers as well such as Ti, Ni, Pt, or Ge, and their diffusion patterns at high temperatures.

(8) Also, it would be interesting to investigate gold films slightly thicker that may be more stable, regarding the phenomenon of interdiffusion.

References

1. Mashburn, L.M.; Whiteley, M. Membrane Vesicles Traffic Signals and Facilitate Group Activities in a Prokaryote. *Nature* **2005**, *437*, 422–425, doi:10.1038/nature03925.

2. Kulp, A.; Kuehn, M.J. Biological Functions and Biogenesis of Secreted Bacterial Outer Membrane Vesicles. *Annu Rev Microbiol* **2010**, *64*, 163–184, doi:10.1146/annurev.micro.091208.073413.

3. M., K.; K., R.; G., K.K. What Are Eukaryotic Cells? Available online: https://socratic.org/questions/what-are-eukaryotic-cells (accessed on 27 May 2024).

4. Fuhrmann, G.; Herrmann, I.K.; Stevens, M.M. Cell-Derived Vesicles for Drug Therapy and Diagnostics: Opportunities and Challenges. *Nano Today* **2015**, *10*, 397–409, doi:10.1016/j.nantod.2015.04.004.

5. Yáñez-Mó, M.; Siljander, P.R.-M.; Andreu, Z.; Bedina Zavec, A.; Borràs, F.E.; Buzas, E.I.; Buzas, K.; Casal, E.; Cappello, F.; Carvalho, J.; et al. Biological Properties of Extracellular Vesicles and Their Physiological Functions. *J. Extracell. Vesicles* **2015**, *4*, 27066, doi:10.3402/jev.v4.27066.

6. György, B.; Szabó, T.G.; Pásztói, M.; Pál, Z.; Misják, P.; Aradi, B.; László, V.; Pállinger, É.; Pap, E.; Kittel, Á.; et al. Membrane Vesicles, Current State-of-the-Art: Emerging Role of Extracellular Vesicles. *Cell Mol Life Sci* **2011**, *68*, 2667–2688, doi:10.1007/s00018-011-0689-3.

7. Conde-Vancells, J.; Rodriguez-Suarez, E.; Embade, N.; Gil, D.; Matthiesen, R.; Valle, M.; Elortza, F.; Lu, S.C.; Mato, J.M.; Falcon-Perez, J.M. Characterization and Comprehensive Proteome Profiling of Exosomes Secreted by Hepatocytes. *J. Proteome Res.* **2008**, *7*, 5157–5166.

8. Pol, E. van der; Böing, A.N.; Harrison, P.; Sturk, A.; Nieuwland, R. Classification, Functions, and Clinical Relevance of Extracellular Vesicles. *Pharmacol Rev* **2012**, *64*, 676–705, doi:10.1124/pr.112.005983.

9. Yuana, Y.; Oosterkamp, T.H.; Bahatyrova, S.; Ashcroft, B.; Garcia Rodriguez, P.; Bertina, R.M.; Osanto, S. Atomic Force Microscopy: A Novel Approach to the Detection of Nanosized Blood Microparticles. *J Thromb Haemost* **2010**, *8*, 315–323, doi:10.1111/j.1538-7836.2009.03654.x.

10. Dragovic, R.A.; Gardiner, C.; Brooks, A.S.; Tannetta, D.S.; Ferguson, D.J.P.; Hole, P.; Carr, B.; Redman, C.W.G.; Harris, A.L.; Dobson, P.J.; et al. Sizing and Phenotyping of Cellular Vesicles Using Nanoparticle Tracking Analysis. *Nanomedicine* **2011**, *7*, 780–788, doi:10.1016/j.nano.2011.04.003.

11. Tominaga, N.; Yoshioka, Y.; Ochiya, T. A Novel Platform for Cancer Therapy Using Extracellular Vesicles. *Advanced Drug Delivery Reviews* **2015**, *95*, 50–55, doi:10.1016/j.addr.2015.10.002.

12. Wilson, C.M.; Magnaudeix, A.; Naves, T.; Vincent, F.; Lalloue, F.; Jauberteau, M.-O. The Ins and Outs of Nanoparticle Technology in Neurodegenerative Diseases and Cancer. *Curr Drug Metab* **2015**, *16*, 609–632, doi:10.2174/1389200216666150812121902.

13. van der Pol, E.; Hoekstra, A.G.; Sturk, A.; Otto, C.; van Leeuwen, T.G.; Nieuwland, R. Optical and Non-Optical Methods for Detection and Characterization of Microparticles and Exosomes. *J Thromb Haemost* **2010**, *8*, 2596–2607, doi:10.1111/j.1538-7836.2010.04074.x.

14. van der Pol, E.; Böing, A.N.; Gool, E.L.; Nieuwland, R. Recent Developments in the Nomenclature, Presence, Isolation, Detection and Clinical Impact of Extracellular Vesicles. *J Thromb Haemost* **2016**, *14*, 48–56, doi:10.1111/jth.13190.

15. Chargaff, E.; West, R. The Biological Significance of the Thromboplastic Protein of Blood. *J Biol Chem* **1946**, *166*, 189–197.

16. Wolf, P. The Nature and Significance of Platelet Products in Human Plasma. *Brit. J. Haematol* **1967**, *13*, 269–288, doi:10.1111/j.1365-2141.1967.tb08741.x.

17. He, M.; Zeng, Y. Microfluidic Exosome Analysis toward Liquid Biopsy for Cancer. *J Lab Autom.* **2016**, *21*, 599–608, doi:10.1177/2211068216651035.

18. Canadian Cancer Statistics Advisory Committee; Canadian Cancer Society; Statistics Canada; The Public Health Agency of Canada *Canadian Cancer Statistics 2023*; Canadian Cancer Society: Toronto, ON, 2023;

19. Cooke, B.A.; Molen, H.J.V.D.; King, R.J.B. *Hormones and Their Actions, Part 1*; 1st ed.; Elsevier, 1988; Vol. 18A; ISBN 978-0-08-086077-0.

20. Ozhikandathil, J.; Badilescu, S.; Packirisamy, M. A Brief Review on Microfluidic Platforms for Hormones Detection. *J Neural Transm (Vienna)* **2017**, *124*, 47–55, doi:10.1007/s00702-016-1610-x.

21. Kowal, J.; Arras, G.; Colombo, M.; Jouve, M.; Morath, J.P.; Primdal-Bengtson, B.; Dingli, F.; Loew, D.; Tkach, M.; Théry, C. Proteomic Comparison Defines Novel Markers to Characterize Heterogeneous Populations of Extracellular Vesicle Subtypes. *Proc Natl Acad Sci U S A* **2016**, *113*, E968–E977, doi:10.1073/pnas.1521230113.

22. Simons, M.; Raposo, G. Exosomes--Vesicular Carriers for Intercellular Communication. *Curr Opin Cell Biol* **2009**, *21*, 575–581, doi:10.1016/j.ceb.2009.03.007.

23. Nieuwland, R.; Sturk, A. Why Do Cells Release Vesicles? *Thrombosis Research* **2010**, *125*, S49–S51, doi:10.1016/j.thromres.2010.01.037.

24. Chargaff, E.; West, R. THE BIOLOGICAL SIGNIFICANCE OF THE THROMBOPLASTIC PROTEIN OF BLOOD. *J. Biol. Chem.* **1946**, *166*, 189–197, doi:10.1016/S0021-9258(17)34997-9.

25. Trams, E.G.; Lauter, C.J.; Norman Salem, Jr.; Heine, U. Exfoliation of Membrane Ecto-Enzymes in the Form of Micro-Vesicles. *Biochim Biophys Acta Biomembr.* **1981**, *645*, 63–70, doi:10.1016/0005-2736(81)90512-5.

26. Johnstone, R.M.; Adam, M.; Hammond, J.R.; Orr, L.; Turbide, C. Vesicle Formation during Reticulocyte Maturation. Association of Plasma Membrane Activities with Released Vesicles (Exosomes). *J. Biol. Chem.* **1987**, *262*, 9412–9420, doi:10.1016/S0021-9258(18)48095-7.

27. Raposo, G.; Nijman, H.W.; Stoorvogel, W.; Liejendekker, R.; Harding, C.V.; Melief, C.J.; Geuze, H.J. B Lymphocytes Secrete Antigen-Presenting Vesicles. *J. Exp. Med.* **1996**, *183*, 1161–1172, doi:10.1084/jem.183.3.1161.

28. Zitvogel, L.; Regnault, A.; Lozier, A.; Wolfers, J.; Flament, C.; Tenza, D.; Ricciardi-Castagnoli, P.; Raposo, G.; Amigorena, S. Eradication of Established Murine Tumors Using a Novel Cell-Free Vaccine: Dendritic Cell Derived Exosomes. *Nat Med* **1998**, *4*, 594–600, doi:10.1038/nm0598-594.

29. Mathivanan, S.; Simpson, R.J. ExoCarta: A Compendium of Exosomal Proteins and RNA. *Proteomics* **2009**, *9*, 4997–5000, doi:10.1002/pmic.200900351.

30. Valadi, H.; Ekström, K.; Bossios, A.; Sjöstrand, M.; Lee, J.J.; Lötvall, J.O. Exosome-Mediated Transfer of mRNAs and microRNAs Is a Novel Mechanism of Genetic Exchange between Cells. *Nat Cell Biol* **2007**, *9*, 654–659, doi:10.1038/ncb1596.

31. Liga, A.; B. Vliegenthart, A.D.; Oosthuyzen, W.; W. Dear, J.; Kersaudy-Kerhoas, M. Exosome Isolation: A Microfluidic Road-Map. *Lab Chip* **2015**, *15*, 2388–2394, doi:10.1039/C5LC00240K.

32. Liu, C.; Yang, Y.; Wu, Y. Recent Advances in Exosomal Protein Detection Via Liquid Biopsy Biosensors for Cancer Screening, Diagnosis, and Prognosis. *AAPS J* **2018**, *20*, 41, doi:10.1208/s12248-018-0201-1.

33. Ding, L.; Yang, X.; Gao, Z.; Effah, C.Y.; Zhang, X.; Wu, Y.; Qu, L. A Holistic Review of the State-of-the-Art Microfluidics for Exosome Separation: An Overview of the Current Status, Existing Obstacles, and Future Outlook. *Small* **2021**, *17*, 2007174, doi:10.1002/smll.202007174.

34. Mohammadi, M.; Zargartalebi, H.; Salahandish, R.; Aburashed, R.; Wey Yong, K.; Sanati-Nezhad, A. Emerging Technologies and Commercial Products in Exosome-Based Cancer Diagnosis and Prognosis. *Biosens. Bioelectron* **2021**, *183*, 113176, doi:10.1016/j.bios.2021.113176.

35. Chaput, N.; Théry, C. Exosomes: Immune Properties and Potential Clinical Implementations. *Semin Immunopathol* **2011**, *33*, 419–440, doi:10.1007/s00281-010-0233-9.

36. EL Andaloussi, S.; Mäger, I.; Breakefield, X.O.; Wood, M.J.A. Extracellular Vesicles: Biology and Emerging Therapeutic Opportunities. *Nat Rev Drug Discov* **2013**, *12*, 347–357, doi:10.1038/nrd3978.

37. Suntres, Z.E.; Smith, M.G.; Momen-Heravi, F.; Hu, J.; Zhang, X.; Wu, Y.; Zhu, H.; Wang, J.; Zhou, J.; Kuo, W.P. Therapeutic Uses of Exosomes. *Exosomes and Microvesicles* **2013**, *1*, 5, doi:10.5772/56522.

38. Saad, M.G.; Beyenal, H.; Dong, W.-J. Exosomes as Powerful Engines in Cancer: Isolation, Characterization and Detection Techniques. *Biosensors* **2021**, *11*, 518, doi:10.3390/bios11120518.

39. Soltész, B.; Buglyó, G.; Németh, N.; Szilágyi, M.; Pös, O.; Szemes, T.; Balogh, I.; Nagy, B. The Role of Exosomes in Cancer Progression. *Int. J. Mol. Sci.* **2022**, *23*, 8, doi:10.3390/ijms23010008.

40. Zhou, Y.; Zhang, Y.; Gong, H.; Luo, S.; Cui, Y. The Role of Exosomes and Their Applications in Cancer. *Int J Mol Sci* **2021**, *22*, 12204, doi:10.3390/ijms222212204.

41. Ciferri, M.C.; Quarto, R.; Tasso, R. Extracellular Vesicles as Biomarkers and Therapeutic Tools: From Pre-Clinical to Clinical Applications. *Biology* **2021**, *10*, 359, doi:10.3390/biology10050359.

42. Chaffer, C.L.; Weinberg, R.A. A Perspective on Cancer Cell Metastasis. *Science* **2011**, *331*, 1559–1564, doi:10.1126/science.1203543.

43. Diehl, F.; Schmidt, K.; Choti, M.A.; Romans, K.; Goodman, S.; Li, M.; Thornton, K.; Agrawal, N.; Sokoll, L.; Szabo, S.A.; et al. Circulating Mutant DNA to Assess Tumor Dynamics. *Nat Med* **2008**, *14*, 985–990, doi:10.1038/nm.1789.

44. Sedlackova, T.; Repiska, G.; Celec, P.; Szemes, T.; Minarik, G. Fragmentation of DNA Affects the Accuracy of the DNA Quantitation by the Commonly Used Methods. *Biol Proced Online* **2013**, *15*, 5, doi:10.1186/1480-9222-15-5.

45. Chen, C.; Skog, J.; Hsu, C.-H.; Lessard, R.T.; Balaj, L.; Wurdinger, T.; Carter, B.S.; Breakefield, X.O.; Toner, M.; Irimia, D. Microfluidic Isolation and Transcriptome Analysis of Serum Microvesicles. *Lab Chip* **2010**, *10*, 505–511, doi:10.1039/B916199F.

46. Nawaz, M.; Camussi, G.; Valadi, H.; Nazarenko, I.; Ekström, K.; Wang, X.; Principe, S.; Shah, N.; Ashraf, N.M.; Fatima, F.; et al. The Emerging Role of Extracellular Vesicles as Biomarkers for Urogenital Cancers. *Nat Rev Urol* **2014**, *11*, 688–701, doi:10.1038/nrurol.2014.301.

47. Merchant, M.L.; Rood, I.M.; Deegens, J.K.J.; Klein, J.B. Isolation and Characterization of Urinary Extracellular Vesicles: Implications for Biomarker Discovery. *Nat Rev Nephrol* **2017**, *13*, 731–749, doi:10.1038/nrneph.2017.148.

48. Théry, C.; Amigorena, S.; Raposo, G.; Clayton, A. Isolation and Characterization of Exosomes from Cell Culture Supernatants and Biological Fluids. *Curr Protoc Cell Biol* **2006**, *30*, 3.22.1-3.22.29, doi:10.1002/0471143030.cb0322s30.

49. Lamparski, H.G.; Metha-Damani, A.; Yao, J.-Y.; Patel, S.; Hsu, D.-H.; Ruegg, C.; Le Pecq, J.-B. Production and Characterization of Clinical Grade Exosomes Derived from Dendritic Cells. *J. Immunol. Methods* **2002**, *270*, 211–226, doi:10.1016/S0022-1759(02)00330-7.

50. van der Meel, R.; Krawczyk-Durka, M.; van Solinge, W.W.; Schiffelers, R.M. Toward Routine Detection of Extracellular Vesicles in Clinical Samples. *Int. J. Lab. Hematol.* **2014**, *36*, 244–253, doi:10.1111/ijlh.12247.

51. Caradec, J.; Kharmate, G.; Hosseini-Beheshti, E.; Adomat, H.; Gleave, M.; Guns, E. Reproducibility and Efficiency of Serum-Derived Exosome Extraction Methods. *Clin. Biochem* **2014**, *47*, 1286–1292, doi:10.1016/j.clinbiochem.2014.06.011.

52. Wang, W.; Luo, J.; Wang, S. Recent Progress in Isolation and Detection of Extracellular Vesicles for Cancer Diagnostics. *Adv. Healthc. Mater.* **2018**, *7*, 1800484, doi:10.1002/adhm.201800484.

53. Lozano-Ramos, I.; Bancu, I.; Oliveira-Tercero, A.; Armengol, M.P.; Menezes-Neto, A.; Portillo, H.A.D.; Lauzurica-Valdemoros, R.; Borràs, F.E. Size-Exclusion Chromatography-Based Enrichment of Extracellular Vesicles from Urine Samples. *J. Extracell. Vesicles* **2015**, *4*, 27369, doi:10.3402/jev.v4.27369.

54. Mol, E.A.; Goumans, M.-J.; Doevendans, P.A.; Sluijter, J.P.G.; Vader, P. Higher Functionality of Extracellular Vesicles Isolated Using Size-Exclusion Chromatography Compared to Ultracentrifugation. *Nanomedicine* **2017**, *13*, 2061–2065, doi:10.1016/j.nano.2017.03.011.

55. Chen, J.; Li, P.; Zhang, T.; Xu, Z.; Huang, X.; Wang, R.; Du, L. Review on Strategies and Technologies for Exosome Isolation and Purification. *Front. Bioeng. Biotechnol.* **2022**, *9*, 811971.

56. Shirejini, S.Z.; Inci, F. The Yin and Yang of Exosome Isolation Methods: Conventional Practice, Microfluidics, and Commercial Kits. *Biotechnol. Adv* **2022**, *54*, 107814, doi:10.1016/j.biotechadv.2021.107814.

57. Yamamoto, K.R.; Alberts, B.M.; Benzinger, R.; Lawhorne, L.; Treiber, G. Rapid Bacteriophage Sedimentation in the Presence of Polyethylene Glycol and Its Application to Large-Scale Virus Purification. *Virology* **1970**, *40*, 734–744, doi:10.1016/0042-6822(70)90218-7.

58. Gallart-Palau, X.; Serra, A.; Wong, A.S.W.; Sandin, S.; Lai, M.K.P.; Chen, C.P.; Kon, O.L.; Sze, S.K. Extracellular Vesicles Are Rapidly Purified from Human Plasma by PRotein Organic Solvent PRecipitation (PROSPR). *Sci Rep* **2015**, *5*, 14664, doi:10.1038/srep14664.

59. Chen, C.; Lin, B.-R.; Wang, H.-K.; Fan, S.-T.; Hsu, M.-Y.; Cheng, C.-M. Paper-Based Immunoaffinity Devices for Accessible Isolation and Characterization of Extracellular Vesicles. *Microfluid Nanofluid* **2014**, *16*, 849–856, doi:10.1007/s10404-014-1359-1.

60. Ghosh, A.; Davey, M.; Chute, I.C.; Griffiths, S.G.; Lewis, S.; Chacko, S.; Barnett, D.; Crapoulet, N.; Fournier, S.; Joy, A.; et al. Rapid Isolation of Extracellular Vesicles from Cell Culture and Biological Fluids Using a Synthetic Peptide with Specific Affinity for Heat Shock Proteins. *PLOS ONE* **2014**, *9*, e110443, doi:10.1371/journal.pone.0110443.

61. Wang, S.; Zhang, L.; Wan, S.; Cansiz, S.; Cui, C.; Liu, Y.; Cai, R.; Hong, C.; Teng, I.-T.; Shi, M.; et al. Aptasensor with Expanded Nucleotide Using DNA Nanotetrahedra for Electrochemical Detection of Cancerous Exosomes. *ACS Nano* **2017**, *11*, 3943–3949, doi:10.1021/acsnano.7b00373.

62. Wan, Y.; Cheng, G.; Liu, X.; Hao, S.-J.; Nisic, M.; Zhu, C.-D.; Xia, Y.-Q.; Li, W.-Q.; Wang, Z.-G.; Zhang, W.-L.; et al. Rapid Magnetic Isolation of Extracellular Vesicles via Lipid-Based Nanoprobes. *Nat Biomed Eng* **2017**, *1*, 1–11, doi:10.1038/s41551-017-0058.

63. Su, W.; Li, H.; Chen, W.; Qin, J. Microfluidic Strategies for Label-Free Exosomes Isolation and Analysis. *TrAC Trends in Analytical Chemistry* **2019**, *118*, 686–698, doi:10.1016/j.trac.2019.06.037.

64. C. Contreras-Naranjo, J.; Wu, H.-J.; M. Ugaz, V. Microfluidics for Exosome Isolation and Analysis: Enabling Liquid Biopsy for Personalized Medicine. *Lab Chip* **2017**, *17*, 3558–3577, doi:10.1039/C7LC00592J.

65. Iliescu, F.S.; Vrtačnik, D.; Neuzil, P.; Iliescu, C. Microfluidic Technology for Clinical Applications of Exosomes. *Micromachines* **2019**, *10*, 392, doi:10.3390/mi10060392.

66. Rojalin, T.; Phong, B.; Koster, H.J.; Carney, R.P. Nanoplasmonic Approaches for Sensitive Detection and Molecular Characterization of Extracellular Vesicles. *Front. Chem.* **2019**, *7*, 00279.

67. Ohannesian, N.; Gunawardhana, L.; Misbah, I.; Rakhshandehroo, M.; Lin, S.H.; Shih, W.-C. Commercial and Emerging Technologies for Cancer Diagnosis and Prognosis Based on Circulating Tumor Exosomes. *J. Phys. Photonics* **2020**, *2*, 032002, doi:10.1088/2515-7647/ab8699.

68. Choi, J.-H.; Lee, J.-H.; Choi, J.-W. Applications of Bionano Sensor for Extracellular Vesicles Analysis. *Materials* **2020**, *13*, 3677, doi:10.3390/ma13173677.

69. Wang, L.; Pan, M.-M.; Xu, L.; Yu, X.; Zheng, S.-Y. Recent Advances of Emerging Microfluidic Chips for Exosome Mediated Cancer Diagnosis. *Smart Mater Med* **2021**, *2*, 158–171, doi:10.1016/j.smaim.2021.06.001.

70. Ma, X.; Hao, Y.; Liu, L. Progress in Nanomaterials-Based Optical and Electrochemical Methods for the Assays of Exosomes. *Int. J. Nanomed.* **2021**, *16*, 7575–7608, doi:10.2147/IJN.S333969.

71. Bari, S.M.I.; Hossain, F.B.; Nestorova, G.G. Advances in Biosensors Technology for Detection and Characterization of Extracellular Vesicles. *Sensors* **2021**, *21*, 7645, doi:10.3390/s21227645.

72. Suwatthanarak, T.; Thiodorus, I.A.; Tanaka, M.; Shimada, T.; Takeshita, D.; Yasui, T.; Baba, Y.; Okochi, M. Microfluidic-Based Capture and Release of Cancer-Derived Exosomes via Peptide–Nanowire Hybrid Interface. *Lab Chip* **2021**, *21*, 597–607, doi:10.1039/D0LC00899K.

73. Xu, Y.-Q.; Bao, Q.-Y.; Yu, S.-X.; Liu, Q.; Xie, Y.; Li, X.; Liu, Y.-J.; Shen, Y.-H. A Novel Microfluidic Chip for Fast, Sensitive Quantification of Plasma Extracellular Vesicles as Biomarkers in Patients With Osteosarcoma. *Front. Oncol.* **2021**, *11*, 709255.

74. Weaver, E.; Uddin, S.; Cole, D.K.; Hooker, A.; Lamprou, D.A. The Present and Future Role of Microfluidics for Protein and Peptide-Based Therapeutics and Diagnostics. *Appl. Sci.* **2021**, *11*, 4109, doi:10.3390/app11094109.

75. Malhotra, S.; Amin, Z.M.; Dobhal, G.; Cottam, S.; Nann, T.; Goreham, R.V. Novel Devices for Isolation and Detection of Bacterial and Mammalian Extracellular Vesicles. *Mikrochim Acta* **2021**, *188*, 139, doi:10.1007/s00604-021-04790-5.

76. Takahashi, H.; Baba, Y.; Yasui, T. Oxide Nanowire Microfluidics Addressing Previously-Unattainable Analytical Methods for Biomolecules towards Liquid Biopsy. *Chem. Commun.* **2021**, *57*, 13234–13245, doi:10.1039/D1CC05096F.

77. Li, G.; Zhu, N.; Zhou, J.; Kang, K.; Zhou, X.; Ying, B.; Yi, Q.; Wu, Y. A Magnetic Surface-Enhanced Raman Scattering Platform for Performing Successive Breast Cancer Exosome Isolation and Analysis. *J. Mater. Chem. B* **2021**, *9*, 2709–2716, doi:10.1039/D0TB02894K.

78. Chen, W.; Xie, Y.; Chang, Y.; Xu, Y.; Zhao, M.; Deng, P.; Qin, J.; Li, H. A Portable Device for Simple Exosome Separation from Biological Samples. *Micromachines* **2021**, *12*, 1182, doi:10.3390/mi12101182.

79. Zhu, N.; Zhang, Y.; Cheng, J.; Mao, Y.; Kang, K.; Li, G.; Yi, Q.; Wu, Y. Immuno-Affinitive Supramolecular Magnetic Nanoparticles Incorporating Cucurbit[8]Uril-Mediated Ternary Host-Guest Complexation Structures for High-Efficient Small Extracellular Vesicle Enrichment. *J. Colloid Interface Sci.* **2022**, *611*, 462–471, doi:10.1016/j.jcis.2021.12.109.

80. Li, G.; Zhu, N.; Cheng, J.; Zhang, Y.; Yu, Y.; Zhang, X.; Yi, Q.; Wu, Y. Dynamic Biological Interfaces Functionalized Fructose-Responsive Immunomagnetic Beads for High-Efficient and High-Purity Exosome Enrichment. *Mater. Des.* **2022**, *213*, 110366, doi:10.1016/j.matdes.2021.110366.

81. Vaz, R.; Serrano, V.M.; Castaño-Guerrero, Y.; Cardoso, A.R.; Frasco, M.F.; Sales, M.G.F. Breaking the Classics: Next-Generation Biosensors for the Isolation, Profiling and Detection of Extracellular Vesicles. *Biosens. Bioelectron: X* **2022**, *10*, 100115, doi:10.1016/j.biosx.2022.100115.

82. Xu, K.; Jin, Y.; Li, Y.; Huang, Y.; Zhao, R. Recent Progress of Exosome Isolation and Peptide Recognition-Guided Strategies for Exosome Research. *Front. Chem.* **2022**, *10*, 844124.

83. M. Abreu, C.; Costa-Silva, B.; L. Reis, R.; C. Kundu, S.; Caballero, D. Microfluidic Platforms for Extracellular Vesicle Isolation, Analysis and Therapy in Cancer. *Lab Chip* **2022**, *22*, 1093–1125, doi:10.1039/D2LC00006G.

84. Tian, F.; Liu, C.; Deng, J.; Sun, J. Microfluidic Separation, Detection, and Engineering of Extracellular Vesicles for Cancer Diagnostics and Drug Delivery. *Acc. Mater. Res.* **2022**, *3*, 498–510, doi:10.1021/accountsmr.1c00276.

85. Wang, Z.; Wu, H.; Fine, D.; Schmulen, J.; Hu, Y.; Godin, B.; J. Zhang, J.X.; Liu, X. Ciliated Micropillars for the Microfluidic-Based Isolation of Nanoscale Lipid Vesicles. *Lab Chip* **2013**, *13*, 2879–2882, doi:10.1039/C3LC41343H.

86. Jørgensen, M.; Bæk, R.; Pedersen, S.; Søndergaard, E.K.L.; Kristensen, S.R.; Varming, K. Extracellular Vesicle (EV) Array: Microarray Capturing of Exosomes and Other Extracellular Vesicles for Multiplexed Phenotyping. *J. Extracell. Vesicles* **2013**, *2*, 20920, doi:10.3402/jev.v2i0.20920.

87. Jørgensen, M.M.; Bæk, R.; Varming, K. Potentials and Capabilities of the Extracellular Vesicle (EV) Array. *J. Extracell. Vesicles* **2015**, *4*, 26048, doi:10.3402/jev.v4.26048.

88. He, M.; Crow, J.; Roth, M.; Zeng, Y.; K. Godwin, A. Integrated Immunoisolation and Protein Analysis of Circulating Exosomes Using Microfluidic Technology. *Lab Chip* **2014**, *14*, 3773–3780, doi:10.1039/C4LC00662C.

89. Singh Kanwar, S.; James Dunlay, C.; M. Simeone, D.; Nagrath, S. Microfluidic Device (ExoChip) for on-Chip Isolation, Quantification and Characterization of Circulating Exosomes. *Lab Chip* **2014**, *14*, 1891–1900, doi:10.1039/C4LC00136B.

90. Lee, K.; Shao, H.; Weissleder, R.; Lee, H. Acoustic Purification of Extracellular Microvesicles. *ACS Nano* **2015**, *9*, 2321–2327, doi:10.1021/nn506538f.

91. Zhao, Z.; Yang, Y.; Zeng, Y.; He, M. A Microfluidic ExoSearch Chip for Multiplexed Exosome Detection towards Blood-Based Ovarian Cancer Diagnosis. *Lab Chip* **2016**, *16*, 489–496, doi:10.1039/C5LC01117E.

92. Zhang, P.; He, M.; Zeng, Y. Ultrasensitive Microfluidic Analysis of Circulating Exosomes Using a Nanostructured Graphene Oxide/Polydopamine Coating. *Lab Chip* **2016**, *16*, 3033–3042, doi:10.1039/C6LC00279J.

93. Fang, S.; Tian, H.; Li, X.; Jin, D.; Li, X.; Kong, J.; Yang, C.; Yang, X.; Lu, Y.; Luo, Y.; et al. Clinical Application of a Microfluidic Chip for Immunocapture and Quantification of

Circulating Exosomes to Assist Breast Cancer Diagnosis and Molecular Classification. *PLOS ONE* **2017**, *12*, e0175050, doi:10.1371/journal.pone.0175050.

94. Bathini, S.; Pakkiriswami, S.; Ouellette, R.J.; Ghosh, A.; Packirisamy, M. Magnetic Particle Based Liquid Biopsy Chip for Isolation of Extracellular Vesicles and Characterization by Gene Amplification. *Biosens. Bioelectron* **2021**, *194*, 113585, doi:10.1016/j.bios.2021.113585.

95. Im, H.; Shao, H.; Park, Y.I.; Peterson, V.M.; Castro, C.M.; Weissleder, R.; Lee, H. Label-Free Detection and Molecular Profiling of Exosomes with a Nano-Plasmonic Sensor. *Nat Biotechnol* **2014**, *32*, 490–495, doi:10.1038/nbt.2886.

96. Vaidyanathan, R.; Naghibosadat, M.; Rauf, S.; Korbie, D.; Carrascosa, L.G.; Shiddiky, M.J.A.; Trau, M. Detecting Exosomes Specifically: A Multiplexed Device Based on Alternating Current Electrohydrodynamic Induced Nanoshearing. *Anal. Chem.* **2014**, *86*, 11125–11132, doi:10.1021/ac502082b.

97. Zhu, L.; Wang, K.; Cui, J.; Liu, H.; Bu, X.; Ma, H.; Wang, W.; Gong, H.; Lausted, C.; Hood, L.; et al. Label-Free Quantitative Detection of Tumor-Derived Exosomes through Surface Plasmon Resonance Imaging. *Anal. Chem.* **2014**, *86*, 8857–8864, doi:10.1021/ac5023056.

98. Bathini, S.; Raju, D.; Badilescu, S.; Kumar, A.; Ouellette, R.J.; Ghosh, A.; Packirisamy, M. Nano–Bio Interactions of Extracellular Vesicles with Gold Nanoislands for Early Cancer Diagnosis. *Research* **2018**, *2018*, 3917986, doi:10.1155/2018/3917986.

99. Bathini, S.; Pakkiriswami, S.; Raju, D.; Badilescu, S.; Ghosh, A.; Ouellette, R.J.; Packirisamy, M. Microfluidic Isolation of Extracellular Vesicles and Validation through AFM and DNA Amplification. *J. Extracell. Vesicles* **2020**, *13*, 50.

100. Raghu, D.; Christodoulides, J.A.; Christophersen, M.; Liu, J.L.; Anderson, G.P.; Robitaille, M.; Byers, J.M.; Raphael, M.P. Nanoplasmonic Pillars Engineered for Single Exosome Detection. *PLOS ONE* **2018**, *13*, e0202773, doi:10.1371/journal.pone.0202773.

101. Lv, X.; Geng, Z.; Su, Y.; Fan, Z.; Wang, S.; Fang, W.; Chen, H. Label-Free Exosome Detection Based on a Low-Cost Plasmonic Biosensor Array Integrated with Microfluidics. *Langmuir* **2019**, *35*, 9816–9824, doi:10.1021/acs.langmuir.9b01237.

102. Ruffino, F.; Grimaldi, M.G. Self-Organized Patterned Arrays of Au and Ag Nanoparticles by Thickness-Dependent Dewetting of Template-Confined Films. *J Mater Sci* **2014**, *49*, 5714–5729, doi:10.1007/s10853-014-8290-4.

103. Thompson, C.V. Solid-State Dewetting of Thin Films. *Annu. Rev. Mater.* **2012**, *42*, 399–434, doi:10.1146/annurev-matsci-070511-155048.

104. Abbott, W.M.; Corbett, S.; Cunningham, G.; Petford-Long, A.; Zhang, S.; Donegan, J.F.; McCloskey, D. Solid State Dewetting of Thin Plasmonic Films under Focused Cw-Laser Irradiation. *Acta Materialia* **2018**, *145*, 210–219, doi:10.1016/j.actamat.2017.12.030.

105. Wong, H.; Voorhees, P.W.; Miksis, M.J.; Davis, S.H. Periodic Mass Shedding of a Retracting Solid Film Step. *Acta Materialia* **2000**, *48*, 1719–1728, doi:10.1016/S1359-6454(00)00016-1.

106. Qiu, G.; Gai, Z.; Tao, Y.; Schmitt, J.; Kullak-Ublick, G.A.; Wang, J. Dual-Functional Plasmonic Photothermal Biosensors for Highly Accurate Severe Acute Respiratory Syndrome Coronavirus 2 Detection. *ACS Nano* **2020**, *14*, 5268–5277, doi:10.1021/acsnano.0c02439.

107. Srolovitz, D.J.; Goldiner, M.G. The Thermodynamics and Kinetics of Film Agglomeration. *JOM* **1995**, *47*, 31–36, doi:10.1007/BF03221433.

108. Findenegg, G.H.; Herminghaus, S. Wetting: Statics and Dynamics. *Curr. Opin. Colloid Interface Sci.* **1997**, *2*, 301–307, doi:10.1016/S1359-0294(97)80039-8.

109. Baumann, N.; Mutoro, E.; Janek, J. Porous Model Type Electrodes by Induced Dewetting of Thin Pt Films on YSZ Substrates. *Solid State Ion.* **2010**, *181*, 7–15, doi:10.1016/j.ssi.2009.11.019.

110. Batič, B.Š.; Verbovšek, T.; Šetina, J. Decomposition of Thin Au Films on Flat and Structured Si Substrate by Annealing. *Vacuum* **2017**, *138*, 134–138, doi:10.1016/j.vacuum.2016.12.006.

111. Łapiński, M.; Kozioł, R.; Cymann, A.; Sadowski, W.; Kościelska, B. Substrate Dependence in the Formation of Au Nanoislands for Plasmonic Platform Application. *Plasmonics* **2020**, *15*, 101–107, doi:10.1007/s11468-019-01021-9.

112. Trice, J.; Thomas, D.; Favazza, C.; Sureshkumar, R.; Kalyanaraman, R. Pulsed-Laser-Induced Dewetting in Nanoscopic Metal Films: Theory and Experiments. *Phys. Rev. B* **2007**, *75*, 235439, doi:10.1103/PhysRevB.75.235439.

113. Nishijima, Y.; Hashimoto, Y.; Seniutinas, G.; Rosa, L.; Juodkazis, S. Engineering Gold Alloys for Plasmonics. *Appl. Phys. A* **2014**, *117*, 641–645, doi:10.1007/s00339-014-8716-5.

114. Tesler, A.B.; Maoz, B.M.; Feldman, Y.; Vaskevich, A.; Rubinstein, I. Solid-State Thermal Dewetting of Just-Percolated Gold Films Evaporated on Glass: Development of the Morphology and Optical Properties. *J. Phys. Chem. C* **2013**, *117*, 11337–11346, doi:10.1021/jp400895z.

115. Thompson, Carl.V.; Carel, R. Texture Development in Polycrystalline Thin Films. *Mater. Sci. Eng. B* **1995**, *32*, 211–219, doi:10.1016/0921-5107(95)03011-5.

116. Wei, H.L.; Huang, H.; Woo, C.H.; Zheng, R.K.; Wen, G.H.; Zhang, X.X. Development of 〈110〉 Texture in Copper Thin Films. *Appl. Phys. Lett* **2002**, *80*, 2290–2292, doi:10.1063/1.1466518.

117. Bhalla, N.; Jain, A.; Lee, Y.; Shen, A.Q.; Lee, D. Dewetting Metal Nanofilms—Effect of Substrate on Refractive Index Sensitivity of Nanoplasmonic Gold. *Nanomaterials* **2019**, *9*, 1530, doi:10.3390/nano9111530.

118. C. Marin, B.; Ramírez, J.; E. Root, S.; Aklile, E.; J. Lipomi, D. Metallic Nanoislands on Graphene: A Metamaterial for Chemical, Mechanical, Optical, and Biological Applications. *Nanoscale Horiz.* **2017**, *2*, 311–318, doi:10.1039/C7NH00095B.

119. C. Marin, B.; Liu, J.; Aklile, E.; D. Urbina, A.; S.-C. Chiang, A.; Lawrence, N.; Chen, S.; J. Lipomi, D. SERS-Enhanced Piezoplasmonic Graphene Composite for Biological and Structural Strain Mapping. *Nanoscale* **2017**, *9*, 1292–1298, doi:10.1039/C6NR09005B.

120. Chen, B.; Mokume, M.; Liu, C.; Hayashi, K. Structure and Localized Surface Plasmon Tuning of Sputtered Au Nano-Islands through Thermal Annealing. *Vacuum* **2014**, *110*, 94–101, doi:10.1016/j.vacuum.2014.09.005.

121. Doron-Mor, I.; Barkay, Z.; Filip-Granit, N.; Vaskevich, A.; Rubinstein, I. Ultrathin Gold Island Films on Silanized Glass. Morphology and Optical Properties. *Chem. Mater.* **2004**, *16*, 3476–3483, doi:10.1021/cm049605a.

122. Kalyuzhny, G.; Vaskevich, A.; Schneeweiss, M.A.; Rubinstein, I. Transmission Surface-Plasmon Resonance (T-SPR) Measurements for Monitoring Adsorption on Ultrathin Gold Island Films. *Chem. Eur. J.* **2002**, *8*, 3849–3857, doi:10.1002/1521-3765(20020902)8:17<3849::AID-CHEM3849>3.0.CO;2-1.

123. Colas, F.; Barchiesi, D.; Kessentini, S.; Toury, T.; Chapelle, M.L. de la Comparison of Adhesion Layers of Gold on Silicate Glasses for SERS Detection. *J. Opt.* **2015**, *17*, 114010, doi:10.1088/2040-8978/17/11/114010.

124. Ruach-Nir, I.; Bendikov, T.A.; Doron-Mor, I.; Barkay, Z.; Vaskevich, A.; Rubinstein, I. Silica-Stabilized Gold Island Films for Transmission Localized Surface Plasmon Sensing. *J. Am. Chem. Soc.* **2007**, *129*, 84–92, doi:10.1021/ja064919f.

125. Szunerits, S.; Praig, V.G.; Manesse, M.; Boukherroub, R. Gold Island Films on Indium Tin Oxide for Localized Surface Plasmon Sensing. *Nanotechnology* **2008**, *19*, 195712, doi:10.1088/0957-4484/19/19/195712.

126. Moody, N.R.; Adams, D.P.; Volinsky, A.A.; Kriese, M.D.; Gerberich, W.W. Annealing Effects on Interfacial Fracture of Gold-Chromium Films in Hybrid Microcircuits. *MRS Proceedings* **1999**, *586*, 195, doi:10.1557/PROC-586-195.

127. Habteyes, T.G.; Dhuey, S.; Wood, E.; Gargas, D.; Cabrini, S.; Schuck, P.J.; Alivisatos, A.P.; Leone, S.R. Metallic Adhesion Layer Induced Plasmon Damping and Molecular Linker as a Nondamping Alternative. *ACS Nano* **2012**, *6*, 5702–5709, doi:10.1021/nn301885u.

128. Kang, M.; Ahn, M.-S.; Lee, Y.; Jeong, K.-H. Bioplasmonic Alloyed Nanoislands Using Dewetting of Bilayer Thin Films. *ACS Appl. Mater. Interfaces* **2017**, *9*, 37154–37159, doi:10.1021/acsami.7b10715.

129. Karakouz, T.; Tesler, A.B.; Bendikov, T.A.; Vaskevich, A.; Rubinstein, I. Highly Stable Localized Plasmon Transducers Obtained by Thermal Embedding of Gold Island Films on Glass. *Adv. Mater.* **2008**, *20*, 3893–3899, doi:10.1002/adma.200703092.

130. Goss, C.A.; Charych, D.H.; Majda, Marcin. Application of (3-Mercaptopropyl)Trimethoxysilane as a Molecular Adhesive in the Fabrication of Vapor-Deposited Gold Electrodes on Glass Substrates. *Anal. Chem.* **1991**, *63*, 85–88, doi:10.1021/ac00001a018.

131. Cantale, V.; Simeone, F.C.; Gambari, R.; Rampi, M.A. Gold Nano-Islands on FTO as Plasmonic Nanostructures for Biosensors. *Sens. Actuators B Chem.* **2011**, *152*, 206–213, doi:10.1016/j.snb.2010.12.008.

132. Ghorbanpour, M.; Falamaki, C. A Novel Method for the Production of Highly Adherent Au Layers on Glass Substrates Used in Surface Plasmon Resonance Analysis: Substitution of Cr or Ti Intermediate Layers with Ag Layer Followed by an Optimal Annealing Treatment. *J Nanostruct Chem* **2013**, *3*, 66, doi:10.1186/2193-8865-3-66.

133. De Almeida, J.M.M.M.; Vasconcelos, H.; Jorge, P.A.S.; Coelho, L. Plasmonic Optical Fiber Sensor Based on Double Step Growth of Gold Nano-Islands. *Sensors* **2018**, *18*, 1267, doi:10.3390/s18041267.

134. Kwak, J.; Lee, W.; Kim, J.-B.; Bae, S.-I.; Jeong, K.-H. Fiber-Optic Plasmonic Probe with Nanogap-Rich Au Nanoislands for on-Site Surface-Enhanced Raman Spectroscopy Using Repeated Solid-State Dewetting. *J Biomed Opt* **2019**, *24*, 037001, doi:10.1117/1.JBO.24.3.037001.

135. Badilescu, S.; Packirisamy, M. Plasmonic Biosensors on a Chip for Point-of-Care Applications. *Electrochem. Soc. Interface* **2019**, *28*, 65, doi:10.1149/2.F09193IF.

136. Kedem, O.; Tesler, A.B.; Vaskevich, A.; Rubinstein, I. Sensitivity and Optimization of Localized Surface Plasmon Resonance Transducers. *ACS Nano* **2011**, *5*, 748–760, doi:10.1021/nn102617d.

137. Ozhikandathil, J.; Packirisamy, M. Simulation and Implementation of a Morphology-Tuned Gold Nano-Islands Integrated Plasmonic Sensor. *Sensors* **2014**, *14*, 10497–10513, doi:10.3390/s140610497.

138. Doron-Mor, I.; Cohen, H.; Barkay, Z.; Shanzer, A.; Vaskevich, A.; Rubinstein, I. Sensitivity of Transmission Surface Plasmon Resonance (T-SPR) Spectroscopy: Self-Assembled Multilayers on Evaporated Gold Island Films. *Chem. Eur. J.* **2005**, *11*, 5555–5562, doi:10.1002/chem.200500103.

139. Bonyár, A.; Csarnovics, I.; Veres, M.; Himics, L.; Csik, A.; Kámán, J.; Balázs, L.; Kökényesi, S. Investigation of the Performance of Thermally Generated Gold Nanoislands for

LSPR and SERS Applications. *Sens. Actuators B Chem.* **2018**, *255, Part 1*, 433–439, doi:10.1016/j.snb.2017.08.063.

140. Longobucco, G.; Fasano, G.; Zharnikov, M.; Bergamini, L.; Corni, S.; Rampi, M.A. High Stability and Sensitivity of Gold Nano-Islands for Localized Surface Plasmon Spectroscopy: Role of Solvent Viscosity and Morphology. *Sens. Actuators B Chem.* **2014**, *191*, 356–363, doi:10.1016/j.snb.2013.09.026.

141. Choi, J.-H.; Lee, J.-H.; Son, J.; Choi, J.-W. Noble Metal-Assisted Surface Plasmon Resonance Immunosensors. *Sensors* **2020**, *20*, 1003, doi:10.3390/s20041003.

142. Lopez, G.A.; Estevez, M.-C.; Soler, M.; Lechuga, L.M. Recent Advances in Nanoplasmonic Biosensors: Applications and Lab-on-a-Chip Integration. *Nanophotonics* **2017**, *6*, 123–136, doi:10.1515/nanoph-2016-0101.

143. Jia, K.; Bijeon, J.-L.; Adam, P.-M.; Ionescu, R.E. Large Scale Fabrication of Gold Nano-Structured Substrates Via High Temperature Annealing and Their Direct Use for the LSPR Detection of Atrazine. *Plasmonics* **2013**, *8*, 143–151, doi:10.1007/s11468-012-9444-3.

144. Ozhikandathil, J.; Badilescu, S.; Packirisamy, M. Gold Nanoisland Structures Integrated in a Lab-on-a-Chip for Plasmonic Detection of Bovine Growth Hormone. *J Biomed Opt* **2012**, *17*, 077001, doi:10.1117/1.JBO.17.7.077001.

145. Ozhikandathil, J.; Badilescu, S.; Packirisamy, M. *Technical Note:* A Portable on-Chip Assay System for Absorbance and Plasmonic Detection of Protein Hormone in Milk. *J. Dairy Sci.* **2015**, *98*, 4384–4391, doi:10.3168/jds.2014-8934.

146. Badilescu, S.; Packirisamy, M. Microfluidics-Nano-Integration for Synthesis and Sensing. *Polymer* **2012**, *4*, 1278–1310, doi:10.3390/polym4021278.

147. Ozhikandathil, J.; Badilescu, S.; Packirisamy, M. Silver Nanoislands for Plasmonic Detection of Proteins. *Proc. World Congr. New Technol 5*, e16009.

148. Prevo, B.G.; Fuller, J.C.; Velev, O.D. Rapid Deposition of Gold Nanoparticle Films with Controlled Thickness and Structure by Convective Assembly. *Chem. Mater.* **2005**, *17*, 28–35, doi:10.1021/cm0486621.

149. Duraichelvan, R.; Srinivas, B.; Badilescu, S.; Ouellette, R.; Ghosh, A.; Packirisamy, M. Exosomes Detection by a Label-Free Localized Surface Plasmonic Resonance Method. *ECS Trans.* **2016**, *75*, 11, doi:10.1149/07517.0011ecst.

150. Badilescu, S.; Bathini, S.; Chelvan, D.; Packirisamy, M. Microfluidic Plasmonic Bio-Sensing of Exosomes. *Int. J. Biol. Biomed. Eng* **2018**, *12*, 226–229.

151. Feng, T.; Ding, L.; Chen, L.; Di, J. Deposition of Gold Nanoparticles upon Bare and Indium Tin Oxide Film Coated Glass Based on Annealing Process. *J. Exp. Nanosci.* **2019**, *14*, 13–22, doi:10.1080/17458080.2018.1520399.

152. Tokel, O.; Inci, F.; Demirci, U. Advances in Plasmonic Technologies for Point of Care Applications. *Chem. Rev.* **2014**, *114*, 5728–5752, doi:10.1021/cr4000623.

153. Yu, T.; Wei, Q. Plasmonic Molecular Assays: Recent Advances and Applications for Mobile Health. *Nano Res.* **2018**, *11*, 5439–5473, doi:10.1007/s12274-018-2094-9.

154. Badilescu, S.; Packirisamy, M. Plasmonic Biosensors on a Chip for Point-of-Care Applications. *Electrochem. Soc. Interface* **2019**, *28*, 65, doi:10.1149/2.F09193IF.

155. Raju, D.; Bathini, S.; Badilescu, S.; Ouellette, R.J.; Ghosh, A.; Packirisamy, M. LSPR Detection of Extracellular Vesicles Using a Silver-PDMS Nano-Composite Platform Suitable for Sensor Networks. *Enterp. Inf. Syst.* **2020**, *14*, 532–541, doi:10.1080/17517575.2018.1526326.

156. Fei Guo, C.; Sun, T.; Cao, F.; Liu, Q.; Ren, Z. Metallic Nanostructures for Light Trapping in Energy-Harvesting Devices. *Light Sci Appl* **2014**, *3*, e161–e161, doi:10.1038/lsa.2014.42.

157. Ryu, J.; Kim, H.-S.; Hahn, H.T.; Lashmore, D. Carbon Nanotubes with Platinum Nano-Islands as Glucose Biofuel Cell Electrodes. *Biosens. Bioelectron* **2010**, *25*, 1603–1608, doi:10.1016/j.bios.2009.11.019.

158. Do, M.T.; Tong, Q.C.; Lidiak, A.; Luong, M.H.; Ledoux-Rak, I.; Lai, N.D. Nano-Patterning of Gold Thin Film by Thermal Annealing Combined with Laser Interference Techniques. *Appl. Phys. A* **2016**, *122*, 360, doi:10.1007/s00339-016-9951-8.

159. Gerislioglu, B.; Dong, L.; Ahmadivand, A.; Hu, H.; Nordlander, P.; Halas, N.J. Monolithic Metal Dimer-on-Film Structure: New Plasmonic Properties Introduced by the Underlying Metal. *Nano Lett.* **2020**, *20*, 2087–2093, doi:10.1021/acs.nanolett.0c00075.

160. Gerislioglu, B.; Bakan, G.; Ahuja, R.; Adam, J.; Mishra, Y.K.; Ahmadivand, A. The Role of $Ge_2Sb_2Te_5$ in Enhancing the Performance of Functional Plasmonic Devices. *Mater. Today Phys.* **2020**, *12*, 100178, doi:10.1016/j.mtphys.2020.100178.

161. Théry, C.; Ostrowski, M.; Segura, E. Membrane Vesicles as Conveyors of Immune Responses. *Nat Rev Immunol* **2009**, *9*, 581–593, doi:10.1038/nri2567.

162. Nath, N.; Chilkoti, A. A Colorimetric Gold Nanoparticle Sensor to Interrogate Biomolecular Interactions in Real Time on a Surface. *Anal. Chem.* **2002**, *74*, 504–509, doi:10.1021/ac015657x.

163. Nath, N.; Chilkoti, A. Label-Free Biosensing by Surface Plasmon Resonance of Nanoparticles on Glass: Optimization of Nanoparticle Size. *Anal. Chem.* **2004**, *76*, 5370–5378, doi:10.1021/ac049741z.

164. Weikel, A.L.; Conklin, S.D.; Richardson, J.N. A Multiple Reflection Attenuated Total Reflectance Sensor Incorporating a Glass–Indium Tin Oxide Surface Modified via Direct Attachment or Film Encapsulation of Colloidal Gold Nanoparticles. *Sens. Actuators B Chem.* **2005**, *110*, 112–119, doi:10.1016/j.snb.2005.01.017.

165. Frederix, F.; Friedt, J.-M.; Choi, K.-H.; Laureyn, W.; Campitelli, A.; Mondelaers, D.; Maes, G.; Borghs, G. Biosensing Based on Light Absorption of Nanoscaled Gold and Silver Particles. *Anal. Chem.* **2003**, *75*, 6894–6900, doi:10.1021/ac0346609.

166. Hulteen, J.C.; Treichel, D.A.; Smith, M.T.; Duval, M.L.; Jensen, T.R.; Van Duyne, R.P. Nanosphere Lithography: Size-Tunable Silver Nanoparticle and Surface Cluster Arrays. *J. Phys. B* **1999**, *103*, 3854–3863, doi:10.1021/jp9904771.

167. Fida, F.; Varin, L.; Badilescu, S.; Kahrizi, M.; Truong, V.-V. Gold Nanoparticle Ring and Hole Structures for Sensing Proteins and Antigen–Antibody Interactions. *Plasmonics* **2009**, *4*, 201–207, doi:10.1007/s11468-009-9093-3.

168. Fujiwara, K.; Watarai, H.; Itoh, H.; Nakahama, E.; Ogawa, N. Measurement of Antibody Binding to Protein Immobilized on Gold Nanoparticles by Localized Surface Plasmon Spectroscopy. *Anal Bioanal Chem* **2006**, *386*, 639–644, doi:10.1007/s00216-006-0559-2.

169. Malinsky, M.D.; Kelly, K.L.; Schatz, G.C.; Van Duyne, R.P. Chain Length Dependence and Sensing Capabilities of the Localized Surface Plasmon Resonance of Silver Nanoparticles Chemically Modified with Alkanethiol Self-Assembled Monolayers. *J. Am. Chem. Soc.* **2001**, *123*, 1471–1482, doi:10.1021/ja003312a.

170. Ye, J.; Bonroy, K.; Nelis, D.; Frederix, F.; D'Haen, J.; Maes, G.; Borghs, G. Enhanced Localized Surface Plasmon Resonance Sensing on Three-Dimensional Gold Nanoparticles Assemblies. *Colloids Surf. A Physicochem. Eng. Asp.* **2008**, *321*, 313–317, doi:10.1016/j.colsurfa.2008.01.028.

171. Guo, L.; Chen, G.; Kim, D.-H. Three-Dimensionally Assembled Gold Nanostructures for Plasmonic Biosensors. *Anal. Chem.* **2010**, *82*, 5147–5153, doi:10.1021/ac100346z.

172. Toderas, F.; Baia, M.; Baia, L.; Astilean, S. Controlling Gold Nanoparticle Assemblies for Efficient Surface-Enhanced Raman Scattering and Localized Surface Plasmon Resonance Sensors. *Nanotechnology* **2007**, *18*, 255702, doi:10.1088/0957-4484/18/25/255702.

173. Shon, Y.-S.; Choi, H.Y.; Guerrero, M.S.; Kwon, C. Preparation of Nanostructured Film Arrays for Transmission Localized Surface Plasmon Sensing. *Plasmonics* **2009**, *4*, 95–105, doi:10.1007/s11468-009-9079-1.

174. Turkevich, J.; Stevenson, P.C.; Hillier, J. A Study of the Nucleation and Growth Processes in the Synthesis of Colloidal Gold. *Discuss. Faraday Soc.* **1951**, *11*, 55–75, doi:10.1039/DF9511100055.

175. Diao, J.J.; Qiu, F.S.; Chen, G.D.; Reeves, M.E. Surface Vertical Deposition for Gold Nanoparticle Film. *J. Phys. D: Appl. Phys.* **2003**, *36*, L25, doi:10.1088/0022-3727/36/3/101.

176. SadAbadi, H.; Badilescu, S.; Packirisamy, M.; Wüthrich, R. PDMS-Gold Nanocomposite Platforms with Enhanced Sensing Properties. *J Biomed Nanotechnol* **2012**, *8*, 539–549, doi:10.1166/jbn.2012.1418.

177. Nath, N.; Chilkoti, A. Label-Free Biosensing by Surface Plasmon Resonance of Nanoparticles on Glass: Optimization of Nanoparticle Size. *Anal. Chem.* **2004**, *76*, 5370–5378, doi:10.1021/ac049741z.

178. Frederix, F.; Friedt, J.-M.; Choi, K.-H.; Laureyn, W.; Campitelli, A.; Mondelaers, D.; Maes, G.; Borghs, G. Biosensing Based on Light Absorption of Nanoscaled Gold and Silver Particles. *Anal. Chem.* **2003**, *75*, 6894–6900, doi:10.1021/ac0346609.

179. Algorri, J.F.; Poudereux, D.; García-Cámara, B.; Urruchi, V.; Sánchez-Pena, J.M.; Vergaz, R.; Caño-García, M.; Quintana, X.; Geday, M.A.; Otón, J.M. Metal Nanoparticles-PDMS Nanocomposites for Tunable Optical Filters and Sensors. *Opt. Data Process. Storage* **2016**, *2*, 1–6, doi:10.1515/odps-2016-0001.

180. Beecroft, L.L.; Ober, C.K. Nanocomposite Materials for Optical Applications. *Chem. Mater.* **1997**, *9*, 1302–1317, doi:10.1021/cm960441a.

181. Faupel, F.; Zaporojtchenko, V.; Strunskus, T.; Elbahri, M. Metal-Polymer Nanocomposites for Functional Applications. *Adv Eng Mater* **2010**, *12*, 1177–1190, doi:10.1002/adem.201000231.

182. Caseri, W. Nanocomposites of Polymers and Metals or Semiconductors: Historical Background and Optical Properties. *Macromol. Rapid Commun.* **2000**, *21*, 705–722, doi:10.1002/1521-3927(20000701)21:11<705::AID-MARC705>3.0.CO;2-3.

183. Caseri, W. Inorganic Nanoparticles as Optically Effective Additives for Polymers. *Chem. Eng. Commun.* **2008**, *196*, 549–572, doi:10.1080/00986440802483954.

184. Carotenuto, G.; Peruta, G.L.; Nicolais, L. Thermo-Chromic Materials Based on Polymer-Embedded Silver Clusters. *Sens. Actuators B Chem.* **2006**, *114*, 1092–1095, doi:10.1016/j.snb.2005.07.044.

185. Camargo, P.H.C.; Satyanarayana, K.G.; Wypych, F. Nanocomposites: Synthesis, Structure, Properties and New Application Opportunities. *Mater. Res.* **2009**, *12*, 1–39, doi:10.1590/s1516-14392009000100002.

186. Althues, H.; Henle, J.; Kaskel, S. Functional Inorganic Nanofillers for Transparent Polymers. *Chem. Soc. Rev.* **2007**, *36*, 1454–1465, doi:10.1039/B608177K.

187. Li, S.; Meng Lin, M.; Toprak, M.S.; Kim, D.K.; Muhammed, M. Nanocomposites of Polymer and Inorganic Nanoparticles for Optical and Magnetic Applications. *Nano Rev.* **2010**, *1*, 5214, doi:10.3402/nano.v1i0.5214.

188. Chuang, H.-S.; Wereley, S. Design, Fabrication and Characterization of a Conducting PDMS for Microheaters and Temperature Sensors. *J. Micromech. Microeng.* **2009**, *19*, 045010, doi:10.1088/0960-1317/19/4/045010.

189. Cataldi, U.; Cerminara, P.; De Sio, L.; Caputo, R.; Umeton, C.P. Fabrication and Characterization of Stretchable PDMS Structures Doped With Au Nanoparticles. *Mol. Cryst. Liq. Cryst.* **2012**, *558*, 22–27, doi:10.1080/15421406.2011.653675.

190. Li, D.; Li, C.; Wang, A.; He, Q.; Li, J. Hierarchical Gold/Copolymer Nanostructures as Hydrophobic Nanotanks for Drug Encapsulation. *J. Mater. Chem.* **2010**, *20*, 7782–7787, doi:10.1039/C0JM01059F.

191. Nicolais, L.; Carotenuto, G. Preparation and Characterization of Metal Polymer Nanocomposites. In *Nanocomposites*; John Wiley & Sons, Ltd, 2013; pp. 73–96 ISBN 978-1-118-74265-5.

192. Scott, A.; Gupta, R.; Kulkarni, G.U. A Simple Water-Based Synthesis of Au Nanoparticle/PDMS Composites for Water Purification and Targeted Drug Release. *Macromol. Chem. Phys.* **2010**, *211*, 1640–1647, doi:10.1002/macp.201000079.

193. De Jesús, M.A.; Giesfeldt, K.S.; Sepaniak, M.J. Improving the Analytical Figures of Merit of SERS for the Analysis of Model Environmental Pollutants. *J. Raman Spectrosc.* **2004**, *35*, 895–904, doi:10.1002/jrs.1231.

194. Ahmadivand, A.; Gerislioglu, B.; Ramezani, Z.; Ghoreishi, S.A. Attomolar Detection of Low-Molecular Weight Antibiotics Using Midinfrared-Resonant Toroidal Plasmonic Metachip Technology. *Phys. Rev. Applied* **2019**, *12*, 034018, doi:10.1103/PhysRevApplied.12.034018.

195. Ahmadivand, A.; Gerislioglu, B.; Ahuja, R.; Kumar Mishra, Y. Terahertz Plasmonics: The Rise of Toroidal Metadevices towards Immunobiosensings. *Mater. Today* **2020**, *32*, 108–130, doi:10.1016/j.mattod.2019.08.002.

196. Kumar, S.K.; Krishnamoorti, R. Nanocomposites: Structure, Phase Behavior, and Properties. *Annu Rev Chem Biomol Eng* **2010**, *1*, 37–58, doi:10.1146/annurev-chembioeng-073009-100856.

197. Stepanov, A.L.; Khaibullin, R.I. Optics of Metal Nanoparticles Fabricated in Organic Matrix by Ion Implantation. *Rev. Adv. Mater. Sci.* **2004**, *7*, 108–125.

198. Niklaus, M.; Shea, H.R. Electrical Conductivity and Young's Modulus of Flexible Nanocomposites Made by Metal-Ion Implantation of Polydimethylsiloxane: The Relationship between Nanostructure and Macroscopic Properties. *Acta Materialia* **2011**, *59*, 830–840, doi:10.1016/j.actamat.2010.10.030.

199. Kovacs, G.J.; Vincett, P.S. Subsurface Particle Monolayer and Film Formation in Softenable Substrates: Techniques and Thermodynamic Criteria. *Thin Solid Films* **1984**, *111*, 65–81, doi:10.1016/0040-6090(84)90350-X.

200. Ramesh, G.V.; Porel, S.; Radhakrishnan, T.P. Polymer Thin Films Embedded with in Situ Grown Metal Nanoparticles. *Chem. Soc. Rev.* **2009**, *38*, 2646–2656, doi:10.1039/B815242J.

201. Giesfeldt, K.S.; Connatser, R.M.; De Jesús, M.A.; Dutta, P.; Sepaniak, M.J. Gold-Polymer Nanocomposites: Studies of Their Optical Properties and Their Potential as SERS Substrates. *J. Raman Spectrosc.* **2005**, *36*, 1134–1142, doi:10.1002/jrs.1418.

202. Hasell, T.; Lagonigro, L.; Peacock, A.C.; Yoda, S.; Brown, P.D.; Sazio, P.J.A.; Howdle, S.M. Silver Nanoparticle Impregnated Polycarbonate Substrates for Surface Enhanced Raman Spectroscopy. *Adv. Funct. Mater.* **2008**, *18*, 1265–1271, doi:10.1002/adfm.200701429.

203. Bonyar, A.; Izsold, Z.; Himics, L.; Veres, M.; Csarnovics, I. Investigation of PDMS-Gold Nanoparticle Composite Films for Plasmonic Sensors. *2017 IEEE 23rd International Symposium for Design and Technology in Electronic Packaging (SIITME)* **2017**, 25–28, doi:10.1109/SIITME.2017.8259850.

204. Bonyár, A.; Izsold, Z.; Borók, A.; Csarnovics, I.; Himics, L.; Veres, M.; Harsányi, G. PDMS-Au/Ag Nanocomposite Films as Highly Sensitive SERS Substrates. *Proceedings* **2018**, *2*, 1060, doi:10.3390/proceedings2131060.

205. Firestone, M.A.; Hayden, S.C.; Huber, D.L. Greater than the Sum: Synergy and Emergent Properties in Nanoparticle–Polymer Composites. *MRS Bull.* **2015**, *40*, 760–767, doi:10.1557/mrs.2015.202.

206. Deshmukh, R.D.; Composto, R.J. Surface Segregation and Formation of Silver Nanoparticles Created In Situ in Poly(Methyl Methacrylate) Films. *Chem. Mater.* **2007**, *19*, 745–754, doi:10.1021/cm062030s.

207. Simpson, T.R.E.; Parbhoo, B.; Keddie, J.L. The Dependence of the Rate of Crosslinking in Poly(Dimethyl Siloxane) on the Thickness of Coatings. *Polymer* **2003**, *44*, 4829–4838, doi:10.1016/S0032-3861(03)00496-8.

208. Batch, G.L.; Macosko, C.W.; Kemp, D.N. Reaction Kinetics and Injection Molding of Liquid Silicone Rubber. *Rubber Chem. Technol.* **1991**, *64*, 218–233, doi:10.5254/1.3538554.

209. Simpson, T.R.E.; Tabatabaian, Z.; Jeynes, C.; Parbhoo, B.; Keddie, J.L. Influence of Interfaces on the Rates of Crosslinking in Poly(Dimethyl Siloxane) Coatings. *J Polym Sci A Polym Chem* **2004**, *42*, 1421–1431, doi:10.1002/pola.20006.

210. Zhang, Q.; Xu, J.-J.; Liu, Y.; Chen, H.-Y. In-Situ Synthesis of Poly(Dimethylsiloxane)-Gold Nanoparticles Composite Films and Its Application in Microfluidic Systems. *Lab Chip* **2008**, *8*, 352–357, doi:10.1039/b716295m.

211. Goyal, A.; Kumar, A.; Patra, P.K.; Mahendra, S.; Tabatabaei, S.; Alvarez, P.J.J.; John, G.; Ajayan, P.M. In Situ Synthesis of Metal Nanoparticle Embedded Free Standing Multifunctional PDMS Films. *Macromol. Rapid Commun.* **2009**, *30*, 1116–1122, doi:10.1002/marc.200900174.

212. Jr, K.R.B.; Russell, A.G.; Blake, P.A.; Roper, D.K. Gold Nanoparticles Reduced in Situ and Dispersed in Polymer Thin Films: Optical and Thermal Properties. *Nanotechnology* **2012**, *23*, 375703, doi:10.1088/0957-4484/23/37/375703.

213. Ryu, D.; Loh, K.J.; Ireland, R.; Karimzada, M.; Yaghmaie, F.; Gusman, A.M. In Situ Reduction of Gold Nanoparticles in PDMS Matrices and Applications for Large Strain Sensing. *Smart Struct. Syst.* **2011**, *8*, 471–486.

214. Massaro, A.; Spano, F.; Cingolani, R.; Athanassiou, A. Experimental Optical Characterization and Polymeric Layouts of Gold PDMS Nanocomposite Sensor for Liquid Detection. *IEEE Sens. J.* **2011**, *11*, 1780–1786, doi:10.1109/JSEN.2011.2104414.

215. Ozhikandathil, J.; Badilescu, S.; Packirisamy, M. Gold Nanoisland Structures Integrated in a Lab-on-a-Chip for Plasmonic Detection of Bovine Growth Hormone. *J Biomed Opt* **2012**, *17*, 077001, doi:10.1117/1.JBO.17.7.077001.

216. Badilescu, S.; Packirisamy, M. Microfluidics-Nano-Integration for Synthesis and Sensing. *Polymer* **2012**, *4*, 1278–1310, doi:10.3390/polym4021278.

217. Fanous, M.; Badilescu, S.; Packirisamy, M. Thermal Manipulation of Gold Nanocomposites for Microfluidic Platform Optimization. *Plasmonics* **2018**, *13*, 305–313, doi:10.1007/s11468-017-0515-3.

218. SadAbadi, H.; Badilescu, S.; Packirisamy, M.; Wüthrich, R. Integration of Gold Nanoparticles in PDMS Microfluidics for Lab-on-a-Chip Plasmonic Biosensing of Growth Hormones. *Biosens Bioelectron* **2013**, *44*, 77–84, doi:10.1016/j.bios.2013.01.016.

219. Kovacs, G.J.; Vincett, P.S. Formation and Thermodynamic Stability of a Novel Class of Useful Materials: Close-Packed Monolayers of Submicron Monodisperse Spheres Just below a Polymer Surface. *J. Colloid Interface Sci.* **1982**, *90*, 335–351, doi:10.1016/0021-9797(82)90302-2.

220. Kovacs, G.J.; Vincett, P.S.; Tremblay, C.; Pundsack, A.L. Vacuum Deposition onto Softenable Substrates: Formation of Novel Subsurface Structures. *Thin Solid Films* **1983**, *101*, 21–40, doi:10.1016/0040-6090(83)90490-X.

221. Kovacs, G.J.; Vincett, P.S. Subsurface Particulate Film Formation in Softenable Substrates: Present Status and Possible New Applications. *Thin Solid Films* **1983**, *100*, 341–353, doi:10.1016/0040-6090(83)90159-1.

222. Borrell, M.; Gong, Y.; Leal, L.G. Surface Functionalized Nanoparticles As Surfactants. Presented at the 2007 AIChE Annual Meeting, Salt Lake City, UT, USA, 2007.

223. Nanda, K.K.; Maisels, A.; Kruis, F.E. Surface Tension and Sintering of Free Gold Nanoparticles. *J. Phys. Chem. C* **2008**, *112*, 13488–13491, doi:10.1021/jp803934n.

224. Lamber, R.; Wetjen, S.; Schulz-Ekloff, G.; Baalmann, A. Metal Clusters in Plasma Polymer Matrixes: Gold Clusters. *J. Phys. Chem.* **1995**, *99*, 13834–13838, doi:10.1021/j100038a014.

225. Ozhikandathil, J.; Badilescu, S.; Packirisamy, M. Detection of Fluorophore-Tagged Recombinant Bovine Somatotropin (rbST) by Using a Silica-on-Silicon (SOS)-PDMS Lab-on-a-Chip. *IEEE Sens. J.* **2012**, *12*, 2791–2798, doi:10.1109/JSEN.2012.2202105.

226. van der Pol, E.; Böing, A.N.; Harrison, P.; Sturk, A.; Nieuwland, R. Classification, Functions, and Clinical Relevance of Extracellular Vesicles. *Pharmacol Rev* **2012**, *64*, 676–705, doi:10.1124/pr.112.005983.

227. Théry, C.; Amigorena, S.; Raposo, G.; Clayton, A. Isolation and Characterization of Exosomes from Cell Culture Supernatants and Biological Fluids. *Curr Protoc Cell Biol* **2006**, *30*, 3.22.1-3.22.29, doi:10.1002/0471143030.cb0322s30.

228. Nath, N.; Chilkoti, A. Label Free Colorimetric Biosensing Using Nanoparticles. *J. Fluoresc.* **2004**, *14*, 377–389, doi:10.1023/B:JOFL.0000031819.45448.dc.

229. Nath, N.; Chilkoti, A. Label-Free Biosensing by Surface Plasmon Resonance of Nanoparticles on Glass: Optimization of Nanoparticle Size. *Anal. Chem.* **2004**, *76*, 5370–5378, doi:10.1021/ac049741z.

230. Badilescu, S.; Raju, D.; Bathini, S.; Packirisamy, M. Gold Nano-Island Platforms for Localized Surface Plasmon Resonance Sensing: A Short Review. *Molecules* **2020**, *25*, 4661, doi:10.3390/molecules25204661.

231. Łapiński, M.; Kozioł, R.; Cymann, A.; Sadowski, W.; Kościelska, B. Substrate Dependence in the Formation of Au Nanoislands for Plasmonic Platform Application. *Plasmonics* **2020**, *15*, 101–107, doi:10.1007/s11468-019-01021-9.

232. Malureanu, R.; Lavrinenko, A. Ultra-Thin Films for Plasmonics: A Technology Overview. *Nanotechnol. Rev.* **2015**, *4*, 259–275, doi:10.1515/ntrev-2015-0021.

233. Sudheer; Mondal, P.; Rai, V.N.; Srivastava, A.K. A Study of Growth and Thermal Dewetting Behavior of Ultra-Thin Gold Films Using Transmission Electron Microscopy. *AIP Adv.* **2017**, *7*, 075303, doi:10.1063/1.4989823.

234. Sun, H.; Yu, M.; Sun, X.; Wang, G.; Lian, J. Ultrathin Gold Island Films for Time-Dependent Temperature Sensing. *J Nanopart Res* **2014**, *16*, 2273, doi:10.1007/s11051-014-2273-x.

235. Kozioł, R.; Łapiński, M.; Syty, P.; Koszelow, D.; Sadowski, W.; Sienkiewicz, J.E.; Kościelska, B. Evolution of Ag Nanostructures Created from Thin Films: UV–Vis Absorption and Its Theoretical Predictions. *Beilstein J. Nanotechnol.* **2020**, *11*, 494–507, doi:10.3762/bjnano.11.40.

236. Todeschini, M.; Bastos da Silva Fanta, A.; Jensen, F.; Wagner, J.B.; Han, A. Influence of Ti and Cr Adhesion Layers on Ultrathin Au Films. *ACS Appl. Mater. Interfaces* **2017**, *9*, 37374–37385, doi:10.1021/acsami.7b10136.

237. Colas, F.; Barchiesi, D.; Kessentini, S.; Toury, T.; Chapelle, M.L. de la Comparison of Adhesion Layers of Gold on Silicate Glasses for SERS Detection. *J. Opt.* **2015**, *17*, 114010, doi:10.1088/2040-8978/17/11/114010.

238. Volkov, V.S.; Yakubovsky, D.I.; Stebunov, Y.V.; Kirtaev, R.V.; Ermolaev, G.A.; Mironov, M.S.; Novikov, S.M.; Voronin, K.V.; Arsenin, A.V. Ultra-Thin Gold Films: Towards 2D Metals for Photonic and Optoelectronic Applications. *J. Phys.: Conf. Ser.* **2020**, *1461*, 012184, doi:10.1088/1742-6596/1461/1/012184.

239. Najiminaini, M.; Vasefi, F.; Kaminska, B.; Carson, J.J.L. Optical Resonance Transmission Properties of Nano-Hole Arrays in a Gold Film: Effect of Adhesion Layer. *Opt. Express, OE* **2011**, *19*, 26186–26197, doi:10.1364/OE.19.026186.

240. Karakouz, T.; Tesler, A.B.; Bendikov, T.A.; Vaskevich, A.; Rubinstein, I. Highly Stable Localized Plasmon Transducers Obtained by Thermal Embedding of Gold Island Films on Glass. *Adv. Mater.* **2008**, *20*, 3893–3899, doi:10.1002/adma.200703092.

241. Karakouz, T.; Maoz, B.M.; Lando, G.; Vaskevich, A.; Rubinstein, I. Stabilization of Gold Nanoparticle Films on Glass by Thermal Embedding. *ACS Appl. Mater. Interfaces* **2011**, *3*, 978–987, doi:10.1021/am100878r.

242. Leandro, L.; Malureanu, R.; Rozlosnik, N.; Lavrinenko, A. Ultrathin, Ultrasmooth Gold Layer on Dielectrics without the Use of Additional Metallic Adhesion Layers. *ACS Appl. Mater. Interfaces* **2015**, *7*, 5797–5802, doi:10.1021/am508681u.

243. Logeeswaran, V.J.; Chan, M.-L.; Bayam, Y.; Saif Islam, M.; Horsley, D.A.; Li, X.; Wu, W.; Wang, S.Y.; Williams, R.S. Ultra-Smooth Metal Surfaces Generated by Pressure-Induced

Surface Deformation of Thin Metal Films. *Appl. Phys. A* **2007**, *87*, 187–192, doi:10.1007/s00339-006-3836-1.

244. Davis, T.J.; Gómez, D.E.; Roberts, A. Plasmonic Circuits for Manipulating Optical Information. *Nanophotonics* **2017**, *6*, 543–559, doi:10.1515/nanoph-2016-0131.

245. Fang, X.; Mak, C.L.; Dai, J.; Li, K.; Ye, H.; Leung, C.W. ITO/Au/ITO Sandwich Structure for Near-Infrared Plasmonics. *ACS Appl. Mater. Interfaces* **2014**, *6*, 15743–15752, doi:10.1021/am5026165.

246. Alsultany, F.H.; Ahmed, N.M.; Matjafri, M.Z. Effects of CW CO_2 Laser Annealing on Indium Tin Oxide Thin Films Characteristics. *SNL* **2014**, *4*, 83, doi:10.4236/snl.2014.44012.

247. Qiu, G.; Ng, S.P.; Wu, C.M.L. Differential Phase-Detecting Localized Surface Plasmon Resonance Sensor with Self-Assembly Gold Nano-Islands. *Opt. Lett.* **2015**, *40*, 1924–1927, doi:10.1364/OL.40.001924.

248. Qiu, G.; Ng, S.P.; Wu, L.C.-M. Dielectric Functionalization for Differential Phase Detecting Localized Surface Plasmon Resonance Biosensor. *Sens. Actuators B Chem.* **2016**, *234*, 247–254, doi:10.1016/j.snb.2016.04.151.

249. Thakur, A.; Qiu, G.; Ng, S.-P.; Guan, J.; Yue, J.; Lee, Y.; Wu, C.-M.L. Direct Detection of Two Different Tumor-Derived Extracellular Vesicles by SAM-AuNIs LSPR Biosensor. *Biosens. Bioelectron* **2017**, *94*, 400–407, doi:10.1016/j.bios.2017.03.036.

250. Grochowska, K.; Siuzdak, K.; Karczewski, J.; Szkoda, M.; Śliwiński, G. Properties of Thermally Dewetted Thin Au Films on ITO-Coated Glass for Biosensing Applications. *Plasmonics* **2017**, *12*, 1939–1946, doi:10.1007/s11468-016-0465-1.

251. Verma, A.; Saxena, S.; Biswas, N.K.; Srivastav, A.; Singh, U.B.; Khan, Saif.A.; Shrivastav, R.; Avasthi, D.K.; Dass, S. Fabrication and Characterization of Plasmonic Au Nanoparticles on ITO-Coated Glass Sheets. *Plasmonics* **2022**, *17*, 2141–2151, doi:10.1007/s11468-022-01693-w.

Appendix A. SEM images of the Cr-Au platform annealed at 600°C and 650°C for 1hr

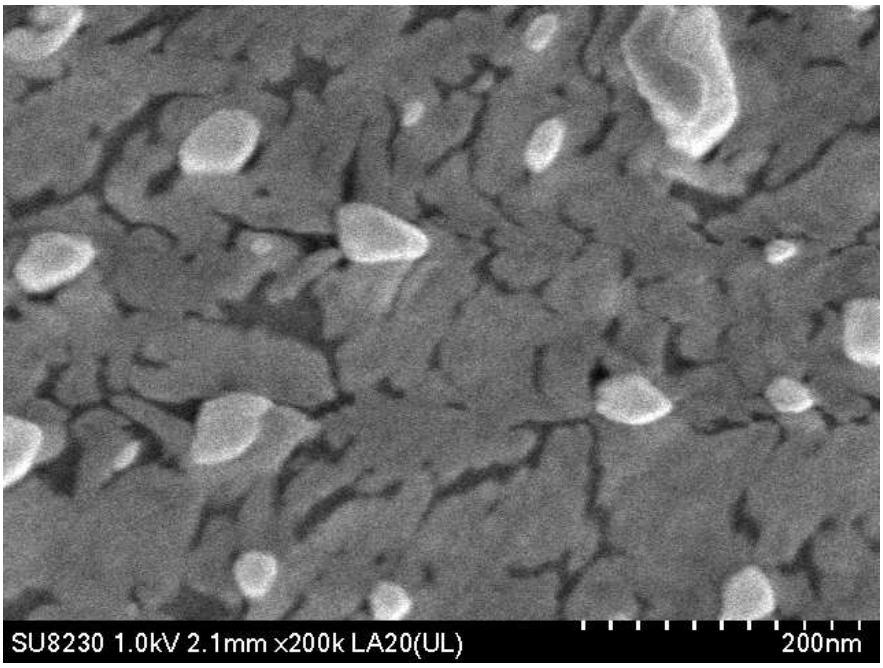

Figure A-1: SEM image for the platform with the Cr adhesion layer and gold layer annealed at 600°C for 1hr.

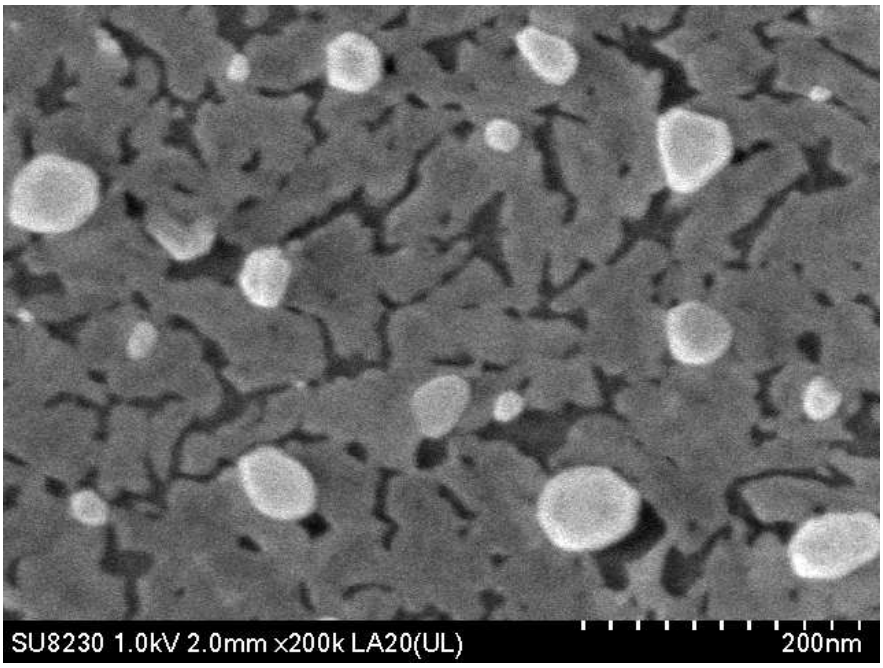

Figure A-2: SEM image for the platform with the Cr adhesion layer and gold layer annealed at 650°C for 1hr.

Appendix B. SEM of the Cr-Au platform annealed at 250°C for 1hr and SEM and AFM image of the ITO-Au platform annealed at 250°C for 1hr

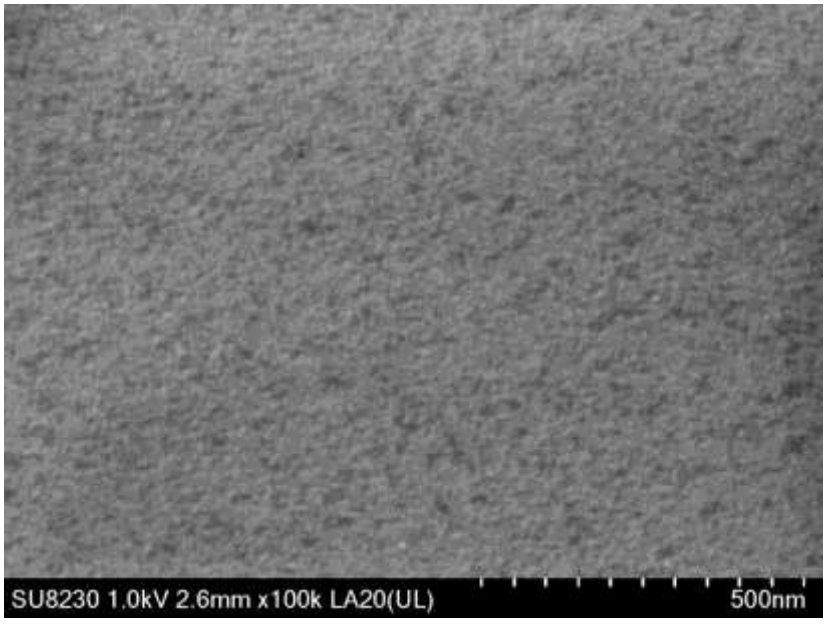

Figure B-1: SEM for the platform with the Cr adhesion layer and gold layer annealed at 250°C for 1hr.

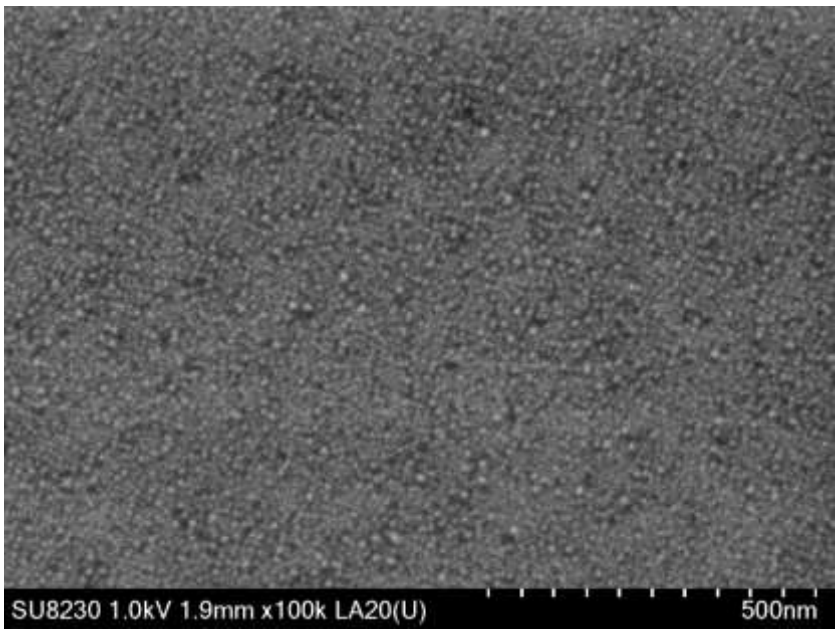

Figure B-2: SEM for the platform with the ITO adhesion layer and gold layer annealed at 250°C for 1hr.

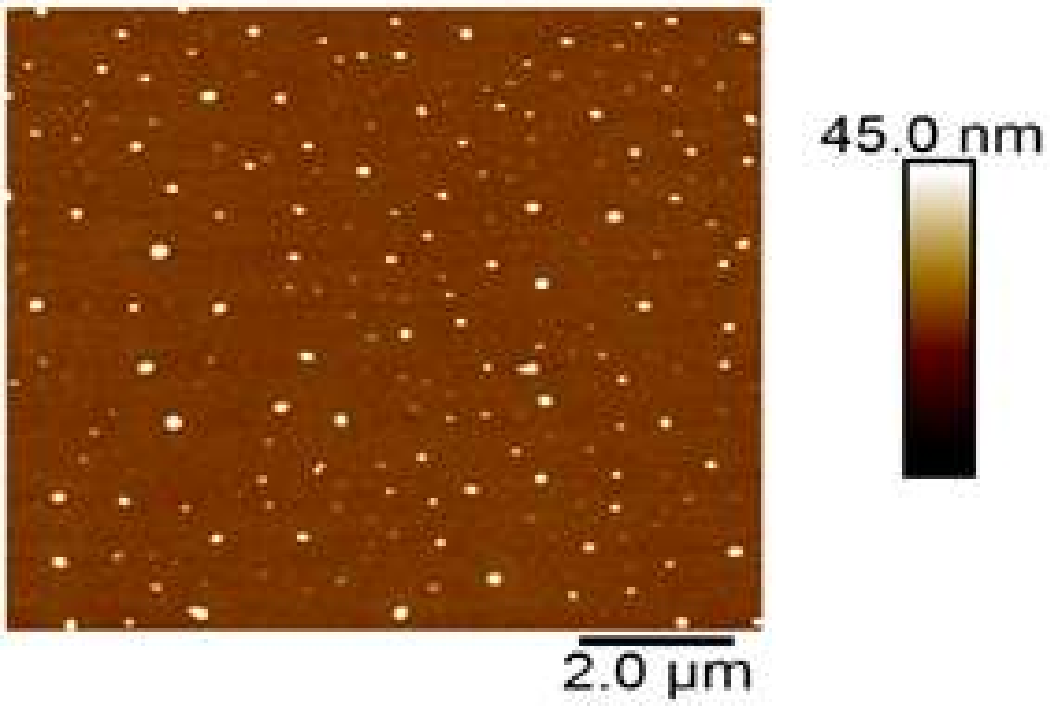

Figure B-3: AFM image for the platform with the ITO adhesion layer and gold layer annealed at 250°C for 1hr.

Appendix C. The step-by-step procedure to perform the particle size distribution analysis using the ImageJ software

The step-by-step procedure to perform the particle size distribution for an SEM image is described. For discussion and explanation purposes the SEM image of the Cr-Au platform that was annealed at 550°C for 1hr considered.

Step 1: To open the ImageJ software as shown in Figure C-1.

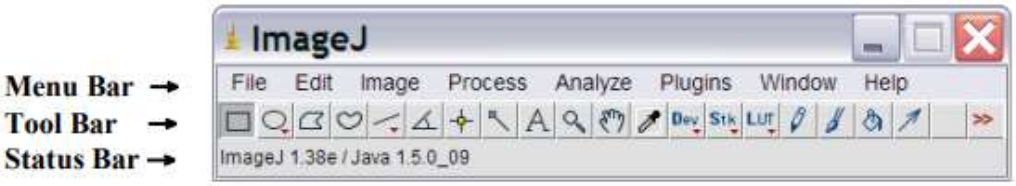

Figure C-1: ImageJ software menu, tool, and status bar.

Step 2: To open the obtained SEM image as shown in Figure C-2.

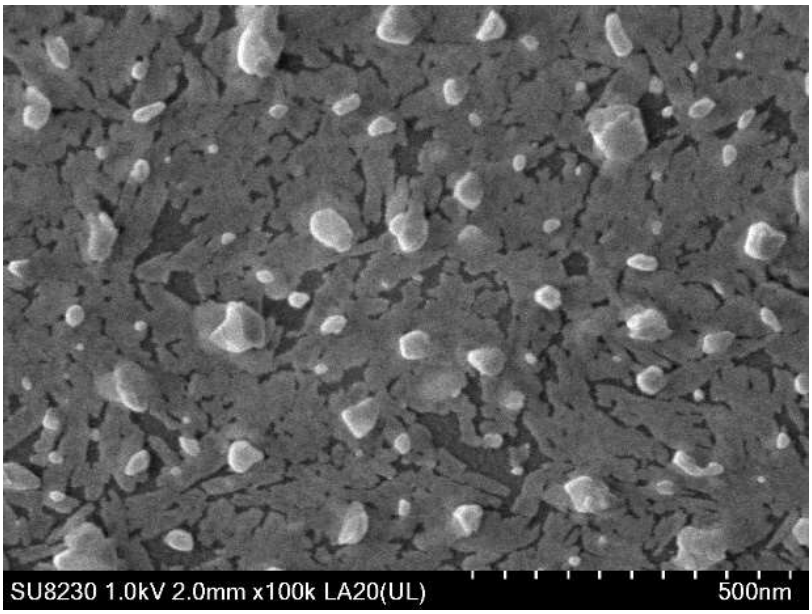

Figure C-2: SEM for the platform with the Cr adhesion layer and gold layer annealed at 550°C for 1hr.

Step 3: After opening the SEM image in the ImageJ software, remove the existing scale using the analyze menu and then set scale under this menu, and then click on remove scale as shown in

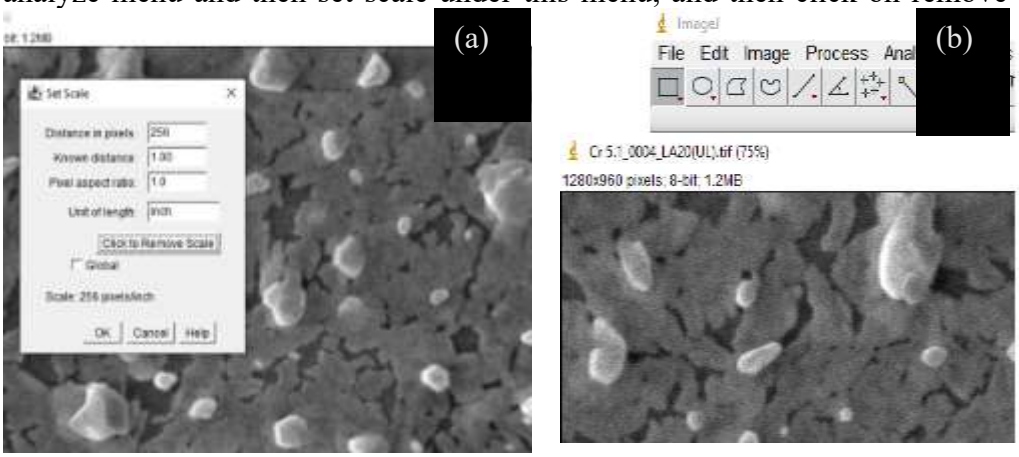

Figure C-3 (a). Once this step is completed the opened image will get converted to the number of pixels as shown in Figure C-3 (b).

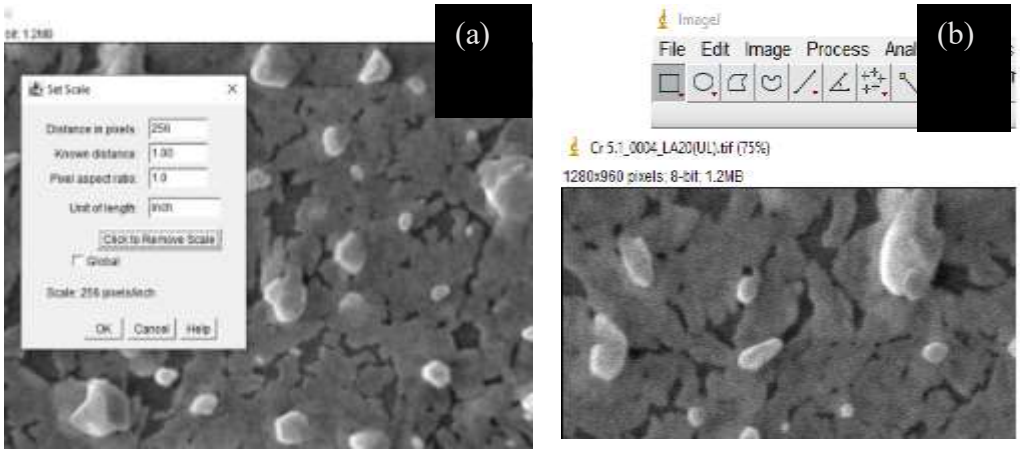

Figure C-3: Image scale removal and pixel conversion. (a) Removing the existing scale of the image. (b) Image converted to the number of pixels.

Step 4: The next step is to calibrate the image using the existing scale in the image that is being studied Therefore, using the line tool a line will be drawn as shown in Figure C-4 (a), and then set scale was set to the known dimension of the image as shown in the Figure C-4 (b) and calibrate it.

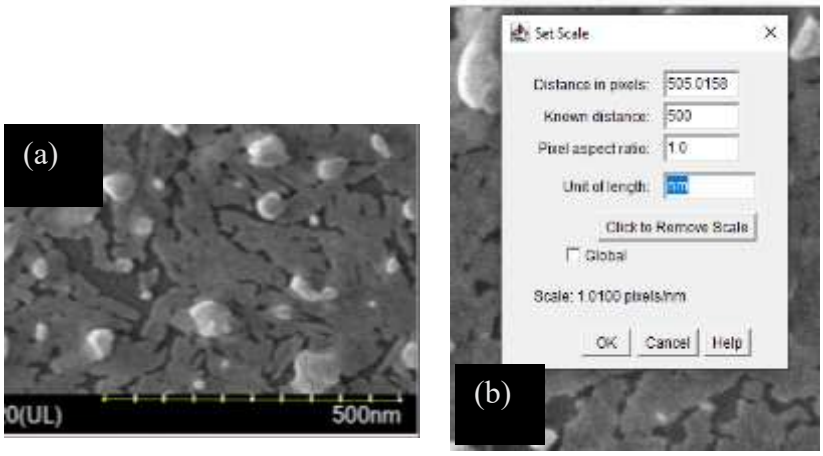

Figure C-4: Calibration of the image. (a) Drawing a line to the known dimension of the image. (b) Setting up the scale to the known dimension with the corresponding unit.

Step 5: Once the calibration step is completed the image will get converted into the unit that was set in the calibration step as shown in the figure.

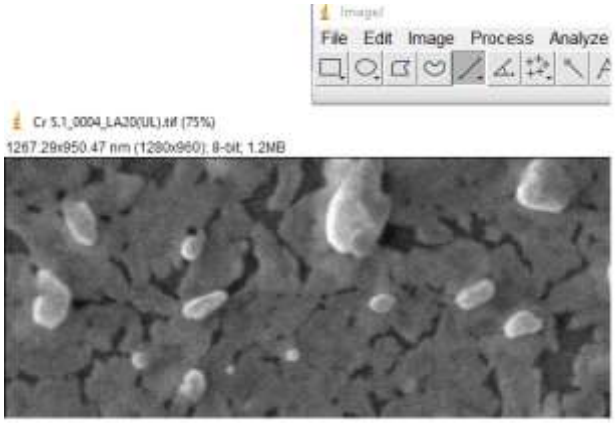

Figure C-5: Calibrated image as per the set scale.

Step 6: For particle size analysis an evenly illuminated area of the image is important therefore it is suggested to select the area as shownFigure C-6 (a) that has better illumination and duplicated as shown in Figure C-6 (b).

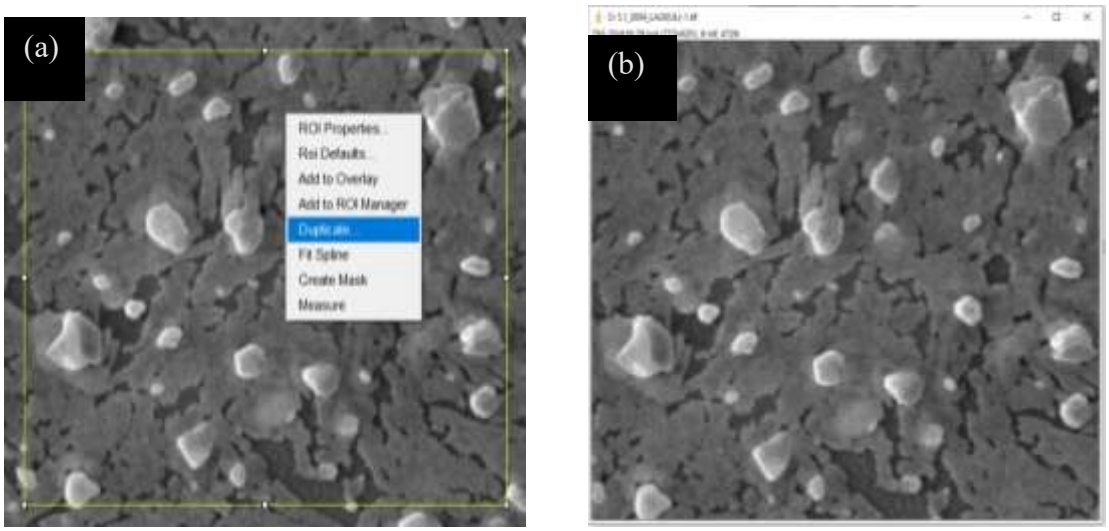

Figure C-6: Selecting the area of the image for particle analysis. (a) Selection of the area. (b) Duplication of selected area.

Step 7: To flatten the image by applying a bandpass filter using the process menu as shown in Figure C-7.

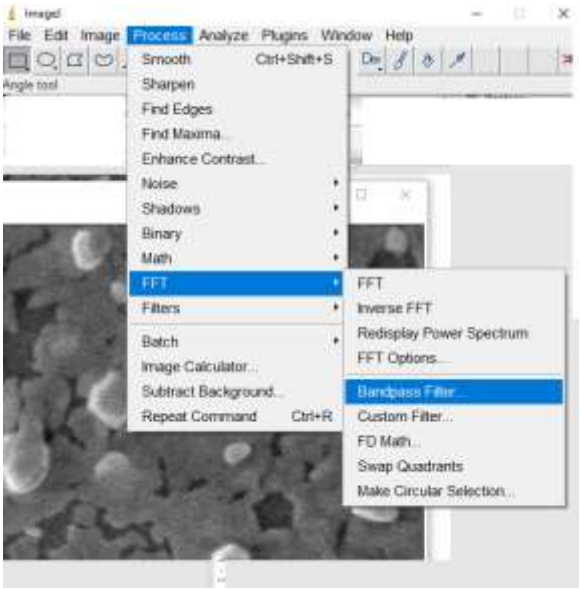

Figure C-7: Applying bandpass filter to flatten the image.

Step 8: Set up the threshold for the image as shown in Figure C-8 (a) and once it is completed the image will be as shown in Figure C-8 (b).

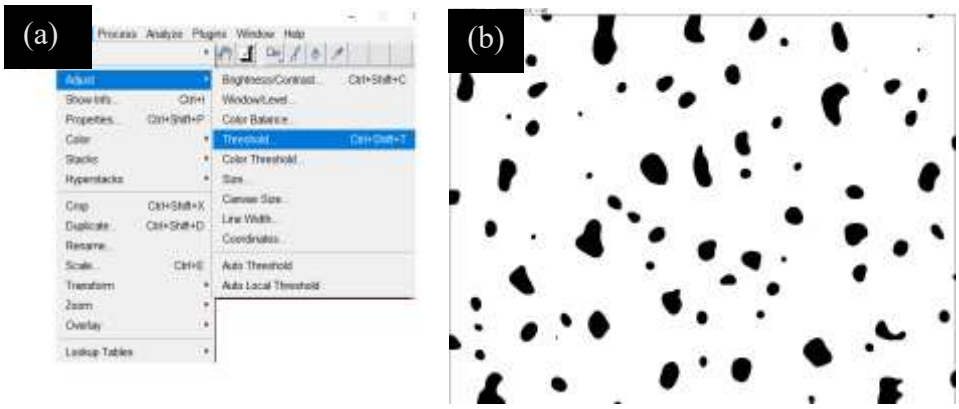

Figure C-8: Adjusting the image. (a) Setting up the threshold. (b) The image after the threshold is set up.

Step 9: To analyze the number of particles for the image as shown in Figure C-9 after setting up the minimum size of the particles.

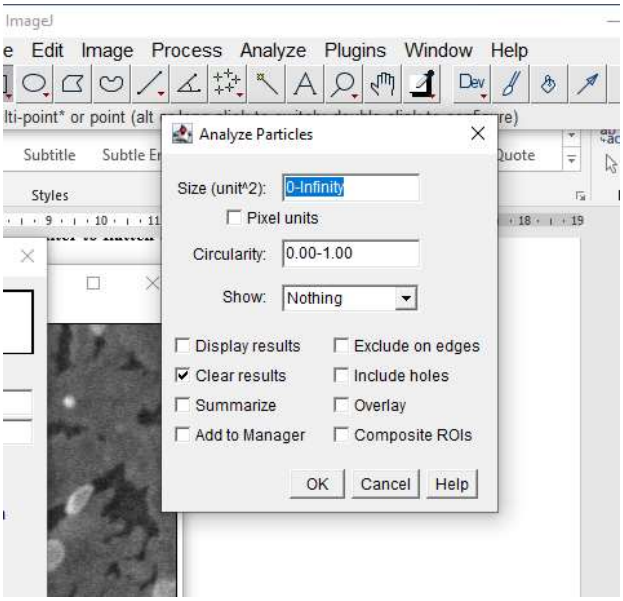

Figure C-9: Analyzing the number of particles for the image.

Step 10: The number of particles present in the image will appear as shown in Figure C-10.

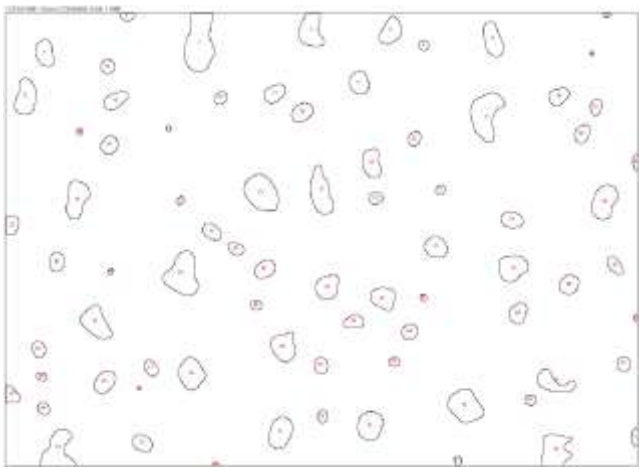

Figure C-10:Number of particles present in the image.

Step 11: The data for all the particles present in the image as shown in Figure C-10 will be available as shown in Figure C-11 after this the data can be saved as a text or Excel file.

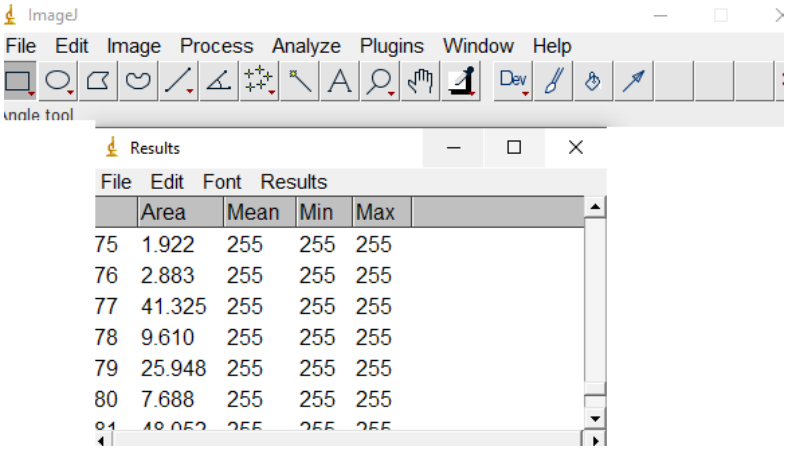

Figure C-11: Particle data file.

Step 12: The data will contain the area for each of the particles present in the image from which the diameter can be calculated and then using software like Origin or Excel the size distribution of the particles can be obtained as shown in Figure C-12

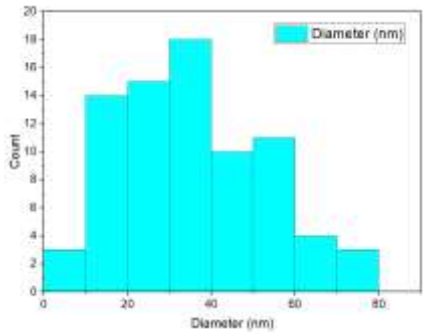

Figure C-12: Particle size distribution for the analyzed image.